MASTER OF SCIENCE THESIS

Investigation on supersonic, large wall roughness elements using QIRT and PIV

Author:
N. A. VOOGT

Supervisors:
Dr. ir. B. W. VAN OUDHEUSDEN
Dr. ir. F. J. J. SCHRIJER

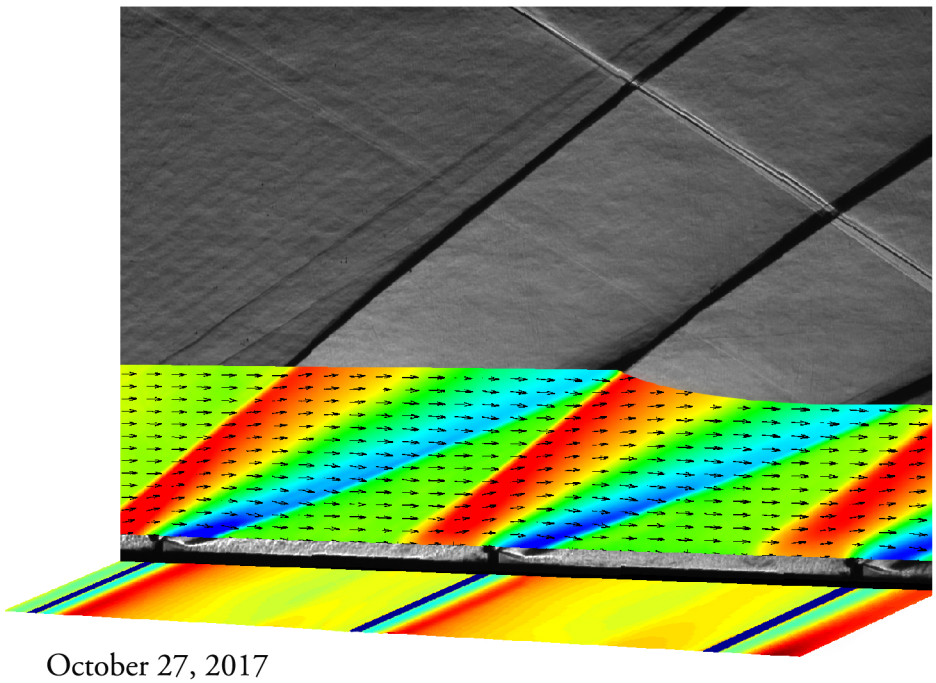

October 27, 2017

Aerodynamics

TU Delft

Faculty of Aerospace Engineering

Delft University of Technology

Facta non verba

Acknowledgments

This thesis marks the completion of my Master degree in Aerodynamics, at the department of Aerospace Engineering at the Delft University of Technology (TU Delft). During the course of my studies, I came across various subjects within the field of aerodynamics. It quickly became clear to me, however, that supersonic and hypersonic aerodynamics were definitely my favorite. Being a hands-on person, it only seemed logical to pursue a thesis topic which involved a lot of physical testing, designing and experimentation. Considering that I got the opportunity to conduct three different kinds of experimental techniques, one of which required to be self-designed and self-constructed, I could not possibly have asked for any more.

The last three years of academic and professional endeavoring have been of great value to my personal growth. I have to admit, though, that especially the past eleven months of thesis were undoubtedly the most valuable. A project as this one requires the researcher to be involved in a multitude of work, and brings about a great level of responsibility. Thus, apart from the understanding of the physics and techniques, I most of all learned how to manage a project like this. Fortunately, I received a great deal of help throughout the various phases of my thesis. To this end, I would like to thank, in no particular order, those who made this experience both educational and enjoyable. This is done in my mother tongue, Dutch.

Door de sturende, doch onbelemmerde houding van mijn begeleiders Dr. ir. B.W. (Bas) van Oudheusden en Dr. ir. F.F.J. (Ferry) Schrijer, was het voor mij mogelijk om zelfstandig de experimentele hordes en moeilijkheden aan te pakken en op te lossen. Vanuit deze filosofie ontstond een vruchtbare bodem die direct heeft bijgedragen aan een snelle, persoonlijke ontwikkeling; bedankt hiervoor. Speciale dankbetuigingen gaan uit naar de technici, Frits Donker Duyvis, Peter Duyndam, Dennis Bruikman, Stefan Bernardy en Nico van Beek, wie ik altijd kon storen voor een “serieus” verzoek of een praatje pot. Daarnaast wil ik graag alle bewoners van De Kelder bedanken voor het delen van voor- en tegenspoed, en uiteraard het accepteren van mijn hoogstaande, scherpzinnige en altijd bedachtzame humor. Graag wil ik Yorin van Weersch vernoemen, met wie ik alle ‘ups and downs’ van de thesis heb kunnen delen en altijd als meest dierbare vriend zal beschouwen. In het bijzonder wil ik mijn lieve vriendin en maatje, Nadine van Unnik, bedanken voor haar voltallige steun, geloof en vertrouwen. Haar optimisme, humor en volharding maakte het doorkomen van de vele uitdagingen draaglijk en aanvaardbaar. Tot slot wil ik mijn familie bedanken voor al hun steun gedurende de gehele lengte van mijn academische loopbaan. In het speciaal, mijn ouders James en Yvonne Voogt, mijn zus Karen Bouwens, zwager(t) Eric Bouwens en natuurlijk mijn (nu nog kleine) neefje Lennon Bouwens.

Geen woorden, maar daden,
-Nick

Abstract

The aim of the present study is to obtain quantitative insights on the influence of ribbed wall roughness elements on the mean flow, heat transfer and turbulence properties of a turbulent, supersonic boundary layer (M = 2.0 [-]). A total of fifteen test geometries, including one smooth and fourteen rough surfaces consisting of various relative roughness heights, e/δ and pitches, p/e are tested using spark-Schlieren, particle image velocimetry (PIV) and quantitative infrared thermography (QIRT).

As a qualitative visualization technique, Schlieren provided a means to accurately display the boundary layer development across the full length of each roughness geometry. By the derived spark-Schlieren images, it was observed that resulting flow fields displayed close resemblance with supersonic cavity type flows (combined with BL development). This led to a generalized flow characterization as *repeated cavity flows*, where geometries with a $p/e < 10$ are classified as *open*, those with $10 \leq p/e < 15$ as *transitional* and $p/e > 15$ as *closed*. In accordance to prior research, it was found that geometries with $p/e \leq 10$ provided a semi-no-slip condition such that the BL could develop regularly across the crest of the ribs. In contrast, for geometries with $p/e > 10$, interrupted BLs were formed.

By conducting the PIV technique, it was possible to quantify the previously visualized flow fields. Two individual sub-campaigns were conducted; one where the considered field of view (FOV) encompassed the flow directly above the crest of the ribs, and another where there was looked inside the cavity of the final rib pair of select test plates. In either campaigns, both mean flow ($\overline{u}$, $\overline{v}$) and mean turbulence parameters ($\overline{u'}$, $\overline{v'}$ and $\overline{u'v'}$) were obtained. From this, it was observed that p/e variances affect the flow topologies through the occurrence of different discontinuities, whereas e/δ predominantly alters the strength of these discontinuities. Turbulence data has shown that – provided the existence of closed cavity flow – rib impingements enhance the turbulence parameters. Still, averaged turbulence profiles indicate that the most optimal turbulent mixing takes place for a geometries with a p/e = 10.

The heat transfer measurements were performed by means of the heated-thin-foil technique, which practically provided a constant heat flux boundary condition, and by using an infrared camera and K-type thermocouples. This QIRT setup was self-designed and constructed such to provide an accurate and reliable mapping of the temperatures across each surface of the interchangeable test models. These models consisted of a Makrolon insulation, printed circuit board (PCB) surface and geometry-specific SikaBlock ribs. The constant heat flux condition was created by applying electric power to the PCB, delivering Ohmic heating. By tailoring the amount of electric power, steady-state conditions were reached within an average of 23 *sec* at a temperature contrast, ΔT_{con} of 37.3 K. Even though the initial total electric power estimate was slightly higher, the test models functioned as expected.

Equally to the PIV campaign, two sub-campaigns were distinguished for QIRT; one quantitative, comprising the entire roughness geometry as FOV, the other qualitative, covering a single cavity of select test plates. As steady thermal states were reached for each experiment, convective heat transfer coefficients (h, St) were evaluated using a data reduction scheme based-on the heat balance equation. By the novelty of this self-established QIRT setup and data reduction routine, the validity of the derived heat transfer coefficients needed to be proven. The overall functionality of QIRT was verified by conducting a repeatability study, where each test plate was investigated at three increasing power levels. Between the consecutive measurements, an average 1.1% variance existed, displaying the reliability of the setup. In turn, the accuracy of the QIRT system was proven by validating the derived heat transfer results with analogous turbulence profiles. By the proven correspondence between St and τ_{ij}, specific flow phenomena were linked directly between the profiles of independent measurement techniques. Finally, flat plate St measurements remained within $\pm$ 5% of their approximate solution estimates. As such, the QIRT technique is certain to be both accurate and reliable, having an average error margin of 4.6%. With the latter set, it was substantiated to draw conclusions from the obtained heat transfer data.

The heat transfer data was presented in terms of local, averaged St-profiles of the final cavities of each test plate; embodying the most developed flow. Generally, it was found that geometries with a closed cavity flow provided the most optimal heat transfer. This was caused by the highly improved BL-wall interaction. Interestingly it was observed that, opposite to turbulence data, the maximum heat transfer was found for the geometry having a p/e of 25 instead of 10. The reason for this discrepancy was assigned to the difference in measurement location between PIV and QIRT, respectively located 3 *mm* above the rib tops and directly at the surface. Even though the latter geometry has a maximum R_{xy}, this is only beneficial to heat transfer provided there exist wall interaction. This feature is enforced by the insulating effect of increasing the rib height. Across all cavity type flows, increased e/δ enlarge the distance between the BL and the wall; reducing the overall heat transfer.

The conclusions drawn from this thesis help to improve the understanding of what effects various flow phenomena have on the overall heat transfer properties of ribbed roughness geometries. With this gained knowledge, designers of future supersonic (nozzle) cooling channels can more adequately avoid the flow effects associated with wall insulation. It is foreseen that the commonly utilized closely-spaced cooling channels practically insulate their own surfaces by allowing recirculations to form. As such, it is recommended to use geometries at e/δ = 0.2 [-] with a minimal p/e of 15 [-]. Additionally, the designed QIRT is arranged such that any type of roughness can be mounted onto its heated surface. By the fact that the functioning of the QIRT setup is validated and sufficiently accurate, numerous future heat transfer experiments are expected.

Contents

Acknowledgments **v**

Abstract **vii**

1 Introduction **1**

2 Theoretical background **7**
2.1 Heated, flat plate boundary layer . . . 7
2.1.1 Boundary layer concept . . . 7
2.1.2 Typical flow parameters . . . 9
2.1.3 Navier-Stokes equations . . . 11
2.1.4 Reynolds analogy . . . 11
2.1.5 Approximate solutions . . . 12
2.2 The effects of wall roughness . . . 13
2.2.1 Definition of large scale roughness . . . 14
2.2.2 Small-scale roughness in supersonic flows . . . 16
2.2.3 Large-scale roughness in subsonic flows . . . 21
2.2.4 Repeated cavity flow and IRT . . . 27
2.3 Supersonic cavity flows . . . 33
2.3.1 Influence on cavity flow classification . . . 33
2.3.2 Classifications of cavity flow types . . . 34
2.4 Description of the flow fields . . . 36

3 Flow facilities and visualization **39**
3.1 Supersonic wind tunnel . . . 39
3.2 Model description . . . 40
3.2.1 Geometrical definitions . . . 40
3.2.2 Model design: Schlieren and PIV . . . 41
3.3 Schlieren . . . 42
3.3.1 Working principle . . . 42
3.3.2 Experimental setup . . . 44
3.4 Particle image velocimetry . . . 46
3.4.1 Working principle . . . 46
3.4.2 Experimental requirements . . . 47
3.4.3 Experimental considerations . . . 48
3.4.4 Experimental setup . . . 53
3.4.5 Data reduction . . . 54
3.4.6 Uncertainty analysis . . . 56
Ensemble size uncertainty . . . 57
Convergence study . . . 57
PIV inherent uncertainty . . . 58
Summary . . . 60

4 Quantitative infrared thermography **63**
4.1 Heated, thin-film model design . . . 63
4.1.1 Test plate design . . . 64
System requirements . . . 64
One-dimensional, semi-infinite solid analysis . . . 64
4.1.2 Test plate assembly . . . 70
4.1.3 Cavity door design . . . 73
4.1.4 Complete QIRT test setup . . . 74
4.2 Measurement technique . . . 75
4.2.1 Radiation heat transfer . . . 75
4.2.2 Data acquisition system . . . 82
Infrared camera . . . 82
System performance . . . 84
4.2.3 IR system operation . . . 86
4.2.4 Calibration . . . 87
4.2.5 Experimental setup and operation . . . 92
4.3 Data reduction procedure . . . 95
4.3.1 Overview data reduction routine . . . 96
4.3.2 Pre-processing . . . 97
4.3.3 Non-uniform heating correction . . . 98
4.3.4 Transient temperature analysis . . . 100
4.3.5 Heat flux computation . . . 101
Electric heat flux . . . 101
Conductive heat flux . . . 102
Radiative heat flux . . . 105
4.3.6 Post-processing . . . 106
4.3.7 Order of magnitude analysis . . . 107
4.3.8 Uncertainty analysis . . . 110

5 Results **113**
5.1 Flow visualization . . . 113
5.1.1 Nomenclature for discontinuities . . . 113
5.1.2 The effect of pitch . . . 114
5.1.3 The effect of height . . . 122
5.1.4 Boundary layer profiles . . . 127
5.1.5 Summary . . . 129
5.2 QIRT . . . 130
5.2.1 Repeatability of QIRT . . . 131
5.2.2 QIRT validation . . . 133
5.2.3 Heat transfer profiles . . . 135
5.2.4 Primary vs. secondary campaign . . . 140
5.2.5 Trends and correlations . . . 142
5.2.6 Summary . . . 144

6 Conclusions **147**

7 Recommendations **151**

Bibliography **155**

A Heat transfer and skin friction correlations **160**

B Mechanisms of open – transitional – closed cavity flow transition **163**

C Technical drawings **167**
C.1 Schlieren and PIV . . . 167
C.1.1 Leading edge insert . . . 167
C.1.2 Trailing edge insert . . . 168
C.1.3 Exemplary wind tunnel model . . . 169
C.2 QIRT . . . 170
C.2.1 Printed circuit board . . . 170
C.2.2 Insulation plate . . . 171
C.2.3 Cavity door . . . 172

D IR camera description - CEDIP 530L **173**

E IR lens design - LW 25mm 2.0 Jade **174**

F IR camera description – Optris PI 640 **175**

G List of experiments **176**
G.1 Schlieren . . . 176
G.2 PIV . . . 177
G.3 QIRT . . . 178

H Periscope probe placement **183**

I Optical settings PIV **185**

J Experimental setups **186**
J.1 Schlieren . . . 186
J.2 PIV . . . 187
J.3 QIRT: assembly . . . 191
J.4 QIRT: testing . . . 192

K Derivation one-dimensional heat transfer problem **196**

L Working principle of thermocouples **200**

M QIRT experimental checklist **202**

N PCB resistance variance **203**

O Oblique shock wave interference **205**

P Blackbody inhomogeneity **207**

Q Reference flat plate **208**

R PIV fields **209**

S Cavity PIV **218**

List of Figures

1.1 Ariane 5 launch vehicle at lift-off.[1] (ESA, 2013) . . . 1
1.2 Ariane 5 tube nozzle, incl. cooling channels.[2] (ESA, 2013) . . . 1
1.3 Schematics of circular cooling tubes (left), and heat exchange promoters (right) 2
1.4 Thermogramme of cool author . . . 3

2.1 Boundary layer profiles.[17] (Pope, 2001) . . . 7
2.2 *k-type* roughness.[21] (Perry et al, 1996) . . . 15
2.3 *d-type* roughness.[21] (Perry et al, 1996) . . . 15
2.4 Mean velocity profiles (LDA and pitot data).[11] (Latin and Bowersox, 2000) . . 17
2.5 Schlieren photograph 20 Grit sandpaper roughness.[11] (Latin and Bowersox, 2000) . . . 17
2.6 Effective velocity defect (pitot data).[11] (Latin and Bowersox, 2000) . . . 18
2.7 Effective law of the wall (pitot data).[11] (Latin and Bowersox, 2000) . . . 18
2.8 Turbulence intensity profiles, u' and v'.[11] (Latin and Bowersox, 2000) . . . 19
2.9 Reynolds stress profiles, $\overline{u'v'}$.[11] (Latin and Bowersox, 2000) . . . 19
2.10 Compressible Reynolds stress profiles.[11] (Latin and Bowersox, 2000) . . . 20
2.11 Peak difference in the compressible Reynolds stress w.r.t. k_s^+.[11] (Latin and Bowersox, 2000) . . . 20
2.12 Definition of rib design parameters.[6] (Han, 1984) . . . 22
2.13 Friction factors versus Re at various p/e and e/D_h.[8] (Liou and Hwang, 1992) 23
2.14 $\overline{Nu}/\overline{Nu}_s$ versus Re at various p/e and e/D_h.[8] (Liou and Hwang, 1992) . . . 23
2.15 Streamwise distributions of local Nusselt number, turbulent kinetic energy, and wall temperature.[8] (Liou and Hwang, 1992) . . . 24
2.16 Calculated streamlines for characteristic flow fields (a) $p/e = 5$, (b) $p/e = 10$ and (c) $p/e = 15$.[29] (Liou et al, 1990) . . . 26
2.17 Streamwise distributions of mean velocity and turbulence intensity at 1 mm from the rib tops for p/e = 5, 10 and 15.[29] (Liou et al, 1990) . . . 27
2.18 Experimental setup incl. insulated ribbed plate covered with stainless steel foil, IR camera and pitot tube.[10] (Aliaga et al, 1994) . . . 28
2.19 Mean velocity profiles in test section of wind tunnel (Re = 10^6, p/e = 5).[10] (Aliaga, 1993) . . . 29
2.20 Heat transfer coefficient profiles in test section of wind tunnel (Re = 10^6, p/e = 5).[10] (Aliaga, 1993) . . . 29
2.21 Mean velocity profiles in test section of wind tunnel (Re = 10^6, p/e = 12).[10] (Aliaga, 1993) . . . 30
2.22 Heat transfer coefficient profiles in test section of wind tunnel (Re = 10^6, p/e = 12).[10] (Aliaga, 1993) . . . 30
2.23 Local h distribution and flow visualization with indicative recirculation and reattachment regions on test plates.[10] (Aliaga et al, 1993) . . . 31
2.24 Effect of the relative roughness height on St at the cavity surface.[10] (Aliaga et al, 1993) . . . 32
2.25 Surface flow patterns of three-types of cavity flows.[13] (Zhang et al., 2002) . . . 34

2.26 Classification of cavity flow types by varying p/e; respectively closed (top), transitional (middle) and open (bottom) cavity flows.[34] (Stallings and Wilcox, 1987) . . . 35
2.27 Repeated open and closed cavity flow, respectively p/e of 5 (top) and 15 (bottom). *Sketch is based on sources described previously.* . . . 37

3.1 Schematic of the ST-15 supersonic wind tunnel.[42](Sun et al., 2014) . . . 39
3.2 Schematic of the roughness geometries, incl. design definitions. . . . 41
3.3 Schematic of the ST-15 wind tunnel, incl. model placement. . . . 42
3.4 Refraction of light. . . . 43
3.5 Working principle of the Schlieren knife over y-axis. . . . 44
3.6 Experimental setup for Schlieren visualization (upper view). . . . 44
3.7 Continuous versus Spark Schlieren on 3.6/20 test plate. . . . 45
3.8 Spark-Schlieren addition to experimental setup, measuring equipment. . . . 46
3.9 Schematic of a typical PIV measurement system.[47] (Raffel et al., 2013) . . . 47
3.10 PIV camera fields of view projection onto Schlieren image. . . . 48
3.11 Pulse separation time and laser illumination. . . . 49
3.12 Assembly of the laser periscope probe design with cut-outs.[43] (Donker Duyvis, 2005) . . . 50
3.13 Primary PIV campaign camera setup at ST-15. . . . 51
3.14 Schematic of PIV setup (scale of components may be exaggerated for clarity). 53
3.15 PIV image treatment prior to the cross-correlations procedure. . . . 55
3.16 Image windowing and discrete cross-correlation map . . . 55
3.17 PIV velocity fields processing: cavity measurement 2.4/30 model camera (1). 56
3.18 Convergence of the considered flow variables. . . . 58
3.19 Critical flow region for 2.4/30 geometry. . . . 61

4.1 Schematic of the heat transfer problem. . . . 65
4.2 PCB copper track layout, and detailed connector region incl. vias. . . . 68
4.3 Steady-state properties of Makrolon, relative to material thickness . . . 69
4.4 Makrolon insulation plate design. . . . 70
4.5 Initial glue curing setup incl. power supply, bench vice, plastic covered models and straightening plates. . . . 71
4.6 Thermal signature of PCB at steady-state under stagnant conditions. . . . 72
4.7 Rib placement frame and interchangeable geometry combs. . . . 72
4.8 Final design of the ST-15 IRT cavity door, outside view (left) and inside (right). 73
4.9 Mounting of the test plate to the cavity door, mounted (left) and exploded view (right). . . . 74
4.10 Complete representation of the IRT door setup, incl. ST-15 Mach blocks. . . . 74
4.11 Illustration of incident, reflected and absorbed radiation in terms of total radiation properties.[63] (Kreith et al., 2012) . . . 76
4.12 Black body spectral radiant emittance.[63] (Kreith et al., 2012) . . . 77
4.13 Variation of monochromatic absorptivity (or emissivity) with wavelength for three electrical conductors at room temperature.[63] (Kreith et al., 2012) . . . 78
4.14 Effect of temperature on hemispherical total emissivity (ϵ) of several metals.[63] (Kreith et al., 2012) . . . 79
4.15 Variation of total absorptivity (α) with source temperature for multiple material types at room temperature.[63] (Kreith et al., 2012) . . . 79
4.16 Variation of directional emissivity with emission angle for several electrical nonconductors.[63] (Kreith et al., 2012) . . . 80

4.17 Variation of directional emissivity with emission angle for several metals.[63] (Kreith et al., 2012) . . . 80
4.18 Transmissivity of air for different wavelengths.[68] (Mayer, 1996) . . . 81
4.19 Infrared cameras used for respectively the primary and secondary IRT campaigns. . . . 83
4.20 Cedip camera setup. . . . 85
4.21 FOV primary campaign. . . . 85
4.22 Optris camera setup. . . . 85
4.23 FOV secondary campaign. . . . 85
4.24 The effect of the non-uniformity correction on a blackbody, excl. or incl. bad pixel replacement. . . . 87
4.25 Representation of the blackbody concept (A) and technical drawing (B).[75,76] (Astarita and Carlomagno, 2013; Schrijer et al., 2003) . . . 88
4.26 Setup for the calibration measurements. . . . 89
4.27 Recorded image of the blackbody during calibration process. . . . 90
4.28 Calibration curve, including Plank's law fit and optimized fit. . . . 90
4.29 Recorded image of test plate emissivity computation. . . . 91
4.30 Emissivity variation with surface temperature. . . . 91
4.31 Schematic representation of the IRT setup at the ST-15. . . . 92
4.32 Thermocouple acquisition tray, incl. Newport controller. . . . 92
4.33 Delta Electronika SM600-10 power supply. . . . 92
4.34 Upper view of the entire QIRT setup. . . . 93
4.35 Heated model setup at ST-15 wind tunnel. . . . 94
4.36 Flowchart of IRT data reduction routine. . . . 96
4.37 Primary actions performed during the pre-processing routine. . . . 98
4.38 NUHC obtained for the 4.8/5 configuration. . . . 100
4.39 Locations on FOV used for transient temperature analysis. . . . 100
4.40 Transient temperature analysis for steady-state definitions. . . . 101
4.41 Sketch of a printed circuit board. . . . 103
4.42 Cross-sectional view of the PCB model. . . . 104
4.43 Interpolated thermocouple temperature field. . . . 105
4.44 Indication of the spatial region used for profile computation. . . . 106
4.45 Transient convergence study. . . . 107
4.46 Heat transfer coefficient field, including $q_{cond.s}$. . . . 108
4.47 Heat transfer coefficient field, excluding $q_{cond.s}$. . . . 108
4.48 h cavity profile for 3.6/15 model, incl. and exlc. $q_{cond.s}$-term. . . . 109
4.49 Variance of the convective heat transfer coefficient, incl. and excl. $q_{cond.s}$. . . . 110

5.1 Discontinuity types occurring in the ST-15. . . . 114
5.2 The effect of pitch at constant rib height $e = 2.4mm$ or $e/\delta = 0.4$. . . . 115
5.3 Zoomed spark-Schlieren representation of open- and closed cavity flow. . . . 116
5.4 Selected planar v/U_∞ – fields, for $e/\delta = 0.4$ and $5 \leq p/e \leq 30$. . . . 117
5.5 Development of Reynolds stress, sequence 4. . . . 118
5.6 Planar $\overline{u'v'}/U_\infty^2$ – fields, for $e/\delta = 0.4$ and $p/e \leq 30$. . . . 119
5.7 Planar flow fields for the final cavity of the 2.4/30 model. . . . 120
5.8 Planar flow fields for the final cavity of the 2.4/15 model. . . . 121
5.9 The effect of rib height for open (L) - and closed-cavity (R) type flows. . . . 122
5.10 Development of mean flow (left) and turbulence properties (right), sequence 1. 123
5.11 Planar v/U_∞ – fields, for $p/e = 5$ and respectively $e/\delta = 0.2, 0.6$. . . . 124
5.12 Planar $\overline{u'v'}/U_\infty^2$ – fields, for $p/e = 5$ and respectively $e/\delta = 0.2, 0.6$. . . . 124
5.13 Planar $\overline{u'v'}/U_\infty^2$ – fields, for $p/e = 20$ and respectively $e/\delta = 0.2, 0.6$. . . . 125

5.14 Development of mean flow (left) and turbulence properties (right), sequence 3. 126
5.15 Planar v/U_∞ – fields, for $p/e = 20$ and respectively $e/\delta = 0.2, 0.6$. 127
5.16 BL development across open cavity geometries, 2.4/5 (left) and 3.6/5 (right). 128
5.17 BL development across closed cavity geometries, 2.4/20 (left) and 3.6/20 (right).128
5.18 Transitional BL profiles. 129
5.19 h-comparison between three 2.4/10 models. 132
5.20 Comparison of turbulence and heat transfer profiles for 2.4/25 model. 133
5.21 Comparison of turbulence and heat transfer profiles for 3.6/5 model. 134
5.22 Measurement locations used for combined profile analysis; PIV (red), QIRT (blue). 134
5.23 Comparison of the final cavity profiles, e/δ = 0.4 136
5.24 Final open cavity profiles, p/e = 5 at 1.2 mm (left) and 3.6 mm (right). 138
5.25 Final closed cavity profiles, p/e = 15 at 1.2 mm (left) and 4.8 mm (right). . . . 139
5.26 Final closed cavity profiles, p/e = 20 at 1.2 mm (left) and 3.6 mm (right). . . . 139
5.27 Cavity profile for 1.2/5 geometry. 140
5.28 St-profiles over two campaigns; 2.4/10 (left) and 3.6/15 (right) models. . . . 141
5.29 Correlations for the heat transfer and turbulence properties, sequence 4 . . . 142
5.30 Correlated trends between $\overline{u'v'}$ and St for sequence 2 (left) and 3 (right). . . . 143
5.31 Correlated trends between $\overline{u'v'}$ and St for sequence 1 (left) and 4 (right). . . . 143

6.1 Schematic representation of flow field development and corresponding heat transfer and turbulence profiles. 149

7.1 Damage to test model and Germanium window after PCB shear-off. 152

A.1 Comparison of prediction methods with present friction data.[6] (Han, 1984). . 161
A.2 Comparison of prediction methods with present heat transfer data.[6] (Han, 1984). 162

B.1 Changes of cavity flow types with l/h. (Zhang et al., 2002)[13] 164
B.2 Sketches of flow fields during the opening of closed-type cavity flow.[13] (Zhang et al., 2002) 165
B.3 Characteristic lengths for closed cavity flows.[13] (Zhang et al., 2002) 166

H.1 Placement of the laser periscope probe and cut-off plate, primary campaign. . 183
H.2 Placement of the laser periscope probe, secondary campaign. 184

J.1 Schlieren-visualization setup: image capturing side. 186
J.2 Schlieren-visualization setup: illumination side. 186
J.3 Placement of the test plate and inserts, test section exposed. 187
J.4 Complete overview of the ST-15 facility with PIV equipment. 187
J.5 Upper view of PIV setup at the ST-15. 188
J.6 PIV setup: illumination side (left) and imaging side (right). 188
J.7 Calibration plate used for image scaling, camera and laser alignment. 189
J.8 Laser path: traveling from the laser exit to the probe into the test section. . . . 189
J.9 Laser probe located downstream of the test section. 190
J.10 Laser probe and cut-off knife, functionality display. 190
J.11 Gluing station, incl. power supply and compression setups. 191
J.12 Plastic wrapped test plate right after gluing. 191
J.13 Rib mounting, incl. mounting frame as placement aiding tool. 192
J.14 Calibration equipment, incl. thermal bath (left) and blackbody (right). 192
J.15 QIRT setup, excl. black cloth and protective screens for clarity. 193

J.16 QIRT setup: primary (left) and secondary campaign (right). 193
J.17 QIRT test plate placement, incl. aerodynamic tape at the leading edge. 194
J.18 QIRT cavity door, outside view. 194
J.19 Primary QIRT camera cover used for NUC and BPR routines. 195
J.20 Interlock switch and power supply connector. 195

L.1 Thermocouple read-out for ice bath or cold junction.[76] (Schrijer et al., 2003) . 200

N.1 Base resistivity of all PCBs. 203
N.2 Base resistivity of selected PCBs. 204

O.1 Placement test models, including OSW at nozzle discontinuation. 205
O.2 Schematic of OSW shock wave interference and corresponding flow parameters.206
O.3 Physical placement of the test models. 206

P.1 combined characteristics of the blackbody and calibration procedure. 207

Q.1 Flat plate heat transfer profile, incl. error margins. 208
Q.2 Spark-Schlieren image, flat plate model. 208

R.1 Planar u'/U_∞ – fields, for varying e/δ and $p/e = 5$. 209
R.2 Planar u/U_∞ – fields, for varying e/δ and $p/e = 15$. 210
R.3 Planar v'/U_∞ – fields, for varying e/δ and $p/e = 15$. 211
R.4 Planar u/U_∞ – fields, for varying e/δ and $p/e = 20$. 212
R.5 Planar v'/U_∞ – fields, for varying e/δ and $p/e = 20$. 213
R.6 Planar u/U_∞ – fields, for $e/\delta = 0.4$ and $p/e \leq 15$. 214
R.7 Planar u/U_∞ – fields, for $e/\delta = 0.4$ and $p/e \geq 20$. 215
R.8 Planar v'/U_∞ – fields, for $e/\delta = 0.4$ and $p/e \leq 15$. 216
R.9 Planar v'/U_∞ – fields, for $e/\delta = 0.4$ and $p/e \geq 20$. 217

S.1 Planar flow fields, insufficient image pair quality. 218

List of Symbols

Latin symbols

Symbol	Unit	Description
a	mm	Schlieren light offset
a_p	m/s^2	Particle acceleration
A	m^2	Surface area
B	$[-]$	Scanner calibration factor
c	m/s	Speed of light
C_f	$[-]$	Skin friction coefficient
c_p	kJ/kgK	Specific heat capacity at constant pressure
d	mm	Diameter
D_h	mm	Hydraulic diameter
dz	mm	Laser sheet thickness
e	mm	Roughness height
E	W/m^3	Spectral radiation energy
f	mm	Focal length
F	$[-]$	Response calibration factor
$f_\#$	$[-]$	Aperture
h	W/m^2K	Convective heat transfer coefficient
H	$[-]$	Boundary layer shape factor
I	A	Electrical current
k	W/mK	Thermal conductivity
K	m^3/kg	Gladstone-Dale constant
l	mm	Length
L	mm	Thickness
M	$[-]$	Mach number
M (optics)	$[-]$	Magnification factor
n	$[-]$	Refraction constant
N	$\#$	Number of images
Nu	$[-]$	Conductive heat transfer coefficient
p	mm	Pitch
P	Pa	Pressure
P (QIRT)	W	Electric power
Pr	$[-]$	Prandtl number
q	W/m^2	Heat flux
r	$[-]$	Recovery factor
R	Ω	Electrical resistance
R (Calibration)	$[-]$	Shape calibration factor
R_0	Ω	Base resistance

Re	$[-]$	Reynolds number
s	$[-]$	Reynolds analogy factor
S_k	$[-]$	Stokes number
St	$[-]$	Convective heat transfer coefficient
t	sec	Experimental duration
T	K	(surface) Temperature
u	m/s	Horizontal velocity component
$\overline{u'v'}$	m^2/s^2	Reynolds stress
U	V	Voltage
v	m/s	Vertical velocity component
w	mm	Width
x	mm	Streamwise direction
y	mm	Normal flow direction
z	mm	Normal surface direction

Greek symbols

Symbol	**Unit**	**Description**
α	m^2/s	Thermal diffusivity
α (R)	K^{-1}	Temperature coefficient of resistance
α (Rad. theory)	$[-]$	Absorptivity
γ	$[-]$	Heat capacity ratio
γ^*	$[-]$	PCB width ratio
δ	mm	Boundary layer thickness
ΔT_{con}	K	Temperature contrast with respect to T_{aw}
Δt	sec	Image pair separation time
δt	sec	Pulse separation time
δ^*	mm	Displacement thickness
δ_z	mm	Focal depth
ϵ	$\%$	Error
ϵ (Rad. Theory)	$[-]$	Spectral emissivity coefficient
θ	mm	Momentum thickness
θ (Rad. theory)	$^\circ$	Propagation direction
κ	Ω/m	Electrical conductivity
λ	m	Wavelength
μ	kg/ms	Viscosity
ν	m^2/s	Kinematic viscosity
ρ	kg/m^3	Density
ρ (R)	Ω/m	Electrical resistivity
ρ (Rad. Theory)	$[-]$	Reflectivity
σ	$[-]$	Standard deviation
σ (Rad. theory)	W/m^2K^4	Stefan-Boltzmann constant
τ	kg/ms^2	Skin friction
τ (Rad. theory)	$[-]$	Transmissivity
τ (PIV)	sec	Time scale
τ_{ij}	m^2/s^2	Reynolds stress ($\overline{u'v'}$)

Superscripts

Symbol	Description
$+$	Equivalent
$*$	Friction
$'$	Fluctuating, turbulent component
–	Average

Subscripts

Symbol	Description
0	Total
99	At 99% freestream velocity
∞	Freestream
λ	Per wavelength
amb	Ambient
atm	Atmospheric
aw	Adiabatic
$base$	Starting set point
bb	Blackbody
c	Copper wire
cal	Calibration
cav	Cavity
cc	Cross-correlation
$cond$	Conductivity
$cond.b$	Condcutivity into body
$cond.s$	Condcutivity across surface
$conv$	Convective heat transfer
cr	Critical
cu	Copper
$diff$	Diffraction
e	External
eff	Effective
el	Electrical power
eq	Equilivalent
est	Estimate
f	FR-4 base material
g	Glue
in	Input
max	Maximum
$meas$	Measured
min	Minimum
mk	Makrolon
$model$	Wind tunnel test plate
$o(bj)$	object
p	particle
PCB	Per printed circuit board

ps	Power supply
ref	Based on reference location in freestream
res	Resolution
s	Surface
sft	Safety limit
sp	Spatial
ss	Steady-state
sys	Systematic
T	Thermal
$test$	At moment of testing
var	Inherit sensitivity/ randomized variance
w	Wall
xx	Streamwise
xy	Shear
yy	Perpendicular to flow
zz	Normal to surface plane

Acronyms

Symbol	**Description**
1D	One-dimensional
2D	Two-dimensional
3D	Three-dimensional
BL	Boundary layer
BPR	Bad-pixel replacement
CCD	Charge-coupled device
CO_2	Carbon dioxide
CW	Compression wave
DEHS	Di-Ethyl-Hexyl-Sebacate
DL	Digital levels
DVR	Dynamic velocity range
EW	Expansion wave
FOV	Field of view
FPA	Focal plane array
H_2O	Di-hydrogen monoxide (water)
HEM	Heated empty measurement
HFOV	Horizontal field of view
HSC	High speed controller
HSL	High speed laboratory
IFOV	Instantaneous field of view
IR	Infrared
IRT	Infrared thermography
KE	Kinetic energy
LDV	Laser doppler velocimetry
LE	Leading edge
LWB	Long wave band
MCT	Mercury cadmium telluride
NETD	Noise equivalent temperature difference

NI	National instruments
NUC	Non-uniformity correction
NUHC	Non-uniform heating correction
OSW	Oblique shock wave
PCB	Printed circuit board
PIV	Particle image velocimetry
QIRT	Quantitative infrared thermography
RC	Recirculation
SC	Settling chamber
SL	Shear layer
SNR	Signal-to-noise
ST	Supersonic tunnel
SW	Shock wave
SWB	Short wave band
TB	Terminal block
TE	Trailing edge
TK	Thermocouple
TKE	Turbulent kinetic energy
TiO_2	Titanium dioxide
UEM	Unheated empty measurement
UFPA	Uncooled focal plane array
VFOV	Vertical field of view
WB	Wave band
WS	Window size
WTM	Wind tunnel measurement

Chapter 1

Introduction

Launch vehicles In spaceflight, a launch vehicle or carrier rocket is a rocket used to carry a payload from the Earth's surface into outer space. Although the payload for such a carrier rocket is often an artificial satellite, some spacecraft also include supplies for the international space station (ISS) or even astronauts. Launch vehicles are often classified by the amount of mass they can carry or the type of orbit they can reach; i.e. low-, medium- or high-earth-orbit (LEO, MEO, HEO). In accordance to the classifications, their designs are tailored by being equipped with boosters, which supply high initial thrust, or by adding multiple stages. Generally, launcher propulsion or thrust is delivered by rocket engines which are triggered subsequently for the rocket stages. By traveling supersonically, launch vehicles are exposed to harsh environmental conditions during the various phases of operation. However, the most extreme operational conditions are encountered within the rocket engines themselves.



FIGURE 1.1: Ariane 5 launch vehicle at lift-off.[1] (ESA, 2013)



FIGURE 1.2: Ariane 5 tube nozzle, incl. cooling channels.[2] (ESA, 2013)

A rocket engine roughly consists of three main components: a fuel pump, combustion chamber and nozzle. The first components delivers both oxidizer and fuel into the combustion chamber, where the two components are mixed and ignited. After this, the energized flow is expanded controllably by the nozzle contour up to a Mach number of 3. Within this process, combustion temperatures can reach an excess of 3000 K followed by a 'mere' 1100 K at the

nozzle surface. Considering that these temperatures tremendously exceed the maximum operating temperatures of typical launcher materials (i.e. aluminum, steel etc.), active cooling is required to enable continuous operation of the engines. The latter can be achieved in multiple ways, for example: *film cooling*, *ablation* and *cooling channels*.

In the case of film cooling, a cool fluid is injected into the stream which creates a thermal barrier between the nozzle wall and hot exhaust fumes. With an ablated wall, the exhaust heat is used to actively burn off parts of the inner surface of the launcher. By thus converting the heat into energy required to initiate this burning, the shell of the nozzle is protected. Another option is to install cooling channels onto the inner surface of the nozzle. By then pumping fuel through these channels, part of the heat protrudes the nozzle wall and is taken up by this fluid. Additionally, fuel is sufficiently pre-heated prior to entering the combustion chamber; optimizing rocket engine performance. As this is the only system which does not require additional fluids as cooling material, it is highly suited for the new generation of reusable launch vehicles such as the Falcon 9 by SpaceX.[3] (SpaceX, 2016) The downside of this system, however, is that the otherwise smooth nozzle surface is influenced by this introduction of uniform surface roughness (Figure 1.3).

Thermal control by cooling channels Practically any aerodynamic vehicle, requires its design to avoid surface roughness as much as possible. Especially in supersonic flows, the occurrence of roughness elements generally gives rise to an increased skin friction and heat transfer. Nevertheless, the application of cooling channels is such an example where surface roughness is introduced deliberately to promote the local turbulent mixing and heat transfer properties. In more common subsonic applications, similar turbulence promoters are embodied by consecutive ribbed roughness elements, and can be found in the heat exchangers of power plants, nuclear reactors and even turbine blades.

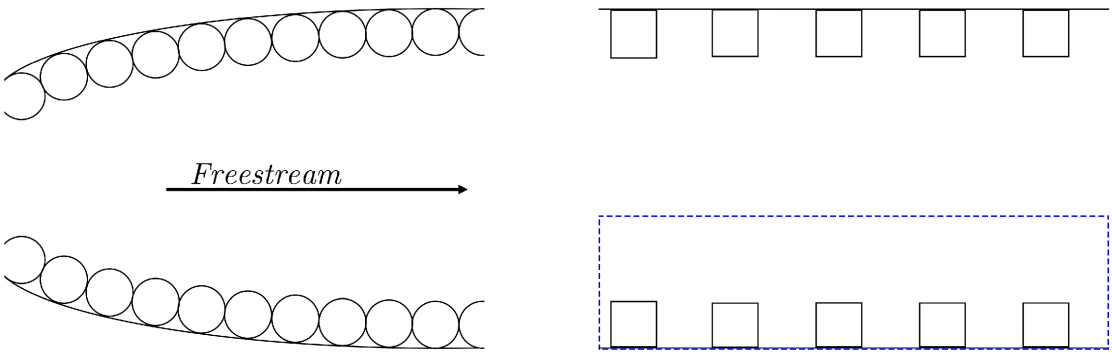

FIGURE 1.3: Schematics of circular cooling tubes (left), and heat exchange promoters (right)

.

An example of cooling channels is found on the inner surface of the second stage tube nozzle of Ariane 5 launcher.[4] (B. Church, 2015) These channels are formed by constant cross-sectional, hollow tubes which are welded onto the inner surface of the nozzle (Figure 1.2). Even though the application of these circular cooling channels are quite common, detailed investigations on their more fundamental design properties are absent for flow conditions similar to those encountered in rocket nozzles. As such, it is decided eliminate the custom design aspects and reduce the complexity of the nozzle roughness elements to periodically placed, ribbed roughness elements (blue boxed area, Figure 1.3). In turn, experimental research is performed on the relative heat transfer properties of such roughness elements in turbulent, supersonic flow conditions (i.e. M = 2.0 [-]).

Experiments on large ribbed roughness geometries It turns out that fundamental investigations regarding the effects of two-dimensional, ribbed roughness elements are more substantially represented in subsonic flow research. Experiments conducted for these researches not only include the effects on the mean flow properties, but also flow separation, skin friction and heat transfer effects are considered. The most commonly investigated geometric variables are the relative pitch, p/e and height, e/δ whereas the unit Reynolds number, Re is the dominant flow variable. One of the first parametric studies was conducted by Han (1984), who identified an increase in both average friction factor ($\overline{C_f}$) and average Stanton number ($\overline{St}$) by increasing the e/δ of periodic square-rib roughness geometries.[6] In contrast, Han et al. (1985) found a decrease in $\overline{C_f}$ and $\overline{St}$ by increasing the p/e of the ribbed-wall geometries from $10 \leq p/e \leq 40$.[7] Liou et al. (1990) complemented this research by acquiring turbulence properties of the boundary layers over geometries with $5 \leq p/e \leq 15$. As turbulent mixing is a good indicator for heat exchange, the resulting observations can be assumed to correlate with previous heat transfer research.[8,9] (Liou and Hwang, 1992; White, 2006) In turn, Liou et al. found a peak in turbulence (u') for a ribbed roughness geometry with a p/e of 10, indicating a maximum heat transfer. Combining the previous conclusions, it is expected that the heat transfer is maximized for a geometry with p/e = 10.

By these fundamental studies, multiple trends and correlations were formed for long, wall-roughened ducts. The causes of which, however, needed to be hypothesized as flow visualization techniques were not utilized. This changed when Aliaga et al. (1993) combined velocimetry with infrared thermography (IRT), allowing the researcher to directly assign specific flow phenomena to variations in heat transfer properties.[10]

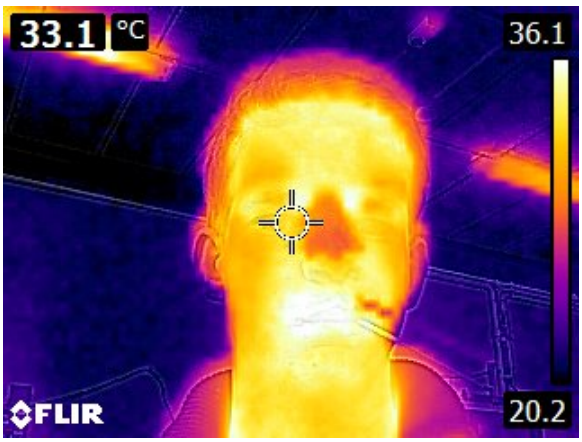

FIGURE 1.4: Thermogramme of cool author

Thesis approach To the best knowledge of the researcher, there is only one case where the flow effects of periodic, two dimensional roughness were investigated within supersonic conditions. The latter was considered by Latin and Bowersox (2000), who conducted a supersonic roughness study using only small roughness elements ($e/\delta < 0.2$).[11] As such, there is an absence of a parametric supersonic study on the heat transfer properties of ribbed roughness elements, equivalent to those seen for subsonic conditions. Therefore, it is decided to conduct an experimental investigation for which ribbed roughness designs are varied solely for $e/\delta \geq 0.2$ and $5 \leq p/e \leq 30$. In addition, the ambient conditions are kept constant at M = 2.0 [-] such to represent nozzle operating conditions. The (large) height criterion originates from the *discrete element requirement* (Jimenez, 2004), whereas the pitch criterion stems from the requirement of meeting specific cavity type flows (Zhang et al., 2002).[12,13]

As heat transfer measurements are considered, it is decided to use IRT as this method is non-intrusive and provides a complete, transient planar temperature field. The experimental setup required to apply this technique for the proposed investigation, however, is not yet present at the High-Speed Laboratory (HSL). The overall goal of the current thesis is to "*establish a parametric study onto the heat transfer effects of two-dimensional, periodic, ribbed roughness elements in supersonic flows by conducting IRT*". To achieve this, though, the first aim is design, construct and utilize an IRT setup capable of delivering quantitative data (i.e. QIRT). This supersonic QIRT technique will be based on the *heated thin-film* approach, similar to Aliaga et al (1994).[14] Such QIRT approach is common to active thermography, as it provides a steady surface temperature larger than the adiabatic wall temperature, T_{aw} and yields uniform, predictable material properties. Therefore, it is possible to directly construct heat transfer properties from the temperature values.[15] (Astarita and Carlomagno, 2012)

Since the resulting QIRT experimental setup is new to the HSL and ST-15 wind tunnel, independent, complementary data is required. From the qualitative correspondence between turbulence intensities ($\overline{u'}$, $\overline{v'}$, $\overline{u'v'}$) and heat transfer coefficients ($\overline{Nu}$, $\overline{St}$), a measurement technique is chosen which is capable of obtaining these turbulence properties for a complete planar field of view. All of these requirements are encompassed in particle image velocimetry (PIV), which provides quantitative information on the whole flow field, whilst also providing intuitive visualization of the flow. As PIV is relatively elaborate compared to some other qualitative visualization techniques, it is decided to conduct a Schlieren visualization technique beforehand. Through this technique, it is possible to clearly visualize and record images of the complete flow field whilst using minimal equipment. This way, it becomes relatively simple to make qualitative judgments on the flow fields and verify whether flow phenomena emerge as expected from literature.

Research objective and questions It can thus be concluded that once the QIRT setup has been designed, built and the derived data is compared with supplement PIV (and Schlieren) data, substantiated conclusions can be drawn with respect to the obtained heat transfer properties. Once the latter is settled, apart from the question whether the QIRT setup performed accurately and reliably, the current thesis should answer:

1. *What types of flow fields are found by variations in respective roughness geometries?*
2. *How do these flow fields compare to their subsonic counterparts?*
3. *What are the general effects of the encountered flow phenomena on the heat transfer?*
4. *Which effects on the heat transfer are observed for variations in relative pitch, p/e?*
5. *Which effects on the heat transfer are observed for variations in relative height, e/δ?*
6. *Can geometry-dependent correlations be formed with respect to heat transfer, similar to those observed for subsonic flow conditions*?
7. *Which roughness geometry provides the maximal heat transfer in supersonic conditions?*

By combining these primary research questions, it can be seen that the overall research objective can be summarized as *"Accurately map the flow phenomena in the velocity field and correlate these to the resulting surface heat transfer patterns such to improve insights into the effects of large wall-roughness elements on the development of turbulent, supersonic boundary layers by measurements obtained through quantitative infrared thermography (QIRT) and particle image velocimetry (PIV) on varying geometrical properties of the periodic, two-dimensional roughness elements."*

Report structure The overall approach to reaching the thesis objective and answering research questions has shown that the current experimental investigation can be subdivided in three primary components: (1) constructing a QIRT setup, (2) substantiate QIRT through PIV (and Schlieren), and (3) derive heat transfer results from QIRT. At this stage of the research, it can be said that all three components have been fulfilled as expected. The purpose of this report is to provide the reader insights into the exact steps and considerations taken to fulfill the aim of the research. Since a diversity of aspects are encompassed in the current research, this report is built-up such to illustrate where each primary research component is treated. As such, the structure of the report is to first provide a detailed theoretical background on the effects of wall roughness across the flow regimes in Chapter 2. In turn, the methodology of the visualization and validation techniques PIV and Schlieren are explained in Chapter 3. Then, a complete overview to the design considerations, construction and data gathering of the QIRT technique is provided in Chapter 4. With the approach of the latter clarified, the results from the three techniques are described and combined in Chapter 5. Finally, there is reflected upon the complete thesis approach and results in Chapter 6 followed by recommendations on future investigations in Chapter 7.

Chapter 2

Theoretical background

The current thesis considers the experimental investigation of a turbulent, supersonic boundary layer which is influenced by various large-roughness geometries. Through this research, it is desired to obtain a proper understanding of the flow and heat transfer mechanisms behind the evolving flow fields. To accommodate the latter, effectively a heated flat plate imposed with periodic, large roughness elements is measured upon (Section 4.1.1). With these complex flow conditions in mind, a base understanding has to be formed prior to conducting the experiments. This is achieved by performing a literature search, in which the fundamental theories of heat transfer and roughness effects are considered. In this chapter, the main findings of such accompanying research are provided. This is done by gradually increasing the level of complexity, where, in Section 2.1, the heated flat plate boundary layer is treated. In turn, the effects of roughness elements is added in Section 2.2 followed by the most closely related counterpart – supersonic cavity flows – in Section 2.3.

2.1 Heated, flat plate boundary layer

Prior to adding the complexity of ribbed roughness elements, a basic understanding is formed on the flow properties of a heated flat plate boundary layer. To this end, the boundary layer concept, non-dimensionalized constants, fundamental equations and finally the approximate solutions are discussed.

2.1.1 Boundary layer concept

The physical concept of the boundary layer theory is based on the fact that the viscous effects are confined to thin layers near solid walls.[16] (Prandtl, 1904) This means that the flow field can be separated in two distinct flow regions; an inviscid outer flow and a viscous boundary layer. As a result, flow properties of these regions can be solved separately after which a mathematical description couples their respective solutions. For a generalized flat plate flow, this separation in flow regions is characterized as follows:

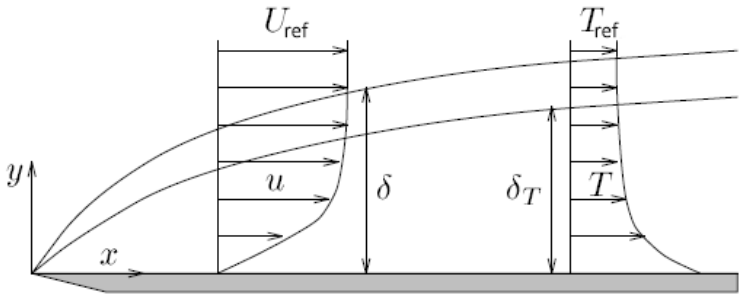

FIGURE 2.1: Boundary layer profiles.[17] (Pope, 2001)

In Figure 2.1, the two distinct (in)viscid regions are identified by the confined wall region and the external flow region. In the wall region, y-dependent boundary layer profiles exist which are dependent on a variety of flow conditions (i.e. external pressure gradient, wall suction etc.). The external velocity and temperature properties, however, can be assumed constant for y-coordinates exceeding the local boundary layer and thermal boundary layer thicknesses, respectively δ and δ_T. As such, these external properties, u_{ref} and T_{ref}, are commonly used as outer-scale reference for non-dimensionalizations.

Directly at the wall, viscous interaction stagnates the flow completely. This is called the *no-slip condition* and is the assumed solution at the wall for all boundary layer profiles.[9] (White, 2006) It can thus be concluded that the boundary layer profiles merely link the wall properties with the external flow, for which the boundary conditions are:

$$u(x,0) = 0 \qquad T(x,0) = T_s(x) \tag{2.1}$$

$$u(x,\delta) = u_{ref} \qquad T(x,\delta_T) = T_{ref} \tag{2.2}$$

The nature of the flow can be identified by the shape factor H of the boundary layer profiles, given by:

$$H = \frac{\delta^*}{\theta} \tag{2.3}$$

Where δ^* is the displacement thickness and θ corresponds to the momentum thickness. This displacement thickness is commonly used as the mathematical link between the boundary layer and the external flow. By first computing the displacement thickness resulting from the boundary layer, this δ^* is used as a constant translation to the initially computed external flow streamlines. Once the translation is completed, the representation of the flow fields in both regions are accurately represented by their solutions. The definitions of δ^* and θ are given by:

$$\delta^* = \int_0^\delta \left(1 - \frac{u}{U_\infty}\right) dy \tag{2.4}$$

$$\theta = \int_0^\delta \frac{u}{U_\infty}\left(1 - \frac{u}{U_\infty}\right) dy \tag{2.5}$$

Where the velocity u is a function of y and is normalized by the external velocity U_{ref}. For most applications, the variance of the external velocity is negligible along x and y. Therefore, U_{ref} is assumed constant for Equations 2.4 and2.5.

It remains to determine the loads which the boundary layer imposes on the surface as a result of the viscosity. Two type of surface loads can be described; the mechanical and thermal surface loads. These loads represent fluxes acting through the horizontal plane as a result of respectively local velocity or thermal gradient, equal to:

$$\tau_s = \mu \left.\frac{\partial u}{\partial y}\right|_{y=0} \tag{2.6}$$

$$q_s = -k \left.\frac{\partial T}{\partial y}\right|_{y=0} \tag{2.7}$$

Where viscosity, μ and thermal conductivity, k are transport properties specific to the fluid (i.e. air). In reality, the no-slip condition is accommodated by a thin boundary layer which only occurs for flows with a small viscosity. The relative viscosity of a fluid is mostly described by flows with a large Reynolds number; inviscid ($Re \to \infty$) and viscous ($Re \gg 1$). The Reynolds number, together with other dimensionless coefficients are described in the next section.

2.1.2 Typical flow parameters

In general, flow properties are characterized by the absolute parameters derived from the flow itself. However, for an accurate comparison between individual experimental conditions, non-dimensional coefficients are used. For an improved understanding of the experimental results, a brief overview of the utilized dimensionless coefficients is given with respect to flow conditions and heat transfer. Once the meaning of these coefficients is clarified, it becomes easier to interpret the data from previous research and identify the physical effects to which their variations correspond.

Reynolds number The first dimensionless coefficient is the Reynolds number, Re which describes the ratio between the inertial and viscous forces corresponding to a specific characteristic length, L. The definition of which is given by:

$$Re = \frac{\rho U L}{\mu} = \frac{\text{inertial forces}}{\text{viscous forces}} \tag{2.8}$$

Where ρ is the fluid density and U the external flow velocity. The Re is a very important dimensionless quantity which is used to define fluid behaviour and predict the onset to turbulence. The experiments for the current thesis are conducted in a supersonic wind tunnel (Section 3.1), for which it is known that the $Re \gg 1$ inside the test section. As such, it is assured that the current experimental conditions are turbulent.

Skin friction coefficient Previously, Equation 2.6 showed that the skin friction is defined by the local velocity gradient at the wall and the viscosity term, μ. The non-dimensionalized counterpart is given by:

$$C_f = \frac{\tau_w}{\frac{1}{2}\rho_\infty u_\infty^2} = \frac{\text{skin friction}}{\text{external flow momentum}} \tag{2.9}$$

Which effectively represents the ratio between the skin friction and external flow momentum. The definition shown in Equation 2.9 is mostly used to compare the drag performance of aerodynamic bodies. In the current thesis, it is mostly used within the Reynolds analogy.

Heat transfer coefficients The surface heat flux q_s (Equation 2.7) is non-dimensionalized according to two modes of heat transfer:

$$Nu = \frac{q_s L}{k(T_{aw} - T_s)} = \frac{\text{surface heat transfer}}{\textbf{conductive} \text{ heat transfer}} \tag{2.10}$$

$$St = \frac{q_s}{\rho u_\infty c_p (T_{aw} - T_s)} = \frac{\text{surface heat transfer}}{\textbf{convective} \text{ heat transfer}} \tag{2.11}$$

Where the Nusselt number, Nu is a measure for conductive and Stanton number, St for convective heat transfer. In addition, T_{aw} is the adiabatic wall temperature, T_s the local surface temperature and c_p the specific heat coefficient of air. From Equations 2.10 and 2.11, it is seen that each term is non-dimensionalized differently; depending on the flux mechanism. The commonality, however, is the use of the convective heat transfer coefficient:

$$h = \frac{q_s}{(T_{aw} - T_s)} \tag{2.12}$$

By the interest of the effects of various flow phenomena, a primary focus is laid on identifying variances in local Stanton numbers as being characteristic for each roughness geometry. Apart from the differences in associated heat flux type, the choice for considering St as primary heat transfer coefficient is also less cumbersome and more reliable. This is caused

by the dependence of Nu on the choice of characteristic length L, which is difficult to define accurately. Additionally, in the case that this L is defined as the distance from the flat plate leading edge, Nu is zero at the start and increases with the growth of the boundary layer. This is not convenient as in reality the heat transfer decreases as the boundary layer grows thicker along x. Therefore, during the analysis of the heat transfer properties of each roughness geometry, the Stanton number is used as primary *heat transfer coefficient*.

Prandtl number Another important dimensionless parameter is the Prandtl number, Pr which represents the ratio between the viscous and thermal diffusion as:

$$Pr = \frac{\mu c_p}{k} = \frac{\text{viscous diffusion}}{\text{thermal diffusion}} \tag{2.13}$$

For which the same constants are used as for the previously defined heat transfer and viscous coefficients. The *Pr* plays an important role by relating two transport mechanisms with one another; i.e. viscous and thermal diffusion. Even though some specific flows allow for the assumption of the thermal and viscous boundary layer profiles to be analogous (i.e. *Pr* = 1), generally they are not exactly the same. For air (and most other gases) the *Pr* is approximately 0.71 [-] which thus shows that the viscous and thermal diffusion remain of the same order of magnitude. Nevertheless, the thermal diffusion is slightly dominant, which implies that thermal boundary layer (δ_t) is slightly thicker than the momentum boundary layer (δ). Following the previous definition of the Pr, it can also be expressed as:

$$Pr = \frac{Nu}{Re\ St} \tag{2.14}$$

Where the dependence of *Pr* on the dimensionless coefficients *Nu*, *Re* and St more explicitly indicates its interlinking of the two transport mechanisms. The definition of Equation 2.14 is used to prove the existence of the Reynolds analogy: a direct relation between the heat transfer and skin friction. This analogy is derived from an approximate form of the governing equations for fluid mechanics; the Navier-Stokes equations.

Adiabatic wall temperature In the boundary layer, the velocity at the surface is equal to zero. Under the assumptions that neither heat transfer, nor irreversible effects take place whilst decelerating the flow, the wall temperature would equal to total temperature for $M \ll 1$ (i.e. isentropic laws). In reality though, the flow is decelerated anisentropically. This means that during flow deceleration, part of the kinetic energy is dispersed to viscous stress, skin friction etc. Hence, the temperature at the surface does not equal the total temperature. The correction between non-idealized deceleration is encompassed in the definition of the adiabatic wall temperature T_{aw} as:

$$T_{aw} = T_{tot}\left(1 + r\frac{\gamma - 1}{2}M_e^2\right) \tag{2.15}$$

Where r is the *recovery factor*, γ the ratio of specific heats and M_e the external Mach number. The definition of r is given by:

$$r = \frac{(T_{aw} - T_\infty)}{(T_0 - T_\infty)} \tag{2.16}$$

Which, for a flat plate laminar flow, is defined as $r = \sqrt{Pr}$, whereas, for a flat plate turbulent flow, $r = Pr^{\frac{1}{3}}$.[9] (White, 2006) In turn, for isentropic flows and stagnation points, $r = 1$; returning Equation 2.15 to the isentropic relation. The definition of the adiabatic wall temperature is stated as the minimum static temperature of an imperfectly decelerated flow. As a result, T_{aw} corresponds to the wall temperature for which convective heat transfer can no

longer take place. Therefore, for the convective heat transfer computations, $T_{ref} = T_{aw}$.[18] (Shapiro, 1953)

2.1.3 Navier-Stokes equations

The most fundamental equations for any compressible viscous flow is described completely by the Navier-Stokes equations. In their most primitive form, it is possible to derive the momentum and thermal properties of any viscous fluid flow. In this form, however, no analytical solutions exist (yet). This means that their solutions can merely be found through numerical analysis. As a result, in most applications of the Navier-Stokes equations, assumptions are formulated which allow for a great level of simplification.

Currently, a heated, rib roughened surface is considered in turbulent, supersonic conditions, the base experimental setup inside the wind tunnel is given by a two-dimensional, heated model in steady supersonic flow conditions (Section 4.1). In order to form a basic understanding on the order of magnitude of the flow parameters (i.e. h, St etc.), the considered reference case is given by a heated flat plate model for an incompressible flow. Once this is clear, roughness effects should be appropriately introduced into the solution. In summary of the aforementioned properties, the Navier-Stokes equations are simplified to:

$$\text{continuity:} \qquad \frac{\partial u}{\partial x} + \frac{\partial v}{\partial y} = 0 \tag{2.17}$$

$$\text{momentum:} \qquad \rho\left(u\frac{\partial u}{\partial x} + v\frac{\partial u}{\partial y}\right) = \mu\frac{\partial^2 u}{\partial y^2} \tag{2.18}$$

$$\text{heat transfer:} \qquad \rho\left(u\frac{\partial T}{\partial x} + v\frac{\partial T}{\partial y}\right) = \frac{\mu}{Pr}\frac{\partial^2 T}{\partial y^2} \tag{2.19}$$

For which it is primarily assumed that the flow is characterized by high Reynolds numbers, ($Re \gg 1$), the shear layer is thin ($\delta \ll x$) and the flow is developed such that similarity occurs. From Equations 2.18 – 2.19, the desired approximate solutions are formed.

2.1.4 Reynolds analogy

As for now incompressible flows are considered, it is allowed to conclude the analysis of the heat transfer and viscosity terms by a decomposition of the two terms within the overall solution of the boundary layer. It can be seen from the momentum and heat transfer equation (2.18 and 2.19) that in the case of *Pr* equal to unity, the equations for *u* and *T* become analogous. As a consequence, it is seen that there exists a direct correlation between the heat transfer and skin friction relations:

$$\frac{1}{\Delta T}\left(\frac{\partial T}{\partial y}\right)_s = -\frac{1}{u_e}\left(\frac{\partial u}{\partial y}\right)_s \quad \rightarrow \quad \frac{q_s}{k\Delta T} = \frac{\tau_s}{\mu u_e} \tag{2.20}$$

This relation between the heat transfer and skin friction is more generally embodied by the definition of the Reynolds analogy factor:

$$s = 2\frac{St}{C_f} = \frac{q_s/\rho c_p u_e \Delta T}{\tau_s/\rho u_e^2} = \frac{1}{Pr}\frac{q_s/k\Delta T}{\tau_s/\mu u_e} \tag{2.21}$$

where s is seen to effectively correspond to the ratio between the heat transfer and skin friction. The case where *Pr* = 1 corresponds to a particular situation which is commonly ascribed to that of an isothermal flat plate. By solving the incompressible flow relations, it is proven that for a general flat plate boundary layer, it holds that:

$$\frac{\delta}{\delta_T} \approx Pr^{1/3} \quad \rightarrow \quad \frac{q_w}{k\Delta T} \approx Pr^{1/3}\frac{\tau_w}{\mu u_e} \tag{2.22}$$

Thus, generally, the Reynolds analogy factor, $s \approx Pr^{-2/3}$. The approximation of the Reynolds analogy (Equation 2.22), is frequently used to further simplify relations derived through the Navier-Stokes equations. In the following section, the most appropriate approximate solution are shown for the heated, turbulent flat plate boundary layer.

2.1.5 Approximate solutions

The simplification of the Navier-Stokes equations for steady, two-dimensional, turbulent, incompressible flat plate flows led to the derivation of a specific form of the boundary layer equations. Even though these forms of the continuity, momentum and heat transfer equations (Equations 2.17, 2.18 and 2.19) are relatively simple, it is desired to define even more simplified analytical solutions. Through these approximate solutions, it is possible to make quick yet reliable estimations on the momentum and heat transfer properties. In this section, the adjoining analytical solutions are stated according to two experimental conditions, namely: a completely and partially (unheated starting length) heated surface operating at constant temperature and constant heat flux.

Fully heated, turbulent flat plate In 1908, Blasius defined the self-similar solution for the flat plate boundary layer by characterizing an external flow at constant velocity (i.e. du_e/dx = 0). Even though the solutions to resulting Blasius equation are exact, these are based on the assumption of a laminar boundary layer. For the turbulent boundary layer, correlations similar to the exact form of the Blasius equation were derived experimentally. These are given by the Dittus and Boelter relations (1930), equal to:[19]

Constant temperature

$$Nu_x = 0.023Pr^{2/5}Re_x^{4/5} \tag{2.23}$$

$$St_x = 0.023Pr^{-3/5}Re_x^{-1/5} \tag{2.24}$$

and,

Constant heat flux

$$Nu_x = 0.0308Pr^{2/5}Re_x^{4/5} \tag{2.25}$$

$$St_x = 0.0308Pr^{-3/5}Re_x^{-1/5} \tag{2.26}$$

Where for both Equations 2.23 and 2.25, the definition of the Prandtl number (Equation 2.14) was used to write the original heat transfer correlations in terms of the Stanton number, St. Comparing the relations, it is seen that for the same Pr and Re_x, effectively more heat is transferred between the flow and the wall once the latter operates at a constant heat transfer condition (Equations 2.24 and 2.26). Even though it is difficult to achieve either thermal situation in reality, this should be taken into account once the experimental models are designed.

With the approximate expressions for St_x known, it is possible to obtain similar correlations for the skin friction coefficient. This is done rewriting the Reynolds analogy for turbulent flows (Equation 2.21) as:

$$2\frac{St}{C_f} = Pr^{-2/3} \tag{2.27}$$

$$C_f = 2StPr^{2/3} \tag{2.28}$$

whilst substituting the relations of St_x for turbulent flow (Equations 2.24 and 2.26). Finally, the corresponding correlation for the turbulent skin friction coefficient becomes:

$$C_f = 0.0616 Pr^{1/15} Re_x^{-1/5} \tag{2.29}$$

Which effectively closes the required set of analytical solutions for the fully heated, turbulent flat plate flow. Note that, as the incompressible flow characteristics are independent of the thermal wall conditions, only one correlation is required. The second experimental setup considered is that of a heated flat plate, which includes an unheated starting length.

Turbulent flat plate, unheated starting length The second experimental setup considers a heated flat plate for which the boundary layer develops from an *unheated starting length*. As seen in Section 4.1.1, this description narrowly illustrates the final QIRT setup. The resulting expressions for respectively the Nusselt and Stanton numbers are provided by the exact Kays and Crawford relations (1993), given by:

$$\textbf{Constant temperature:} \qquad St_x \approx \frac{0.023 Pr^{-3/5} Re_x^{-1/5}}{\left[1 - (x_0/x)^{3/4}\right]^{1/3}} \tag{2.30}$$

$$\textbf{Constant heat flux:} \qquad St_x \approx \frac{0.0308 Pr^{-3/5} Re_x^{-1/5}}{\left[1 - (x_0/x)^{3/4}\right]^{1/3}} \tag{2.31}$$

Where the constants are modified such to relate to the turbulent boundary layer. The latter are obtained by substituting the Dittus-Boelter relations for a flat plate; operating at constant temperature and heat flux.

With the latter correlations for turbulent, incompressible, flat plate boundary layers in place, a complete set of analytical approximations has been derived. In reality though, the supersonic, roughness-induced flow fields are a lot more complex and require either direct experimental measurements or advanced CFD simulations to be solved thoroughly. Nevertheless, judging by the accuracy of these basic correlations with experimental data, it is said that the mentioned correlations are sufficiently accurate as an initial approximation for the thermal properties of the reference flat plate model under supersonic conditions.[19] (Dittus and Boelter, 1930) With this in mind, there is added to the flow complexity. This is done in the following section, where a brief overview is provided on the effects of wall roughness.

2.2 The effects of wall roughness

The principles of heat transfer between the boundary layer and a flat plate can be easily approximated by using the theories and analytical solutions mentioned in the previous section. Once roughness elements are introduced to these flat plates, however, it is understandable that the flow behavior, boundary layer development and heat transfer properties are altered. As mentioned in the introduction (Chapter 1), research on the effects of roughness has primarily been conducted for subsonic flows. Nevertheless, it is expected that trends observed from this research can be directly linked to flow phenomena found in supersonic flows. Therefore, in this section, there is started with a discussion on an unambiguous definition of large-scale roughness. This is then followed by the known effects of roughness elements in supersonic flows, which, unfortunately, is limited to small-scales. In turn, a summary of the literature found on the effects of large-scale, periodically placed ribbed roughness in subsonic flows are reflected upon. Then, due to the absence of otherwise related supersonic results, research on the most closely related topic to the tested roughness geometries, "supersonic cavity flows", are treated in Section 2.3.

2.2.1 Definition of large scale roughness

Originally, Nikuradse (1933) established the framework for a rough-wall flow analysis utilizing merely (randomized) sand-grain roughened pipes.[20] For these roughened flow fields, it was found that for an increasing Reynolds number, the flow behavior deviated from the turbulent smooth-wall law and depended on the relative scale of roughness Reynolds number. The resulting *law of resistance*, in turn, was found to categorize according to:

- $Re < Re_{crit}$: *Transition flow region*, dependent on both e/D_h and Re.
- $Re \geq Re_{crit}$: *Fully rough region*, dependent solely on e/D_h.

This implies that for a sufficiently high Reynolds number, Nikuradse's law of resistance is independent of viscosity. In addition, it was determined that the smooth-wall velocity defect law applied to the bulk of the flow, irrespective of the scale e of the roughness. The effect of roughness on the velocity profile was thus, like viscosity, confined to a thin wall layer. On the basis of this limited effect of roughness on the velocity profile and viscosity, the Nikuradse-Clauser form of the roughness function for turbulent, fully rough flows was defined as:

$$\frac{\Delta u}{u_\tau} = \frac{1}{\kappa} log_e \left(\frac{e u_\tau}{\nu} \right) + C \tag{2.32}$$

Where Δu is the velocity defect $U_{ref} - u$, e is the roughness height, u_τ the friction velocity, κ the von Kármán constant, ν the kinematic viscosity and C is an arbitrary constant. Through Equation 2.32, Nikuradse has demonstrated that surface roughness has a direct impact on the law of the wall and can be described by a single parameter eu_τ/ν or *roughness Reynolds number* (k^+). As mentioned, this equation was derived on the basis of experimental research using merely sand-grain roughened walls; characterized by having a relatively small-scale and unstructured geometry. In general though, roughness elements are characterized by their respective size and geometrical structure; where the first feature defines the level of boundary layer protrusion, and the latter corresponds to either two-dimensional, periodic or three-dimensional, randomized flow effects.

The effects of roughness geometry and resulting flow topology has been investigated by Perry et al. (1969), who derived similar scaling laws for varying p/e-ratios at constant e.[21] In their research, it was found that geometries can be classified as a *d* and *k* type, relative to the pitch ratios applied to the two-dimensional roughness geometries. In the case of *k* type roughness, eddies with a length scale proportional to roughness height k (i.e. e) are assumed to be shed into the flow above the crest of the roughness elements. In contrast, on a *d* type rough wall, the elements are more closely spaced and stable vortices are setup within the cavities. As a result, eddy shedding from the *d* roughness elements into the outer flow is negligible. This distinction in flow topology is illustrated by the following figures:

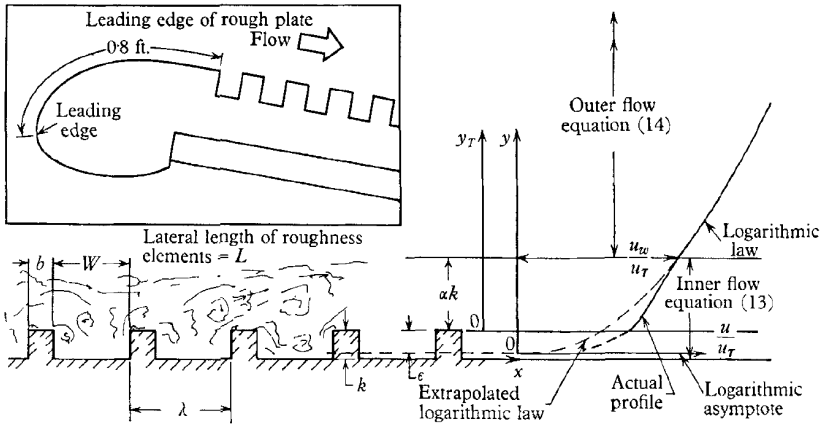

FIGURE 2.2: *k-type* roughness.[21] (Perry et al, 1996)

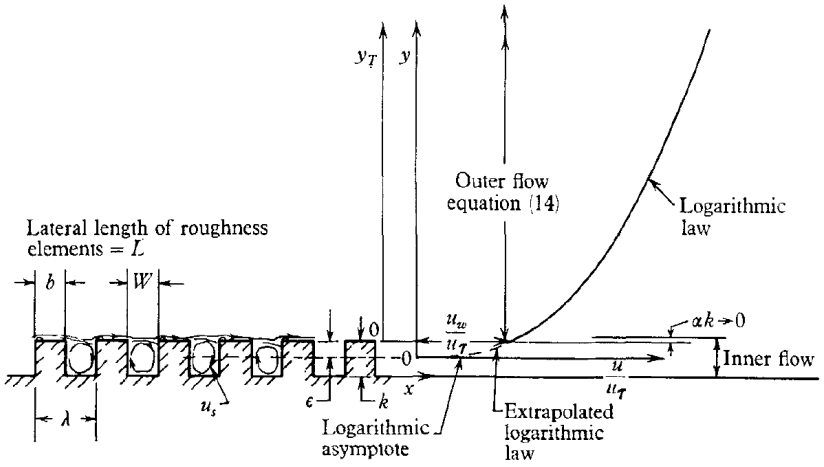

FIGURE 2.3: *d-type* roughness.[21] (Perry et al, 1996)

For which Figure 2.2 corresponds to *k-type*, and Figure 2.3 to *d-type* roughness geometries. The idea of k-type and d-type roughness classification was introduced by Perry et al. once geometrical cases were found to which the Nikuradse-Clauser correlation scheme for the roughness function was no longer applicable. For a fully rough flow, the roughness function for both k-type and d-type is found to be a function of the length of scale ϵ. The function can thus be expressed as:

$$\frac{\Delta u}{u_\tau} = \frac{1}{\kappa} log_e \left(\frac{\epsilon u_\tau}{\nu} \right) + C \tag{2.33}$$

where, in the case of a zero-pressure gradient boundary layer, a:

$$\text{k-type: } \epsilon \propto e \text{ , and} \tag{2.34}$$

$$\text{d-type: } \epsilon \propto \delta \tag{2.35}$$

For these correlations, ϵ is the distance below the crest of the roughness elements which the effective wall of the boundary layer follows (Figures 2.2 and 2.3), and C is a constant characteristic for the roughness elements (i.e. C_e or C_δ). It was later proven by Schlichting (1955) that the latter laws (Equation 2.33) hold, regardless of the flow regime.[22]

The k- and d-type roughness classifications introduced by Perry et al. (1996) have proven that a structured spatial distribution (i.e. periodic roughness) has a significant impact on the boundary layer development and respective flow fields.[20,21] It turns-out, however, that

the application of these geometry-dependent roughness scaling laws are limited to specific roughness heights. Jimenez (2004) found that once roughness elements extend beyond a ratio of $e/\delta \geq 0.2$, the general boundary layer model shifts towards an element model.[12] In this *discrete-element model*, roughness elements introduce such levels of disturbance into the boundary layer that single-variable roughness scaling cannot be performed.[22] (Schlichting, 1955) In contrast, the focus changes from using a uniform boundary layer law to finding the blockage and form drag of the individual elements.[23] (Hodge and Taylor, 1991) As such, the related effects are periodically distributed and develop up to the point where a fully invariant flow topology occurs; *hydraulically developing flow*. This is observed in the velocity and heat transfer results derived by Aliaga et al. (1993), where ostensibly similar conditions are formed downstream of the third rib regardless of the p/e and associated flow topology.[10]

The goal of the current thesis is to a investigate the effects which two-dimensional roughness geometries have on the heat transfer properties of the boundary layer. Considering the dimensional scale and desired novelty of this investigation, it is decided to define the roughness geometries such to extend beyond the existence of uniform roughness laws. As a result, only *large roughness elements* are considered which are defined by rib heights, $e/\delta \geq$ 0.2 [-]. In turn, by choosing the discrete-element shift criterion as starting criterion for the roughness geometries, there is added to both sub- and supersonic research.[11,7] (Latin and Bowersox, 2000; Han et al., 1985)

2.2.2 Small-scale roughness in supersonic flows

In contrast to subsonic research, the effects of two-dimensional, ribbed-wall roughness elements on the turbulent boundary layer and flow topology in supersonic flows are relatively unexplored. To the best knowledge of the researcher, experimental investigations of roughness effects in supersonic flows are limited to small-scale, sand-grain roughened walls (Liepmann and Goddard, 1957; Latin, 1998), and the attempted development of a discrete-element roughness model (Hodge and Taylor, 1991) for estimating the effects of two-dimensional, machined roughness.[24,25,23] Even though the latter model has proven to be promising, it has only been validated for a limited set of flow regimes and roughness geometries. This, in turn, identifies the requirement for a more elaborate experimental study.

An experimental investigation which comes close to a parametric study of roughness geometries in supersonic flows, is conducted by Latin and Bowersox (2000).[11] The objective of their study was to provide an experimental characterization of the influence of small-scale roughness (k_s^+ = 100-570) on the mean and turbulent boundary layer flow in supersonic freestream conditions (i.e. M = 2.9). In this research, the considered equivalent roughness heights, k_s^+ were relatively small. Nevertheless, the consideration of machined, periodic two-dimensional roughness geometry was innovative. Unfortunately, none of the investigated roughness geometries exceeded the *discrete element criterion* (i.e. $e/\delta \geq 0.2$). As such, as application to the current investigation, there is focused on observations which relate the effects of roughness topologies onto the scaling properties of the supersonic boundary layer.

Velocity profile Supersonic rough-wall boundary layers possess features that do not have an incompressible counterpart. Provided the roughness elements protrude the sonic portion of the boundary layer, shock and expansion waves are generated; altering the mean flow and turbulence properties. For a zero-pressure-gradient boundary layer at M_e = 3.0, 99% of the boundary layer is supersonic.[26] (Van Driest, 1952) Hence, the presence of small roughness elements could generate significant compressibility effects. The velocity profiles of each test

geometry were non-dimensionalized with the freestream velocity u_e and boundary layer thickness δ. Their respective results are summarized in the following figure:

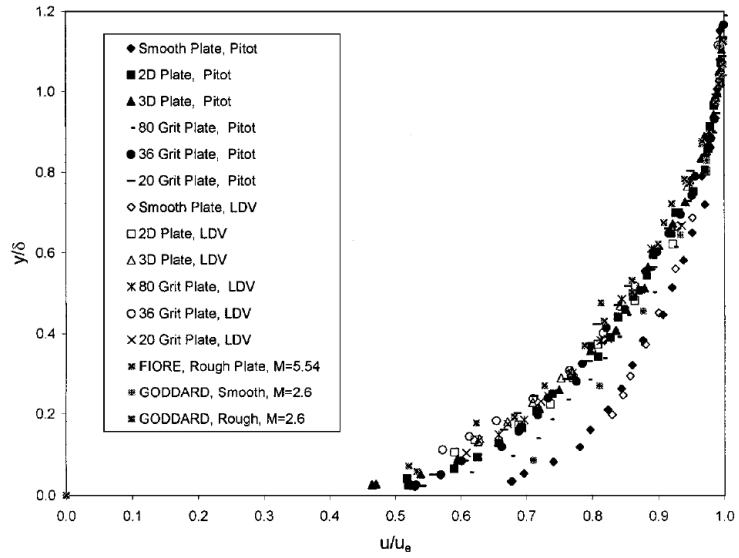

FIGURE 2.4: Mean velocity profiles (LDA and pitot data).[11]
(Latin and Bowersox, 2000)

In Figure 2.4, it is seen that the boundary layer profiles merge well with one another. From this property, it holds that the boundary-layer development of the two-dimensional roughness plate remains comparatively equal to the three-dimensional models. This implies that the boundary layer development remains relatively undisturbed for the two-dimensional roughness geometry, where the minimal crest height ϵ seems to have a minimal impact for the relatively small-sized roughness (Figure 2.3).

This flow topology was confirmed by the Schlieren measurements, where it was found that all roughness elements protruded deeply into the supersonic region of the boundary layer (Figure 2.5). It was seen that correspondingly the strength and intensity of the shock waves increased as the roughness increased. In turn, these roughness-induced waves distorted the boundary-layer edge and were clearly visible in the freestream.

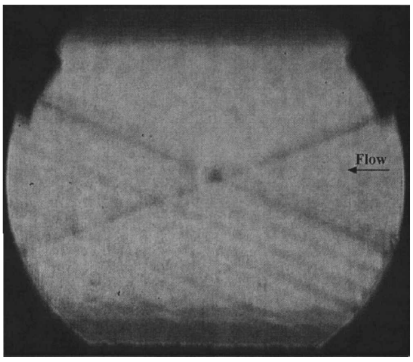

FIGURE 2.5: Schlieren photograph 20 Grit sandpaper roughness.[11]
(Latin and Bowersox, 2000)

The latter observations were found to hold for each of the roughened-walls except the two-dimensional plate, which displayed hardly any shock waves. The utilized two-dimensional plate had a p/e of 3.9, which is referred to as a d-type roughness.[21,12] (Perry et al, 1961;

Jimenez, 2004) It appears that the subsonic observation, where a d-type rough wall allows the outer flow to ride relatively undisturbed over the crest of the elements, is still applicable to supersonic flows. This is validated by the limited boundary layer defect observed by Latin and Bowersox (2000) in Figure 2.4; proving the validity of a repeated cavity flow for two-dimensional roughness. The latter is explained in more detail in Section 2.3, where supersonic cavity classifications are listed.

Velocity defect, law of the wall Nikuradse (1933) showed that the effects of sandpaper wall-roughness were confined to a thin layer close to the surface.[20] The resulting defect in the *law of the wall* was shown to be directly dependent on the relative surface roughness k^+, which was extended by Schlichting's (1955) representation of equivalent surface roughness k_s^+.[22] In relation to these findings, Latin and Bowersox (2000) derived the effective velocity defect and law of the wall for each wall roughness geometry. Their findings are provided in the following figures:

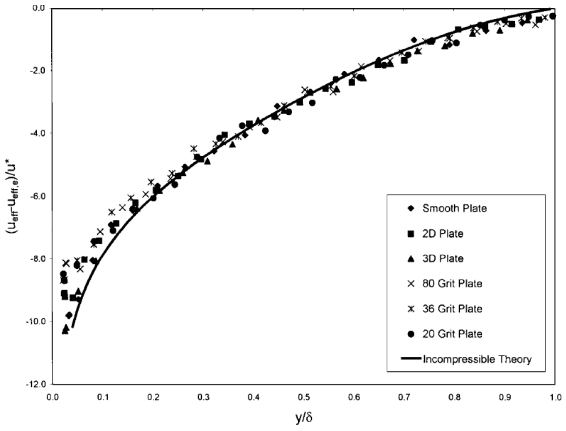

FIGURE 2.6: Effective velocity defect (pitot data).[11] (Latin and Bowersox, 2000)

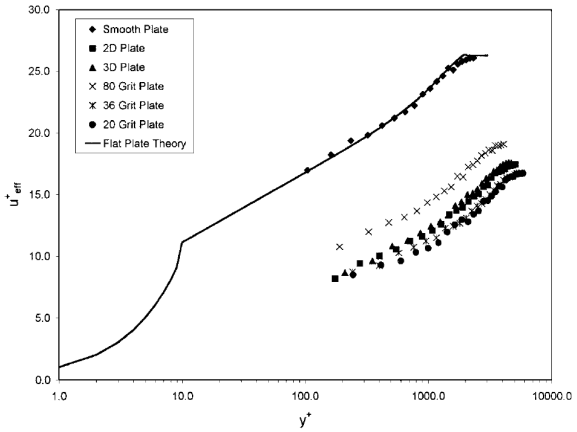

FIGURE 2.7: Effective law of the wall (pitot data).[11] (Latin and Bowersox, 2000)

Where Figure 2.6 displays the effective velocity defect, and Figure 2.7 the effective law of the wall. The data displayed in Figure 2.6 was transformed by the Van Driest II compressibility relations, and scaled by the friction velocity (u^*). In turn, it was found that the application of this transformation causes the profiles of all models to collapse onto a single curve. As a result, it was proven that the following correlation holds for the considered roughness heights k_s^+:

$$\frac{u_{eff} - u_{e.eff}}{u^*} = \frac{1}{\kappa}\ln\left(\frac{\mathrm{y}}{\delta}\right) + \frac{2\Pi}{\kappa}\left[1 - \sin^2\left(\frac{\pi}{2}\frac{\mathrm{y}}{\delta}\right)\right] \tag{2.36}$$

Where κ is the Von Karman constant (i.e. 0.41 [-]) and function Π is estimated following the method as described by White (2006).[9]

The effective velocity defect in Figure 2.7 shows that each roughness has a nearly constant defect, regardless of geometry and topology (i.e. 2D or 3D). The minor difference in the shift of the law of the wall can be assigned directly to the variance in the equivalent roughness height. This dependence on k_s^+ is most prominently seen by the 80 Grit plate curve, which clearly has a lower defect than the other five plates. The relatively small variance for the 36 Grit and 20 Grit proves that the initial implementation of roughness in supersonic flow does lead to a large increase in skin friction compared to a smooth wall; i.e. supersonic BL impingement. However, a further increment in k_s^+ has a relatively lower effect on this

increment of skin friction. As the velocity does not change significantly over the range of k_s^+, little defect variations are expected.

Turbulence intensities Through measurements on roughness-induced boundary layers in subsonic flows, Liou et al (1990) have proven the coherence between the turbulence intensities (u', v') and heat transfer coefficients (St, Nu). This relation originates from the Reynolds-averaged Navier-Stokes equations, which display a direct dependence on the Reynolds stress, τ_{ij}.[9] (White, 2006) In subsonic flows, the effect of τ_{ij} is independent of density variations as ρ can be assumed constant (i.e. $\tau_{ij} = -\overline{u'v'}$). In contrast, significant density variations occurring for the supersonic flow regime do not allow this assumption, making $\tau_{ij} = -\rho\overline{u'v'}$. Therefore, it is desired to draw preliminary conclusions on the interrelation between respectively the kinematic Reynolds stress $-\overline{u'v'}$, and compressible Reynolds stress, $-\rho\overline{u'v'}$. Once this relation is established, it is possible to conclude upon the relative the heat transfer properties of the currently considered surface-roughened plates.

In addition to mean velocity measurements, Latin and Bowersox (2000) conducted a campaign focused on the turbulence intensities of each test plate. The following figures display respectively the turbulence intensity u', v' and Reynolds stress, $\overline{u'v'}$-profiles:

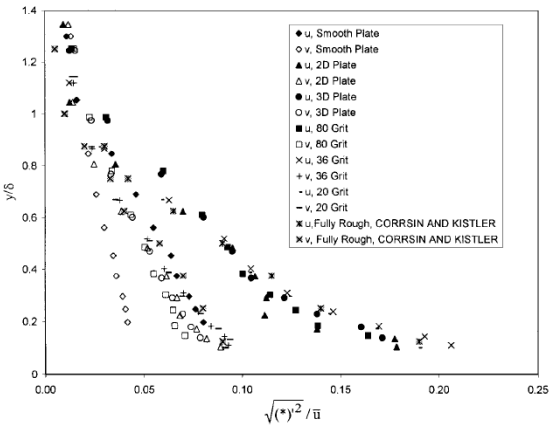

FIGURE 2.8: Turbulence intensity profiles, u' and v'.[11] (Latin and Bowersox, 2000)

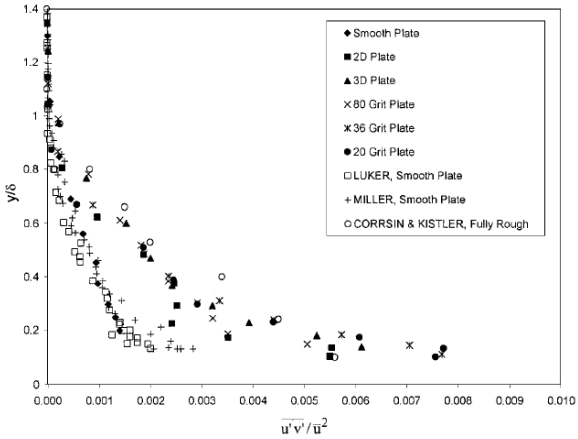

FIGURE 2.9: Reynolds stress profiles, $\overline{u'v'}$.[11] (Latin and Bowersox, 2000)

From both Figures 2.8 and 2.9, it is found that each non-dimensionalized turbulence component of the rough plates collapses when scaled by the u-component of the mean velocity and boundary layer thickness δ. The rough plate turbulence intensities are approximately twice that of the smooth plate values; for the u and τ_{ij}-component 18% versus 9%, and for the local v-component 9% versus 4%. For comparison purposes, the Corrsin and Kistler incompressible rough-wall results are shown, indicating a close agreement with Latin and Bowersox' results.[27]

The u' and v'-component turbulence intensity and $\overline{u'v'}$-profiles are shown to mostly collapse very well for $y/\delta > 0.6$. The only exceptions were the axial and Reynolds stress results for the two-dimensional machined plate (i.e. 2D Plate). This is most likely caused by the fact that only the two-dimensional plate did not produce shock and expansion waves equal to the sand grain roughnesses. Hence, the two-dimensional plate turbulence production mechanisms in the inner region, most likely driven by d-type cavity flow dynamics, were fundamentally different than that of the other plates where the roughness elements were

three-dimensional. The same discrepancy for the 2D plate was observed for the compressible Reynolds stress, $-\rho\overline{u'v'}$ shown in the following figure:

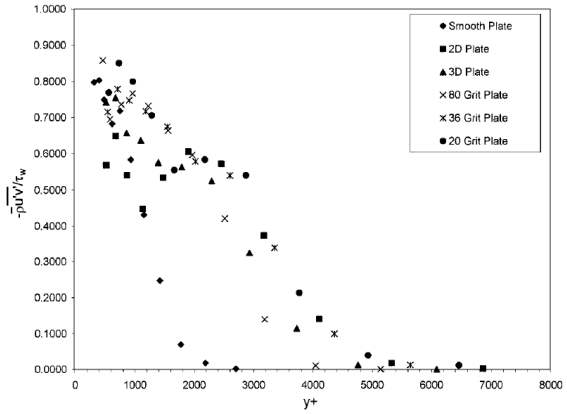

FIGURE 2.10: Compressible Reynolds stress profiles.[11]
(Latin and Bowersox, 2000)

In Figure 2.10, it is seen that the compressible Reynolds stress is scaled by the inner-variables in order to form collapsed boundary layer profiles. The exact scaling parameters are respectively the roughness Reynolds number $y^+ = \rho_w u^* y/\mu_w$ and wall shear stress τ_w. Latin and Bowersox (2000) concluded that this trend for the inner-variables results from an explicit thermodynamic dependence, causing $-\rho\overline{u'v'}$ to scale almost linearly with respect to k_s^+ instead of the mean flow properties.[11] Farther out into the boundary layer, the curves converge and a noticeable trend with roughness Reynolds number, k_s^+ is observed. An indication of this k_s^+-dependent trend is displayed in the following figure, indicating the $x-y$ and $x-z$ compressible Reynolds stress peak differences relative to the smooth-plate peak:

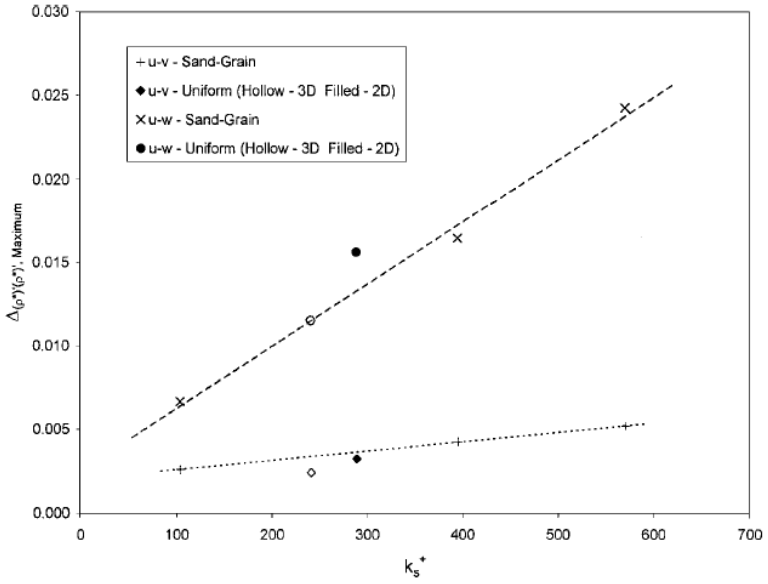

FIGURE 2.11: Peak difference in the compressible Reynolds stress w.r.t. k_s^+.[11]
(Latin and Bowersox, 2000)

where, in contrast to the compressible Reynolds stress (Figure 2.10), the peak difference turbulent quantities shown in Figure 2.11 correlate with respect to the outer variables and k_s^+.

The sand-grain roughness results for both components were shown to be linearly dependent on k_s^+. The three-dimensional plate correlates very well with the x-z trend established by sand-grain roughness. However, two-dimensional was significantly higher (i.e. 25%) relative to the trend, indicating that the turbulent structures for two-dimensional plate were even less correlated with the x-z plane than predicted. These results are consistent with turbulence intensity profiles shown before, and strengthen the view of flow topological dependence. The x-y component sand-grain results are increased linearly with k_s^+ as well, but at a much lower rate than the x-z component. The three-dimensional plate was below the sand-grain roughness trend (i.e. 20%). This is the result of the uniformity of the wall-surface area which had a frontal surface which was 93.45% smooth for the three-dimensional mode. This, in turn, causes damping effects on the transverse fluctuation levels whilst having negligible effects on lateral fluctuation levels.[28] (Christoph and Fiore, 1983)

Implications on research By comparing the results on incompressible, $\overline{u'v'}$ and compressible Reynold stress, $\rho\overline{u'v'}$ in respectively Figures 2.9 and 2.10, it is seen that both scale completely differently. Whereas $-\overline{u'v'}$ is non-dimensionalized by the external flow properties, $-\rho\overline{u'v'}$ is scaled by the internal flow properties. Regardless of these scaling properties, both parameters are found to correlate similarly with respect to the effects of roughness geometry (i.e. 2D plate). Therefore, it is expected that both would be proper indicators with respect to the surface heat transfer (St). In order to construct the compressible Reynolds stress, however, cross-film anemometry had to be utilized to gather the required turbulence measurements. The latter measurement technique was used in addition to LDV and hot-wire probes. Considering that both Reynolds stress types respond similarly to variations in boundary later flow topologies, it is beneficial to utilize a method which combines the acquisition of mean flow properties with flow fluctuations (i.e. u' and v'). One method capable of this is called Particle Image Velocimetry (PIV), which is discussed further in Section 3.4.

In contrast to the mentioned differences in scaling of the turbulence parameters, mainly coherence was found for the remaining scaled flow properties. By using the mean velocity u_{ref} and boundary layer thickness δ as external flow scaling properties, both the velocity profile and law of the wall were found to collapse. This implies that the effect of the 2D roughness elements are in-line with the subsonic flow topologies. Nevertheless, only one 2D roughness geometry was used; having the closely spaced characteristic known for undisturbed boundary layer flow. From subsonic observations, it is known that the two-dimensional roughness topology has a significant impact on the overall flow topology and resulting boundary layer properties. Therefore, no concrete conclusions can be drawn with respect to the general boundary-layer scaling laws once roughness topology is taken into account. In addition, it has to be noted that the current boundary-layer observations are solely derived for relatively small roughness elements. Acknowledging the discrepancies in the turbulence profiles which are already occurring for these small roughnesses, it is likely that these deficiencies become more profound once there is protruded deeper into the supersonic boundary layer. The latter is investigated in the current thesis, and is optimally depicted in the Schlieren images provided in Section 5.1.

2.2.3 Large-scale roughness in subsonic flows

Opposite to the supersonic flow regime, it turns out that the effects of square-rib roughness elements are already widely investigated in subsonic flows. The reason for this is that these elements are frequently used as turbulence promoters in a wide variety of applications such

as the cooling of turbine blades (Han, 1984) or as optimization of the heat sink in nuclear reactors (Liou et al, 1990).[6,29] By investigating the effects of respectively the geometry's pitch and height, optimization studies were performed into maximizing the heat transfer between the turbulent boundary layer and the wall. Considering that the current study involves the same effects of a ribbed wall geometry in supersonic flows, the associated subsonic literature is well in place. A summary of the literature related to the effects of large square-rib roughness is provided in this section.

Square-rib roughness geometry A well-known method to enhance surface heat transfer is to roughen this surface by the use of repeated ribs positioned periodically and perpendicular to the flow direction. Due to their effect on the flow, these ribs are commonly referred to as *turbulence promoters*. Even though this shape is relatively simplistic, the most dominant design parameters - relative height e/D_h and pitch p/e - are still included. The following image displays the physical definitions of these design parameters:

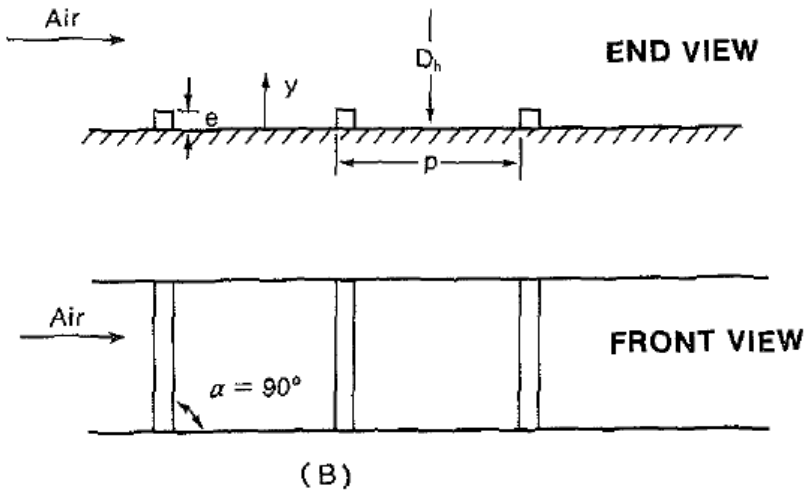

FIGURE 2.12: Definition of rib design parameters.[6] (Han, 1984)

Where roughness height e is defined from the wind tunnel surface to the rib top, the pitch p is equal to the rib face-to-face spacing and the hydraulic diameter D_h the distance between the bottom and top of the wind tunnel. Throughout subsonic literature, these definitions have remained constant and are therefore used equally in this report. By the character of subsonic boundary layers, the rib heights are non-dimensionalized with respect to D_h; opposite to δ for supersonic flows.

Trends on skin friction and heat transfer One of the first systematic experimental studies on the effects of ribbed surface roughness in subsonic flows was conducted by J.C. Han in 1984.[6] For this research, emphasis was laid on the effects which ribbed geometries have on the heat transfer and skin friction for the fully developed, turbulent flow region. The considered geometries included square-ribbed roughness elements for which relative pitch ratios, p/e were 10, 20 and 40 and relative height ratios, e/D_h were 0.021, 0.042 and 0.063. At a later stage, Liou and Hwang (1992) decided to add to Han's research by conducting similar experiments with slightly different roughness elements.[8] This was done by selecting larger ribs at e/D_h of 0.063, 0.081 and 0.106 at a similar p/e equal to 10, 15 and 20. By then exposing these geometries to similar flow conditions $5.0 \cdot 10^3 \leq Re \leq 5.4 \cdot 10^4$, the analogy was valid. A minor difference between the researches was that Liou and Hwang considered Nu, and Han utilized St as heat flux parameter. By the interrelation of these non-dimensionalized

properties, though, their respective trends and correlations are similar (Equation 2.14). In the current discussion, St is used as primary heat transfer coefficient.

The goal of these studies was to derive general prediction methods and simplified correlations for both the average friction factor $\overline{f}$ (i.e. $\overline{C_f}$, Equation 2.9) and average heat transfer coefficient $\overline{St}$ (Equation 2.11) which cover the entire range of mentioned geometric design parameters. Fortunately, within their combined set of geometrical models, the existence of consistent trends and flow effects has been proven.

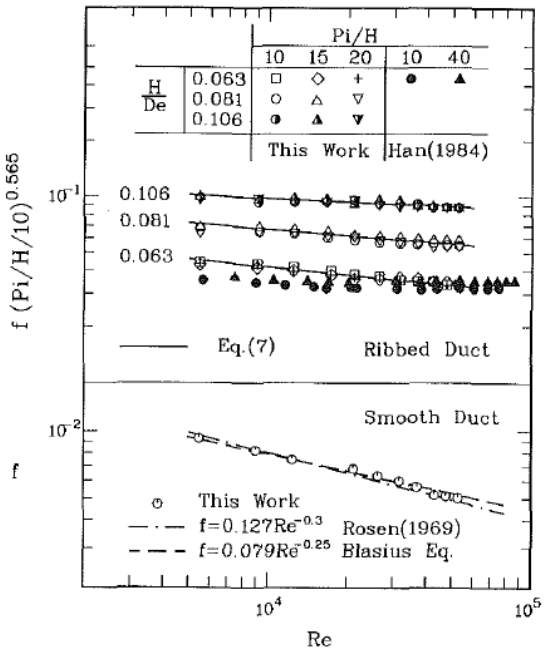

FIGURE 2.13: Friction factors versus Re at various p/e and e/D_h.[8] (Liou and Hwang, 1992)

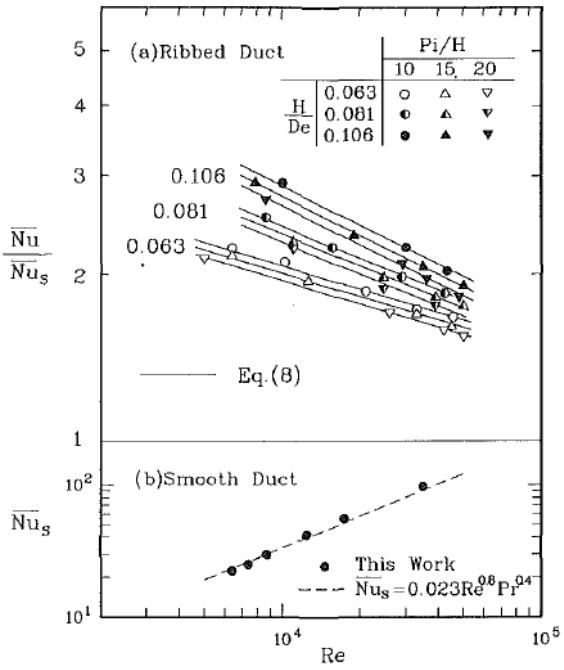

FIGURE 2.14: $\overline{Nu}/\overline{Nu_s}$ versus Re at various p/e and e/D_h.[8] (Liou and Hwang, 1992)

The data displayed in Figures 2.13 and 2.14 was gathered experimentally, using respectively static pressure probes and thermocouples placed along the length of the wind tunnel. The wind tunnel walls consisted of four aluminum plates covered by a thin copper film, which were heated electrically to a uniform state of constant wall heat flux, q_s. Through these temperature and static pressure measurements, the following geometry-dependent property sequences were investigated:

- The effect of rib height on $\overline{St}$ and $\overline{f}$ at a constant p/e of 10, 15 and 20 with varying Re.
- The effect of rib pitch on $\overline{St}$ and $\overline{f}$ at a constant e/D_h of 0.063 with varying Re.

Multiple conclusions can be drawn regarding the trends with respect the geometrical parameters, displayed in respectively Figures 2.13 and 2.14. With respect to relative height ratio, e/D_h the data of $\overline{St}$ and $\overline{f}$ primarily displays that:

- Per Re both average friction, $\overline{f}$ and heat transfer coefficient, $\overline{St}$ increase with e/D_h.
- At a fixed e/D_h, the $\overline{f}$ approaches a constant value for an increasing Re.
- At a fixed e/D_h, the $\overline{St}$ continues to decrease with an increasing Re.

For the current sequence, it is found that each doubling of relative rib height causes $\overline{f}$ to increase by approximately 50 percent. In contrast, only a small increment in $\overline{St}$ is observed as on average merely six percent is added by an equal increase in roughness height. The latter gives rise to the hypothesis that at a fixed *p/e*-ratio, the relative roughness height primarily influences the drag of the geometry; affecting the $\overline{f}$. In contrast, the turbulence levels (i.e. u', v' and τ_{ij}) which are important to heat transfer, are barely affected.[30] (Kao et al, 1988). With respect to relative pitch ratio, p/e the data of $\overline{St}$ and $\overline{f}$ indicates that:

- Per Re both average friction, $\overline{f}$ and heat transfer coefficient, $\overline{St}$ decrease with p/e.
- At a fixed p/e ratio, the $\overline{f}$ approaches a constant value for an increasing Re.
- At a fixed p/e ratio, the $\overline{St}$ continues to decrease with an increasing Re.

More specifically, it is seen that – on average – each doubling in p/e-ratio results in a 45 percent decrement in $\overline{f}$. In addition, the same change in *p/e* causes a 65 percent decrement in $\overline{St}$. These trends on average skin friction and heat transfer data strengthens the hypothesis of the limited effect which changes of roughness height impose on the turbulence properties of the flow near the wall. As the periodic placement does affect both the average friction factor and Stanton number, it becomes highly likely that the change of flow topology is more dominantly changed by pitch than roughness height. The latter is proven by the simultaneous mean velocity and heat transfer measurements conducted by Aliaga et al (1993), through which the exact flow phenomena were directly assigned to trends observed in the adjoining changes in heat transfer (Section 2.2.4).[10]

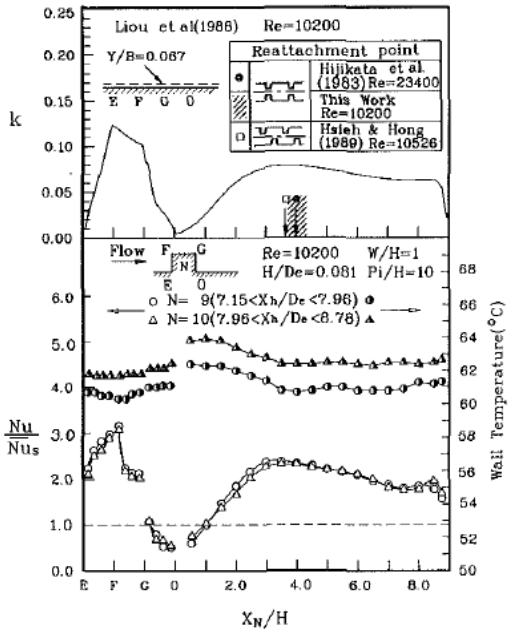

FIGURE 2.15: Streamwise distributions of local Nusselt number, turbulent kinetic energy, and wall temperature.[8] (Liou and Hwang, 1992)

Two additional properties which can be observed, are the steepened slope of $\overline{Nu}$ and flattened slope of $\overline{f}$ by an increment of roughness height, e/D_h. The physical reasoning behind this is that at higher e/D_h, the cross-sectional blockage increases with the rib height and, therefore, the inertial loss of the flow is relatively more dominant rather than the friction itself. As a result, at larger the rib heights, the turbulence added to the flow surpasses the

increment of drag. This remains in-line with the statement made before that turbulence levels correlate directly with heat transfer, whereas drag corresponds to the average friction. In fact, this mentioned correlation between turbulence and heat transfer was proven by Liou and Hwang through Figure 2.15. Within this figure, the direct coherence between the turbulent kinetic energy, k and heat transfer ratio, Nu/Nu_s is shown along the streamwise direction of the flow. The example included in the figure corresponds to a rib geometry with a p/e of 10, and e/D_h of 0.081. Nevertheless, following the physical explanation, these observations apply for all prior investigated ribbed-roughness geometries with $p/e \geq 10$ and $e/D_h \leq 0.106$.

Correlations on skin friction and heat transfer The main goal for Han's research[6] was to form prediction functions through which the average friction and heat transfer over ribbed surfaces could be estimated accurately and reliably. The latter was done by conducting a systematic campaign from which the required data was gathered and correlation fits were formed. The resulting relations (Appendix A) were found to remain largely in-line with the datasets. Nevertheless, for larger Re, these correlations deviated by nearly 10% from the experimental data. In contrast, the correlations derived by Liou and Hwang (1992) have proven to remain within approximately $\pm 4.2\%$ of both datasets.[8] In addition, the compact form and close resemblance to the widely accepted smooth-wall Dittus-Boelter and Blasius relations, make the Liou and Hwang correlations preferred as current reference.[31]

The correlations derived by Liou and Hwang (1992) represent two main categories; average heat transfer coefficient ($\overline{Nu}$) and friction factor ($\overline{f}$). Each of which is created as a function of relative roughness height (e/D_h) and pitch (p/e) as the design parameters, and Re as flow variable. The first correlation, including the effects of Reynolds number and pitch ratio on the average friction factor $\overline{f}$, is represented by the following expression:

$$\overline{f} = C_1 \cdot Re^{-m} \cdot (p/e)^{-n} \tag{2.37}$$

$$= C_1 \cdot Re^{-m} \cdot (p/e)^{-0.565} \tag{2.38}$$

or

$$\overline{f} = C_1' \cdot Re^{-m} \cdot (p/e/10)^{-0.565} \tag{2.39}$$

Where C_1, C_1', m and n are constants dependent on the rib height, and are listed in Table 2.1 for various e/D_h.

TABLE 2.1: Coefficients C_2, C_2' and r for average Nu correlation.

e/D_h	C_1	C_1'	m	n	$Err.$ (%)
0.063	0.5603	0.1526	0.1402	0.5655	2.2
0.081	0.7139	0.1943	0.1129	0.5642	1.4
0.106	0.9069	0.2469	0.0953	0.5611	2.8

The second correlation, which includes the dependence of the average Nusselt number on the rib height, rib pitch, and Reynolds number is well-represented by an equation of the form:

$$\overline{Nu} = C_2 \cdot Re^{r} \cdot (p/e)^{-S} \tag{2.40}$$

$$= C_2 \cdot Re^{r} \cdot (p/e)^{-0.122} \tag{2.41}$$

or

$$\overline{Nu} = C_2' \cdot Re^r \cdot (p/e/10)^{-0.122} \tag{2.42}$$

Where the constants C_2, C_2' and r vary with the rib height, and are listed in Table 2.2 for the three respective roughness heights.

TABLE 2.2: Coefficients C_2, C_2' and r for average Nu correlation.

e/D_h	C_2	C_2'	r	s	$Err.$ (%)
0.063	0.2466	0.1862	0.6556	0.1211	1.8
0.081	0.3552	0.2682	0.6294	0.1223	4.2
0.106	0.5809	0.4286	0.5931	0.1216	2.1

The coherence of the correlations with the respective experimental data can be identified from the 'straight lines' in Figures 2.13 and 2.14. When using these correlations, one has to be aware of the fact that equations 2.39 and 2.42 have been derived for a limited range of Reynolds numbers ($5.5 \cdot 10^3 \leq \text{Re} \leq 5.4 \cdot 10^4$) and a specific set of ribbed roughness geometries for which $p/e \geq 10$. Nevertheless, the physics on which the form of these equations are based, are applicable to a wide variety of flow conditions. Therefore, it is expected that correlations of similar form can be derived through future experiments in supersonic flows.

Heat transfer optimization Previously, the trends of $\overline{f}$ and $\overline{St}$ displayed that an adaptation of e/D_h primarily influenced the average friction and had little effect on the heat transfer. In contrast, a change of relative pitch clearly affected both $\overline{f}$ and $\overline{St}$. The physical explanation for this is that the changes in flow topology resulting from p/e are significantly more dominant than those originating from a change in e/D_h. This interpretation of the findings is enforced by the Liou et al (1990), who describe the existence of three characteristic flows at respectively p/e of 5, 10 and 15. The first results of these characteristic flow properties is indicated by the following figure:

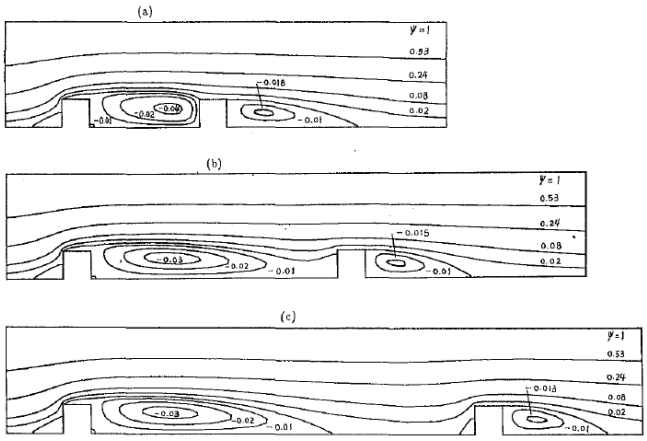

FIGURE 2.16: Calculated streamlines for characteristic flow fields (a) $p/e = 5$, (b) $p/e = 10$ and (c) $p/e = 15$.[29] (Liou et al, 1990)

From which can be observed that as $p/e > 10$, the turbulent boundary layer can reattach to the wall downstream of the first rib. Prior to the reattachment at p/e equal to 15, the boundary layer in between the ribs is seen to form a stable vortex at p/e of 5 which slowly transitions into a reattached flow for $5 \leq p/e \leq 10$. These are characterizations common to the classification of respectively an open, transitional and closed cavity flow. This topic is more elaborately touched upon in Section 2.3.

Judging by the streamlines of Figure 2.16, it is seen that the contact of the flow with the wall is greatly affected by this change in roughness geometry. As the pitch increases, the boundary layer reattaches to the wall and redevelops itself. From the viewpoint of heat transfer, it thus seems logical to use a geometry which optimally takes advantage of the interaction of the boundary layer with the wall. Previously, the coherence between the turbulence properties of the boundary layer and heat transfer at the wall has been proven in Figure 2.15. Turbulence levels can be indicated by the level in which directional mean flow (mean kinetic energy, KE) is represented by randomized, omni-directional flow structures (turbulent kinetic energy, TKE). Once the turbulence levels in the boundary layer have risen, more small-scale deviating flow structures exist near the wall; improving the thermal interaction of the flow with the wall itself.[17] (Pope, 2001) To indicate the likely thermal performance of each ribbed wall geometry, the standard deviation u'/U_{ref} and u/U_{ref} have been measured at a constant 1 mm height from the rib tops. The results of these measurements are shown in the following figures:

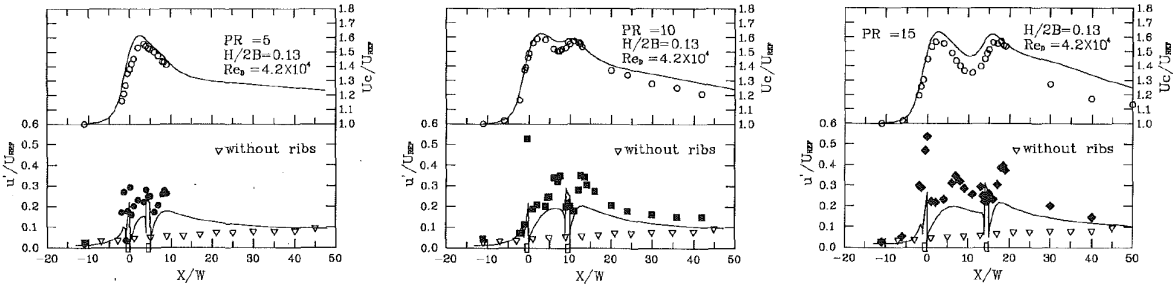

(A) p/e = 5 (B) p/e = 10 (C) p/e = 15

FIGURE 2.17: Streamwise distributions of mean velocity and turbulence intensity at 1 mm from the rib tops for p/e = 5, 10 and 15.[29] (Liou et al, 1990)

From which the existence of an increase in both flow acceleration and local turbulence intensity can be observed between geometries with a p/e of 5 to 10 (Figures 2.17a and 2.17b). Thus, an enhancement of the local heat transfer is expected. In contrast, Figures 2.17b and 2.17c display a slight decrease in combined turbulence enhancement and acceleration between p/e of 10 and 15. The above observation parallels the heat transfer results obtained by Han (1984) and Liou et al (1990), where lower $\overline{Nu}$ and $\overline{St}$ were found for geometries for which p/e > 10.[6,29] Combining the findings of all adjoining researches, it is found that an optimum average heat transfer should exists at a p/e of 10. This observation is supported by the numerically derived characteristic flow fields from Figure 2.16, where, at p/e < 10, a stable-vortex prevents the boundary layer to interact with the cavity wall.

2.2.4 Repeated cavity flow and IRT

Previous experimental research on the effects of ribbed roughness geometries provided correlations through which more accurate estimations can be made with respect to heat transfer and skin friction. (Han, 1984; Liou and Hwang, 1992)[6,8] Physical interpretations of these results can be made through streamwise mean velocity and turbulence measurements as well as flow simulations of characteristic cavity flows for p/e of 5, 10 and 15 (Liou et al, 1990).[29] However, detailed experimental studies into the exact flow phenomena remained to be performed. In 1993, Aliaga et al. conducted an experimental campaign, where the local heat transfer and velocity were measured simultaneously. By using an infrared thermography (IRT) technique on ribbed surfaces with a constant heat flux, local variations of heat transfer coefficients (h) were determined on top of, between and surrounding the ribs. This constant

q_s was obtained by applying electric power to a copper thin-foil, which heats up the surface through Ohmic heating.[10] (Aliaga, 1993) The detailed velocity profiles were measured by repositioning a pitot tube, which accessed the flow from above the channel. The experimental setup is shown in the following figure:

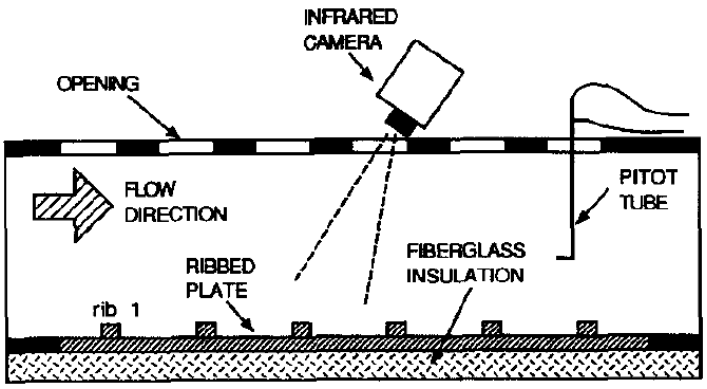

FIGURE 2.18: Experimental setup incl. insulated ribbed plate covered with stainless steel foil, IR camera and pitot tube.[10] (Aliaga et al, 1994)

Through the usage of the IR camera shown in Figure 2.18, it was possible to obtain detailed, direct temperature measurements from the heated stainless steel foil. Heat transfer and velocity measurements were conducted on ribbed plates with p/e equal to 5 and 12, both of which at roughness heights e/D_h 0.052 and 0.093. The tests were conducted in fully turbulent flow conditions, where $0.5 \cdot 10^6 < Re < 1.5 \cdot 10^6$. It can thus be seen that the flow region surpasses the previously considered Re regimes by an order of magnitude. The geometries selected, however, are still comparable.

In prior research, the temperature measurements were mostly obtained through static thermocouple measurements which were placed strategically along the wind tunnel length.[7,6,32] (Han, 1984; Han et al, 1985; Hishida and Takase, 1991) Even though the application of thermocouples is widely accepted due to their high accuracy ($\pm 0.5°C$), two main drawbacks are identified: (1) The measurement technique requires thermocouples to be emerged in the flow (i.e. intrusive), (2) the spatial resolution is limited to one point location (i.e. zero-dimensional). Acknowledging these points, it is worthwhile to obtain measurements through an accurate, non-intrusive technique which increases the spatial resolution of the temperature measurements.

Experimental studies on heat transfer over rough surfaces using infrared thermography (IRT) are very limited, however, through recent developments in IR image resolutions and optical enhancements IRT has gained recognition as a very appropriate research tool in the area of heat transfer.[33] (Carlomagno at al, 2010) It is through these technical developments that the IRT technique utilized by Aliaga et al (1993) can surpass the issues of limited spatial resolution by not requiring optics other than the IR camera itself. In addition, the estimated error margin for the IRT technique of 8.1% is a significant improvement over the average error margin of 12% found for thermocouples.[8] An example of the obtained level of detail for IRT measurements is shown in the following figures:

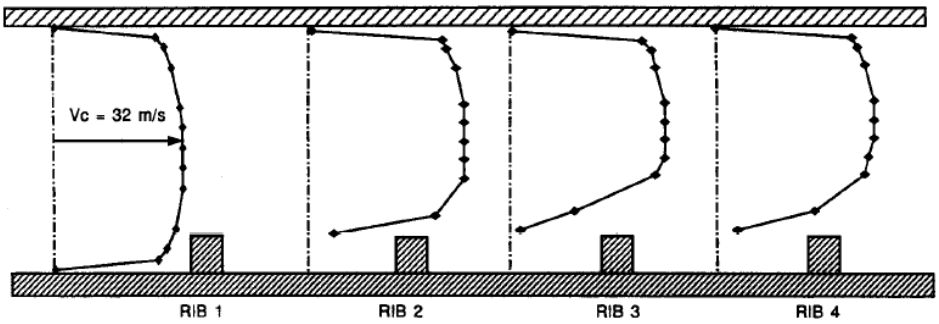

FIGURE 2.19: Mean velocity profiles in test section of wind tunnel ($Re = 10^6$, $p/e = 5$).[10] (Aliaga, 1993)

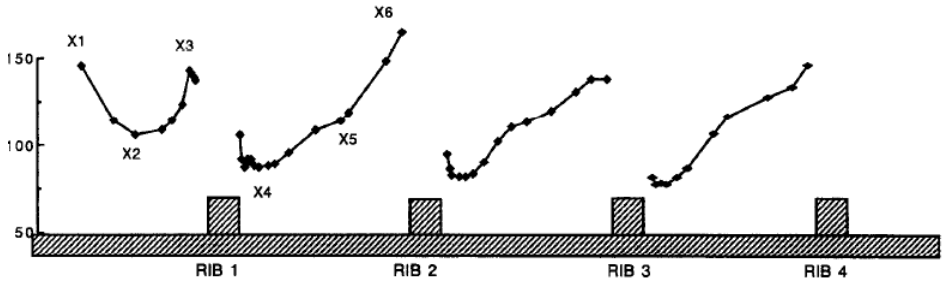

FIGURE 2.20: Heat transfer coefficient profiles in test section of wind tunnel ($Re = 10^6$, $p/e = 5$).[10] (Aliaga, 1993)

Where Figure 2.19 displays the freestream velocity profile along the vertical axis of the wind tunnel, and Figure 2.20 the heat transfer coefficient, h in streamwise direction of the test section (excl. the ribs themselves). This h is derived directly from the IRT temperature measurements by using Equation 2.12. Therefore, the spatial resolution and accuracy of h is a direct result of these temperature measurements. From both figures, where the relative pitch ratio p/e is equal to 5, the following can be observed:

- Developed flow is reached from the third rib: indicated by the unchanging velocity and heat transfer profiles between ribs 3 and 4.
- Directly downstream each rib, the flow is dominated by a recirculation zone: observed by a clear minimum St directly behind each rib.
- The boundary layer thins-out along the cavity length: seen by an increasing heat transfer for each cavity.

These observations are in-line with the streamlines computed by Liou et al. (1990) as shown in Figure 2.16. The corresponding flow field suggests the existence of a stable-vortex flow in between the ribs at a p/e of 5. However, through the large spatial resolution of IRT, a thinning, stable-vortex flow is found. In this same research, Liou et al. mentioned the existence of three characteristic flow fields at respectively p/e 5, 10 and 15. The difference of these characteristic flows was proven to be the direct result of the reattachment of the boundary layer. The following graphs prove the effect of boundary layer reattachment through simultaneous mean flow and heat transfer measurements for p/e equal to 12:

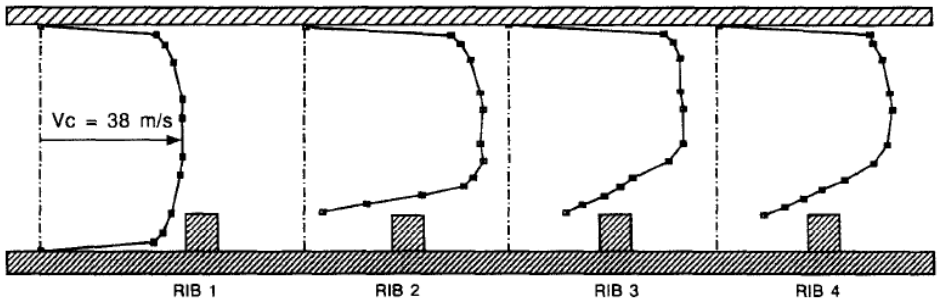

FIGURE 2.21: Mean velocity profiles in test section of wind tunnel ($Re = 10^6$, $p/e = 12$).[10] (Aliaga, 1993)

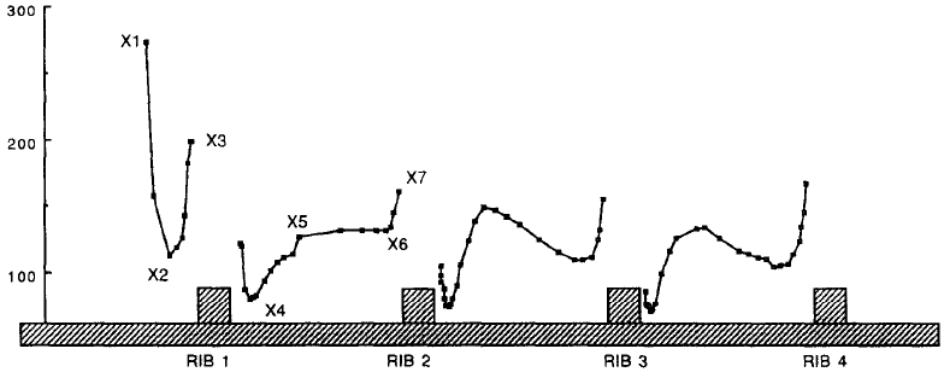

FIGURE 2.22: Heat transfer coefficient profiles in test section of wind tunnel ($Re = 10^6$, $p/e = 12$).[10] (Aliaga, 1993)

Where a highly different heat transfer profile is observed inside the cavities of the consecutive ribs. For the current geometry, Figure 2.21 indicates the mean velocity profiles above the ribs, whereas Figure 2.22 corresponds to the h-profiles inside the rib cavities. For the geometry with p/e of 12, the following observations can be made:

- Developed flow occurs from the third rib: indicated by the unchanging velocity and heat transfer profiles between ribs 3 and 4.
- Directly downstream each rib a more dominant recirculation zone is found: observed by the local minimum in h, which is the lowest h of all geometry measurements.
- Along the length of each cavity, boundary layer reattachment and redevelopment follow: found by a maximum in h followed by a near-linear decrease of h.
- Directly upstream of each rib another recirculation zone is found: observed by the second local minimum in heat transfer coefficient.

By combining the observations based on Figures 2.19 and 2.20 for p/e equal to 5, and Figures 2.21 and 2.22 for p/e equal to 12, it can be seen that the primary differences in velocity profile exist near the rib tops. Where for p/e of 5 an equivalent flat plate profile and at p/e of 12 a more shallow profile exists. This observation builds on the fact that the boundary layer can cross the ribs relatively unaltered for an open cavity, whereas it is more disturbed for closed cavity flows. In addition, it is seen that similar flow conditions are found from the third rib downstream for both p/e of 5 and p/e of 12; indicating developed flow. The most prominent differences are found at the heat transfer profiles, which point towards the differences in cavity flow types. The following figures contain detailed representations of these St profiles in fully developed cavities, accompanied by indicative flow features:

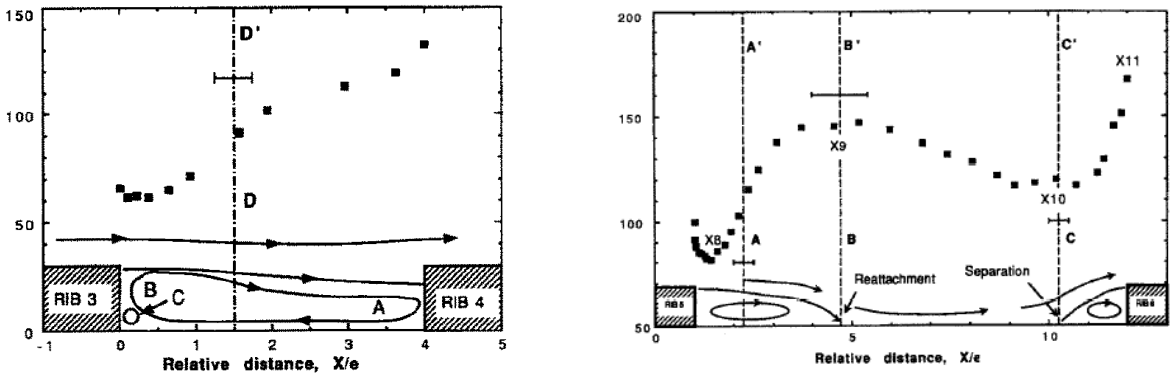

(A) p/e = 5. (B) p/e = 12.

FIGURE 2.23: Local h distribution and flow visualization with indicative recirculation and reattachment regions on test plates.[10] (Aliaga et al, 1993)

From Figures 2.23a and 2.23b, the provided level of detail of the h allows us to directly assign a flow feature to each change in heat transfer. As a result, the following observations are listed:

- A recirculation zone effectively insulates the wall as a *trapped-vortex* prevents unheated air from the freestream to interact with the heated surface. This effect is shown at locations 'X8' and 'X10' in Figure 2.23b, where minima of St are found directly before and after the ribs. The latter of which indicates boundary layer separation prior to the downstream recirculation.

- Another insulating effect also holds more generally for the boundary layer itself. As the boundary layer reattaches, develops and grows thicker, less interaction and thus less thermal exchange is possible between the wall and the freestream. The effect of the boundary layer thickness is seen in both Figures 2.23a and 2.23b, where the first displays an increment in St due to 'thinning' of the stable vortex. The latter, in turn, shows a peak heat transfer at the reattachment location 'X9' after which a linearly h decrease follows up to 'X10', where the boundary layer separates. In between 'X9' and 'X10' regular boundary layer development occurs, implying that the BL simply grows thicker moving downstream.

It is seen that the previously hypothesized flow effects can accurately be pointed-out from the detailed IR data. Previously, Liou et al. (1990) determined that reattachment location X_{R2} aft the second rib was equal to 4.4 for $p/e \leq 20$. This was estimated through LDV measurements of the flow field. The reattachment location $X9$ is found at X/e of 4.6 for the fully developed boundary layer at developed conditions. This displays the coherence of the measurements by Aliaga et al. and Liou et al. (i.e. ΔX_R of 4.3%). In addition, it is seen that between the second cavity X_{R2} and cavity at similarity X_{R5}, little discrepancy exists.[29,10] Judging by the minor difference of reattachment location, the conclusion drawn that developed conditions occur from rib 3, are strengthened.

Finally, the notions with regards to flow topology imply that at a p/e of 5, a thinning, stable vortex is found in between the ribs. In addition, a double recirculation pattern separated by regular boundary layer development is observed for p/e of 12. In terms of cavity flow classifications, the first is commonly known as *open cavity flow*, whereas the latter is ascribed to *closed cavity flow*. It is said that the currently observed flow fields are a combination of pure cavity flow and roughness induced boundary layer development. This can shortly be

referred to as *repeated cavity flows*. These exact formation and classifications of each cavity flow are explained in more detail in Section 2.3.

The detailed observations which were made with respect to the effect of the p/e, are seen to remain in-line with previous correlations derived by Han (1984) and Liou and Hwang (1992). Similarly to the mentioned effects of p/e on the flow topology, Aliaga et al. additionally investigated the respective effects of e/D_h and Re for geometries at the indicated pitch ratios. The effect of varying relative roughness height on respectively p/e of 5 and 12 is shown in the following figures:

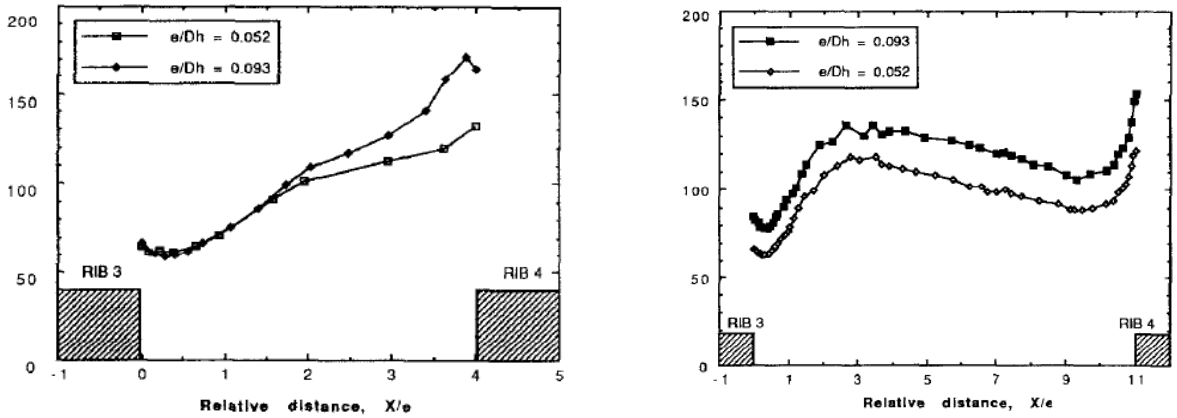

(A) p/e = 5 (B) p/e = 12

FIGURE 2.24: Effect of the relative roughness height on St at the cavity surface.[10] (Aliaga et al, 1993)

Where a limited effect of the roughness height variance e/D_h is seen for p/e of 5 (Figure 2.24a), and a near constant increment in St is observed for the geometry with p/e equal to 12 (Figure 2.24b). The near constant increment in heat transfer coefficient of 10% supports the results of previous studies, which displayed similar trends with respect to e/D_h for $p/e \geq 10$.[6,29] (Han, 1984; Liou et al, 1990) These trends of respectively a limited and constant effect of e/D_h on the heat transfer coefficient can be directly explained through the differences in flow topology. From Han (1984), it is known that a change in e/D_h has a limited effect on $\overline{h}$ compared to increments in $\overline{f}$. Liou et al (1992), in turn showed that increments in heat transfer directly correlate with the turbulence levels of the boundary layer (i.e. $\overline{u'} \cdot \overline{U}$).

Streamwise increments in turbulence levels are caused by the blockage effects of the individual ribs, effectively functioning as turbulence promoters.[12] (Jimenez, 2004) Therefore, as e/D_h increases the blockage increases, causing the overall turbulence levels to increase as well. Still, in order for more heat transfer to take place, the turbulent boundary layer has to interact with the cavity surface. As the stable-vortex flow displayed in Figure 2.23a insulates the wall and thus prevents this interaction to take place, no change in h is expected to be seen. This is supported by Figure 2.24a, since no change in h occurs up to the location where the stable vortex thins-out and the boundary layer does interact with the wall. In addition, the flow topology for p/e of 12 (Figure 2.23b) causes the boundary layer to constantly interact with the cavity bottom more prominently. Thus, as the turbulence levels of the boundary layer have increased, a constant rise of St results along the length of the cavity.

Prior to the research from Aliaga et al (1993), only Liou et al (1990) considered to conduct experimental investigations on geometries for which p/e is equal to 5. In their research, it was concluded that a geometry for which p/e is equal to 5 is less optimal in terms of heat

transfer than a geometry for which p/e is equal to 10.[29] This was based on the $\overline{u'}$-profiles, which were found to correlate with St properties. The detailed heat transfer measurements from Aliaga et al. provide the required insight into the flow topologies such to properly explain these observations. However, to the knowledge of the researcher, an experimental investigation in which the varying flow phenomena are visualized experimentally, are unavailable. Therefore, the need still exists to form explicit proof on the effects of the flow field through design parameters e/D_h and p/e. It is decided to obtain the latter by conducting Schlieren, PIV and IRT experimental techniques, where the initial two function both as a means of visualization as well as a method of IRT validation.

2.3 Supersonic cavity flows

The discussion of the subsonic, large-roughness boundary layer flows has led to the characterization of this particular flow field as *repeated cavity flows*. In turn, by observations on the effects of small-scale roughness in supersonic flows, indications were found of similar supersonic cavity flow-type response. To the best knowledge of the researcher, experimental investigations on the effect of large-scale roughness (i.e. $e/\delta > 0.2$) induced flows in the supersonic boundary layer are absent. Therefore, the theories behind the nearest aerodynamic relative are investigated; *supersonic cavity flows*. For the current thesis, it is important to form background knowledge on the cavity flow-type classifications and their effect on the flow field located within and directly above the cavities. Generally, it is found that not the external flow parameters (M, δ, Re), but geometrical design parameters (p/e, w/e) are dominant for the classification of the cavity flow types. For cavity flow research, it is customary to define p/e as the length-to-depth ratio, l/h. This is not used in this section to avoid ambiguity. Therefore, any graph indicating p/e is altered for clarity.

It turns out that two major experimental investigations on the mechanisms of flow-type changes in supersonic cavity flows have been conducted; first by Stallings and Wilcox in 1987, second by Zhang et al. in 2002.[34,13] The aim of Stallings' and Wilcox' research was to define pressure distributions for rectangular cavities over a range of free-stream Mach numbers and cavity dimensions (i.e. w/e and p/e). In turn, Zhang et al. focused on accurately mapping and clarifying the mechanisms of the transition of cavity-flow types as their p/e-ratio increases or decreases. In this section, there is focused on influence on and the classification of cavity type flows. For a more elaborate explanation on the detailed supersonic cavity flow mechanisms, the reader is referred to Appendix B.

2.3.1 Influence on cavity flow classification

Multiple experimental and numerical investigations have been conducted into the classification of supersonic, compressible cavity-type flows; varying multiple flow and design parameters. Generally though, most researchers have established that the dominantly defining parameter for these flow types is their p/e. As a result, cavity flow classifications are commonly assigned by a critical length-to-depth ratio $(p/e)_{cr}$, which pinpoints the transition of cavity flow types.The respective effects of the $(p/e)_{cr}$ ratios on supersonic cavity flows were investigated by Heller et al. (1971), Ahuja and Mendoza (1995), Tracy and Plentovich (1997), Stallings and Wilcox (1987) and Zhang et al. (2002).[35,36,37,34,13]

Ahjua and Mendoza were the first to conduct an experimental investigation with a turbulent boundary layer, and observed that an increasing boundary layer thickness tends to eliminate most unsteady cavity fluctuations (as opposed to laminar flows investigated by Heller

et al.).[35,36] As a result, it was found that an increasing δ, results in a decrease of pressure inside the cavity and smoothing of all pressure gradients. Nevertheless, hardly any effect was seen on the designation of $(p/e)_{cr}$. The same limited effects on $(p/e)_{cr}$ were found for the freestream Mach (M) and Reynolds number (Re), whereas the width-to-height ratio, w/e was found to have a profound effect on the cavity flow type characterizations.[36]

Between their researches, respectively Stallings and Wilcox, and Zhang et al. determined $(p/e)_{cr}$ to be equal to respectively 13 and 14 [-]. Zhang et al. assigned this difference to the increase in w/e from 5 for Stallings and Wilcox, to 10 for his own research.[34,13] For any wind tunnel test, the presence of lateral side walls decelerates the flow; affecting the lateral velocity and pressure gradients within the test section. For the supersonic cavity, this effect is illustrated in the following figure:

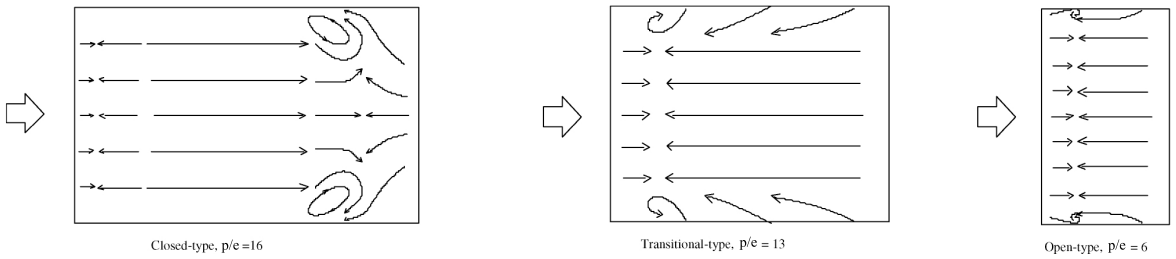

FIGURE 2.25: Surface flow patterns of three-types of cavity flows.[13]
(Zhang et al., 2002)

Where, from left-to-right, Figure 2.25 displays respectively closed, transitional and open cavity flow. The surface flow patterns indicate relatively weak three-dimensional flows in open- and transitional type cavities and a much stronger one in the closed-type cavity. Zhang et al. found that for a closed-type cavity flow, a pair of large vortices exist behind the exiting shock wave beside the side walls. It reveals that the boundary layers over the wind tunnel sidewalls first thicken, after which they separate under the severe adverse pressure gradient associated with the impinging and exiting shock waves over the cavity.

By the notion that these three-dimensional effects do not increase as w/e increases, the lateral flow field of the cavity becomes less dominated by these wall effects for an increment of w/e. In turn, a larger w/e allows for a less disrupted centerline cavity flow, such that the flow topologies develop more uniform laterally as p/e is increased. As a result of this, it is expected that further increments in w/e will have a less profound effect on the measured $(p/e)_{cr}$; provided the cavity flow types are derived from the longitudinal centerline.

2.3.2 Classifications of cavity flow types

Based on the previous discussions, it can be said that – provided the boundary layer is turbulent, supersonic and $w/e \geq 10$ – the classification of the cavity flow types are solely dependent on p/e. As a result, the cavity flow classifications are invariant and equal to: *Open*, $p/e < 10$, *Transitional*, $10 < p/e < 14$ and *Closed*, $p/e > 14$. Generally, the main flow features of these cavity type flows are ascribed to the discontinuities associated with compressible flow. From Figure 2.26, it is concluded that for:[34,13] (Stallings and Wilcox, 1987; Zhang et al. 2002)

- *Open cavity flow*: relatively weak leading edge shock and a stronger trailing edge shock exists, separated by a cavity bridging shear layer.

- *Transitional cavity flow*: leading and trailing edge expansion fan are formed, separated by a compression wave. The shear layer barely bridges the cavity, being heavily deflected by the initial expansion fan.
- *Closed cavity flow*: stronger leading and trailing edge expansion fans are found, separated by two compression waves. The latter of which collide into a single shock wave inside the freestream; forming a delta-wave. This flow field consists of two recirculation zones, separated by a reattached boundary layer. As such, this cavity flow type is commonly called a *dumbbell flow*.

The primary distinction between the cavity type flows originates from the propagation of the shear layer. Generally, for a closed type cavity flow, the shear layer expands over the cavity leading edge and impinges on the cavity floor, whereas for open type cavity flow, the shear layer bridges the cavity. The spreading of the shear layer and its gradual approach towards the cavity floor as p/e increases, tends to suppress the freedom of back flow. Therefore, leaving the cavity *open* or *closed* for a single, recirculating cavity flow. The corresponding flow categorization is illustrated in the following figures:

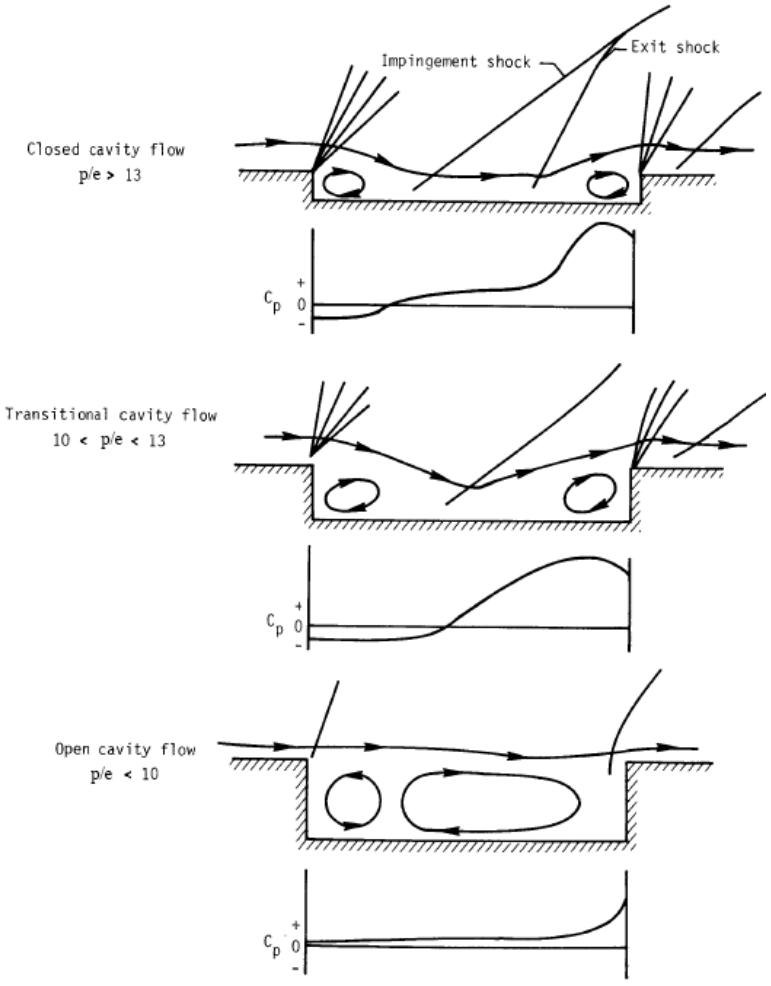

FIGURE 2.26: Classification of cavity flow types by varying p/e; respectively closed (top), transitional (middle) and open (bottom) cavity flows.[34] (Stallings and Wilcox, 1987)

Where schematic representations of respectively open, transitional and closed cavity flows are indicated. Within each schematic, the displayed streamline represents the propagation

of the shear layer. Based on the previous discussion, it is seen that the point of transition from transitional-to-closed cavity can be defined by a so-called *critical length-to-depth ratio*, $(p/e)_{cr}$. The value assigned to $(p/e)_{cr}$ thus represents the pitch-to-height ratio at which the shear layer impinges the bottom of the cavity for the first time. In accordance with larger w/e, this critical value is set at $(p/e)_{cr}$ 14 $\pm$ 0.2 [-] for the remainder of the thesis.

2.4 Description of the flow fields

By evaluating the research described in Sections 2.2 – 2.3, it is seen that the results from individual sources remain largely in-line with one another. The detailed IRT results gathered by Aliaga et al. made it possible to draw substantiated conclusions on the actual flow phenomena which are at the root of previously derived effects on $\overline{St}$.[6,8] (Han, 1984; Liou and Hwang, 1992) In this section, the previously derived trends and encountered flow phenomena are combined, summarized and listed in accordance with design parameters e/D_h and p/e. All correlations on the velocity profiles, heat transfer and friction factor hold for geometries for which $e/D_h \leq 0.106$ and $5 \leq p/e \leq 40$. The corresponding trends for average heat transfer ($\overline{St}$, $\overline{Nu}$) and average friction factor ($\overline{f}$) are listed in the following table:

TABLE 2.3: Trends for heat transfer and friction coefficient.

Design par.	Fixed par.	$\overline{St}$, $\overline{Nu}$	$\overline{f}$
$p/e \geq 10$	e/D_h, Re	-	-
$p/e < 10$	e/D_h, Re	-*	-*
$e/D_h \geq 0.021$	p/e, Re	+*	+*
$e/D_h < 0.021$	p/e, Re	+	+
$7 \cdot 10^3 \leq Re \leq 9 \cdot 10^4$	p/e, e/D_h	-	-**
$1 \cdot 10^6 \leq Re \leq 1.5 \cdot 10^6$	p/e, e/D_h	+	+

Where '+' indicates an equal or positive trend and '-' an opposite or negative trend. The '*' indicates trends which have not been derived through explicit measurements of St or f. In contrast, these have been derived indirectly through observations from the flow topologies and u' measurements from Liou and Hwang (1992). Finally, the '**' marks a correlation of $\overline{f}$ which decreases asymptotically with Re. Note that the correlations with respect to relative pitch indicate a maximum $\overline{St}$ at a p/e of 10. However, the latter is still to be proven directly through heat transfer measurements on geometries with a consecutive pitch variance, including $p/e < 10$, 10 and > 10.

The correlations on the heat transfer and friction properties made it possible to formulate the likely influence of the two geometric design parameters e/δ and p/e on the flow topology. In turn, experimental data from Liou et al. (1990) and Aliaga et al. (1993) allowed to strengthen these proposed influences on the flow phenomena by means on computational analysis and IRT, respectively. In Section 2.2, it was shortly mentioned that the flow field resulting from repeated-rib roughened walls can be best described as *repeated cavity flows*. The multitude of flow phenomena which are at the base of these flow topologies, were found to originate directly from cavity flow fields. Actually, it was found that the effects and classifications of cavity flows remained largely constant across the flow regimes.[38] (Rizzetta and Visbal, 2003) As such, for supersonic flow conditions, the sole difference between the flow fields was found to lie at the occurrence of flow discontinuities compared to subsonic conditions.[39,40] (Auxer et al., 1969; Rossiter, 1964) The corresponding schematics of the expected (and validated, Chapter 5) flow types, are indicated in the following figures:

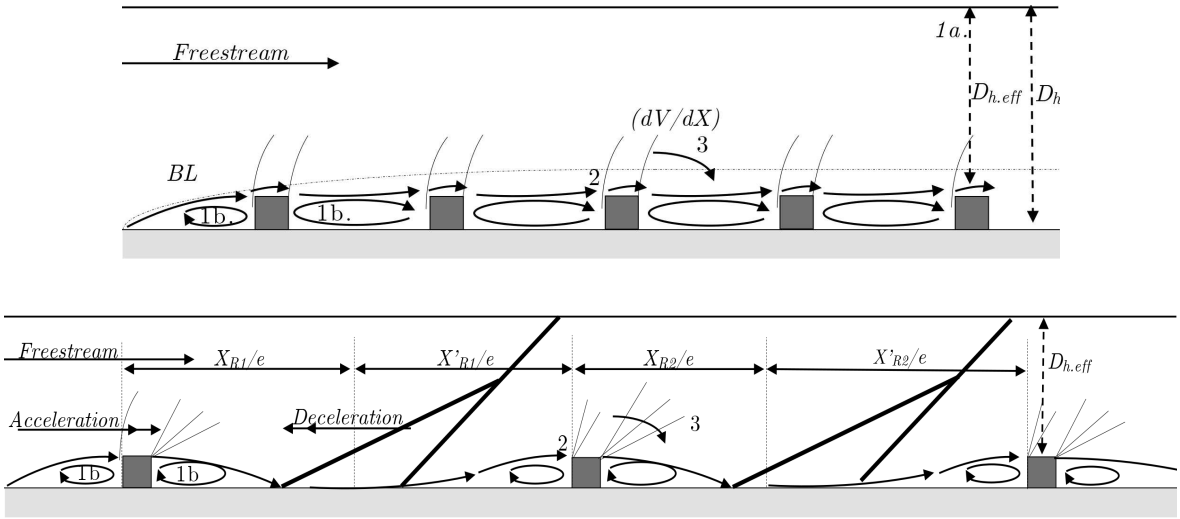

FIGURE 2.27: Repeated open and closed cavity flow, respectively p/e of 5 (top) and 15 (bottom). *Sketch is based on sources described previously.*

Where Figure 2.27 displays the repeated open- and closed flow topologies for geometries with a p/e of 5 and 15, respectively. In general, the presence of roughness elements disturbs the flow field at and near the surface. This increases the intensity of velocity and vorticity fluctuations in the boundary layer, which effectively enhances the turbulence properties. It is said that the relative height (e/δ) mostly influences the turbulence properties, whereas the relative pitch (p/e) primarily affects the flow topology. The relative height defines the magnitude of the following flow effects:

1. *Blockage effect*: The variable e/δ corresponds to the fraction of the boundary layer, which is blocked by the roughness elements. This blockage causes three main flow effects to take place; freestream acceleration, deceleration and flow stagnation.

   (a) *Freestream acceleration*: The blockage of the ribs effectively reduces the surface area, A of the wind tunnel. It is observed that the propagation of the boundary layer effectively forms a nozzle contour around each roughness element. By following nozzle area ratio function (i.e. A/A^*), the flow is found to accelerate.

   (b) *Freestream deceleration*: Provided the boundary layer (BL) reattaches inside the cavity, the hydraulic diameter, D_h is nearly restored to its original size; discontinuing the nozzle shape. In turn, the resulting size of surface area causes the freestream to decelerate. Thus, depending on the cavity flow topology (i.e. p/e), the freestream velocity u fluctuates constantly along the length of the geometry.

   (c) *Flow stagnation*: Directly upstream and downstream of the ribs, the flow velocity, u is reduced to zero. As a result, two zones of nearly stagnant air are formed and interact with the faster flowing freestream. This interaction of slow and fast moving air results in two recirculation regions, which prevent refreshment of the BL to take place; effectively insulating the wall. In terms of heat transfer optimization, this should thus be prevented as much as possible.

2. *Impingement effect*: Provided the turbulent boundary layer interacts with the upstream rib face of the roughness geometry, the BL is said to collide with the rib itself. As a result, the flow becomes more disturbed and turbulence levels are enhanced. Based on

a regular, asymptotic boundary layer (Section 2.1.1), a rib with a larger e/δ, encounters higher velocities. This means that as each rib impinges higher into the BL, the turbulence increments (TKE) of each individual rib will increase as well.

3. *Mean flow gradient*: The occurrence of nearly stagnant air directly downstream of each rib causes the formation of a recirculation zone inside the cavities. In turn, the large difference in static pressure gives rise to velocity gradients at the trailing edge of each rib. As a result, the air from both boundary layer and the freestream is forced inside the cavities, affecting to the reattachment location of the boundary layer.

The strength of the three main effects can be assigned to the size of the relative roughness height e/δ. Looking closely at Figure 2.27, it is observed that to a certain extent, the blockage effect (1a and 1c) and mean flow gradient (3) occur for each consecutive rib traveling downstream; regardless of p/e. In contrast, the flow collisions which are assigned to the the impingement effect (2) are greatly influenced by the relative pitch p/e. This means that, downstream of rib 1, the magnitude of impingement/collision is affected by whether the boundary layer has reattached to the surface prior to the downstream rib face. This same development of the boundary layer, in turn, greatly affects the effective hydraulic diameter, $(D_h)_{eff}$. As mentioned, each variance in $(D_h)_{eff}$ has a linearly opposite effect on the freestream velocity; accelerating or decelerating the flow. This explains the occurrence of periodic velocity fluctuations in the freestream for flow topologies resulting from $p/e \geq 10$ (closed), whereas a single freestream acceleration is found for flow topologies from geometries for $p/e \leq 5$ (open). It can thus be summarized that the magnitude of each flow phenomenon (incl. 1b. and 2) is defined by e/δ, whereas the p/e determines whether or not each of these flow phenomena occurs in the boundary layer.

For the current design space, e/δ defines the effects which each individual rib has on the flow in terms of $\Delta u'$ and ΔU. In turn, p/e solely influences the cavity type flows by determining the distance between downstream rib and reattachment location inside the cavity (i.e. $X_{R'}$, Figure 2.27). Thus, depending on whether $p/e \leq X_R$, $p/e \approx X_R$ or $p/e \geq X_R$, the flow topology is represented by respectively an open, transitional or closed cavity flow field. The latter is explicitly indicated by both sketches, where for Figure 2.27, top $p/e \leq X_R$, and bottom $p/e \geq X_R$. These observations on the flow topologies are in-line with the conclusions drawn with respect to pure supersonic cavity flow classifications.[34] (Stallings and Wilcox, 1987) By analyzing the supersonic cavity flow mechanisms, Zhang et al. found that changes in cavity types flows are predominantly affected by the propagation of the shear layer. As for the current geometries the ribs effectively represent multiple cavities, a similar flow pattern is expected.

The provided flow descriptions are based on the combined knowledge of small-scale supersonic roughness research (Section 2.2.2), large-scale subsonic roughness research (Section 2.2.3) and supersonic cavity flow research (Section 2.3). By comparing these findings to the obtained results (Chapter 5), mostly the same conclusions can be drawn. In addition, it can be concluded that the most vital observations came by the detailed combined velocimetry and heat transfer analysis of IRT.[10] (Aliaga et al., 1993) As such, the current thesis methodology is inspired by a similar approach where subsequently PIV and IRT are used to conduct a parametric investigation into large-scale, supersonic roughness elements.

Chapter 3

Flow facilities and visualization

Due to the novelty of conducting quantitative thermographic experiments (QIRT), it is decided to perform a measurement technique prior as complementary proof. To this end, particle image velocimetry (PIV) is chosen, as it has proven reliability and accurately provides both mean velocity and turbulence properties of a complete flow field. As PIV is relatively cumbersome, a Schlieren experimental campaign was performed beforehand. This is done in order to provide some qualitative insights into the entire flow fields which form under influence of the roughness elements. In this section, the theoretical background, experimental considerations and utilization of the Schlieren and PIV techniques are provided (Sections 3.3 and 3.4). In addition, a description of the supersonic tunnel, roughness geometries and placement of the test models are provided (Sections 3.1 and 3.2).

3.1 Supersonic wind tunnel

From the research objective, it is clear that experiments should be conducted at supersonic freestream conditions. To accommodate this, the High Speed Laboratory (HSL) of the Aerospace faculty has granted access to the ST-15 wind tunnel. This wind tunnel is a so-called *blow down type* and is able to provide freestream Mach numbers of 1.5, 2.0, 2.5 and 3.0 to the test section. The Mach number can be varied manually by installing various nozzle blocks, each having a specific geometry. For the current thesis, it is chosen to run experiments at Mach 2. Whilst operating at this Mach number, the wind tunnel characteristics are similar to those seen at supersonic cavity flow research, i.e. u_e = 534 m/s, P_0 = 3.2e5 Pa, T_0 = 290 K, Re = 3.7e7 and δ = 6.0 mm.[5,41] (Sun et al., 2012; Zhuang, 2006) As a result, it is expected that the occurrence of various cavity type flows becomes more predictable. A schematic of the ST-15 wind tunnel is provided in the following figure:

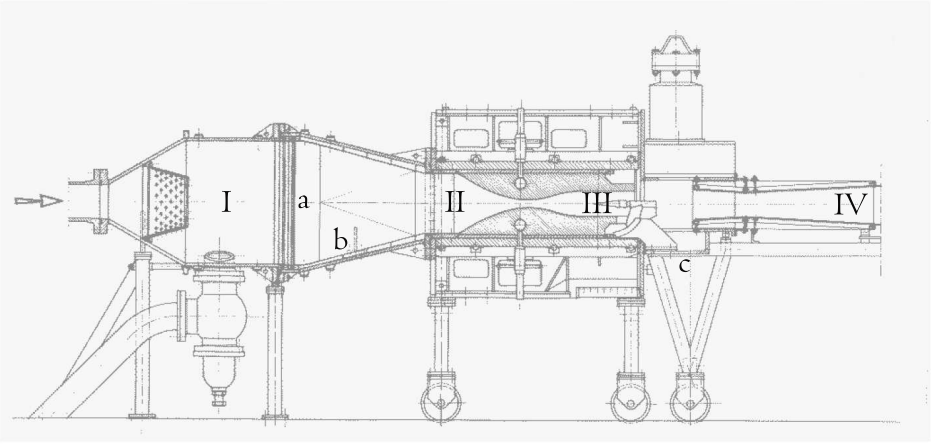

FIGURE 3.1: Schematic of the ST-15 supersonic wind tunnel.[42](Sun et al., 2014)

Where four major components have been indicated, corresponding to respectively the settling chamber (I), nozzle (II), test section (III) and adjustable diffuser (IV). Dried air is compressed and stored in a 300 m^3 external reservoir at pressures of up to 40 *bar*. The wind tunnel is operated by opening a valve which allows the high-pressure, dry air from the reservoir to enter the settling chamber. In the settling chamber, two layers of wire mesh screens (a) straighten the incoming flow and reduce the turbulence levels. The air inside the settling chamber is assumed to be stagnant such that the pressure and temperature measured here corresponds to their total equivalents, respectively p_0 and T_0 . In turn, the nozzle accelerates the flow up to the distinct Mach number as the air enters the test section. The size of the test section for the Mach 2 nozzle block is 0.15 x 0.16 m^2. Visual access to the test section is provided by two optical windows placed on both sides, each with a diameter of 0.25 m. These windows can be varied, depending on the requirements of the measurement technique. In the case of infrared thermography, both optical windows are replaced by respectively a Germanium window and a blank cavity door (Section 4.2). Finally, the air exists the test section through the adjustable diffuser which is connected to the ambient.

Over the course of time, particle image velocimetry (PIV) has played an increasingly dominant role at the Aerodynamics faculty. To accommodate these PIV experiments, the original design of the ST-15 wind tunnel has been altered to allow access for a seeding probe and laser periscope probe.[43] (Donker Duyvis, 2005) This has been done by placing a complete seeding rake in the convergent part of the settling chamber (b), and placing flanges directly downstream of the test section (c). The details on the positioning and functioning of these components can be found in Section 3.4. All experimental techniques are conducted using the ST-15 wind tunnel, operated at Mach 2. Therefore, the description as shown in this section can be used as reference throughout the report.

3.2 Model description

The discussion on the effects of roughness (Section 2.2), has provided a means of describing the required geometrical aspects of the test models. In this section, the general geometrical definitions of these models and methods of fixture inside the St-15, specified to Schlieren and PIV, are provided.

3.2.1 Geometrical definitions

An application of large roughness elements in supersonic flows, is found by the cooling channels inside nozzles of rocket launchers.[1] (ESA, 2016) These cooling channels are characterized as periodic, two-dimensional wall roughness elements, where the geometry is tailored to fit a specific case. In order to conduct a more fundamental study into the effects of such wall roughness, it is decided to utilize its most basic form; *the squared-rib* (Figure 3.2). Even though this geometry is relatively simplistic, its shape still allows for a parametric study into the most dominant geometrical aspects of complex, two-dimensional roughness; relative pitch (p/e) and height (e/δ).

In Section 2.2.3, it is seen that experimental investigations on the effects of square-rib roughness elements are already widely investigated in subsonic flows. The reason for this is that these elements are frequently used as turbulence promoters in various heat exchange facilities. Heat transfer optimization studies conducted by Han (1984) and Liou et al. (1990) have resulted in correlations and trends for St as a function of p/e and e/δ.[6,29] In turn,

experimental IRT results from Aliaga et al. (1994) have proven these flow fields can be typically described as *repeated cavity flows*.[14] These cavity type flows have been characterized by Robert and Wilcox (1987) in supersonic conditions and display direct coherence with these repeated cavity flow fields.[44] As a result, it is known that the p/e most dominantly influences the flow fields to represent specific cavity type flows in roughness configurations.

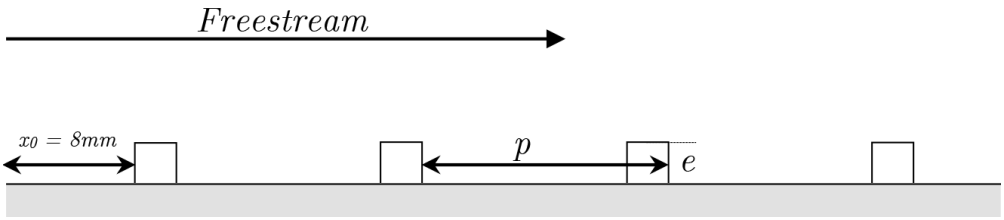

FIGURE 3.2: Schematic of the roughness geometries, incl. design definitions.

For the current experimental investigations, it is decided to choose the ribbed geometries such that supersonic correlations can be achieved (i.e. $St = f(p/e, e/\delta)$), similar those seen from their subsonic counterpart. This is done by focusing on the occurrence of each cavity type flow, respectively p/e < 10 *open*, $10 \leq p/e \leq 14$ *transitional*, $p/e \geq 14$ *closed*, whilst acknowledging the parallel with subsonic research. Roughness heights, in turn, are chosen such to comply with the large roughness criterion for discrete elements as set by Jimenez (2004), i.e. $e/\delta \geq 0.2$.[12] As a result, the following geometry design matrix is defined:

TABLE 3.1: Test matrix incl. the designed ribbed-wall roughness plates.

Relative pitch, p/e **Relative height**, e/δ	*5 [-]*	*10 [-]*	*15 [-]*	*20 [-]*	*25 [-]*	*30 [-]*
0.2 [-]	X		X	X		
0.4 [-]	X	X	X	X	X	X
0.6 [-]	X		X	X		
0.8 [-]	X		X			

Where, as boundary layer thickness, δ = 6 *mm* in the ST-15 test section, the absolute roughness heights, e are equal to respectively 1.2, 2.4, 3.6 and 4.8 *mm*.[5] (Sun et al., 2012) In addition to the fourteen test plates marked in Table 3.1, a flat plate model is added to the sequence as a reference. For the roughened geometries, the first rib face is always located at 8 mm from the test plate leading edge (x_0, Figure 3.2). This is done to provide the boundary layer a sufficient time to settle after engaging the LE insert. By this requirement and the limited streamwise length of the test plates, the number of ribs is limited and varies depending on each rib geometry. For a completely equivalent comparison amongst roughness heights, an equal number of ribs would be beneficial. However, by the limitations of the test section size, this discrepancy is inevitable. Throughout the report, test plates are referred to their geometries by rib height, e in *mm* and p/e [-]; e.g. "2.4/30". These geometrical definitions are used as a base for the design of test plates for respectively Schlieren, PIV and QIRT.

3.2.2 Model design: Schlieren and PIV

The first set of test models are constructed in application to Schlieren visualization and PIV. The overall model design is governed by the arrangement of the Mach 2.0 nozzle block, placed in the ST-15 (Section 3.1). This Mach block defines both the fixture points (i.e. placement) as well as the outer dimensions of the test plates. Considering that fifteen test plates were to be tested, interchangeability needed to be incorporated into the design as well. To

accommodate all features, a setup was devised where test plates are clamped between a leading (LE) and a trailing edge (TE) insert, which smoothly follow the contours of the Mach block. In turn, by loosening the screws of each insert, it is possible to slide the test plate out of the wind tunnel and replace it by the next. A schematic of this design is indicated in the following figure:

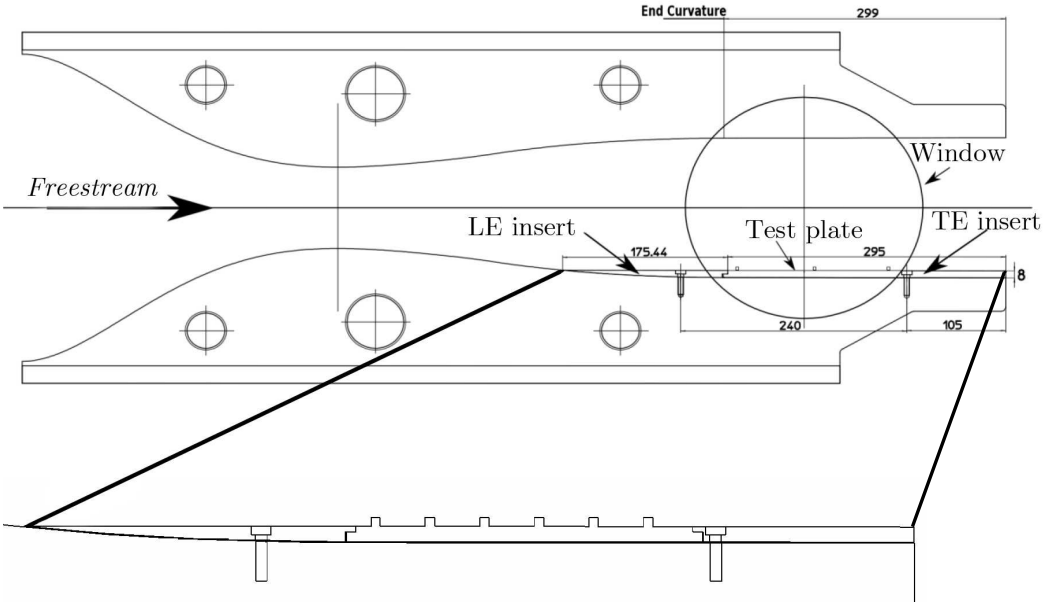

FIGURE 3.3: Schematic of the ST-15 wind tunnel, incl. model placement.

To optimally utilize the window size, the test plates have a length of 178 *mm*, whereas the width spans the test section at 150 *mm*. Both the inserts and test plates are made of 8 *mm* thick anodized aluminum. It is chosen to have each component anodized black, such to prevent laser reflections from obscuring PIV acquisitions (Section 3.4). The complete technical drawings of the leading and trailing edge inserts, as well as a complete description of the test plates can be found in Appendix C. In the following section, the first of three conducted measurement techniques is described.

3.3 Schlieren

The Schlieren method is a non-intrusive flow visualization technique, based on the influence of density gradients on the local refractive properties and deflection of light rays. As this technique is relatively simple, it is a common technique to obtain qualitative, diagnostic information on supersonic flow fields. As a result, it is decided to start the experimental research with Schlieren in order to establish a basic understanding on the resulting flow fields. This is, prior to conducting more complex, quantitative techniques such as PIV and QIRT.[34,45] (Stallings, 1987; Settles, 2001)

3.3.1 Working principle

Schlieren visualization relies on the principle of light refraction due to the variation of the refractive index. Whenever light (or another electromagnetic wave) transcends from one material to another, a change in propagation direction occurs. This phenomenon is described by Snell's law as:

$$n_1 \cdot \sin\alpha_1 = n_2 \cdot \sin\alpha_2 \tag{3.1}$$

or,

$$\sin\alpha_2 = \frac{n_1}{n_2} \cdot \sin\alpha_1 \tag{3.2}$$

Where indices 1 and 2 refer to different physical media, n_i is the refractive index and α_i is the incidence angle of the light beams. From Equation 3.2, it is found that a light beam transcending from a material with a lower n_1 to a higher n_2 the light beam bends towards the normal. In contrast, for the transition from a material with a higher to a lower n, the light beam bends away from the normal. This effect is sketched by the following figure:

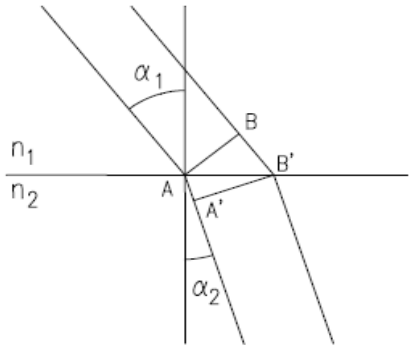

FIGURE 3.4: Refraction of light.

Where it holds that $n_1 > n_2$, and the line perpendicular to the interface of the two materials is considered the normal. The value of the refractive index n is material specific, and is a function of the material density. The relation associated with this is given by the Gladstone-Dale relation, equal to:

$$n = \frac{c_0}{c} = 1 + K\rho \tag{3.3}$$

Where c_0 is the speed of light in a vacuum, c the local speed of light, K the Gladstone-Dale constant ($K_{air} = 2 \cdot 10^{-4}\ m^3/kg$) and ρ the local density. By thus combining Snell's law and the Gladstone-Dale relation, respectively Equations 3.2 and 3.3, it can be concluded that variations in the density field can be directly translated into variations of the refractive index. This is exactly what is done through Schlieren visualization.

Especially in supersonic flow conditions, discontinuities such as expansion fans, compression waves and shock waves give rise to large density variations across the test section. By passing light through a test section, variations in density thus directly result in local changes of refractive index n. This, in turn, changes the local directionality of the light beams crossing each portion of the flow field as:

$$\frac{\partial x}{\partial z} = \frac{1}{n}\int \frac{\partial n}{\partial x} dz \quad \text{or,} \qquad \frac{\partial y}{\partial z} = \frac{1}{n}\int \frac{\partial n}{\partial y} dz \tag{3.4}$$

which can be rewritten in terms of density using Equation 3.3:

$$\frac{\partial x}{\partial z} = \frac{K}{1+K\rho}\int \frac{\partial \rho}{\partial x} dz \quad \text{or,} \qquad \frac{\partial y}{\partial z} = \frac{K}{1+K\rho}\int \frac{\partial \rho}{\partial y} dz \tag{3.5}$$

This feature is used by the Schlieren system through the application of a pair of concave mirrors, which respectively collimate and focus the light beam as it enters and exits the test section. At the focal point of the exiting light beam, a so-called *Schlieren knife* is placed (Figure 3.6). By placing this knife edge at half the width or height of the focused beam, bent

light is blocked in accordance to the deflection gradient, whereas lesser bent light is passed through. This is illustrated in the following sketch:

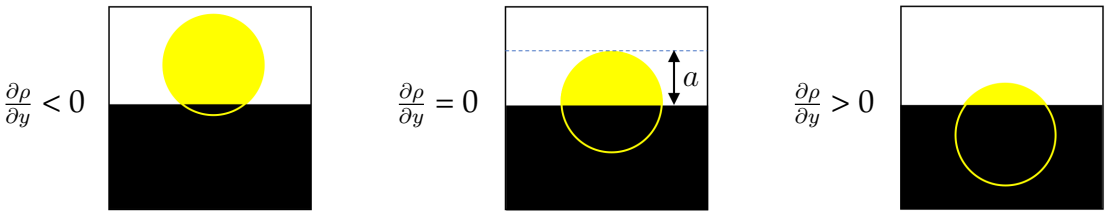

FIGURE 3.5: Working principle of the Schlieren knife over y-axis.

Where the refraction effects of respectively lower density, neutral density and high density air are shown. In a regular flow field, each of these situations occurs simulatenously. Therefore, by placing a CCD camera directly after the Schlieren knife, the captured images correspond directly to the density gradient fields. The corresponding relation of the light intensity gradients of these images with the the density gradient of the flow field is given by:

$$\frac{\Delta I}{I} \propto \frac{K f_2}{a} \int_{x_1}^{x_2} \frac{\partial \rho}{\partial x} dz \quad \text{or,} \quad \propto \frac{K f_2}{a} \int_{y_1}^{y_2} \frac{\partial \rho}{\partial y} dz \tag{3.6}$$

Where f_2 represents the focal length of the concave mirrors and a is the light offset (Figure 3.5). Now that the basic theoretical framework of the Schlieren system is known, it is possible to apply its working principle by establishing an experimental setup. This setup is described in the following section.

3.3.2 Experimental setup

At the HSL of the Aerospace faculty, it is very common to conduct a diagnostic investigation into compressible flow fields using a Schlieren setup. As a result, each trans- and supersonic wind tunnel is equipped with the essential components required to conduct Schlieren visualization. At the ST-15 supersonic wind tunnel, a so-called Z-type Schlieren setup is placed. A schematic representation of this setup is provided in the following figure:

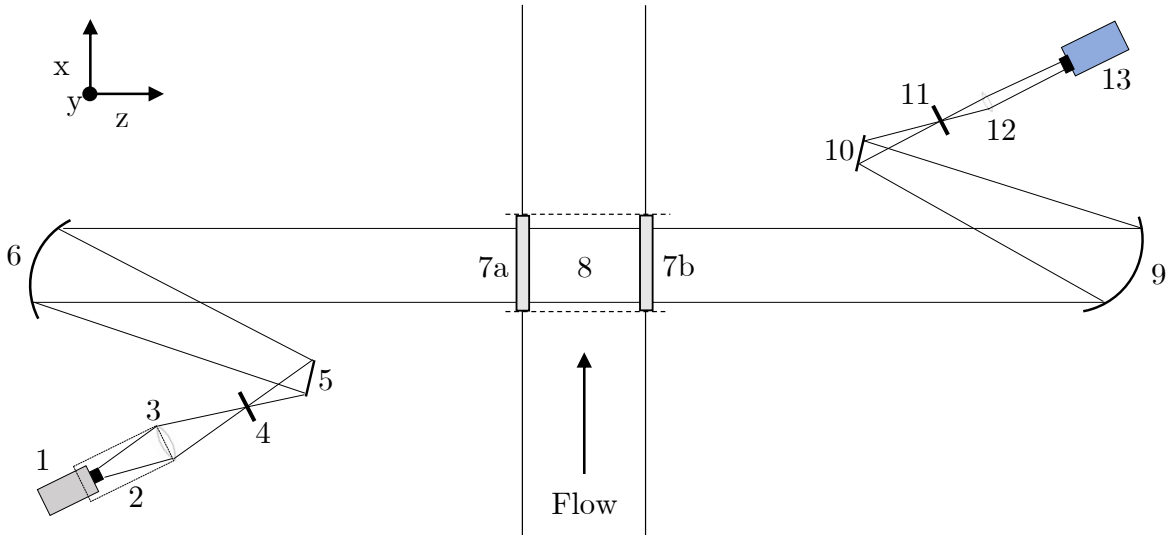

FIGURE 3.6: Experimental setup for Schlieren visualization (upper view).

Where thirteen primary components can be identified, each numbered accordingly. The light source (1) is embodied by a Xenon spark-light or a Solarc Lighting Technology short-arc Xenon lamp. The emitted light beam passes through PVC coverage (2), followed by a converging 150 mm lens (3). This is done to preserve as much light as possible, and bundle the light emitted by the light source. At the focal point of the converging lens, a pinhole (i.e. aperture) is placed (4). Through this aperture, the size and illumination strength of the light beam is regulated; affecting the overall illumination and contrast of the Schlieren images. A mirror (5) then reflects the tailored light beam onto the first parabolic mirror (6) mounted permanently on the wall. This parabolic mirror collimates the light beam and sends it through the test section (8). At both sides of the test section, two optical windows are placed (7a, 7b). These windows are tailor-made for the current Schlieren system, such that they preserve the intensity of the light beam and do not alter its directionality. The light beam exits the test section after which it is converged by the second parabolic mirror (9). In turn, this converging light beam is reflected by a mirror (10) onto the Schlieren knife (11). For the Schlieren knife to function (Figure 3.5), it is placed in the focal point of the second parabolic mirror (i.e. f_2). Then, either a 200 or 400 mm lens (12) focuses the light beam according to the desired magnification factor. Finally, the LaVision Imager Pro high-speed camera (13) captures the light beam and converts it to digital images.

From the previous description of the experimental setup, it becomes clear that – depending on the light source – two types of Schlieren visualization can be conducted: (1) continuous-light Schlieren or (2) spark Schlieren. The first type is conducted by using the Solarc Lighting Technology short-arc Xenon lamp. This illumination source is continuous and as such, the necessary image intensity is controlled by adjusting the shutter speed of the camera. Due to the relatively limited overall light intensity (I), however, this Schlieren type only allows the usage of relatively low shutter speeds. Therefore, the images obtained through this technique represent more of an average flow field rather than a freeze-frame (Figure 3.7a).

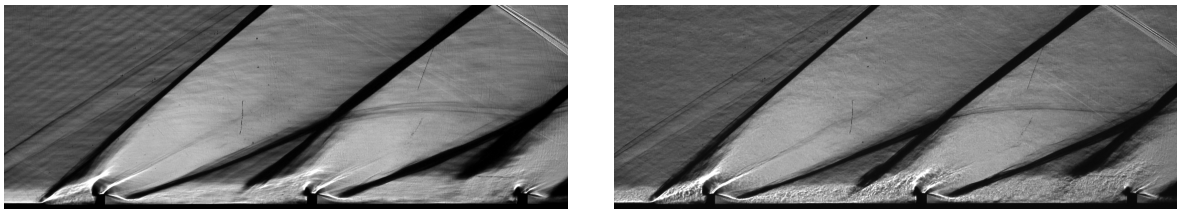

(A) Continuous Schlieren. (B) Spark Schlieren

FIGURE 3.7: Continuous versus Spark Schlieren on 3.6/20 test plate.

The second Schlieren technique utilizes a Xenon spark-light, which provides a very high intensity light beam with a pulse time of 20 ns. Through a LaVision high-speed controller unit (HSC), the high-speed camera and spark-light are synchronized such that only one light pulse occurs for each frame captured by the camera; effectively reducing the camera exposure time to the pulse time of 20 ns.[46] (LaVision, 2013) As a result, the overall exposure time is extremely low and the resulting images can be considered as freeze-frames (Figure 3.7b). The camera is directly connected to the HSC (14), whereas the spark-light is driven indirectly through a Ministrobokin D-22880 high-speed photo system (16) which processes the signal from the HSC. The HSC itself is controlled via the DaVis software installed on a dedicated computer (16). Therefore, in the case spark-Schlieren is conducted, the following addition should be made to the experimental setup (Figure 3.6):

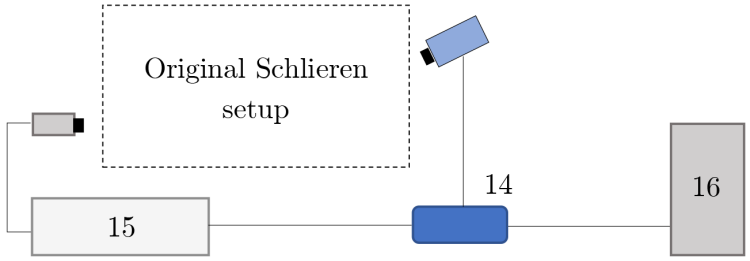

FIGURE 3.8: Spark-Schlieren addition to experimental setup, measuring equipment.

Where it should be noted that the HSC and computer are also used for continuous-light Schlieren, as the high-speed camera requires the DaVis software for shutter triggering. For this measurement technique, no data reduction is required as all images are automatically captured and processed through DaVis. The results of the Schlieren campaign are displayed in Section 5.1.

3.4 Particle image velocimetry

The unique aspect of particle image velocimetry (PIV), is being a velocimetry technique which offers quantitative information on a whole planar field, whilst also providing intuitive visualization of the flow. Even though a high-density of tracer particles is immersed in the flow, their ineffectiveness on the flow itself allows us to consider PIV as a non-intrusive measurement technique. Previous experimental research has shown that the average turbulent mixing properties ($\overline{u'}$, $\overline{v'}$ and $\overline{u'v'}$) of a boundary layer correlate directly with the heat transfer properties ($\overline{h}$, $\overline{St}$).[6,11] (Han, 1984; Latin and Bowersox, 2000) Actually, Liou and Hwang (1990) found that an analysis of heat transfer through both velocity field and turbulence properties provided the same conclusions as direct temperature measurements made by Han et al., 1985.[29,7] Fortunately, through PIV, both mean velocity components ($\overline{u}$, $\overline{v}$) as well as turbulence properties can be derived from the same cross-correlation routine of each image pair. Therefore, all the desired flow properties can be derived for a complete flow field using only one measurement technique. It is this property, as well as the high-level of experience with PIV at the HSL, that have led to the choice for this measurement technique as a means to quantify the flow fields and function as a complementary tool for QIRT.

3.4.1 Working principle

The principle of PIV is based on the measurement of the displacement of small tracer particles that are carried by a fluid during a short time interval. The tracer particles must be sufficiently small to accurately follow the fluid motion and not alter the fluid properties or flow characteristics. The tracer particles are illuminated within a thin light sheet, generated from a pulsed light source (usually a double-head pulsed laser system). The light scattered by these particles is recorded onto two subsequent image frames by a digital imaging device, typically a CCD or CMOS camera placed perpendicular to the measurement plane. An example of a typical PIV experimental setup is given in the following figure:

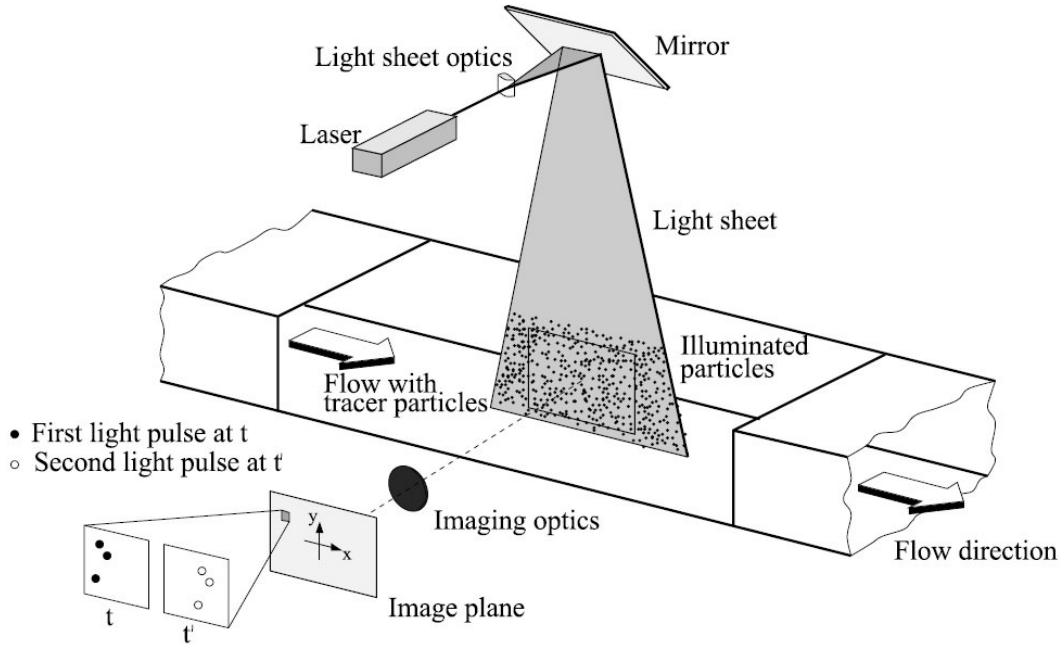

FIGURE 3.9: Schematic of a typical PIV measurement system.[47] (Raffel et al., 2013)

Where not only the experimental components are shown, but also the primary principle of post-processing. The consecutive image pairs located at the bottom left of Figure 3.9 display minor displacements between the flow field at times t and t', which are typically separated by a couple of μs. Each image pair is identically subdivided in small interrogation windows ranging from 16×16 to 128×128 pixels. Through a cross-correlation process (Section 3.4.5), the average displacements are then determined for each of these interrogation windows. By in turn dividing the average, spatially-scaled displacements by the known pulse separation time (Δt), the velocity vectors are derived.

3.4.2 Experimental requirements

Previously, Liou et al. (1990) were able to draw conclusions to the heat transfer characteristics of specific roughness geometries, similar to those obtained from direct temperature measurements conducted by Han et al. (1985).[29,7] This was managed by determining the turbulence properties of the flow at 1 *mm* from the crest of the ribs (Figure 2.15). Fortunately, through PIV, both mean velocity components ($\overline{u}$, $\overline{v}$) as well as turbulence properties ($\overline{u'}$, $\overline{v'}$ and $\overline{u'v'}$) can be derived from a single cross-correlation procedure. Therefore, making this measurement technique an ideal means of validating the results obtained from QIRT.

It is decided to conduct two distinct sub-campaigns, where both correspond to a specific form of a *planar PIV method*. In terms of experimental setup, this means that solely the fields of view are adapted. In both cases, the field of view (FOV) is located along the centerline of the geometry, where for,

- *The primary campaign* the FOV transcends the entire length of the test plate for which the bottom runs parallel to the rib tops (cameras 1 – 4, Figure 3.10).
- *The secondary campaign* the FOV is limited to the final cavity of specific test models, including portions of the upstream and downstream ribs (cameras 5 – 6, Figure 3.10).

From Figure 3.10, it is seen that the exact placement and dimensions of the respective FOVs are only indicated for cameras belonging to the primary campaign. This is done to maintain

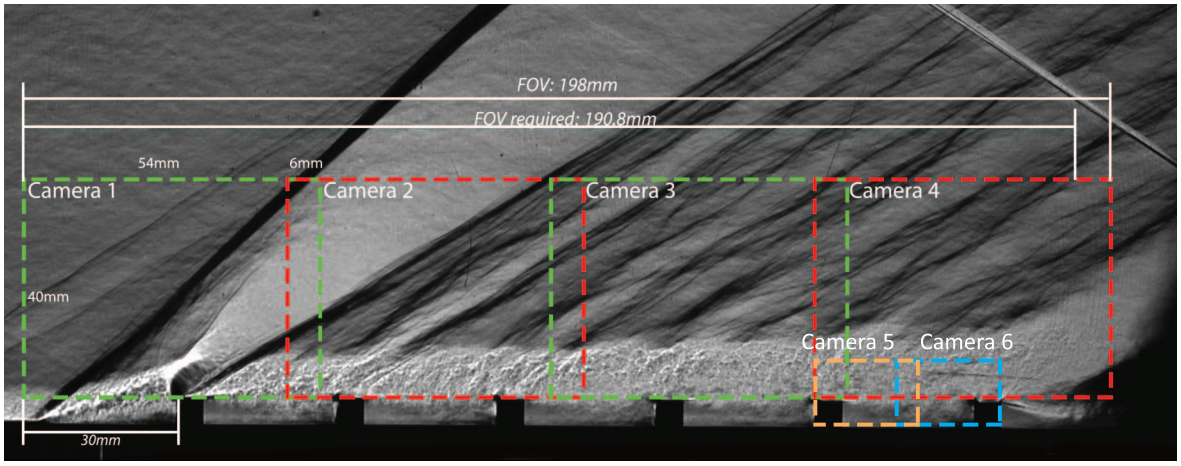

FIGURE 3.10: PIV camera fields of view projection onto Schlieren image.

consistency between the $\overline{u}$, $\overline{v}$ and $\overline{u'v'}$ profiles obtained for the various ribbed wall geometries. By considering the same FOVs between all measurements, the differences in turbulence mixing can be compared accurately. The upstream FOV position is set to 30 *mm* from the first rib face, which corresponds to the farthest upstream position of the blockage shock. In turn, the downstream location is set to 160.8 *mm* aft the first rib, equal to the maximum aft rib position encountered for all test plates (i.e. $e/\delta = 0.4$, $p/e = 5, 10$). The FOV definitions for the secondary campaign differ per test model, and are indicated in Appendix G.

Due to the fact that turbulence properties are to be averaged for each flow field, sufficient image pairs should be taken to provide a converged solution. From the Reynolds stress, $\tau_{i,j}$ convergence study shown in Section 3.4.6, it is known that 500 image pairs suffice. In both campaigns, the latter quantity is obtained by conducting two consecutive wind tunnel runs where each run provides 250 image pairs. This measurement splitting is customary for a supersonic setup as it allows the researcher to maintain constant test section and equipment performance properties.[48] (Giepman et al., 2015)

3.4.3 Experimental considerations

The working principle of PIV (Section 3.4.1) has indicated that a typical experimental setup consists of four primary components, namely: *seeding*, *illumination*, *light-sheet optics* and *imaging*. To each of these four components, specific choices are to be made by considering various (physical) principles. The appropriate setup choices were made by acknowledging the current function of PIV as a verification tool for IRT. In turn, by taking into account the planar FOV requirements stated in the previous section, a setup was constructed as depicted in Figure 3.14. The justifications which have led to the choice of intermediate PIV components, are provided in this section.

Flow seeding The first key component of PIV is the introduction of particles into the flow, commonly referred to as *seeding*. Particle tracers introduced in the flow can be considered as not affecting the flow properties, provided the appropriate amount is used. The choice of seeding material is not trivial, as particles should be small enough to accurately follow the flow whilst scattering sufficient light to be captured by the camera. For supersonic PIV, common particle tracers are titanium dioxide (TiO_2) and Di-Ethyl-Hexyl-Sebacate (DEHS). These particles have similar light scattering properties and are known for maintaining unaltered mechanical properties. Still, minor differences in flow fidelity exists. The particle

Stokes number (Equation 3.7) governs this flow fidelity as:

$$S_k = \frac{\tau_p}{\tau_f} \tag{3.7}$$

Where particle response time τ_p is based on the time taken by a particle to match 63% of the fluid velocity after a step change.[49] (Ragni, 2012) In turn, τ_f represents the smallest time-scale of the flow. For the turbulent boundary layer of the ST-15, this τ_f is equal to the boundary layer thickness divided by the freestream velocity, i.e. δ/U_{ref}. From a practical point of view, the condition where S_k < 1.0 returns an acceptable flow tracing accuracy with errors below 1% (Section 3.4.5). In the case shock waves are present, however, faithful flow tracing can never be reached within the vicinity of a shock wave as a large velocity step occurs over a shock thickness of ~0.1 microns (i.e. $S_k \gg 1.0$).[50] (Tropea et al., 2007)

Applying the typical flow characteristics of a Mach 2 flow within the ST-15, it is found that S_k is equal to respectively 0.017 for DEHS and 0.047 for TiO_2.[42] (Sun, 2014) As S_k < 1.0, it is expected that either tracers are sufficient for the experimental setup. One has to note, however, that the improvement in S_k for TiO_2 is only obtained once this material is dehydrated and dispersed; non-treated TiO_2 has the same typical response time as DEHS.[51] (Ragni et al., 2009) Therefore, as the fluid mechanical and scattering properties are sufficient for both DEHS and TiO_2, the decision of tracer particles comes down to logistical aspects. For an improved τ_p, TiO_2 requires elaborate material treatment. In addition, the usage of of TiO_2 forms a hazard to some wind tunnel materials and human health.[52] (Hext et al., 2005) Therefore, it is decided to use DEHS for all PIV experiments of this thesis.

Illumination The requirements of a light source for PIV are led by the measurement principle of PIV itself; a finite observation time (Δt) between short light pulses (δt) used to detect the particle motion between image pairs (Figure 3.9). As a result of this, two requirements are identified: (1) The formation of short, high-intensity light pulses, which, (2) quickly follow one another to form image pairs. A schematic of the typical pulse separation is given in the following figure:

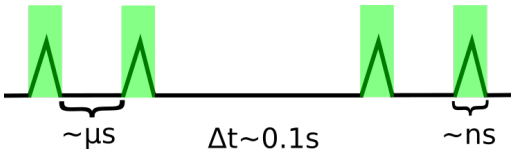

FIGURE 3.11: Pulse separation time and laser illumination.

Which indicates the typical time scales of the light pulses (t_p ~ns), pulse separation time (δt ~μs) and image pair separation time (Δt ~0.1 s).

Lasers are commonly used as illumination sources since they can produce a pulsed, collimated and monochromatic light beam that can be easily shaped into a thin light sheet. Two most common laser types are the Nd:YAG and Nd:YLF, specialized by respectively high pulse energy values in mJ, and high-repetition rates in Hz. Whereas, the Nd:YAG lasers can provide a pulse energy of up to 1000 mJ, its repetition rate ranges between 10 and 50 Hz. In contrast, the Nd:YLF lasers are capable of achieving repetition rates up to 10 kHz at a reduced pulse energy of 30 mJ. Typically, the required pulse energy E is proportional to the largest dimension of area of interest. As a rule of thumb, E ≈ 100 mJ is sufficient to illuminate an area of approximately 10×10 cm^2 in air flows. As a result, Nd:YLF lasers are

primarily used for small-scale, time-resolved experiments, whereas Nd:YAG are used for remaining large-scale applications.

The FOV considered for the current experimental campaign is approximately 200 x 40 mm^2 (Figure 3.10). Therefore, as a divergent laser sheet is formed, an $E \approx 200$ mJ is required for sufficient illumination of the particles. To accommodate this E, the Double pulsed Nd:YAG Spectra Physics Quanta Ray PIV-400 laser is used. This laser is capable of delivering a nominal 400 mJ per pulse, at a pulse duration of 6 *ns*. This laser light has a wavelength of 532 *nm*, which is yields an optimal response from the monochrome Bobcat cameras. The architecture of this PIV laser consists of two separate laser modules, firing independently at the required pulse separation. This means that the δt can be optimized freely for the experimental conditions, typically defined by the dynamic velocity range (DVR ~$\mathcal{O}(100)$). For the current thesis, it was decided set the δt equal to 1 μs for the primary campaign, whilst δt was set to 1.5 μs for the secondary campaign. As a result, the first allowed for a resolvable velocity range of 3.3 – 266.7 *m/s*, whereas for the latter varied from 2.2 – 177.8 *m/s*. This means that effectively, the DVR is lowered to 80 such to resolve lower velocity regions near the rib tops and inside the cavities. As these are the most important regions of interest, this is an appropriate solution to the cross-correlation.

Light-sheet optics The circular cross-sectional beam delivered by the laser is shaped into a thin light sheet by means of a series of cylindrical and spherical lenses. The most practical arrangement utilized to illuminate a large FOV, is the *divergent light sheet formation*. Such an arrangement includes a pair of cylindrical lenses, which first expand the light bundle into a vertically-oriented divergent sheet, after which the resulting sheet is converged horizontally; forming a waist. For the current experimental campaigns, this optical arrangement is embodied by the laser periscope probe, which design provides complete control of aim and orientation of the laser sheet.[43] (Donker Duyvis, 2005).

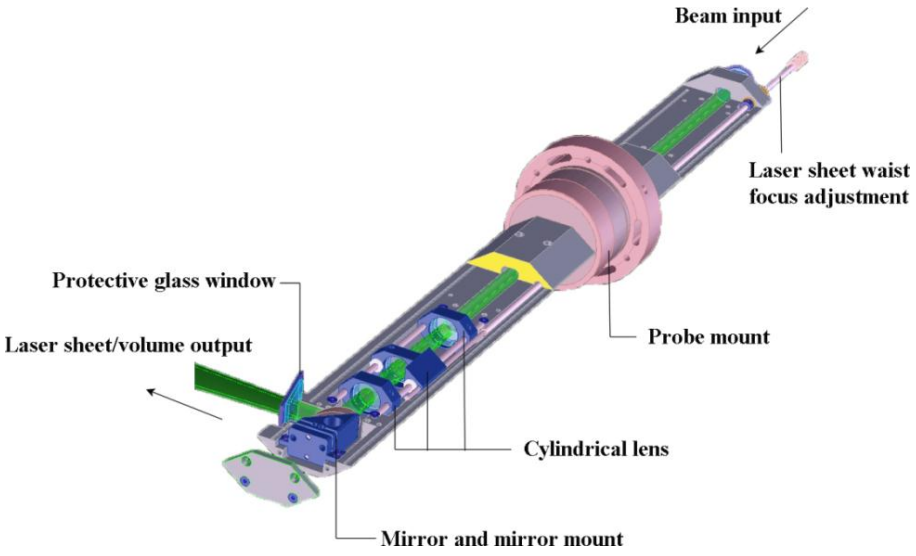

FIGURE 3.12: Assembly of the laser periscope probe design with cut-outs.[43] (Donker Duyvis, 2005)

The technical drawing of this laser periscope probe (Figure 3.12), displays an aerodynamic, rigid shell which incorporates the required cylindrical lenses to convert the circular beam input to a laser sheet. The aim of the divergent laser sheet is varied by adjusting height and

angle of the mirror mount. In turn, the position of the laser sheet waist can be adjusted by focus-adjustment lever, which controls the focal point of the final cylindrical lens. Practically, the waist is adjusted such that it falls beyond the measurement region. This is done to avoid the appearance of a heavily illuminated region, and optimize for (near) uniform illumination. The average laser sheet thickness (dz_{laser}) was estimated to be ~3.0 mm.

Through the laser periscope design, it is possible to comply with the requirements of both FOVs displayed in Figure 3.10. For the primary campaign, it is decided to aim the laser sheet such that the center of the divergent light sheet lies exactly parallel the rib tops. However, as the laser sheet is divergent, the bottom part partially impinges the geometries and forms reflections which can obscure the raw images. To avoid these laser reflections from scattering into the regions of interest, a laser cut-off plate is mounted in between the exiting laser sheet and test model to block the bottom part of the light sheet (Figure 3.14). During the secondary campaign, the periscope probe is positioned such that the laser sheet enters the cavities under a maximum angle (~$10°$) such to minimize shadowing. In this case, light scattering is unavoidable, meaning that the reflections are primarily controlled through the pre- and post-processing routine (Section 3.4.5). For more insight into the setups of the probe, schematic drawings can be found in Appendix H.

Imaging The final primary component of any PIV setup is the imaging, which encompasses all the optical arrangements; i.e. the objectives and cameras themselves. The choice of camera(s) is determined by the desired system resolution in pixels/mm. In order obtain a sufficiently accurate representation of the boundary layers, a minimum number of vectors should be resolved within this boundary layer. Based on a final-pass interrogation window of 32 x 32 pixels, previous planar PIV experiments at the ST-15 (Tambe et al., 2017) have shown that the boundary layers can be properly resolved for a system encompassing an overall resolution of 30 pixels/mm. To this end, four LaVision branded Imperx B1610M Bobcat CCD cameras are used to capture the maximal FOV displayed in Figure 3.13.

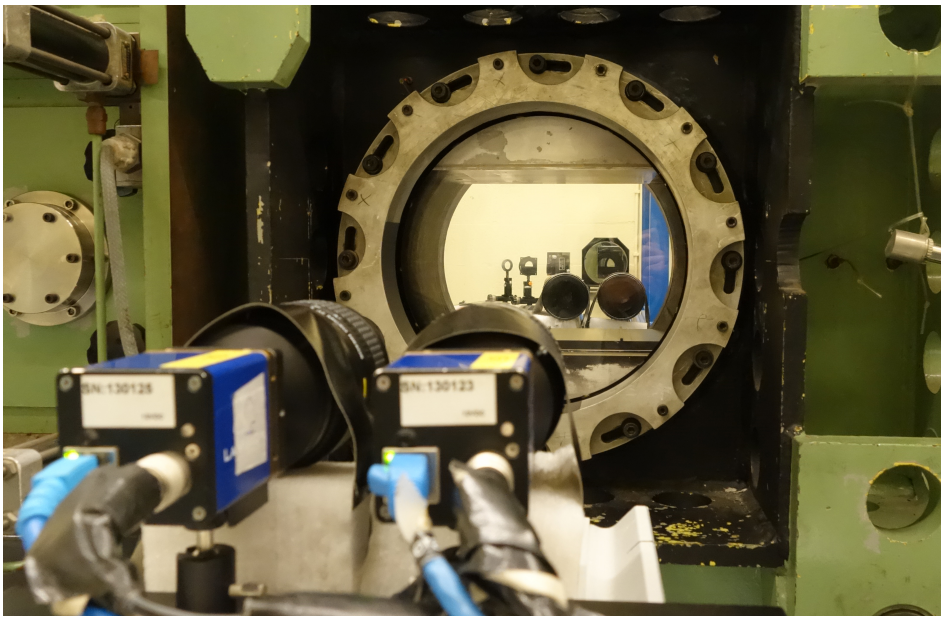

FIGURE 3.13: Primary PIV campaign camera setup at ST-15.

Each camera is equipped with a monochromatic, interline CCD sensor featuring maximum resolution of 1628 x 1236 pixels. By this design, it is possible to capture the images pairs

within the double-trigger time of up to 200 *ns*. From Figure 3.10, it is seen that each camera should provide a FOV of approximately 54 x 40 *mm* to result in a combined FOV of 198 x 40 *mm*. To achieve this, each camera was equipped with the same Nikkor 60*mm* $f/2.8$D objective and placed at a distance of approximately 0.51 *m* from the centerline of the test section. The minimal overlap of approximately 6 *mm* was achieved by placing the cameras in pairs on each side of the test section, whilst under a slight angle of $\leq 2^{\circ}$.

When selecting the objective for any PIV experiment, two fundamental parameters have to be considered: the f-stop ($f_{\#}$), and the magnification factor M. As a consequence of the experimental setup, the magnification factor is evaluated as the ratio between the image size (i.e. sensor size) and the imaged object size (i.e. FOV):

$$M = \frac{\text{sensor size}}{\text{imaged object size}} = \frac{\text{pixel size x pixels on sensor (\#)}}{\text{FOV}} \tag{3.8}$$

The f-stop controls the depth of image sharpness or focal depth, and is defined as:

$$f_{\#} = \frac{f}{D_a} \tag{3.9}$$

Where f is the focal length of the lens and D_a is the aperture diameter. If the tracer particles were imaged as spots, according to the geometric optics, the particle images would have the diameter:

$$d_{geom} = M d_p \tag{3.10}$$

Where d_p is the effective particle diameter. However, diffraction effects limit the minimum particle image diameter to:

$$d_{diff} = 2.44\lambda(1 + M)f_{\#} \tag{3.11}$$

An acceptable approximation of the resulting particle image diameter is given by the Euclidean sum of the above terms:

$$d_{\tau} = \sqrt{(d_{geom})^2 + (d_{diff})^2} \tag{3.12}$$

For typical optical parameters in PIV, it is concluded that $d_{diff} \gg d_{geom}$ and therefore d$\tau \approx d_{diff}$. In other words, the diffraction limit generally dominates the particle image formation (i.e. d_p < 20 μm), and the particle image diameter is quite uniform despite variations in d_p. It is common practice to set the objective aperture such that $d\tau$ = 2 pixel widths (w_{pixel}). This is to prevent images from being either under-resolved ($d_p < w_{pixel}$), causing *peak locking*, or over-resolved ($d_p > 2\ w_{pixel}$), causing *merging*. Using this design characteristic, it is possible to estimate the optimal $f_{\#}$ by substituting $d_{diff} = 2w_{pixel}$ into Equation 3.11. For the Bobcat camera CCD, w_{pixel} = 4.4 μm. As a result, the M of the current setup is 0.13, with a corresponding ideal $f_{\#}$ equal to ~5.6.

The particle-image diameter (Equation 3.12) only holds for particle images in focus, i.e. when the light sheet thickness (Δz_0) is smaller than the focal depth (δz). The latter property is defined by:

$$\delta z = 4.88\lambda f_{\#}^2 \left(\frac{M+1}{M}\right)^2 \tag{3.13}$$

For the example given prior, the focal depth of the imaging system is about 6 *mm*. As a practical rule, the light sheet thickness is typically chosen to be approximately half focal depth, i.e. $\Delta z_0 = 0.5\delta_z$. This is done to avoid 3D-effects from interfering the planar correlations,

whilst providing sufficient light to properly illuminate the particles. Keeping this in mind, the laser periscope probe was adjusted such that an average laser sheet thickness of 3 *mm* was formed over the length of the test section. A complete list of all optical PIV settings is provided in Appendix I.

3.4.4 Experimental setup

The successive determination of the four primary components of the PIV setup, has led to the construction of the complete planar PIV setup shown in Figure 3.14. In this section, the exact placement and operation of this setup is solely described through this schematic. For physical images of this setup, the reader is advised to look into Appendix J.2.

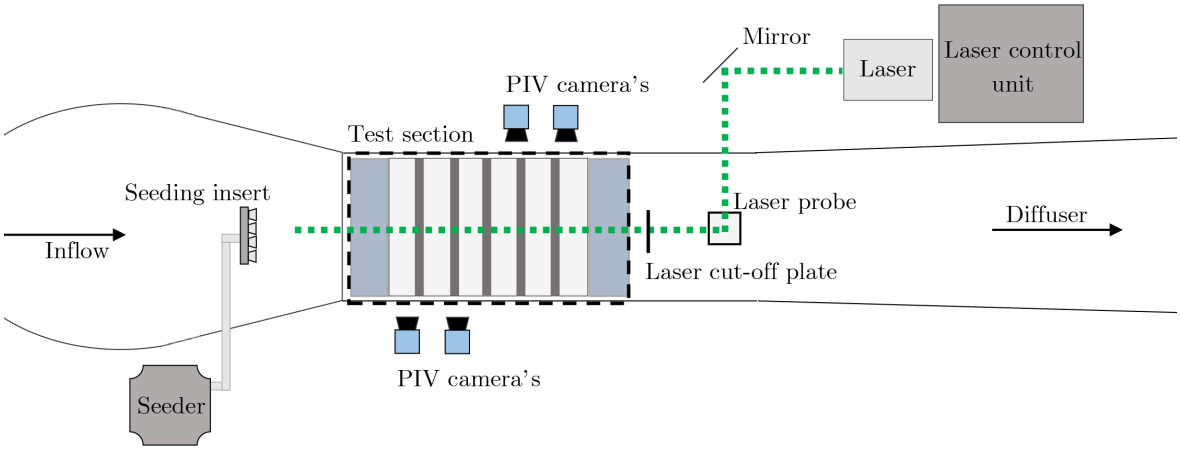

FIGURE 3.14: Schematic of PIV setup (scale of components may be exaggerated for clarity).

The Spectra-Physics Quanta-Ray PIV-400 laser shoots consecutive, double laser-pulses onto a mirror which reflects the circular light beam into the laser periscope probe. The intensity and timing of the laser is determined by its control unit, which in turn is synchronized with the shutters of the four Bobcat B1610 PIV cameras through the high-speed controller (HSC) and DaVis PIV software.[53] (LaVision, 2016) The laser sheet exiting the probe, may be partially blocked by the laser cut-off plate located in between the probe and the test section. In turn, the tailored laser sheet travels the test section exactly over the longitudinal centerline. The DEHS particles are formed by the PIVTECH atomizer (i.e. seeder), which is connected to a specialized seeding rake located permanently in the ST-15 settling chamber (Figure 3.1). This rake consists of 15 injectors, which can be activated through the PIVPART-45 control unit. This control unit allows the user to alter between respectively 6, 9, 12 or 15 injectors. To achieve the desired seeding density, however, all 15 injectors were used during the experiments. In addition, the PIVTEC atomizer consistently delivered the particles at an overpressure of 1 bar above total pressure in the settling chamber such that particles could exit the rake smoothly.

The heart of the experimental setup (Figure 3.14) is formed by a computer equipped with DaVis, which allows the user to control the primary acquisition settings such as: recording frequency (f), total number of images per run ($\#$) and pulse separation time (δt). As it is desired to obtain average turbulence properties of each flow field, sufficient image pairs are taken to provide a statistically converged solution (Section 3.4.6). For both campaigns, this is achieved by conducting two consecutive wind tunnel runs each of 250 image pairs. With the raw image pairs acquired, it is possible to conduct pre- and post-processing routines and

obtain the velocity fields through cross-correlation. The final method of data processing is discussed in the following section.

3.4.5 Data reduction

In addition to controlling the acquisition of the image pairs, the DaVis software tool enables the user to pre- and post-process the raw image pairs such to obtain the instantaneous velocity fields. During the current thesis, DaVis version 8.1.2 was used. Even though DaVis is relatively straightforward to operate, a multitude of image (pre-)treatments and cross-correlation settings can be varied to obtain high-quality velocity fields. Therefore, prior to choosing the settings of processing, an optimization study was performed. This is, keeping in mind that the average flow fields with quantities $\overline{u}$, $\overline{v}$ and $\overline{u'v'}$ were to be obtained for the both primary and secondary campaign. The cross-correlation and outlier removal characteristics were varied for respectively:

- Pre-processing:
  1. Window size (# pixels)
  2. Window overlap (%)
  3. Window shape
  4. Number of passes
- Post-processing:
  1. Type of outlier filter
  2. Definition of outlier
  3. Remove correlation < # vectors
  4. Number of passes

A total of 20 different pre-processing settings were investigated on a set of experiments, representative of all test plates: incl. all roughness heights, cavity type flows and image qualities. In turn, a selection of four pre-processing settings was made and tested in combination with 48 different post-processing routines. In the end, an optimal combination of settings is chosen; resulting in averaged flow fields at the maximum resolution which maintains a respectably low number of outliers. The final list of processing settings is given by:

1. Pre-treatment:
   - Combine images taken from two runs (500 image pairs)
   - Perform linear calibration scaling
   - Subtract illuminative minimum of image series
   - Apply geometric mask to badly illuminated image regions
2. Pre-processing: *Sequential cross-correlation*,
   - Multi-pass (decrease size)
   - Window: 64 x 64 (1), 24 x 24 (3)
   - Window shape: Gaussian (1), Gaussian (3)
   - Window overlap: 50% (1), 50% (3)
3. Post processing: *Median filter – universal outlier detection (2)*,
   - Remove if residual > 1.5 Filter region: 9 x 9
   - (Re)insert if residual < 1.5 Min number of vectors: 5
   - Remove groups with < 5 vectors
   - Fill-up empty spaces

Through pre-treatment, the quality of the image pairs is improved by increasing the contrast of the seeding (white) with respect to the background (black) and mitigate reflections; increasing the signal-to-noise ratio (SNR). In DaVis, both actions are performed by respectively (1) subtracting the minimum illumination from all images pairs, after which (2) a geometric mask is applied to block the occurring reflections (Figures 3.15b, 3.15c). Fortunately, by the implementation of the laser cut-off knife, most reflections were avoided during the primary campaign. During the secondary campaign, however, the effects of reflections and shadowing were unavoidable and had to be accounted for.

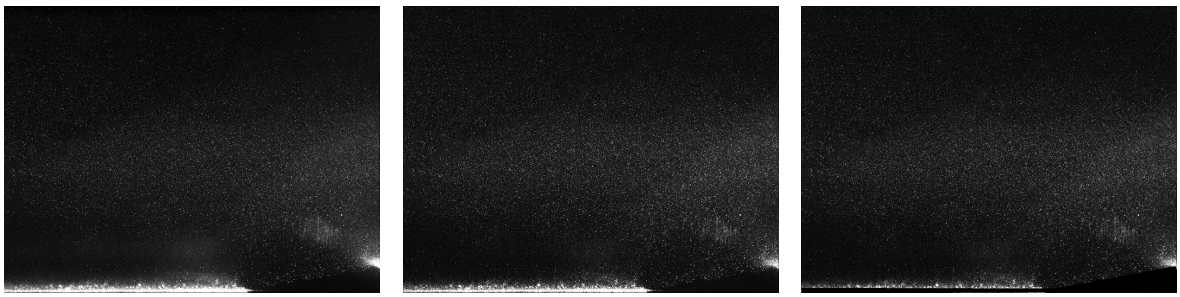

(A) Original PIV image. (B) Subtract minimum. (C) Apply geometric mask.

FIGURE 3.15: PIV image treatment prior to the cross-correlations procedure.

Once all image pairs have undergone the pre-treatment indicated in Figures 3.15a – 3.15c, the pre-processing routine was applied. This routine is embedded in DaVis and represents a cross-correlation procedure, which effectively consists of the four main components: Image windowing, cross-correlation analysis, correlated peak sub-pixel interpolation and scaling.

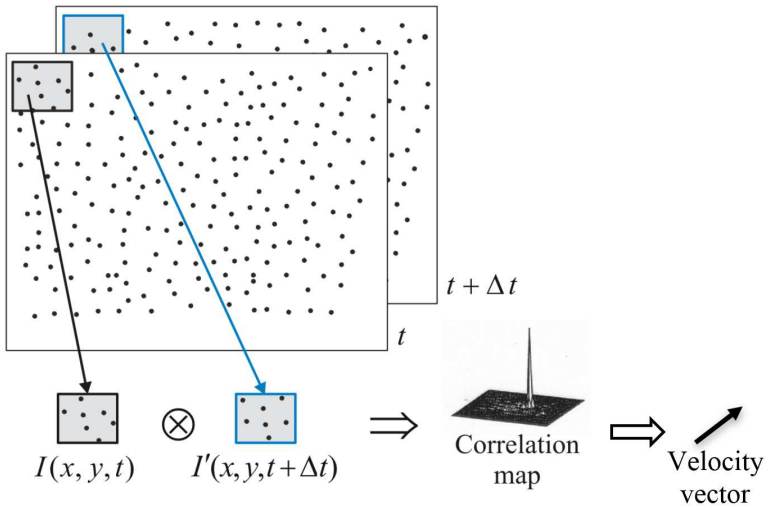

FIGURE 3.16: Image windowing and discrete cross-correlation map

Once each image pair is subdivided into interrogation windows, a statistical tracking operator is applied. This process returns a discrete-correlation map for each window, whose peak position indicates the average particle images displacement relative to the origin. In turn, the highest peak is selected around which an additional Gaussian fit is applied; narrowing the peak location. The resulting pixel displacement estimation is scaled in both time and space through respectively δt and predefined linear calibration. Finally, the resulting velocity vectors are combined into an instantaneous velocity map.

The indicated DaVis pre-processing settings revolve solely around the shape, size and overlap of the interrogation windows. In contrast to the cross-correlation procedure in Figure 3.16, however, the indicated settings are sequential. This means that correlations are conducted for multiple passes where, for each pass, the window size decreases. Once the correlations are completed, the resulting velocity fields are still relatively rough (Figure 3.17a) by the existence of (minor) outliers. To compensate this, the post-processing routine is applied:

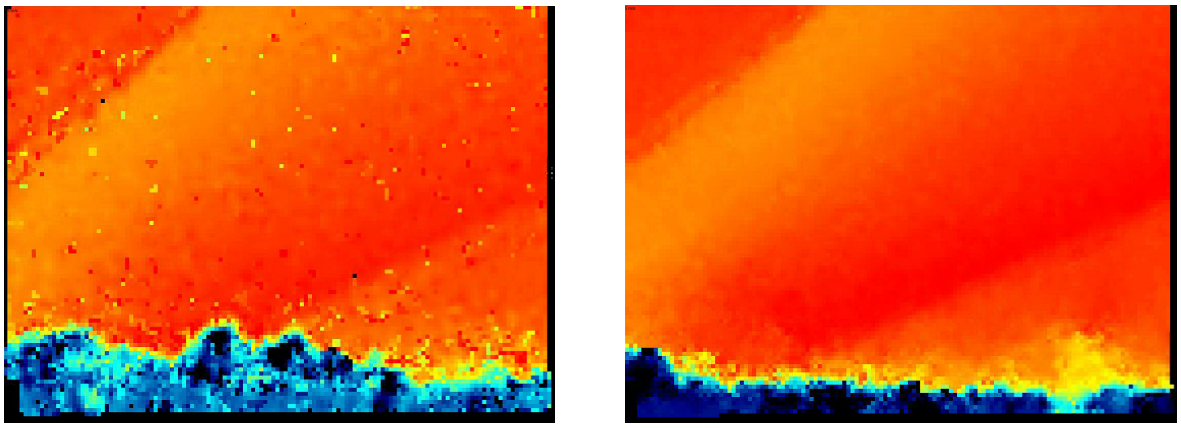

(A) Result pre-processing. (B) Result post-processing.

FIGURE 3.17: PIV velocity fields processing: cavity measurement 2.4/30 model camera (1).

From Figure 3.17b, it is seen that existing outliers have been mitigated through the *universal outlier detection* filter. In this processing routine, a vector is defined as an outlier once its magnitude and directionality are $\pm$ 1.5 times its direct surroundings.

For each wind tunnel run, the mentioned procedures are performed for each image pair and each camera (i.e. 500 x 4 image pairs). Once this is done, the post-processed velocity fields are averaged into one image for each camera; providing either $\overline{u}$, $\overline{u'}$ or $\overline{u'v'}$. Within DaVis, it is chosen to discard those instantaneous images which fall beyond $\pm 3\sigma$ from the mean flow field. The latter is to avoid the impact of obscured velocity fields on the mean. Fortunately though, for all wind tunnel runs, on average only 3 out of 500 images were found to be outliers to the mean. The resulting averages were exported from DaVis into '.DAT' files. In turn, the individual camera data was restructured and merged through a self-written MatLab code. Within this code, the overlaps of the camera frames were found from the calibration files and verified through an alignment check with the vertical velocity fields ($\overline{v}$). Then, the overlapping portions were merged through a linear interpolation function; converting the four frames into one smooth, rectangular frame. The resulting images are provided in Section 5.1, where both complete FOVs and extracted profiles are shown.

3.4.6 Uncertainty analysis

In most forms of experimental research, a setup is designed to approximate real-life as optimally as possible. Nevertheless, uncertainties arise which separate reality from the obtained measurements (i.e. errors). In order to substantiate the observations and conclusions which are attained from measurement results, it is vital to perform a complete uncertainty analysis. For the current thesis, this is done for both PIV and QIRT such to confirm the degree to which comparisons can be made and conclusions can be drawn.

There are two major sources of uncertainty within the scope of the present planar PIV study. One is caused by the limited ensemble size, whereas the other results from uncertainty components inherent to PIV. Although multiple error factors exist, such as freestream property variance during the wind tunnel operation (Δp_0 and ΔT_0), which contribute to the total uncertainty, these are considered to exert negligible influence on the present experiments. In this section, the major sources of uncertainty are discussed for representative cases from both primary and secondary campaigns.

Ensemble size uncertainty

Ideally, all unsteady motions of the repeated cavity flows should be captured such to precisely match the theoretical main flow field. However, it would require an infinite number of images to temporally resolve all the variations in flow features of the current experiment. As such, the mean flow field is studied as an ensemble average of all recorded images. An acceptable result is gathered by utilizing several hundred images (i.e. 500, Section 3.4.5).

The uncertainty analyses of the mean velocity, RMS velocity fluctuations and Reynolds stress, associated to a finite ensemble size follow those introduced by Benedict and Gould (1996) and later discussed by Humble (2009) and Sun (2014).[54,55,42] Generally, the normalized uncertainty, ϵ is quantified through:

$$\epsilon = \frac{\sigma}{\mu\sqrt{N}} \tag{3.14}$$

Which means that the measurements are modeled as a Gaussian process, dependent on the standard deviation (σ), mean (μ) and number of images within the recorded ensemble (N). Equation 3.14 shows that as the $N \to \infty$, $\epsilon \to 0$; inherently capturing the origin of the finite ensemble error.

All uncertainties are normalized by the mean freestream velocity U_∞ and presented as a percentage thereof. In the current experimental campaign, planar PIV is conducted. As a result, the ensemble uncertainties are computed only along a streamwise ($\overline{u}$) and normal ($\overline{v}$) flow direction. The associated uncertainties of the mean velocities are given by:

$$\epsilon_{\overline{u}} = \frac{\sqrt{\overline{u'^2}}}{\sqrt{N}} \qquad \epsilon_{\overline{v}} = \frac{\sqrt{\overline{v'^2}}}{\sqrt{N}} \tag{3.15}$$

Where $\sqrt{\overline{u'^2}}$ represents the RMS of the velocity fluctuation, $\langle u' \rangle$. In turn, the uncertainty of the RMS of the streamwise and normal velocity fluctuation is estimated through:

$$\epsilon_{\sqrt{\overline{u'^2}}} = \frac{\sqrt{\overline{u'^2}}}{\sqrt{2N}} \qquad \epsilon_{\sqrt{\overline{v'^2}}} = \frac{\sqrt{\overline{v'^2}}}{\sqrt{2N}} \tag{3.16}$$

Finally, the uncertainty of the Reynolds stress terms is given by the following terms:

$$\epsilon_{\overline{u'v'}} = \frac{\sqrt{1 + R^2_{\overline{u'v'}}}\sqrt{\overline{u'^2}}\sqrt{\overline{v'^2}}}{\sqrt{N}} \quad \text{where,} \quad R_{\overline{u'v'}} = \frac{\overline{u'v'}}{\sqrt{\overline{u'^2}}\sqrt{\overline{v'^2}}} \tag{3.17}$$

For which $R_{\overline{u'v'}}$ corresponds to the correlation coefficient.

Convergence study

The error estimation relations indicated in Equations 3.15 – 3.17, provide a sufficient means of analyzing the uncertainties due to the limited ensemble size. Nevertheless, it is decided

to conduct a convergence study for the considered flow parameters $\overline{u}$, $\overline{u'}$ and $\overline{u'v'}$ in order to prove the stability of the averaged flow fields. The results of which are indicated in the following figure:

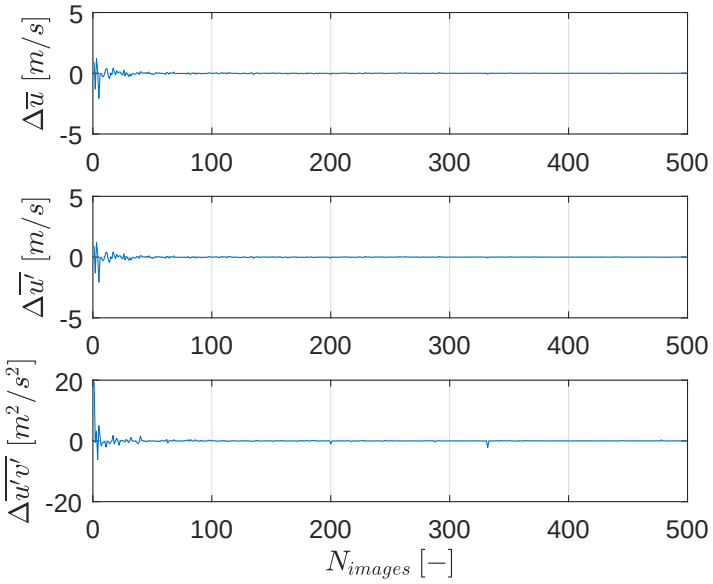

FIGURE 3.18: Convergence of the considered flow variables.

Where the difference between the mean of a specified area (Figure 3.19) of the flow field is compared for each N and $N+1$ for all image pairs, up to $N = 500$. It becomes clear that the mean velocity and standard deviation terms converge equally fast, whereas the Reynolds stress propagates more slowly. The latter is consistent with the observations made by Hain et al. (2016), and proves the necessity of a large number of image pairs.[56] For the current study, the maximum available number of image pairs (i.e. 500, excl. outliers) is always considered for the construction of average flow fields of any physical parameters.

PIV inherent uncertainty

Through the experimental technique of PIV itself, various sources of error arise inherently. The flow velocity vectors are computed from the motion immersed particles. As these particles do not follow the flow exactly, a discrepancy arises between the recorded and real fluid motion (Section 3.4.3). In turn, the finite spatial resolution of the setup limits the scale to which flow features can be resolved. Finally, the cross-correlation procedure which derives velocity vectors from image pairs contains some fundamental errors. The latter three sources of error are the most dominant to a PIV system.[55] (Humble, 2009) Therefore, only these are discussed in this section.

Particle slip uncertainty In Section 3.4.3, it was stated that DEHS particles are used in the present experimental investigation to visualize the flow fields. Even though DEHS is known to accurately follow the flow, it does have a density ρ_p and size a_p different than the fluid in which it is immersed (i.e. air). These features cause the seeding particles to become buoyant relative to the fluid, and not follow the studied flow fields precisely. The resulting difference in fluid and particle velocity is called *the paricle slip velocity*, u_{slip} and is defined as the product of the particle response time, τ_p and the particle acceleration, a_p:

$$u_{slip} \approx \tau_p \cdot a_p \tag{3.18}$$

The normalized form Equation 3.18, u_{slip}/U_∞ is used as the particle slip uncertainty estimation ϵ_{slip}. The particle slip time of various types of particle has been systematically studied by Ragni et al. (2011) by measuring the velocity transient in response to a oblique shock wave at M = 2.0.[57] From this research, it was concluded that the $\tau_{\text{DEHS}} \approx 2.0\ \mu s$. In turn, the particle acceleration is given by:

$$a_p = \frac{du_p}{dt} = \frac{u_p - u_f}{\tau_p} \tag{3.19}$$

Which is based on the simplification that $\rho_p/\rho_f \gg 1$, which is typical for DEHS seeding particles.[42] (Sun, 2014) Equation 3.19 shows that particle acceleration is a function of the difference between particle and fluid velocity, respectively u_p and u_f, divided by τ_p. According to Ragni (2012), for regions of steady flow, a_p can be simplified to:

$$a_p = \vec{U} \cdot \nabla \vec{U} \tag{3.20}$$

Subsequently, substituting the expression of Equation 3.20 into Equation 3.18, the particle slip velocity can be approximated through:

$$u_{slip} \approx \tau_p \cdot \left(\vec{U} \cdot \nabla \vec{U} \right) \tag{3.21}$$

Where the expression from Equation 3.21 is able to produce reasonable particle slip approximations in those regions in which strong vortices are absent (i.e. right over the ribs). However, for flow regions where the vortical structures are dominant (i.e. rib cavities), estimations for the u_{slip} are based on the centrifugal acceleration term as dominant force. According to Sun (2014), particle acceleration is thus estimated through:

$$a_p \approx \frac{|V^2|}{r} \tag{3.22}$$

Where the swirling velocity magnitude $|V|$ is estimated as the difference between freestream velocity U_∞ and convective shear layer velocity U_{conv}.[42] Additionally, the vortex radius r is approximated to be the same height as rib height e. The latter property is confirmed by the open and closed cavity flows, observed from Schlieren visualization in Section 5.1. Finally, combining the vortical particle acceleration term (Equation 3.22) with approximate relation from Equation 3.18, it is found that:

$$u_{slip} \approx \tau_p \cdot \left(\frac{|\vec{U}^2|}{r} \right) \tag{3.23}$$

As a result, Equation 3.23 is used as particle slip uncertainty estimation for the cavity flows during secondary PIV campaign ($\epsilon_{slip.c}$), whereas Equation 3.21 is applied to the region above the ribs as estimate for the primary campaign ($\epsilon_{slip.t}$).

Spatial resolution uncertainty The cross-correlation routine of the PIV processing method solves velocity vectors over interrogation windows of finite size. For the current thesis, the smallest window size considered equaled 24 $\times$ 24 pixels, corresponding to approximately 0.8 $\times$ 0.8 *mm*. Due to this inherently limited window size, structures and motions of the flow can only be solved up to a specific scale. Schrijer and Scarano (2008) investigated the uncertainty related to the spatial resolution in detail, and defined it as:

$$\frac{u}{u_0} = \text{sinc}\left(\frac{\text{WS}}{\lambda} \right) \tag{3.24}$$

Where the ratio of the minimum window size to the spatial wavelength λ is also known as the *normalized window size*, l^*.[58] It was identified by De Kat and Van Oudheusden (2012)

that a typical cross-correlation procedure has an accepted l^* = 0.5.[59] This means that the smallest resolvable flow feature is twice the size of the final window pass (~1.6 *mm*). For a decreasing, multi-pass correlation, such as discussed in Section 3.4.5, $l^* \leq 0.5$. However, to remain conservative, the latter is chosen for the current uncertainty estimation (i.e. ϵ_{sr}).

Cross-correlation uncertainty The error associated with the cross-correlation operation performed by DaVis has been defined by Humble (2009), who found that:

$$\epsilon_{cc} = \frac{\epsilon_{corr}}{k\delta t} \tag{3.25}$$

Where ϵ_{corr} is the approximate pixel discrepancy, k the system resolution in $pixels/m$ and δt the pulse separation time.[55] The ϵ_{corr} is conservatively estimated to be equal to ~0.1 *pixel* for planar PIV experiments by both Humble (2009), and Lynch and Scarano (2014), who performed a zero-time-delay test.[60] The latter term is assumed constant throughout the entire measurement campaign, meaning that only k and Δt influence this uncertainty estimation.

Summary

The previous explanations of the uncertainty estimates are used to compute both absolute and percentile errors for representative experimental cases. In Section 3.4.2, it identified that two PIV campaigns are conducted; corresponding to respectively the flow directly above the rib tops and inside the cavities (Figure 3.10). As a result of the two experimental setups and varying characteristics, uncertainty estimates are performed on a case representing both setups. To this end, the 2.4/30 test plate is chosen. As this geometry is investigated twice, once for the full rib top FOV ($2.4/30_{\text{FOV}}$), another for the final cavity $2.4/30_{\text{cav}}$, it is ideal for comparative purposes. The results are summarized in the following table:

TABLE 3.2: Uncertainty estimation, based on 2.4/30 geometry.

Error name	*Primary (rib tops)*		*Secondary (cavities)*	
	Abs. [m/s]	%	Abs. [m/s]	%
$\epsilon_{\overline{u}}$	2.72	0.54	4.07	0.80
$\epsilon_{\overline{v}}$	1.36	0.27	1.58	0.27
$\epsilon_{\sqrt{\overline{u'^2}}}$	1.92	0.38	2.88	0.57
$\epsilon_{\sqrt{\overline{v'^2}}}$	0.96	0.19	1.12	0.22
$\epsilon_{\overline{u'v'}}$	n.a.	0.03	n.a.	0.06
ϵ_{slip}	3.39	0.67	4.96	0.98
ϵ_{sp}	3.22	0.64	3.22	0.64
ϵ_{cc}	3.33	0.66	1.00	0.20

Where the averaged flow variables $\overline{u'}$, $\overline{v'}$ and $\overline{u'v'}$ are obtained from the flow regions which are most critical. For the primary campaign, this region is defined as the final rib impingement location, whereas, for the secondary campaign, the region correlates with the recirculation region directly upstream the final rib of the cavity (Figure 3.19). Note that the 'not applicable' is indicated for the Reynolds stress uncertainty estimate as the dimension of $\overline{u'v'}$ is m^2/s^2. As a result, $\overline{u'v'}$ is non-dimensionalized with U_∞^2, implying that an absolute error comparison is futile compared to the other uncertainties.

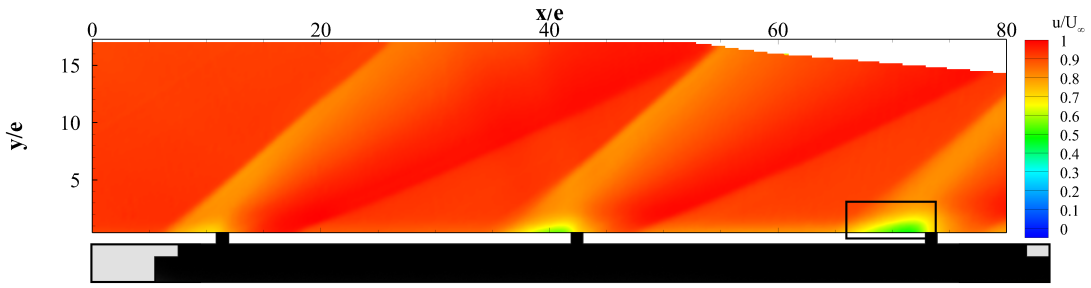

FIGURE 3.19: Critical flow region for 2.4/30 geometry.

It remains to compute the total error estimates for the flow variables of interest, i.e. $\overline{u}$, $\overline{u'}$ and $\overline{u'v'}$. This is done by combining the dependent inherent and ensemble uncertainties through the standard error propagation relation. For each flow variable, the corresponding relation is given by:

$$\epsilon_{tot} = \sqrt{\epsilon_{ens}^2 + \epsilon_{slip}^2 + \epsilon_{sp}^2 + \epsilon_{cc}^2}$$

Meaning that $\epsilon_{\overline{u}.tot}$ = 1.26% and 1.43%, $\epsilon_{\overline{u'}.tot}$ = 1.17% and 1.23% and $\epsilon_{\overline{u'v'}.tot}$ = 1.14% and 1.19% for respectively the primary and secondary campaign. By acknowledging these to total errors during the discussion of the PIV results, it is known to what level of detail conclusions are allowed to be drawn from the data.

Chapter 4

Quantitative infrared thermography

The usage of IRT is inspired by the experimental investigation on heat transfer properties of roughness induced subsonic flows conducted by Aliaga et al. (1994).[14] Within this research, the velocity properties were combined with the thermal properties of the flow, enabling them to directly assign flow phenomena to variations in heat transfer. It is decided to take a similar approach for the current thesis by usage of Schlieren, PIV and IRT, providing respectively flow development, velocity, turbulence and heat transfer data. The application of the IRT methodology is a concept, proven to provide sufficiently accurate temperature data. Nevertheless, the most reliable data for heat transfer is obtained once a thermally steady-state is realized. Therefore, this is striven towards.[33] (Carlomagno and Cardone, 2010)

In this chapter, the design, assembly and usage of the final QIRT methodology are described. This is done by first discussing the experimental considerations in Section 4.1, where individually the test plates, insulation and heat sink design are examined; followed by a description of the assembly. In turn, the workings of the IRT acquisition system is elaborated upon in Section 4.2. This is done by first describing the theoretical background of radiation heat transfer, followed by the operational aspects and system performance of IR cameras. Finally, the data reduction procedures and corresponding uncertainty estimates are treated in Section 4.3, including the recommended settings of optimal heat transfer results.

4.1 Heated, thin-film model design

In the case that no additional thermal input is delivered to the test model (i.e. *passive IRT*), the surface heat exchange is solely dependent on the material properties of the model and the characteristics of the boundary layer. In the case of unheated, supersonic flow – such as for the ST-15 – the convective heat transfer will be relatively high compared to frictional heat.[33,5] (Carlomagno, 2010; Sun, 2012) The resulting cooling process is expected to provide a steady-state within multiple minutes (t_{ss}).[61] (Haberman, 2012) In turn, once this natural cooling process becomes steady, the test plate will be at the adiabatic wall temperature (Equation 4.41) such that there is no heat transfer (i.e. $\Delta T_{con} = 0$). To gain more control over this t_{ss} and obtain a non-zero temperature difference once $t \geq t_{ss}$, an active IRT method should be developed. A common approach to active thermography is the so-called *heated-thin-foil method*, where a thermally thin metallic foil or printed circuit board (PCB) is steadily and uniformly heated by the Joule effect (Ohmic heating).[33] (Carlomagno and Cardone, 2010) Previously, both Aliaga et al. (1994) and Han (1984) utilized a thin copper plate to which an electric current was applied.[14,6] In both cases, the researchers concluded that a thermal steady-state was found for which a sufficient temperature contrast (i.e. ΔT_{con}) remained in order to obtain the heat transfer coefficients h, St and Nu. As an active thermographic system does not yet exits for the ST-15 wind tunnel, this needs to be designed. The entire process leading to the desired QIRT setup, is provided in this section.

4.1.1 Test plate design

The measurements of convective heat fluxes must be performed by means of a thermal sensor (i.e. test plate), from which temperatures are to be measured with proper transducers (i.e. IR camera and thermocouples). Generally, heat-flux sensors consist of plane slabs with a known thermal behaviour.[33] (Carlomagno and Cardone, 2010) As a result, once the model is thermally stable, the energy conservation law can be used to relate the surface temperatures to convective heat flux. For the current thesis, it is decided to design and construct a series of test plates consisting of an insulating slab, covered by a PCB. By knowing all material characteristics, aspects of assembly and electrical power input, a complete monitoring of both the thermal in- and output is possible. As a result, the test plates effectively represent a thermal sensor through which very precise data analysis can be performed (Section 4.3).

System requirements

Prior to the design of the test plates, a set of system limitations and requirements was determined, which is given by the following:

1. Outer dimensions of PCB copper area (l x w): 178 x 150 mm.
2. Minimal temperature contrast (ΔT_{con}) at steady-state: 10 K
3. Maximum time to reach steady-state (t_{ss}): 50 s.
4. Maximum allowable current (I_{max}): 6.0 A.
5. Maximum conductive heat loss into body (q_{cond}): $\leq 1\%$ of q_{el}.

Where the first requirement is set equal to the outer dimensions of the Schlieren and PIV test plates, such to allow for direct, unscaled geometrical comparisons. The temperature contrast is derived from the maximum temperature difference found for the repeated closed cavity flow fields by Aliaga et al. (1994); equal to 7.5K + 30% for redundancy.[14] The t_{ss} is limited such to make IRT testing more practical, and obtain experimental durations similar to those from PIV. As a result, the flow conditions within the test section are prevented from declining too significantly; making the anticipated experimental conditions assumably constant. The maximal allowable current originates from the limited power output (q_{el}) of the laboratory power supply (Section 4.2). Finally, the conductive limitation of the insulation and geometrical elements (i.e. ribs) is set to make the thermal behaviour of the models as predictable as possible. Effectively though, this means that IRT is only possible within the cavities and excludes the ribs from the measurements.

One-dimensional, semi-infinite solid analysis

In order to decide upon the exact design characteristics of the PCB heating element and insulation, it is chosen to conduct a simplified analysis of the physical problem. A common method is to use *the semi-infinite solid approach*, in which the unsteady, one-dimensional (1D) heat conduction equation is solved.[48] (Giepman et al., 2015) This method relies on the assumption that the physical problem can be represented by a 1D, semi-infinite slab with constant material properties along the complete surface. In turn, as this form is closed, it allows the derivation of an analytical solution.

The focus of the entire test plate design is to obtain a system which has near-perfectly uniform material properties along its complete surface. As such, the assumptions of this 1D analysis are allowed and lead to the following schematic of the physical problem:

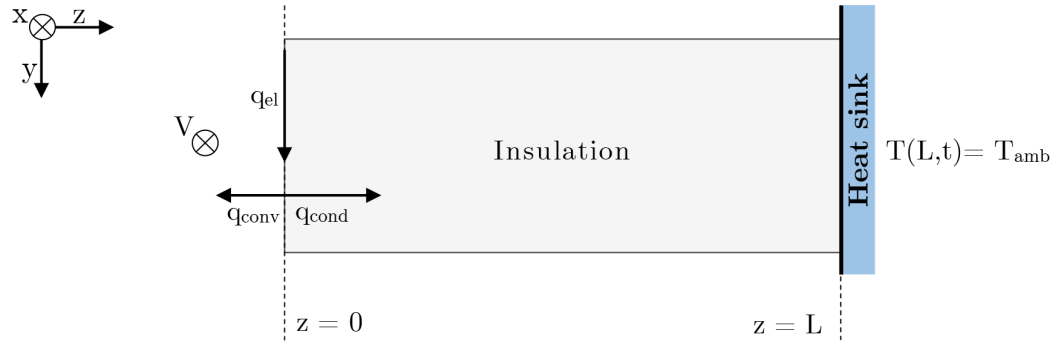

FIGURE 4.1: Schematic of the heat transfer problem.

Where, for simplicity, an infinitesimally thin heating element is placed on top of an insulating slab. In addition, it is assumed that the material properties are uniform in z-direction and correspond to those of the insulation material. It is shown in Section 4.3.8, that this assumption remains valid for the real-life setup. Following Figure 4.1, the transient model and system of conditions is given by:

$$\frac{\partial T}{\partial t} = \alpha \left(\frac{\partial^2 T}{\partial z^2} \right) \tag{4.1}$$

with boundary conditions (BCs),

$$(1)\ T(L,t) = T_{amb} \qquad (2)\ -k \left. \frac{\mathrm{d}T}{\mathrm{d}z} \right|_{z=0} = q_{el} - h\left(T(0,t) - T_{aw}\right)$$

and initial condition (IC),

$$T(z,0) = T_{amb}$$

For which the first BC is valid for the assumption that the back of the insulation is attached to a heat sink. It is actually shown in Section 4.1.3, that the cavity door neatly approximates this feature. In turn, the second BC is defined under the assumption of a steady flow at unchanging ambient conditions (i.e. p_0, T_0, M_∞). Following the observations made by Sun et al. (2014), this should not be an issue provided $t_{ss} \leq 60$ seconds of wind tunnel run time.[42] The form of the second BC is defined from the definition of convective heat transfer:

$$q_{conv} = h\Delta T_{con} = h(T_s - T_{aw}) \tag{4.2}$$

Where ΔT_{con} is the temperature difference between the model's surface (T_s) and the adiabatic wall temperature (T_{aw}) and h is equal to the convective heat transfer coefficient, given by:

$$h = \rho_\infty u_\infty c_p St \tag{4.3}$$

For which ρ_∞ is the fluid density in the freestream, u_∞ the freestream velocity, c_p the specific heat capacity at constant pressure and St the local Stanton number. These freestream conditions are obtained directly from the experiments conducted by Sun et al. (2012) for a M = 2.0 flow in the ST-15 wind tunnel.[5] The Stanton number, however, is estimated through two analytical equations as a means of verification. The latter are represented by:

- The Dittus-Boelter relation: $St = 0.0308 Re^{-0.2} Pr^{0.6}$
- The Reynolds analogy: $St = C_f/(2Pr^{0.67})$

Where the Dittus-Boelter relation is based on turbulent, flat plate flow conditions with a constant surface heat flux (q_s).[62] (Mccabe et al., 1993) For both methods, the constants Re and C_f are found in accordance to Sun's research (2012), whereas Pr is a constant defined for the turbulent boundary layer (White, 2006).[5,9] As a result, the unit $Re \approx 3.7 \cdot 10^7$ [-], $C_f = 2.6 \cdot 10^{-3}$ [-] and $Pr \approx 0.71$ [-]. By then applying these coefficients to the Stanton number estimation functions (and add 30% for redundancy):

- The Dittus-Boelter relation: $St = 0.0012$ [-]
- The Reynolds analogy: $St = 0.0016$ [-]

It is seen that these are in reasonable agreement with one another, regardless of the completely different approach. Aliaga et al. (1993) and Han (1984) found that their correlations correspond well with an adjusted form of the Dittus-Boelter relation (Section 2.1.5).[10,6] For redundancy, however, it is chosen to use the higher value of St, derived through the Reynolds analogy. Substituting St and remaining freestream parameters in Equation 4.3, $h \approx 781.5\ W/m^2K$. Finally, by defining that T_{amb} = 298.5 K and T_{aw} = 275.5 K (Equation 4.41), all flow properties are defined. As such, the problem is closed making it possible to obtain an analytical solution for this heat transfer problem which functions as a design estimator.

The analytic solution to the 1D heat transfer system is solved by using the method of separation of variables, where the non-homogeneous system is subdivided into a transient-homogeneous, $o(z,t)$ and a steady-state problem, $T_e(z)$ (Haberman, 2012).[61] As a result, the total solution is given by:

$$T(z,t) = o(z,t) + T_e(z)$$

Where solutions to both components of $T(z,t)$ are found through an elaborate derivation of the accompanying differential equations. For the complete derivation, the reader is advised to study Appendix K. The result of this derivation is also listed here, given by:

$$o(z,t) = \sum_{n=1}^{\infty} A_n \cos\left(\frac{n\pi z}{2L}\right) e^{-(\frac{n\pi}{2L})^2 \alpha t} \quad n = 1, 3, 5, ...$$

Where,

$$A_n = \frac{2}{L}\int_0^L f(z)\cos\left(\frac{n\pi z}{2L}\right) dz \qquad \text{with, } f(z) = T_{amb} - T_e(z) \tag{4.4}$$

and,

$$T_e = \frac{L-z}{k}(q_{el} - h\Delta T) + T_{amb}$$

This system of equations (4.4) is programmed into a MatLab script, which computes the time required to reach a steady-state (t_{ss}) based on the design inputs of the model. In addition, it enables the user to find the transient solutions to the heat transfer profiles for a defined number of time steps for $0 \leq t \leq t_{ss}$. For this system, the following design variables exist:

1. Thermal diffusivity: α [m^2/s]
2. Insulation thickness: L [m]
3. Electric power input: q_{el} [W/m^2]
4. Temperature contrast: ΔT_{con} [K]

Where q_{el} is a variable set by the power supply and ΔT_{con} is equal to the minimal required temperature contrast (i.e. 10 K).[10] (Aliaga et al., 1993) The thermal diffusivity (α) is a measure of the heat transfer rate (m^2/s) and is material specific.[63] (Kreith, 2012) As a result, the required insulation thickness L depends directly on the value of α, which is given by:

$$\alpha = \frac{k}{\rho c_p} \tag{4.5}$$

Where k is the thermal conductivity, ρ is the material density and c_p is the heat capacity at constant pressure. It is decided to vary the latter design parameters such that a basic thermal sensor can be designed, which complies with the required experimental performances.

Printed circuit board Through the MatLab based optimization procedure, it was found that – regardless of the material choice or insulation thickness – the fastest t_{ss} resulted for q_{el} ~q_{conv}. Therefore, as $h \approx 781.5\ W/m^2K$ and ΔT_{con} = 10 K, a PCB layout should be designed capable of delivering $q_{conv} = q_{el}$ = 7815.5 W/m^2. In turn, knowing that the complete copper-clad surface area should have a width and length of 178 $\times$ 198 mm (i.e. 0.0267 m^2), the complete electric power delivered by the PCB is set to 208.7 W. By the working principle of an electric heating element, the equation for ohmic heating is equal to:

$$q_{el} = I^2 R \tag{4.6}$$

Where I is the current delivered by the power supply in A, and R is the electric resistivity of the PCB copper tracks in Ω. Since there is a high-level of uncertainty surrounding the convective heat transfer estimations, it is decided to limit the electric design current input to 3.2 A; maintaining a buffer in the case more power is required. This means that the PCB layout should encompass a minimum base resistivity R_0 of 20.4 Ω (Equation 4.6). The total resistivity R of a continuous wire can be estimated through:

$$R = R_0(1 + \alpha(T - T_{ref})) \quad \text{where,} \tag{4.7}$$

$$R_0 = \frac{L}{\kappa A} \tag{4.8}$$

For which L is the length (m), A is the cross-sectional surface area (m^2), κ is the electrical conductivity and α is the temperature-specific electric resistivity coefficient based on a reference temperature (T_{ref}). In the case of these PCBs, copper is used as a conductor for which κ_{cu} = $5.95 \times 10^7\ \Omega/m$ and α_{cu} = $4.04 \times 10^{-3}\ K^{-1}$ with $T_{ref} = 298K$.

It is decided to obtain the required resistivity by designing a copper track with a so-called serpentine shape. Through such a layout, a single copper wire covers the entire allowable surface area of the PCB such that its length is maximized, whilst still allowing the electrical connectors to be conveniently accessible from a single point (Figure 4.2). It is chosen to position the tracks perpendicular to the flow in order to minimize conductive heat loss along the surface in streamwise direction (Section 4.3). This way, however, more roughness is introduced on the wall surface. Nevertheless, due to the limited roughness height and pitch of the copper wires, these introduced roughness effects are very limited. The final design of the PCB is given in Figure 4.2.

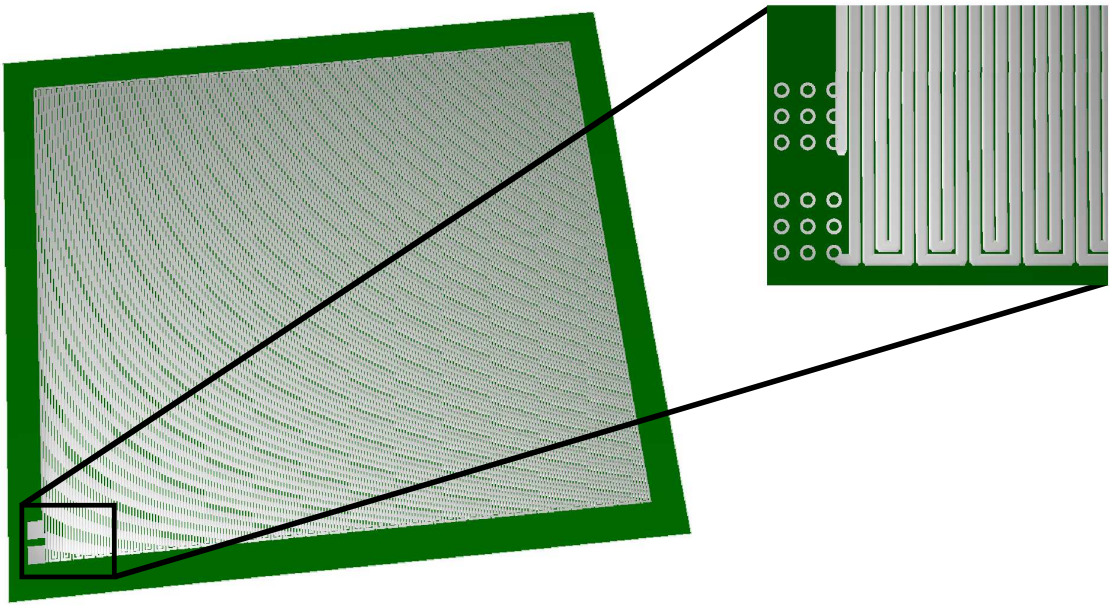

FIGURE 4.2: PCB copper track layout, and detailed connector region incl. vias.

The remaining design parameters of the PCBs, minimum track spacing s_{cu} and copper height h_{cu}, were defined by the manufacturing limitations; set respectively at s = 0.1 mm, h_{cu} = 0.035 mm.[64] (Eurocircuits, 2016) This, in turn, left the wire width, w_{cu} as a final design requirement. In order to comply with the R_0 requirement, w_{cu} is set equal to 0.75 mm. The resulting copper track has a length of 31.22 m, and an overall resistance of 22.6 Ω. By applying this R_0 into Equation 4.7, the corresponding design current, I_{des} is found to be equal to 3.0 A which is sufficiently redundant for the experimental setup. In addition, by the implementation of 9, 0.6$mm^{\oslash}$ vias as electrical connector to each copper wire, it is estimated that the PCBs can withstand a current of up to 7.2 A.[63] (Kreith, 2012) These vias go right trough the 1 *mm* thick FR-4 base material, allowing electrical current to be delivered from the back of the model. The complete surface area of the PCB is 198 $\times$ 170 *mm*, and accommodates a 10 *mm* blank rim which circumscribes the actual copper area. In reality, the surface shown in Figure 4.2 is covered by a black solder mask such to protect the thin wires from breaking whilst maximizing the thermal emissivity properties. The latter is a thermal radiation property, which is clarified more elaborately in Section 4.2. For a more complete view of the PCB dimensions, the reader is advised to study Appendix C.

Insulation Through the final design of the PCB, two of the four main design parameters of the simplified 1D model are fixed (minimally) at $q_{el} = 208.7W$ and ΔT_{con} = 10 K (Figure 4.1). It thus only remains to define the insulation material and corresponding thickness. The latter is done through an optimization procedure in which the analytical model is applied to compute the time to reach steady-state, t_{ss} given material properties and $L_{min} \geq 5\ mm$. (Equation 4.4) For this model, it is decided to define the t_{ss} as the interval required for:

$$T(z,t) - T_e(z) < 0.2K \qquad\qquad T(0,t) - T_e(z) < 0.2K \tag{4.9}$$

Which corresponds to the effective temperature difference between the steady-state and transient temperature profiles. The threshold of this temperature difference is equal to the temperature equivalent error margin of the utilized IR camera (i.e. NETD, Section 4.2). Since no data reductions can be improve the error margins below this threshold, no additional uncertainties are introduced in the case this condition is used for solving Equation 4.4. For the

current analysis, multiple types of materials are considered for the insulation design. A selection of which is provided in the following table:

TABLE 4.1: Materials considered for insulation design.

Material	Thermal diffusivity (m^2/s)	Thermal conduction (W/mK)
Noryl	1.42×10^{-7}	0.19
Makrolon	1.42×10^{-7}	0.20
FR-4 (epoxy)	1.12×10^{-7}	0.29
SikaBlock (M940)	1.28×10^{-7}	0.10
Polystyrene	2.30×10^{-8}	0.03
Copper	1.11×10^{-4}	401

From which it is seen that four relatively similar synthetic materials (Noryl, Makrolon, FR-4 and SikaBlock), one insulator (polystyrene) and one conductor (Copper) are chosen. By initial investigation, however, it is found that materials with either a relatively high or low k are incapable of providing the right level of temperature contrast within the desired t_{ss} (i.e. $\leq$ 60 sec). This is caused by the fact that either too much (i.e. copper) or too little (i.e. polystyrene) heat is transported from the surface. Therefore, the material for the insulation slab is chosen from the remaining, synthetic materials at average k. As their thermal responses are relatively comparable, the final material choice is also largely based on:

- *Manufacturability*: adjustable, available in slabs of right thickness.
- *Homogeneity*: relatively invariant thermal properties.
- *Fixable to PCB*: non-roughened surface, easily glueable onto PCB surface.
- *Maximum operating temperature*: capable of withstanding $T_s \geq 80°$ C.
- *Similar material properties as PCB base*: to avoid unpredictable temperature profiles.

Taking all material requirements into account, it is found that Makrolon offers the most ideal combination of properties. This is caused by the fact that T_{max} is 134°C, whilst this material is known for being relatively uniform ($\pm$ 5%) and accurately millable.[48] (Giepman et al., 2015) The required thickness is based on the average t_{ss} and temperature contrast, which are given as function of L in Figure 4.3a.

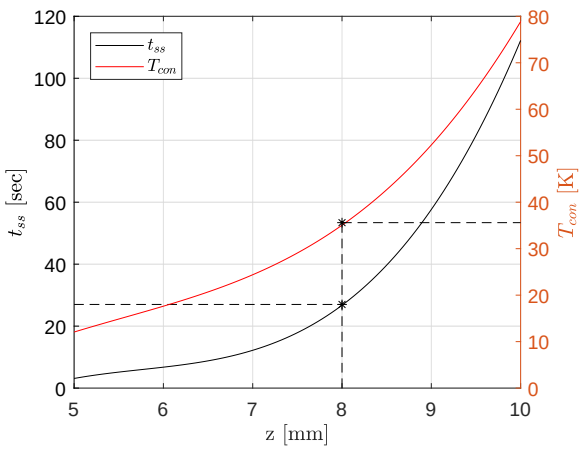

(A) Steady-state t (black) and T (red)

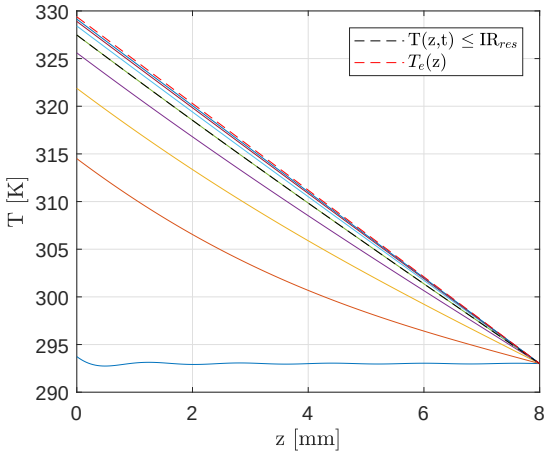

(B) Transient temperature response.

FIGURE 4.3: Steady-state properties of Makrolon, relative to material thickness

Based on the results from Figures 4.3a, it is decided to use an 8 *mm* thick, Makrolon slab as insulation for the PCBs. With this thickness, the average T_{con} and t_{ss} are respectively 35.6 K and 27 sec with a required power, q_{el} of 742.9 W. In addition, 8*mm* Makrolon plates are very common and can be ordered as regular stock material. The complete transient temperature response of this configuration is shown in Figure 4.3b, where the time between curves is ~6 *sec* and the dotted lines indicate respectively steady-state (red) and threshold profiles (black). From this, it becomes clear that a linear temperature profile can be assumed once the threshold is met (Equation 4.9). Even though, the resulting T_{con} is significantly higher than the predefined 10 K, the t_{ss} is very acceptable being ≤ 60 sec. As such, a lot of redundancy remains for the test plates. This is helpful, considering the uncertainties revolving around the flow properties. The final design of the Makrolon insulation plates looks as follows:

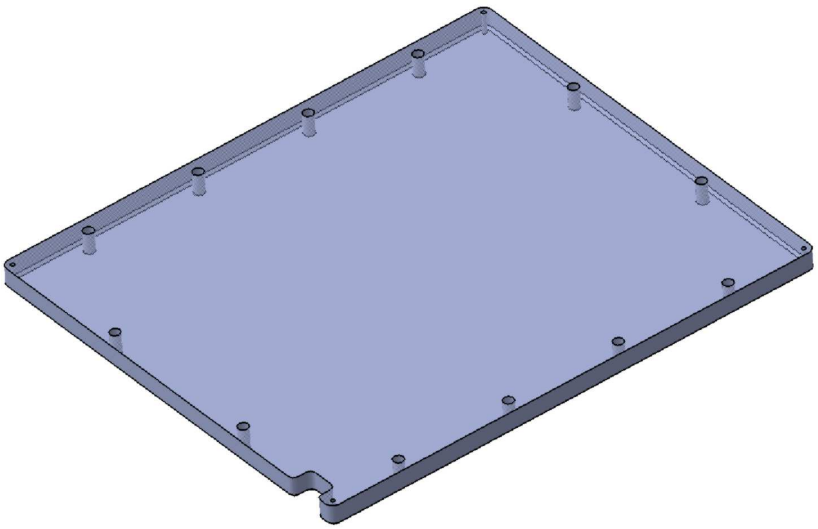

FIGURE 4.4: Makrolon insulation plate design.

For which the outer dimensions are inspired by the size of the overall PCB area, whilst being 2 *mm* shorter on each side; i.e. 194 $\times$ 166 *mm*. This is done to allow access to the sides of the insulation plate once the PCB is mounted on top. A cut-out is included to the bottom downstream corner such to provide access to the soldering pads (i.e. vias) from the back of the PCB heater. To accomplish a tight fixture to the cavity door, twelve screw holes are implemented along the perimeter of the surface. As seen in Section 4.1.3, these fixture points can be accessed from the outside by the required mounting screws. Finally, four smaller screw holes are located at each of the corners of the insulation. These function merely as an alignment tool during the PCB mounting phase (Section 4.1.2). In fact, by their limited size, hardly any additional mounting strength is introduced to each test plate assembly. It has to be noted that, even though this cut-out and screw holes are included in the insulation design, the measured copper area falls right within the unaltered region (Figure 4.2). As such, the assumptions of the analytic model remain in place and are unaffected by these features (Figure 4.1). For a more precise view on the dimensions of the insulation plates, the reader is appointed to check the schematic drawing in Appendix C.

4.1.2 Test plate assembly

The designs of the PCB and insulation plate are tailored such to precisely fit once placed on top of one another. For an optimal thermal contact, however, these components should be glued accurately and uniformly across their adjoined surface. This means that the glue thickness should be even, whilst no air pockets are formed. It is decided to glue the PCBs

to the insulation plates using a bi-component, epoxy-based glue paste. This paste has equal thermal and material properties as the PCB base material (i.e. FR-4) and Makrolon, with $\alpha_{glue} = 1.12 \times 10^{-7}\ m^2/s$ and $k_{glue} = 0.24\ W/mK$. As a result, the adhesive sticks easily to both surfaces and forms a solid connection between the two. In addition, by its equal thermal properties, hardly any material-dependent temperature profile alterations are introduced (Figure 4.3b). After a lot of trial and error, the following gluing procedure is defined:

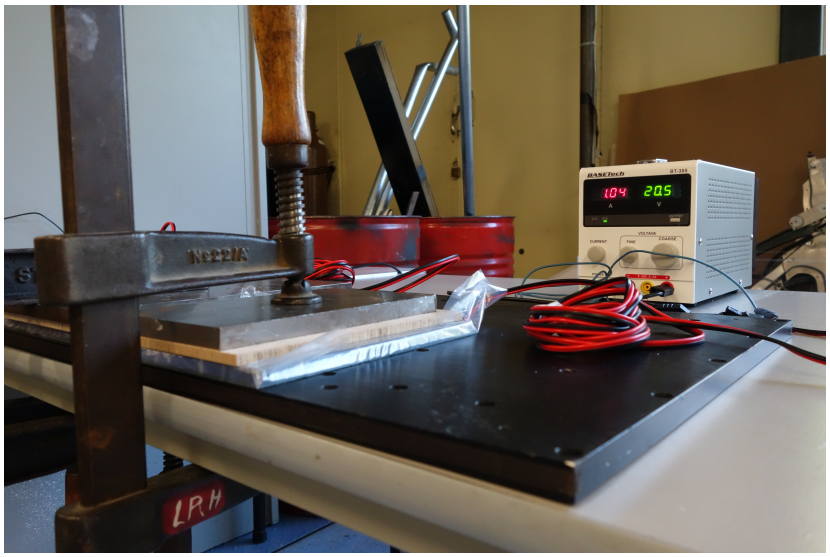

FIGURE 4.5: Initial glue curing setup incl. power supply, bench vice, plastic covered models and straightening plates.

First, lightly sand the surfaces (1) of the PCB and insulation plates to improve adhesion. Then, cover the screw-holes (2) with thin scotch tape to prevent glue from entering them. In turn, apply 3.2g of glue (3) to the sanded Makrolon surface as a center stroke. After this, place (4) the PCB right on top of the insulation and align (5) the two using four countersunk screws located at each corner (Figure 4.4). Cover this combined package (6) tightly with plastic wrapping, such to prevent glue from obscuring the test surface. Place the packed system (7) between two heavy steel plates, which are perfectly straight. Compress this package (8) using a bench vice, which allows the glue to cure evenly and form a perfectly aligned surface. During the first 10 minutes, heat (9) the recently glued combination by a laboratory power supply with 20W of power; resulting in a curing temperature of ~60°C (Figure 4.5). This is done such to make the glue thinner, minimize the cure time, increase the maximum allowable operating temperature (~95°C), improve the adhesive strength (~18 instead of 12 N/mm^2) and prevent air pockets from forming. After this initial cure time, remove (10) the plastic cover and replace (11) it by a clean one whilst removing most severe, intermediate glue residuals (12). Finally, re-compress (13) the re-wrapped system and let to cure (14) for approximately 12 hours. The latter, is done to assure proper curing of the glue. In practice through, most test plates had already completely settled within four hours.

Once all these fourteen steps are followed accurately, an even glue layer is formed whilst having minimal air pockets and even thermal properties. The latter was checked by measuring the temperature fields at the back of the heated PCBs under equal stagnant conditions (i.e. P_{in} = 30W, T_{amb} = 23°C), respectively excluding and including insulation.

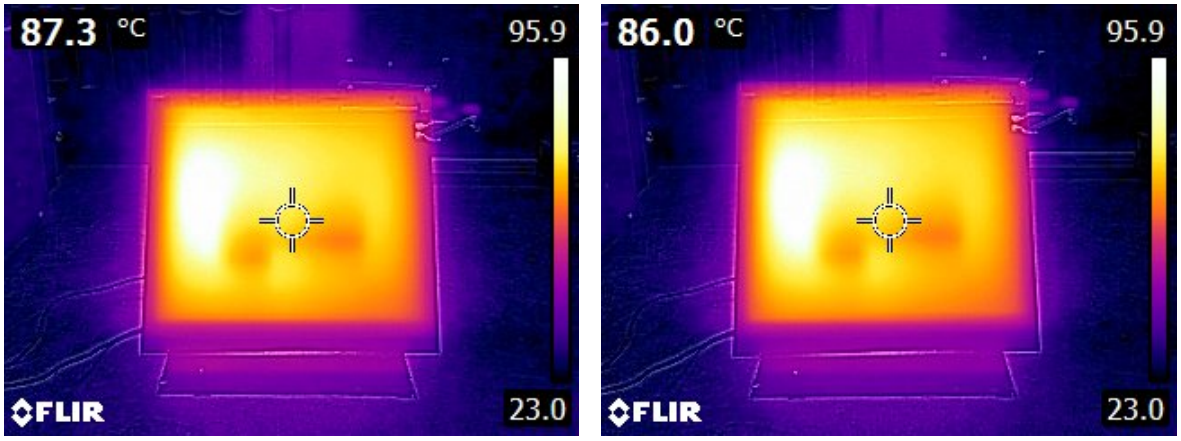

(A) PCB not mounted to insulation. (B) PCB mounted to insulation.

FIGURE 4.6: Thermal signature of PCB at steady-state under stagnant conditions.

From Figures 4.6a and 4.6b, it is seen that – regardless of the use of insulation – the overall temperature values differ slightly whilst the relative thermal signatures remain the same. It is thus safe to assume that the overall glue thickness is effectively uniform and has an negligible influence on the local conductive properties. The glue thickness itself is estimated to be $0.1mm$. This value is derived by measuring the overall thickness of the glued models and comparing this to the combined thickness of the 'dry materials'.

The final step in the process of constructing the test models, is to mount the ribs on to the PCB surfaces. A correct comparison between IRT and PIV campaigns requires these models to have exactly the same geometries as those fabricated for PIV and Schlieren (Section 3.2.1). However, as their construction should be within the accuracy of tenths of millimeters, rib mounting is extremely difficult. To accommodate this, the following rib placement aids is developed:

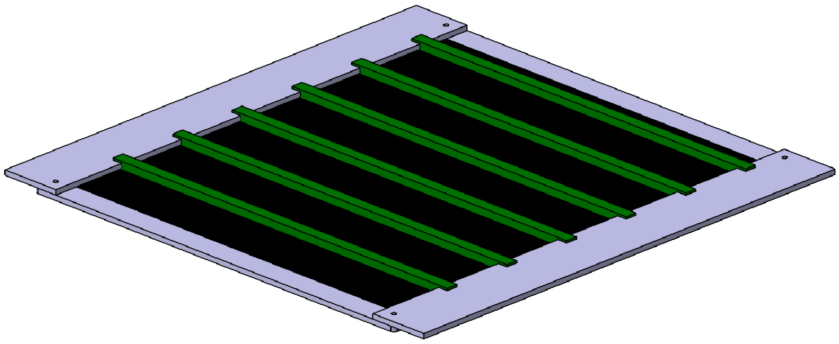

FIGURE 4.7: Rib placement frame and interchangeable geometry combs.

The concept shown in Figure 4.7 involves fifteen different interchangeable combs which are mounted along the sides of the PCB. For each comb, two screw holes are included which precisely align with those incorporated at the corners of the insulation plate and PCB. By utilizing the two screw holes, precise alignment of the ribs is verified and maintained. Each of these combs represents a specific geometry, where periodic cut-outs indicate the location as to where individual ribs are to be placed. Just as for the PIV and Schlieren models, the first rib face is located at $8mm$ form the leading edge followed by the respective pitch (Figure 3.2). As a result, the models for either measurement technique are generally equal.

The ribs are fabricated form the material called SikaBlock (M940), as this is one of the best millable synthetic materials by having high abrasion resistance and high maximum operating temperatures (~95°C).[65] (Sika, 2016) The length of each rib is set to 158 *mm* which is equal to the height of the ST-15 test section. Since the smallest cross-sectional area is 1.2 $\times$ 1.2 *mm*, the high strength and excellent milling properties are very welcome. The ribs are glued to the PCB surface using the same epoxy-based glue paste as for surface mounting. Equally to the previous case, the ribs are cured under pressure. This is done by placing a steel plate across all ribs whilst compressing the whole simultaneously through a bench vice. However, in order to prevent glue from spilling across the PCB surface, no heating is used. By a similar approach as previously, the average glue thickness is estimated to be ~0.01 *mm*.

4.1.3 Cavity door design

In order to allow optical access to the complete surface area of the models, it is decided to mount the test plates vertically inside the ST-15. To accommodate this, the existing wind tunnel window was to be replaced by a custom cavity door capable of mounting the test plates. As this door should be fixed to the existing mounting points of the ST-15 wind tunnel, the foundation of its design is given by the geometry of the original window. The final design is shown in the following figures:

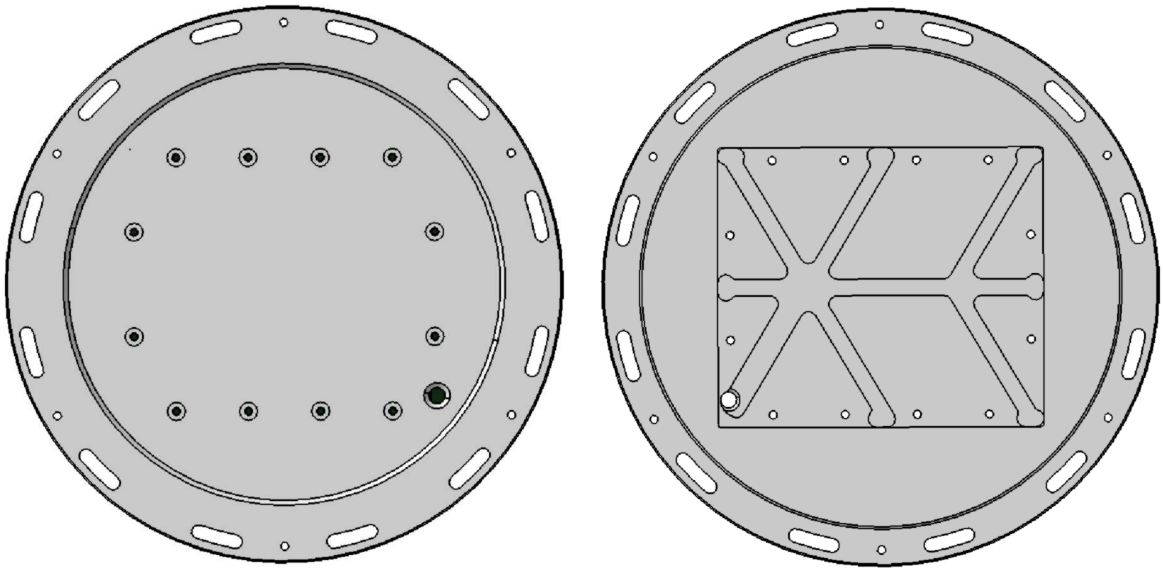

FIGURE 4.8: Final design of the ST-15 IRT cavity door, outside view (left) and inside (right).

Where Figure 4.8 displays the cavity door from respectively the outside and inside of the ST-15. The cavity is designed to be precisely ~9.1 *mm* deep (combined thickness PCB, insulation and glue), such to narrowly fit the models and form a smooth transition between the wind tunnel wall and the test plate surface. Possible variations in surface alignment of the test models can be solved by slightly altering the firmness of fixture of the twelve bolts, applied from the outside. The window is milled from a solid block of aluminum (~10.5 kg), which realizes sufficient contact between the insulation and the door. As a result, it is safe to assume that this door absorbs residual heat whilst maintaining the ambient temperature; i.e. functions as a heat sink. From the inner view of the cavity door, it is seen that cable trays are machined into the bottom of the cavity. These cable trays, together with the spacing between the insulation and cavity door, allow access for implementation of 16 reference thermocouples (Section 4.2.5). The accompanying 16 thermocouple wires and two electric

power cables are redirected outward through a 10 $mm^{\oslash}$ hole. The diameter of this access hole was kept to a minimum, such to prevent possible pressure differences between the wind tunnel and the ambient from obscuring the experiments. As an overview, the relative placement and mounting of the PCB heating plate and Makrolon insulation into the cavity door are indicated in Figure 4.9.

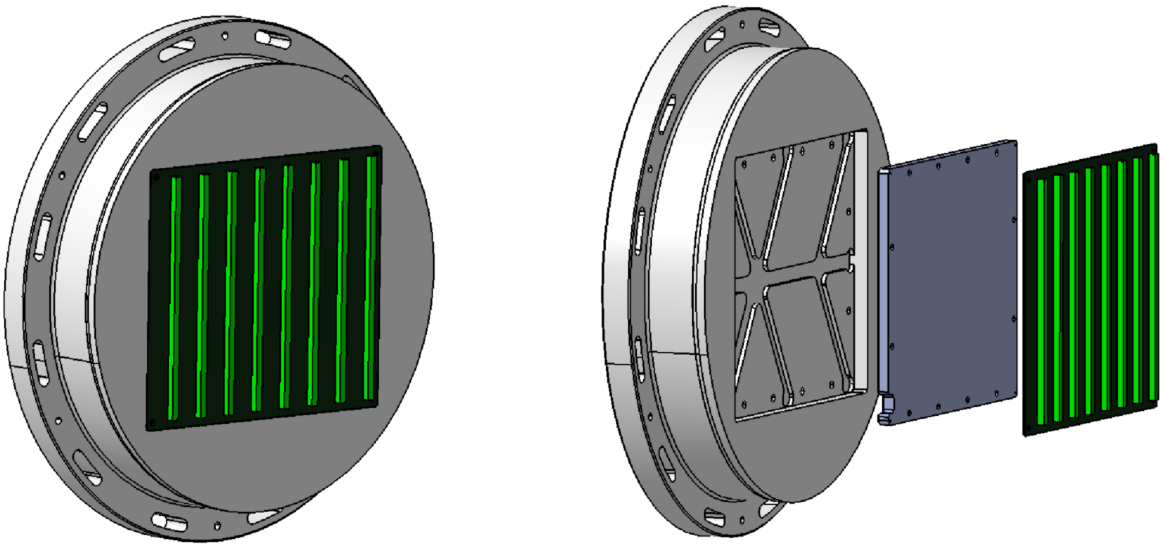

FIGURE 4.9: Mounting of the test plate to the cavity door, mounted (left) and exploded view (right).

As mentioned, the general design of this cavity door was established from the existing dimensions of the blank ST-15 window. In turn, the requirement of fitting the predefined test models vertically resulted in the dimensions and the positioning of the cavity. For the exact dimensions and technical drawings, the reader is recommended to check Appendix C.

4.1.4 Complete QIRT test setup

The resulting setup of the IRT door with respect to the ST-15 Mach block is given by the following figure:

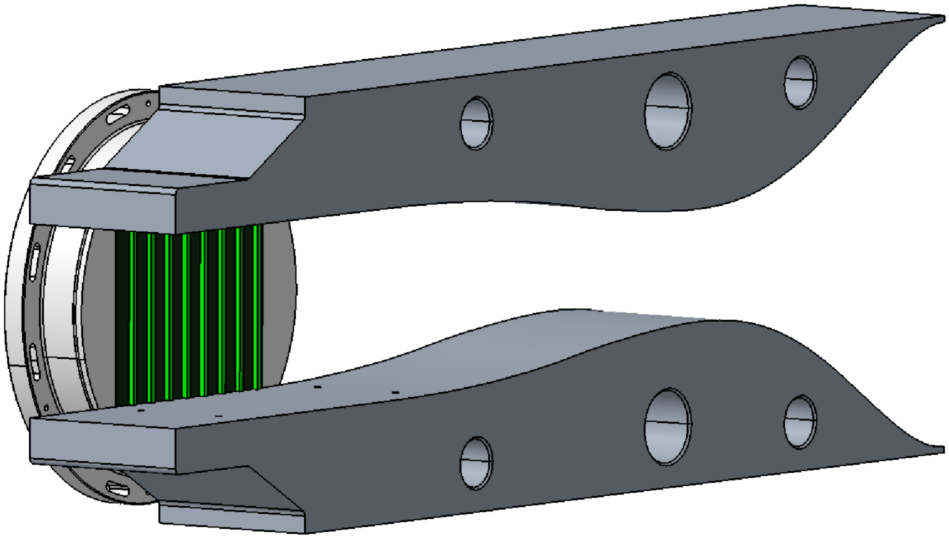

FIGURE 4.10: Complete representation of the IRT door setup, incl. ST-15 Mach blocks.

Where in real-life, on the right-hand-side of the test section, a germanium window grants optical access to an IR camera (Section 4.2.5). Thus, on one hand, the setup shown in Figure 4.10 allows to monitor the temperature over the entire surface of the test plate. Whilst, on the other hand, reference thermocouples obtain the temperatures at fixed locations along the insulation rear and sides (Section 4.3). The goal of the current IRT setup design was to make the in- and outflow of heat narrowly traceable. By carefully choosing materials, assembling the test plates and constructing a tailor-made cavity door, it is believed that this is achieved. Fortunately, in Section 5.2, it proven from the results that this direct temperature measurements from this setup functioned reliably and accurately.

4.2 Measurement technique

Experimental studies on the heat transfer properties of large roughness induced flows using infrared thermography (IRT) are very limited.[12] (Jimenez, 2004) However, due to recent developments in image resolution, optical enhancements as well as computer capabilities, IRT has gained recognition as being an appropriate research tool in the area of heat transfer measurements.[14] (Aliaga et al., 1994) Therefore, the complete wind tunnel setup for the test models is designed such that optical access is granted to the entire top surface by an IR camera (Figure 4.10). In addition, the back and the sides of the insulation are cleared such that temperatures can be monitored by 16 reference thermocouples. This way, a complete, thermal view is created along each surface providing the means for a thorough data reduction. This leads to an accurate, reliable computation of the convective heat transfer.

Since infrared cameras are used as temperature transducer for thermal mapping, it is decided to describe the fundamental principles on which it is based (Section 4.2.1). In turn, the workings and performance characteristics of the IR data acquisition systems (i.e. IR camera, software, etc.) are explained in Section 4.2.2. Then, the methods of IR camera operation are treated in Section 4.2.3 followed by the methods of calibration and emissivity estimation in Section 4.2.4. Finally, the utilized IRT data reduction technique is described in Section 4.3 followed by an error estimation procedure in Section 4.3.8.

4.2.1 Radiation heat transfer

In previous techniques, temperatures are solely measured by thermocouples which are fixed at a single-point.[7,8] (Han et al., 1985; Liou and Hwang, 1992) Hence, in terms of spatial resolution, these sensors are considered zero-dimensional. When considering a two-dimensional field which exhibits high spatial variations, the usage of thermocouples is principally unpractical. As a result, an infrared (IR) camera is used which constitutes a two-dimensional transducer (i.e. sensor), allowing for accurate measurements of surface temperature maps even in the presence of relatively high spatial gradients.[33] (Carlomagno and Cardone, 2010) The operational principle of the IR camera is based on the detection and acquisition of radiation, which makes IRT non-intrusive. As a formal background into IRT, the basic principles of radiation theory are explained in this section.

Black-body radiator Heat transfer by radiation is an energy transport mechanism that occurs in the form of electromagnetic waves. Through this heat transfer mode, energy can travel in vacuum and may be partially absorbed, reflected or transmitted by a body. The conservation of (radiation) energy requires that:

$$\alpha_\lambda + \rho_\lambda + \tau_\lambda = 1 \tag{4.10}$$

Where α_λ, ρ_λ and τ_λ are respectively called the *absorptivity*, *reflectivity* and *transmissivity* coefficients of a body (Figure 4.11). Later in this section, it is shown that these coefficients depend on both radiation wavelength (λ) and propagation direction (θ).

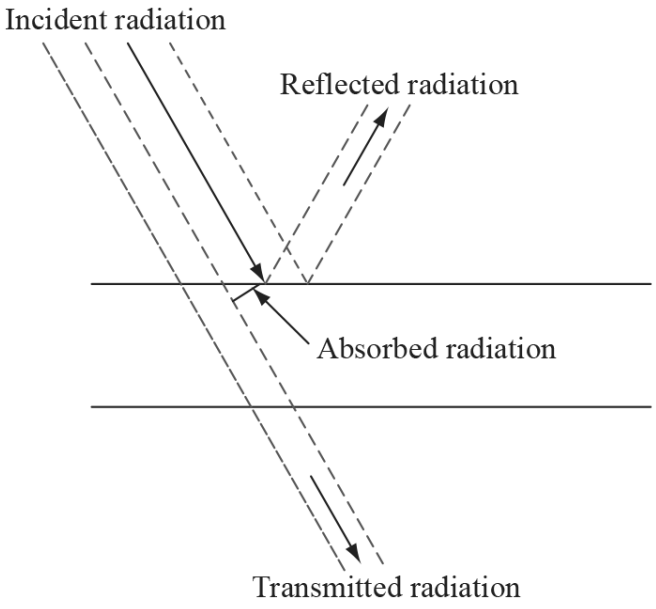

FIGURE 4.11: Illustration of incident, reflected and absorbed radiation in terms of total radiation properties.[63] (Kreith et al., 2012)

Radiation is emitted by all bodies at an absolute temperature above absolute zero, i.e. $T > 0$ K. For non-transparent bodies, this emittance is dependent on their surface properties only. A *blackbody* is a theoretical body which emits and absorbs the maximum possible amount of radiation at any given wavelength. This means that, in Equation 4.10, $\alpha_\lambda = 1$, $\rho_\lambda = 0$ and $\tau_\lambda = 0$. The spectral distribution of radiation energy (W/m^3 per λ) emitted by such a blackbody, is described by *Planck's law of radiation* as:

$$E_{b,\lambda} = \frac{C_1}{\lambda^5(e^{C_2/\lambda T_s}) - 1} \tag{4.11}$$

Where λ is the radiation wavelength (m), T_s the absolute surface temperature (K), and C_1 and C_2 the *first and second universal radiation constants*, respectively equal to 3.7418 $\times 10^{-6}$ Wm^2 and 1.4388 $\times 10^{-2}$ Km.[15] (Astarita and Carlomagno, 2012) From Equation 4.11, it can be concluded that the monochromatic, spectral hemispherical emissive radiation power $E_{b,\lambda}$ is directly correlated with its surface temperature and wavelength. This relation is visualized by the Figure 4.12, from which it is seen that the maximum value of $E_{b,\lambda}$ moves towards shorter wavelengths as the body temperature increases. Actually, the relation between the wavelength at which a blackbody emits its maximum spectral emissive power is a function of the absolute blackbody surface temperate, according to:

$$\lambda_{max} T_s = 2.898 \cdot 10^{-3}\ mK \tag{4.12}$$

Which is known as *Wien's displacement law*. The displacement law of Equation 4.12 is included in Figure 4.12 as the dotted line, which indeed intersects the emissive maxima at each indicated surface temperature T_s.

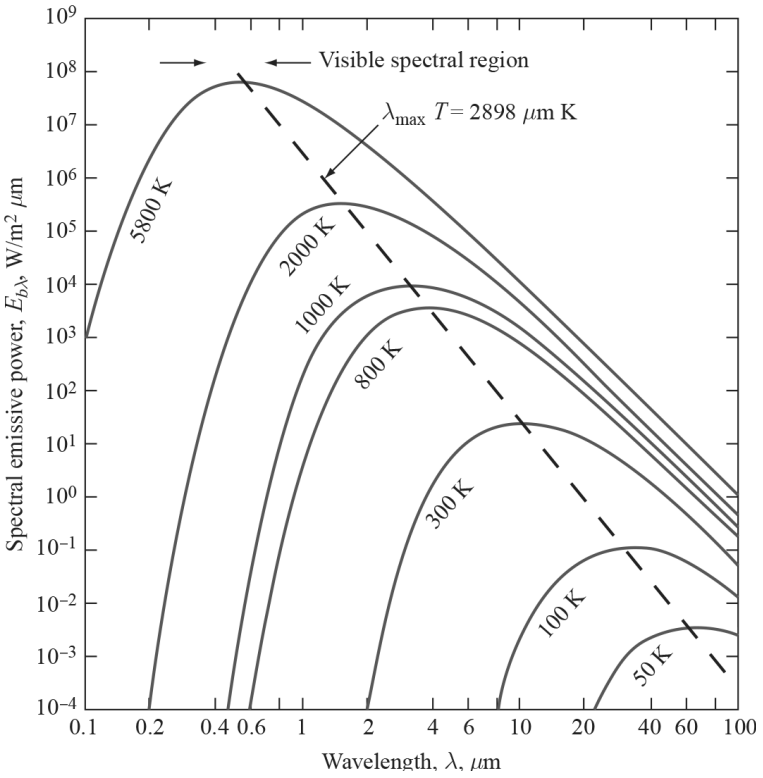

FIGURE 4.12: Black body spectral radiant emittance.[63]
(Kreith et al., 2012)

The total, multichromatic hemispherical emissive power E_b (W/m^2) is obtained by integrating Planck's law over all wavelengths, λ. The resulting law is known as the *Stefan-Boltzmann law*, given by:

$$E_b = \frac{q_{rad}}{A} = \sigma T_s^4 \tag{4.13}$$

Where σ is the *Stefan-Boltzmann constant*, equal to 5.6704 $\cdot 10^{-8}$ W/m^2K^4. When looking at Figure 4.12, E_b represents the total area under the Planck curve for each particular temperature. This, however, is not equal to the emissive power registered by an IR camera as its sensors capture only a limited band of the whole electromagnetic spectrum. This is explained in more detail in Section 4.2.2.

Gray-body radiator The laws described in the previous section are all based on the characteristics of black bodies, or *perfect radiators*. However, even if some surfaces may approach the behavior of a blackbody in certain spectral bands, real objects almost never comply with the characteristics of black bodies. The reason for this is that a real object generally emits only a fraction E_λ of the radiation emitted by the blackbody $E_{b,\lambda}$. The remaining thermal radiation energy is either absorbed (α_λ), reflected (ρ_λ) or transmitted (τ_λ) as described in Figure 4.11. Given a specific temperature, this fraction of spectral hemispherical emissive power, is given by:

$$\epsilon_\lambda = \frac{E_{o,\lambda}}{E_{b,\lambda}} \tag{4.14}$$

and is called the *spectral emissivity coefficient*, dependent on the radiation wavelength (λ). Bodies for which the emissivity is independent of λ are called *gray bodies*. This is considered a widely acceptable assumption as most radiators are not *selective* (Figure 4.13). Therefore, for gray bodies, it holds that $\epsilon_\lambda = \epsilon$ equal to a constant which is smaller than unity.

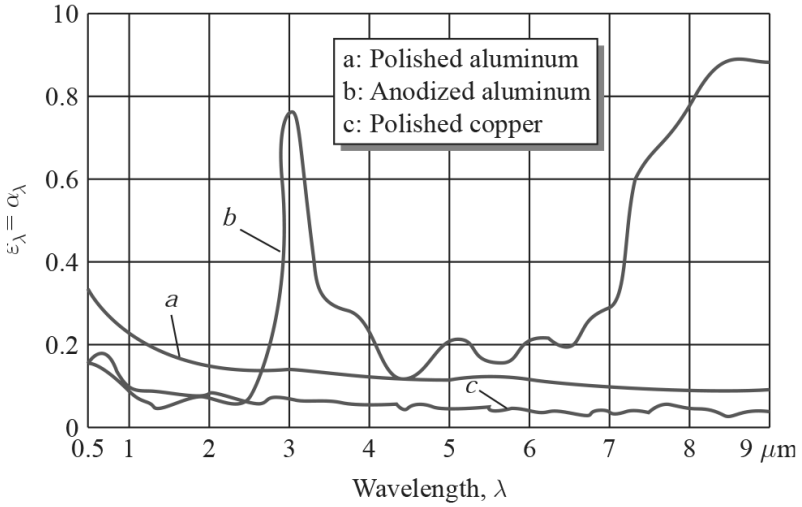

FIGURE 4.13: Variation of monochromatic absorptivity (or emissivity) with wavelength for three electrical conductors at room temperature.[63] (Kreith et al., 2012)

Considering that a gray body has a constant spectral emissivity (ϵ), its total emitted radiation can be correlated to the total radiation emitted by a blackbody (E_b). By integrating Equation 4.14 with respect to all wavelengths ($0 \leq \lambda \leq \infty$) such that ϵ = f(E_o,E_b) and substituting the Stefan-Boltzmann relation (Equation 4.13), it is found that:

$$E = \epsilon \sigma T_s^4 \tag{4.15}$$

According to *Kirchoff's law*, it holds that for any material the spectral emissivity coefficient (ϵ_λ) and spectral absorptivity coefficient (α_λ) are equal for any specified temperature and wavelength; $\epsilon_\lambda = \alpha_\lambda$. As a result, for non-transparent gray bodies, such as the PCB used for the current setup, Equation 4.10 becomes:

$$\epsilon + \rho = 1 \tag{4.16}$$

Therefore, materials with a low emissivity (i.e. metals, e_{cu} = 0.05) primarily reflect radiation which impinges their surface. These raw metals should thus be avoided for IRT purposes or treated by a thermally black paint or black soldering mask at the surface (i.e. treated copper, $e_{cu.tr} = 0.83$).[63] (Kreith et al., 2012)

By combining Equation 4.15 and Kirchoff's law for gray bodies (i.e. $\epsilon = \alpha$), the net radiation energy exchange between the surroundings and the gray body can be calculated. For a specified temperature, it holds that:

$$E_r = E_o - E_a = \epsilon_o \sigma (T_s^4 - T_a^4) \tag{4.17}$$

Where E_o corresponds to the radiation emitted by the surface as a result of T_s, and E_a is equal to the radiation emitted by the ambient due to T_a. However, as $\epsilon = \alpha$, the surface emissivity is equal to its absorptivity; making the absorbed radiation fraction equal to $\epsilon_o \sigma T_a^4$. Equation 4.17 is commonly assigned as a valid approximation for the total radiation energy of a surface, and is used during the data reduction method described in Section 4.3.

Real surface characteristics The method described in the previous section has shown that emissivity is a function of wavelength (Equation 4.14). In reality, however, the ϵ also depends on the surface temperature (T_s) and shape or inclination (θ) of the object itself. For

each type of material, both emissivity (ϵ) and absorptivity (α) are influenced by the surface temperature. The corresponding functions $\epsilon(T_s)$ and $\alpha(T_s)$ are material specific, some examples of which are shown in the following figures:

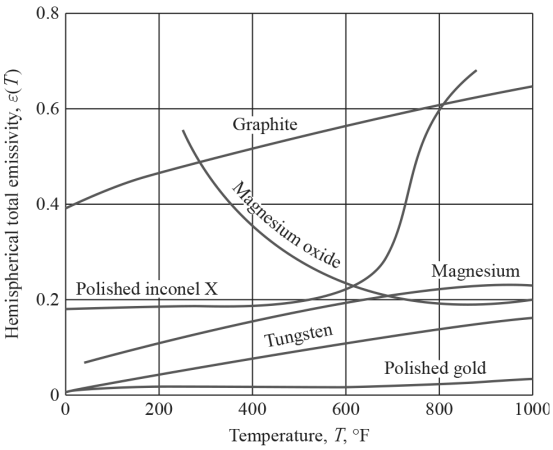

FIGURE 4.14: Effect of temperature on hemispherical total emissivity (ϵ) of several metals.[63] (Kreith et al., 2012)

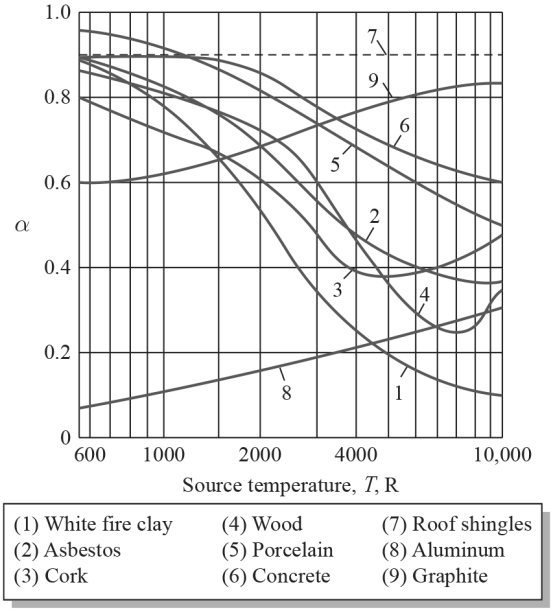

FIGURE 4.15: Variation of total absorptivity (α) with source temperature for multiple material types at room temperature.[63] (Kreith et al., 2012)

Where Figure 4.14 corresponds to the temperature variance of the emissivity of metals, and Figure 4.15 to the temperature dependent absorptivity of multiple types of materials. It can be concluded from Figure 4.14 that the total emissivity of electrical conductors increases with increasing temperature, whereas the one dielectric (i.e. magnesium oxide) displays the opposite trend. A similar observation is made for the absorptivity diagrams. Where the absorptivity of typically good thermal conductors, such as aluminum and concrete, increases with increasing surface temperature, whereas the $\alpha(T_s)$ for nonconductors exhibits the reversed trend.[66] (Sieber, 1939)

The emissivity relation of Equation 4.14 was based on non-directional radiation propagated normally from a surface. Due to an object's shape or surface roughness, real objects almost never emit radiation in an isotropic way.[67] (Schmidt and Eckert, 1935) The following polar plots illustrate the directional dependency of the emissivity coefficients:

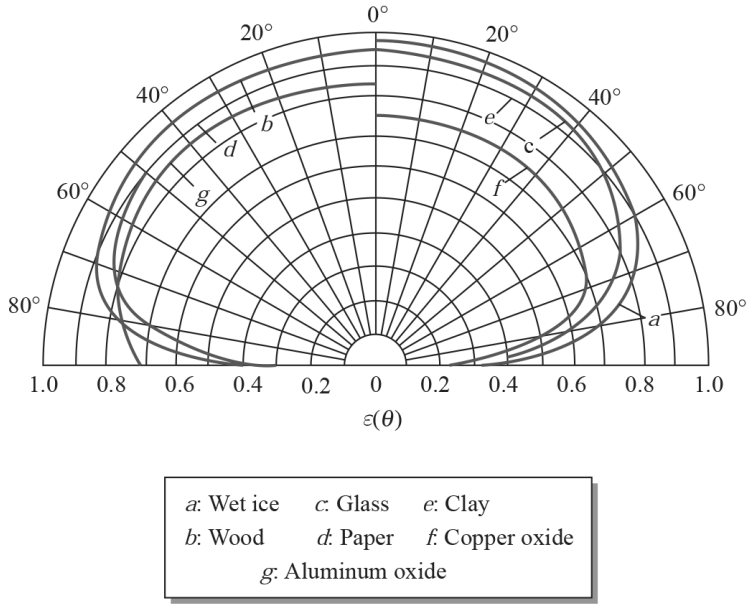

FIGURE 4.16: Variation of directional emissivity with emission angle for several electrical nonconductors.[63] (Kreith et al., 2012)

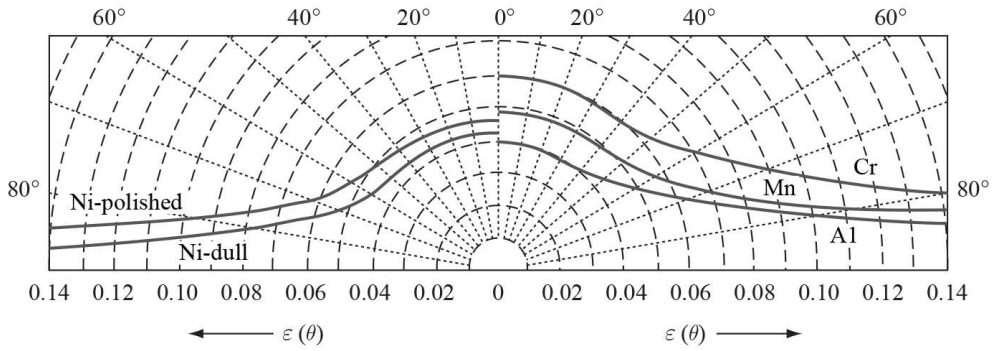

FIGURE 4.17: Variation of directional emissivity with emission angle for several metals.[63] (Kreith et al., 2012)

Where Figures 4.16 and 4.17 include respectively electrical non-conductors and conductors. In these figures, θ is defined as to the angle between the normal and the direction of the radiant beam emitted from the surface. It is seen that the emissivity of non-conductors such as wood, paper and oxide films decrease for an increasing viewing angle (θ), whereas for metals a completely opposite trend exists. Since infrared measurements are often performed with dielectric materials, positioned close to the normal (i.e. low θ), and an IR camera sensor, capturing a limited waveband, the emissivity of a viewed surface is often assumed constant and independent of θ (Figure 4.17). However, one has to keep in mind that with the requirement of larger θ's, careful calibration of ϵ should performed. In Section 4.2.5, it is seen that the IR camera is placed nearly normal to the surface of the test models (θ ~0°). As a result, it is safe to neglect the effects of radiative directionality.

Atmospheric transmittance When performing an actual measurement, an IR camera normally views the tested object through a medium (i.e. frequently air). As a result, the capturing of IR radiation is not only the influenced by real surface characteristics but also by the

ambient. Where a real surface affects the emissive properties, the surroundings affect the transmissivity of radiation. Previous relations were based on the assumption that emitted radiation can freely pass through the ambient. This, however, only holds for a vacuum. In reality, surrounding air will absorb and reflect fractions of emitted radiation.

The magnitude of atmospheric disturbances is influenced by multiple factors, such as: air temperature, air pressure, chemical composition of air, amount of particles in the air and the distance covered by the radiation. At standard atmospheric conditions (p = 1 *atm*, T = 298 K), most of these parameters become negligible. However, the two exceptions are 'the distance covered', and 'the presence of chemical components'. Under the assumption that a flow is not heavily contaminated, the reflectivity of the air can be set to zero ($\rho_{air} = 0$). Thus, Equation 4.10 for air becomes equal to:

$$\alpha_{air} + \tau_{air} = 1$$

The transmissivity of air (τ_{air}) is mostly influenced by the two chemical components, H_2O and CO_2, which both absorb energy at certain wavelengths of the infrared spectrum. The effects of wavelength dependent absorption gives rise to variations in the atmospheric transmissivity properties. In the following figure, the resulting transmissivity of air is indicated over a specific wave band spectrum:

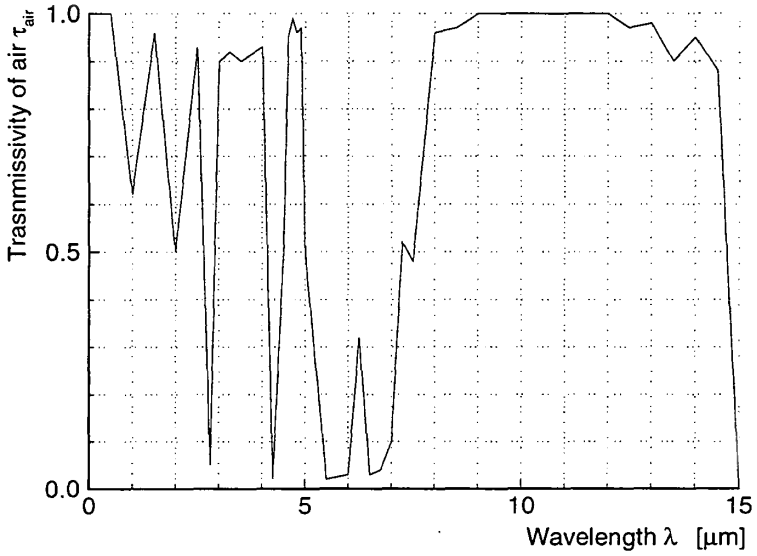

FIGURE 4.18: Transmissivity of air for different wavelengths.[68] (Mayer, 1996)

The spectral region up to the wavelength of ~5 μm is variantly transmissive due to the absorbing effect of CO_2. In turn, in between 5 – 8 μm, air becomes nearly opaque from the presence of water vapor (H_2O). The remaining regions of high transmissivity ($\tau_{air} \approx 1.0$) are known as *atmospheric windows*. Especially for measurements over long distances (> 10m), it is important to operate within these windows. As a result, most infrared sensors operate within two distinct spectral bands:

- Short wave band (SWB): 3 – 5 μm
- Long wave band (LWB): 7.5 – 13.5 μm

For a typical experimental setup, the distance covered by radiation is limited to a couple of meters. Therefore, the transmissivity effects are dominant in representing real-life applications. As a result, the choice of type IR sensor is mainly dependent on the encountered wavelengths (λ). In accordance with Wien's law (Equation 4.12), the wavelength of maximum emissive power (λ_{max}) is directly dependent on the surface temperature T_s. It turns out that for a typical temperature range of 293 – 323 K, maximum power is emitted at 9.0 $\leq \lambda_{max} \leq$ 9.9 μm. In correspondence with these wavelengths, most IR camera sensors capture radiation from within the LWB.[15] (Astarita and Carlomagno, 2012)

4.2.2 Data acquisition system

Compared to standard thermographic techniques, the use of an infrared camera as a temperature transducer in convective heat transfer measurement appears advantageous from several points of view. In fact, since an IR sensor is fully two dimensional (up to 1 M pixels), besides producing a whole temperature field, it permits an easier evaluation of errors due to lateral and longitudinal conduction. Further, it is non-intrusive (omitting the use of thermocouples interfering with the flow field), it has a high sensitivity (down to 20 mK) and low response time (down to 20 ms). As such, IR thermography (IRT) can be effectively employed to measure convective heat fluxes with both steady and transient techniques.[33] (Carlomagno and Cardone, 2010)

Equal to the PIV experiments (Section 3.4), it is decided to conduct two individual IRT campaigns. The *primary campaign* considers the quantitative investigation of the convective properties of complete surface area, whereas the *secondary* campaign is characterized as being more qualitative and focuses solely on the convective profiles within specific cavities. In both cases, the data acquisition system consists of an IR camera and a computer, equipped with the right software to visualize, record and store the radiative data (in DL). However, only the primary campaign incorporates the usage of 16 reference thermocouples, with a dedicated acquisition box (Figure 4.34). This is done to obtain a complete thermal view of the models, which optimizes the reliability of the data reduction. In addition to the setups, significant differences exist between the operation and accuracy of the utilized IR cameras themselves. In this section, the working principles, characteristics and operation of these IR cameras is briefly explained. For more information on the working principles of thermocouples, the reader is advised to study Appendix L.

Infrared camera

An infrared camera consists of four primary components, namely a lens, spectral filter, detector and electronics. The lens determines the optical path of the infrared acquisition device. In turn, the spectral filter selects the wavelength range and limits this to the IR wave band (IRWB). A detector converts the accumulated IR radiation into voltage signals, after which the electronics amplify, linearize and process these signals into a temperature fields.[33] (Carlomagno and Cardone, 2010)

Radiation detector The core of any IR camera system is the radiation detector, commonly known as an IR sensor. The most dominant approach for the detection of IR radiation is granted by *flux detectors*. These types of detectors integrate the optical signal over the complete viewing space or instantaneous field of view (IFOV), such that the response is a function of time. This *integration time* controls the time during which each pixel is exposed to radiation; effectively controlling the level of acquired radiation and thus the observable temperature range. Within this flux detector technology, two primary classes exist: (1) *thermal*

detectors, which are sensitive to the incident energy flux, and, (2) *quantum detectors*, whose sensitivity depends on the absorption of photons.



(A) CEDIP Titanium 530L IR camera.[69] (CEDIP, 2008)



(B) Optris PI 640 IR camera.[70] (Optris, 2015)

FIGURE 4.19: Infrared cameras used for respectively the primary and secondary IRT campaigns.

Currently, the most common type of thermal detector is the uncooled microbolometer, made of a metal compound or semiconductor material. Through the absorption of the IR energy flux, a variation in temperature occurs; affecting the local electric resistance (R_s) which is then directly related to a voltage signal (V_s). The microbolometer typically has a lower cost and broadband IR spectral response, but is less sensitive and quite slow ($\sim ms$) compared to quantum detectors. The latter type functions by measuring the direct excitation of its electrons due to incident photons, and relates this to conduction states (R_s). Quantum detectors have a low response time ($\sim \mu m$) and a higher sensitivity, which makes them most applicable for quantitative infrared thermography (QIRT) applications.

For the primary experimental campaign, the CEDIP Titanium 530L infrared (IR) camera is used (Figure 4.19a). This IR camera is categorized as an quantum detector, which exports either radiative intensities (DL) or self-calibrated temperatures (°C). The camera uses a focal plane array (FPA) sensor, consisting of 320 $\times$ 256 quantum detectors (i.e. pixels). These detectors are the type mercury cadmium telluride (HgCdTe or MCT) and have a spectral response of 7.7 – 9.3 μm (LWB). At full resolution, the maximum frame rate is 250 Hz. Since regular glass optics are opaque to radiation of the infrared wave band, this IR camera is equipped with a specialized CEDIP LW 25mm 2.0 Jade lens which has an average transmissivity of τ_{lens} ~0.96 [-]. A more elaborate list of specifications is provided in Table 4.2. For the technical drawings of both the IR camera and lens, the reader is referred to respectively Appendices D and E.

TABLE 4.2: Primary IRT campaign, system specifications.[69,71] (CEDIP, 2008)

Camera	CEDIP Titanium 530L	**Lens**	LW 25mm 2.0 Jade
Detector type	FPA	Focal length (f)	25 mm
Detector material	MCT	Aperture ($f_{\#}$)	2.0 [-]
Detectors	320 x 256 pixels	HFOV x VFOV	21.7 x 16.4 °
Detector size	30 x 30 μm	τ_{lens}	0.96 [-]
Spectral response	7.7 – 9.3 μm	Spectral band	7.7 – 9.3 μm
NETD	< 0.25 mK @ 298 K	Focus range	0.5 m – ∞

During the secondary campaign, the Optris PI-640 IR camera is used (Figure 4.19b). This camera is of the type microbolometer and distinguishes itself from the CEDIP camera by having twice its resolution (640 $\times$ 480 pixels), whilst having a third of its accuracy at 0.75 mK. It is this worsened accuracy in combination with the unavailability of tailored calibration, which causes this camera to be entitled mainly for qualitative purposes. The camera does conduct self-calibration, however, it is practically impossible for the user to verify or reverse engineer the utilized calibration curves. Thus, even though this camera is less laborious to use, it offers significantly lesser scientific applications. Nevertheless, its improved resolution allows it possibly obtain a more detailed view of the heat transfer phenomena. To even further improve upon the system resolution, this IR camera was equipped with a germanium zoom lens with a 41.5 *mm* focal length. The complete list of specification is provided in Table 4.3, whereas the technical drawings are provided in Appendix F.

TABLE 4.3: Secondary IRT campaign, system specifications.[72,70] (Optris, 2015)

Camera	Optris PI 640	**Lens**	Optris 15
Detector type	UFPA	Focal length (f)	41.5 mm
Detector material	SiGe	Aperture ($f_{\#}$)	2.0 [-]
Detectors	640 x 480 pixels	HFOV x VFOV	15 x 11 $^\circ$
Detector size	17 x 17 μm	τ_{lens}	0.92 [-]
Spectral response	7 – 13 μm	Spectral band	7 – 13 μm
NETD	0.75 mK @ 298 K	Focus range	0.55 m – ∞

System performance

The performance of an infrared camera is conventionally evaluated in terms of thermal resolution and spatial imaging resolution. The thermal resolution is characterized by the smallest detectable temperature difference (NETD), whereas the spatial resolution encompasses the smallest resolvable spatial features (Image resolution).

Noise equivalent temperature difference As any sensor, the quantum detector and microbolometer utilized within respectively the CEDIP or Optris IR camera contain some inherit noise. In turn, the presence of multiple electrical components near these sensors cause electrical fields to build up, which possibly contribute to the total sensor noise. The *noise equivalent temperature difference* (NETD) is the time averaged standard deviation over all pixels of an IR detector. The NETD thus represents the total noise of a sensor, expressed as an equivalent temperature difference in mK. The NETD of the CEDIP 530L is $\pm$ 25 mK, whereas the NETD of the Optris 640 PI is $\pm$ 75 mK. This means that any registered temperature signal is equal to respectively $T\pm$ 25 and $\pm$ 75 mK. As this property is independent of the measured temperature, one should be careful with the introduced errors at low T.

System resolution The capability of an IR system to distinct between surface temperatures of small objects is typically defined as the *instantaneous field of view* (IFOV). The IFOV is the ratio of detector pixel width (pitch) over the lens focal length (f). However, the IFOV only represents an ideal design parameter and does not fully describe the performance of the actual system. Instead, it is desired to base the spatial performance on the complete *system resolution*. This system resolution is defined by the number of IFOVs (pixels) that describe the complete field of view (FOV), i.e. (# pixels)/FOV. As a result, the complete system spatial resolution is found in terms of *pixels/mm* and encompasses all system characteristics.

As a result of the definition of the system resolution, its value is determined by both the IR camera characteristics, objective zoom and camera placement. In order to include each aspect, the pixels/*mm* are determined directly from the respective FOVs. In Figures 4.20 and 4.21, the Cedip camera placement and resulting FOV is shown. In turn, Figures 4.22 and 4.23 display the Optris camera placement and corresponding FOV.

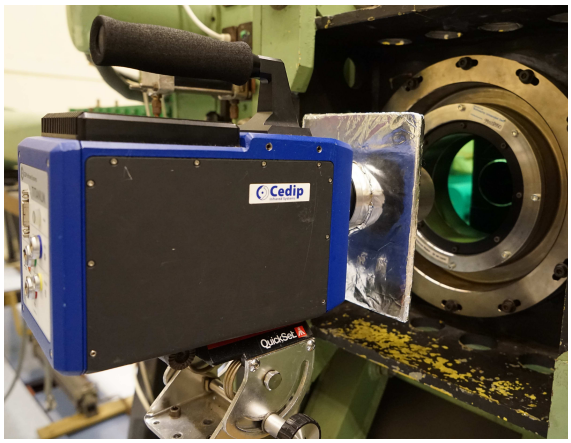

FIGURE 4.20: Cedip camera setup.

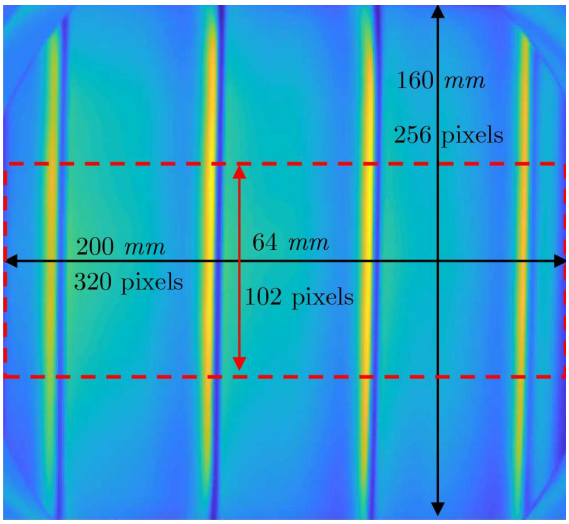

FIGURE 4.21: FOV primary campaign.

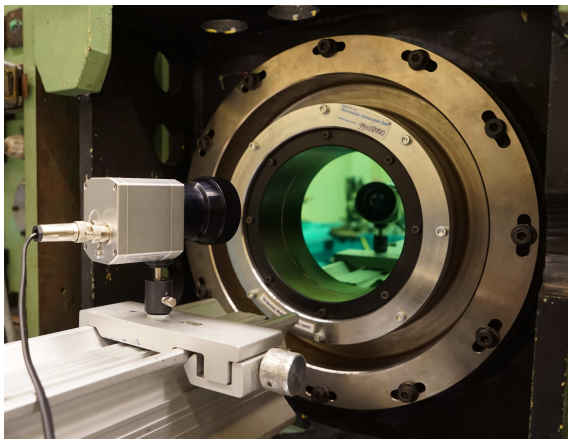

FIGURE 4.22: Optris camera setup.

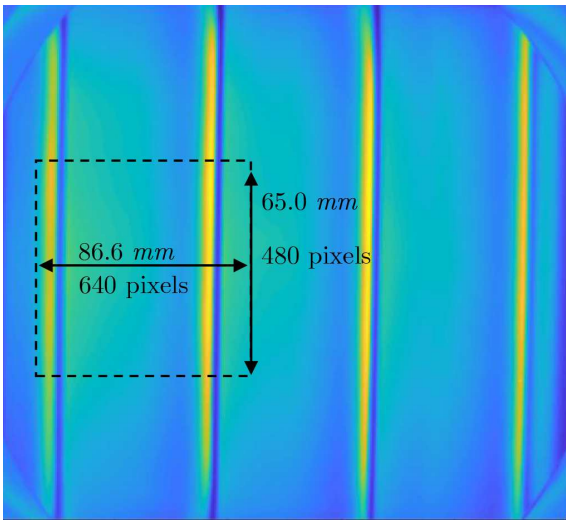

FIGURE 4.23: FOV secondary campaign.

The Cedip FOV resulting from the 25 *mm* wide angle lens and approximate distance of 0.5 *m*, is approximately 200 $\times$ 160 *mm*. With the sensor resolution of 320 $\times$ 256, an overall system resolution of 1.6 pixels/*mm* is found. Compared to the resolution seen for PIV at 30 pixels/*mm*, this system resolution seems quite limited. However, even for the smallest geometries approximately four measurement points are found per cavity (~6 *mm*). In comparison to previous research, the latter is known to be sufficient for QIRT.[10] (Aliaga et al., 1993) The red rectangle indicated in Figure 4.21 corresponds to the area used for data reduction, and is equal to approximately 320 $\times$ 102 pixels. The FOV of the secondary campaign is displayed as a fraction of the Cedip IR image (Figure 4.23). Form the black rectangle, it is seen that there is focused on the final cavity of this particular geometry. The resulting FOV has an dimension of 86.6 $\times$ 65 *mm*, at an average of 7.4 pixel/*mm*. Thus, an overall increase in system resolution of 4.6 times is found compared to the primary setup. The main aim of

this secondary campaign is to provide more detailed, qualitative information on the cavity profiles. Even though the sensitivity and accuracy of the Optris IR camera is significantly lower, this setup should verify the cavity profiles obtained during the primary campaign.

4.2.3 IR system operation

It is stated previously that two IRT campaigns are performed, where the *primary* is characterized by a quantitative approach (QIRT), and the *secondary* is associated as being qualitative (IRT). To accommodate these features, the operational characteristics of the IR camera are chosen to match these requirements. As such, the output of the Cedip IR camera is more controllable than the Optris camera by enabling the user to export the original radiation levels in DL (i.e. digital levels). This allows us to obtain a calibration curve which is in accordance with the current physical setup (Section 4.2.4) Even though the Optris camera conducts a self-calibration, the accuracy of this is set to at best approximate the current setup within a mere $\pm 2^{\circ}$ accuracy.[70] (Optris, 2015) It can thus be summarized that the Cedip camera is more applicable to scientific approaches, whereas the Optris camera is more a plug&play-type; sufficient to obtain quick, qualitative results. Due to this character, the Optris camera is used by simply plugging it into a dedicated computer and acquire images using the 'Optris PI Connect' software.[72] (Optris, 2015) The more elaborate camera operation, calibration and data acquisition for the Cedip camera is described in the following sections.

The complete primary QIRT system consists of the CEDIP 530L IR camera which is connected to a computer. In addition, 16 K-type thermocouples are placed on the rear and sides of the insulation (Appendix L). The temperatures of which are acquired using National Instruments NI 9214 acquisition and TB 9214 aggregate, isothermal terminal blocks. This NI acquisition system is controlled to a self-made LabView program, located on another assigned computer. The main software which enables the user to control the camera is called Altair (CEDIP, 2008), whose main functions are to control the:[73]

- Integration time: observable temperature range (K),
- Camera trigger: frequency (Hz),
- Recording of images: number of frames (#).

The camera's FPA sensor is made up of multiple, individual quantum detectors. As a result, each of the 320 x 256 detectors has its own characteristics, which makes them react differently to variations in radiation intensity. To correct for these responsive differences in radiation, a *non-uniformity correction* (NUC) is applied prior to conducting experiments. This NUC derives the average offset and gain values of each detector (i.e. pixel), after which both characteristics are set identical for the entire sensor. As a result, a homogeneous IR intensity response is created across all the pixels of the detector.

For the current system, such a NUC is performed by software called Cirrus, which is integrated with Altair.[74] (CEDIP, 2008) Two types of NUC are available, a one-point and a two-point NUC requiring respectively one and two blackbody references. For the NUC, such a blackbody is created by covering the camera lens with a hollow, black-coated aluminum cylinder (Appendix J.2). Consequently, only one homogeneous infrared FOV (blackbody) can be created; leading to the use of a one-point NUC. It is chosen to utilize a linear NUC, as a quadratic type does not improve the accuracy and increases computation time of the operation.

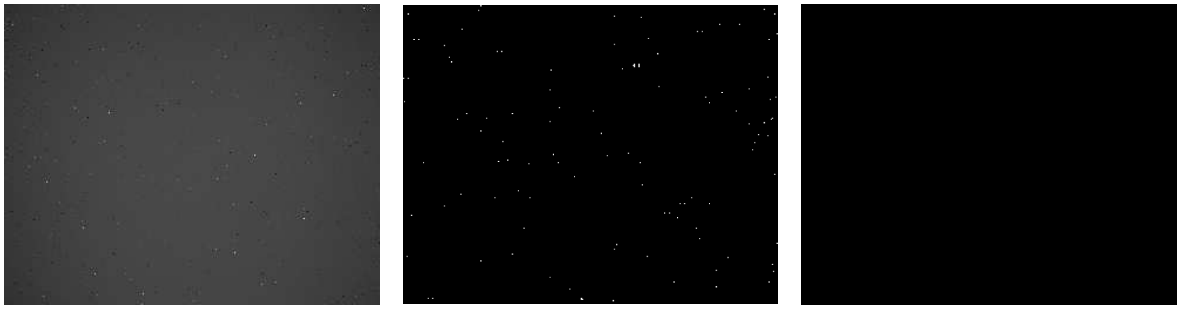

(A) Original blackbody (B) NUC, excluding BPR (C) NUC, including BPR

FIGURE 4.24: The effect of the non-uniformity correction on a blackbody, excl. or incl. bad pixel replacement.

If a 'pure NUC' would be applied, only the offset and gain of each sensor is set equal. However, during measurements, it can be seen that at some positions on the sensor, the gain and offset values are completely out of range in comparison to the rest of the sensor values. These sensors cannot be fixed through a NUC, and simply degrade the obtained images (Figure 4.24a). Sensors (i.e. pixels) for which this happens are inoperable and are called *bad pixels*. For the current thesis, a bad pixel is defined as a pixel for which the responsiveness or gain is $\pm 3\sigma$ from the mean gain of the complete sensor. To correct for each bad pixel, a *bad pixel replacement* (BPR) routine is used. Also this feature is incorporated in Cirrus, and works by replacing the IR radiance of each bad pixel by a weighted average of the surrounding pixels. Examples of the differences between the application of a NUC excluding and including BPR are shown in Figures 4.24b and 4.24c, respectively.

For each day of experiments, the NUC and BPR routine is conducted such to avoid the occurrence of disproportionate radiation response and the presence of bad pixels. After this, the Altair software is simply used to acquire the IR images in terms of DL. For each measurement, a recording frequency of 25 Hz is used at an integration time of 250 μs which results in a temperature range of -20 – 80°C. In the following section, the procedure is described through which calibration curve is obtained; allowing the conversion between $DL \rightarrow K$.

4.2.4 Calibration

As mentioned before, an IR camera effectively measures the emitted IR radiation levels of the object at which it is aimed. In the case of the CEDIP 530L IR camera, this radiation signature is converted into signal of digital levels, or DL. To accurately convert these DL into temperature (K), a calibration is performed at conditions which are representative for all (external) effects of the actual experimental setup. Once this is done, the emissivity (ϵ) of the object can be computed through the resulting calibration curve.

Blackbody For the calibration of the infrared camera, a blackbody is used. As mentioned in Section 4.2.1, a blackbody is an ideal radiator which has an emissivity (and absorptivity) equal to unity. Even though such a body is theoretical, its performance can be approached by an isothermal cavity with a small aperture (Figure 4.25a). For such a cavity, thermal radiation entering or produced inside undergoes several reflections before leaving the cavity. Upon each reflection, this radiation is partially absorbed by the inner surface. Therefore, exiting radiation intensities are degraded to an extremely small level whilst most radiation intensity is maintained inside the blackbody.[75] (Astarita and Carlomagno, 2013)

In Figure 4.25b, the technical drawing of the available blackbody is shown. This blackbody consists of a cylinder, which has an opening narrow enough for the blackbody function whilst providing sufficient optical access for the IR camera.[68] (Mayer, 1996) At the back of the cylinder, a cone is placed to prevent direct reflection of radiation out of the blackbody; maximizing contained reflections. The inside of the cylinder is painted black ($\epsilon \approx 0.9$) to increase the emissivity of the inner walls.

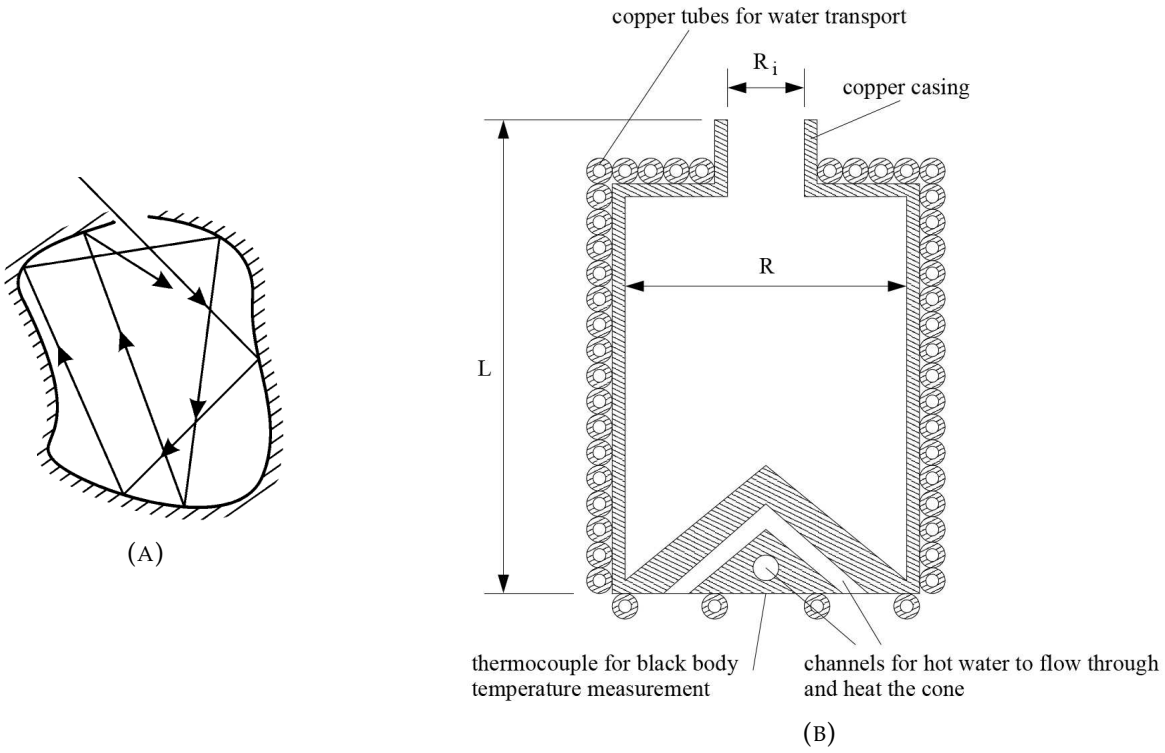

FIGURE 4.25: Representation of the blackbody concept (A) and technical drawing (B).[75,76] (Astarita and Carlomagno, 2013; Schrijer et al., 2003)

The blackbody is heated by circulating hot water through a hollow copper coil, which is tightly wound around the outside of the cylinder such to realize uniform heating. The entire device is insulated with glass wool to minimize heat loss and achieve thermal equilibrium. The temperature of the blackbody is monitored by three thermocouples placed at respectively the entrance, center cone and exit of the copper tubes. By comparing these temperatures, the blackbody can be checked for approximating an isothermal condition. According to Mayer (1996), an apparent emissivity of 0.999 [-] is achieved for this geometry.[68] As a result, it is safe to define a calibration curve of the following form:

$$T_o = \frac{B}{\ln(\frac{R}{I} + F)} \tag{4.18}$$

Which is based on Planck's law of radiation for blackbodies with ϵ = 1.0 [-] (Equation 4.11). The constants B, R and F in Equation 4.18 correspond to respectively the scanner calibration factor, shape factor and response factor.

Calibration In order to produce a calibration curve which accurately represents the relation between captured IR camera radiation levels (DL) and temperature (T), the following calibration setup is used:

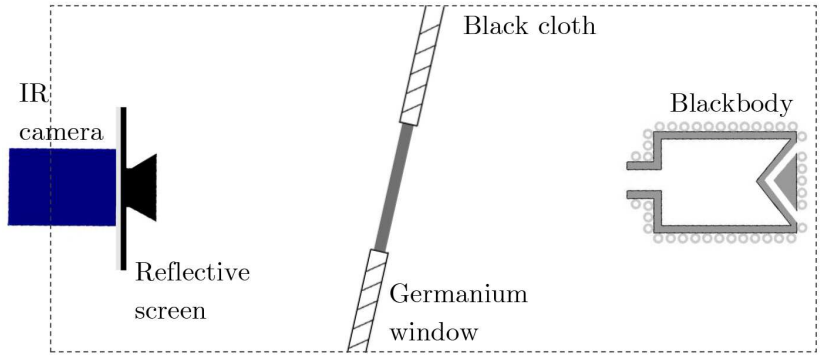

FIGURE 4.26: Setup for the calibration measurements.

Which consists of the IR camera, germanium window and blackbody. To avoid interference of unwanted radiation from the environment, the entire setup is covered by thick, black cloth. As regular glass is opaque to IR radiation ($\tau_{og} \approx 0.2$), a coated germanium window ($\tau_g \approx 0.96$) is used to allow IR optical access during the IRT experiments.[63] (Kreith, 2012) To simulate this testing environment, the Cedip IR camera monitors the radiation emitted by the blackbody through the germanium window. This way, the reduced transmissivity due to the germanium window is taken into account during the calibration. To avoid the reflection of the camera itself from interfering with the calibration (i.e. *Narcissus effect*), the window is placed under an angle (~15°) with respect to the IR camera and blackbody aperture. In addition, a reflective screen is placed between the camera and window to reduce the camera's reflective radiation intensity (Figure 4.19a).

Heated water is delivered to the blackbody by a Tamson TLC2 thermal bath, which is set to specific temperatures to accommodate the calibration curve. Each point of the calibration curve is defined by simulatenously logging the temperatures of the blackbody and digital level of the blackbody aperture. The temperature is defined as the average T registered by entrance and exit thermocouples, which on average varied by ~0.49°C (Appendix P). The digital level is given by the mean DL of an area within the black body aperture, captured by the IR camera (Figure 4.27). To reduce the signal noise of calibration, the average T and DL are taken over respectively 25 temperature logs or image frames once the blackbody reaches a steady-state; typically ~10 min between set points. In order to maintain equivalence between the calibration and the experimental setup, the same NI acquisition and terminal blocks are used for both procedures.

Using the one-dimensional analysis, it is estimated that surface steady state temperatures may vary between 10 – 70°C for respectively (re)attached and separated flows (Section 4.1.1). In turn, for the calibration of the camera, it is chosen to extend this temperature region from 0 – 85°C. This redundancy is created to improve the accuracy of the IR measurements, once temperatures outside the original bounds are found. The calibration procedure is conducted twice; once where the thermal bath is set from 0 – 85°C, the other from 85 – 0°C both using increments of 5°C per set point. The latter is done to identify the possible influence of the camera's operating temperature on the measurements. It was observed that for both calibrations, the camera warmed up from approximately 20°C (ambient temperature) to 31.8°C. However, the insignificant differences between calibration values ($\Delta DL < 0.1\%$) proved

no noticeable effect of the IR camera temperature on the calibration curves. The resulting calibration curve is displayed in Figure 4.28.

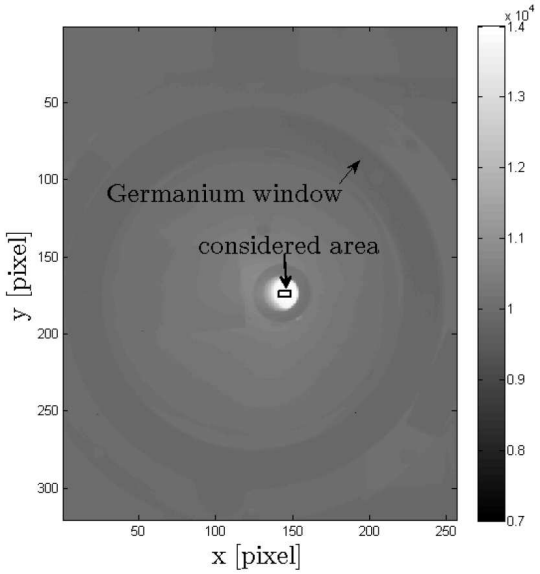

FIGURE 4.27: Recorded image of the blackbody during calibration process.

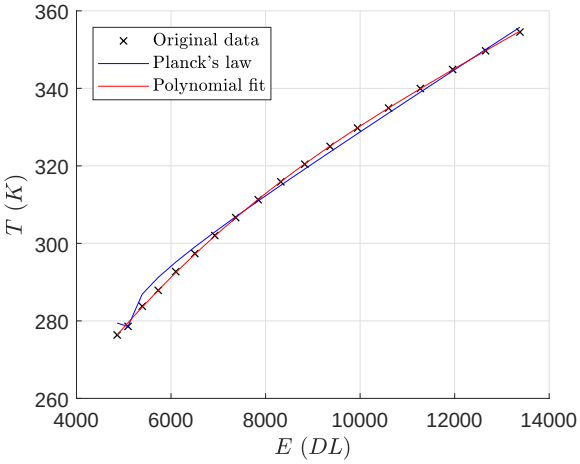

FIGURE 4.28: Calibration curve, including Plank's law fit and optimized fit.

Where the raw calibration data and two calibration curve fit types are shown; respectively through Planck's law (Equation 4.18) and an optimized polynomial fit. The value of the coefficients of Planck's law are found through a MatLab-based minimization routine, and are equal to B = -39.5092, R = -5085.9 and F = 1.012. The same routine is used for the polynomial fit, which is seen to approximate the raw data more closely near the lower portion of the temperature range. Therefore, it is chosen to use the latter for the post-processing routine.

Emissivity estimation real body Unlike the blackbody used during calibration, the surface of the test plates does not behave like a perfect radiator. As a result, only a fraction of its total radiation is emitted and $\epsilon_{model} < 1.0$ [-]. As the PCB surface consist of coated copper, it can be assumed to operate as a gray body; implying that ϵ_{model} becomes equal to a constant ≤ 1 (Section 4.2.1). Nevertheless, its exact value should still be computed.

The radiation measured by the camera (I_{meas}) consists of the radiation emitted by the object (I_o), radiation reflected by the ambient (I_{amb}) and radiation transmitted through the atmosphere (I_{atm}). The corresponding equation is given by:

$$I_{meas} = \tau_{atm}\epsilon I_o + \tau_{atm}(1-\epsilon)I_{amb} + (1-\tau_{atm})I_{atm} \tag{4.19}$$

Where I_{meas}, I_o, I_{amb} and I_{atm} are radiation intensities in DL and τ_{atm} is equal to the atmospheric transmissivity. Since the CEDIP 530L IR camera captures radiation from the LWB, τ_{atm} can be assumed equal to unity (Figure 4.18). As a result, Equation 4.19 is simplified to:

$$\epsilon = \frac{I_{meas} - I_{amb}}{I_o - I_{amb}} \tag{4.20}$$

Thus, Equation 4.20 shows that the test plate emissivity, ϵ_{model} is determined by the radiative intensities of respectively the total measured (I_{meas}), the ambient (I_{amb}) and object's digital levels (I_o). The latter two are obtained by measuring the ambient and surface temperatures in K, and plugging their values into the optimized calibration curve (Figure 4.28).

The setup used for the emissivity computation is equal to that of the calibration, where the blackbody is replaced by a test plate (Figure 4.26). The temperature of the surface and the ambient are obtained by K-type thermocouples, whereas the IR camera directly measures the radiation emitted by the surface surrounding this thermocouple (Figure 4.29).

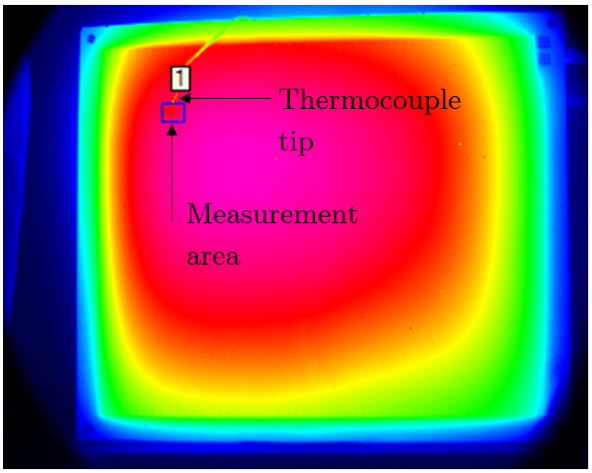

FIGURE 4.29: Recorded image of test plate emissivity computation.

This process is repeated at several surface temperatures, which are regulated by varying the power onto the PCB from 10 – 30 W. By computing this emissivity at different surface temperatures, the error bounds of ϵ_{model} can be determined. Even though ϵ is a material property, independent of surface temperature, some inherit uncertainty is expected. This variance in emissivity with respect to surface temperature is given in the following figure:

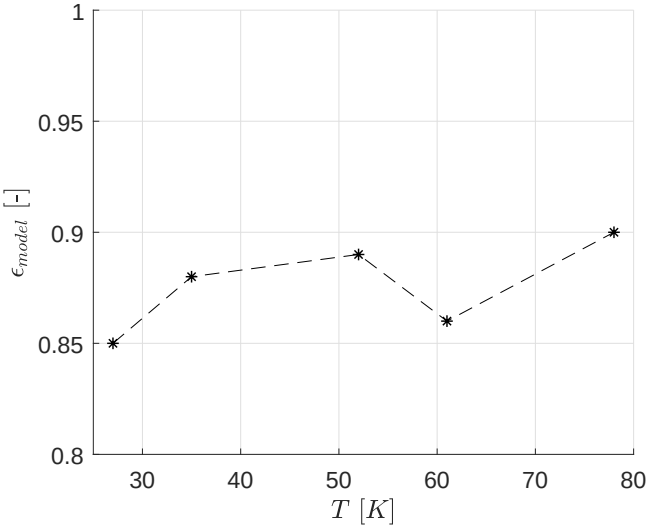

FIGURE 4.30: Emissivity variation with surface temperature.

From this, the mean ϵ_{model} is derived to be equal to 0.88 [-] which is slightly more than regularly coated copper, ϵ_{cu} = 0.82 [-]. In turn, it is seen that the maximum difference with the mean is approximately 2.9%. This is a reasonable estimate for such a substantial temperature range and allows for the assumption of being a gray body. By this assumption, the actual surface temperature T is estimated by multiplying the optimized calibration curve (Figure 4.28) with ϵ_{model}. As seen in Section 4.3, this fact is used during the data reduction.

4.2.5 Experimental setup and operation

Once the test plate assembly, cavity door mounting and calibration procedures were completed, the complete QIRT experimental setup was constructed. The exact layout of this setup is given by the schematic in Figure 4.31, whereas real-life representations of the setup are shown in Figures 4.34 and 4.35.

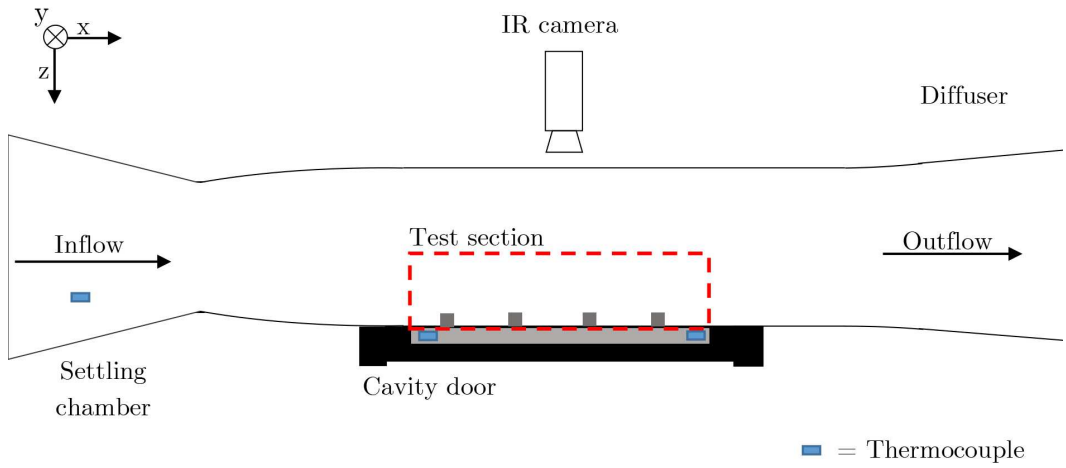

FIGURE 4.31: Schematic representation of the IRT setup at the ST-15.

Description of setup The schematic shown in Figure 4.31 indicates the upper view of the IRT setup, where the IR camera is aimed nearly perpendicular to the germanium window and test plate surface. In reality, though, the IR camera is covered by the black cloth and anti-reflective screens such to mitigate ambient interference (Figure 4.31). For the primary campaign, a total of 17 thermocouples were used; 16 K-type which function as reference over the rear and sides of the insulation (Section 4.3) whilst one J-type is used to determine the transient development of the total temperature in the settling chamber (T_0). The temperature of the reference thermocouples are acquired through a dedicated, multi-channel National instruments NI-9124 acquisition and TB-9214 isothermal terminal blocks. By limitation of the number of channels, the settling chamber thermocouple was connected to a separate Newport 202A-JC2 thermocouple meter which converts the temperature into a digital signal. The resulting voltage signal was in turn assessed by a NI-9381 voltage meter, which is inserted to the same NI acquisition tray as the NI-9124 block (Figure 4.32).

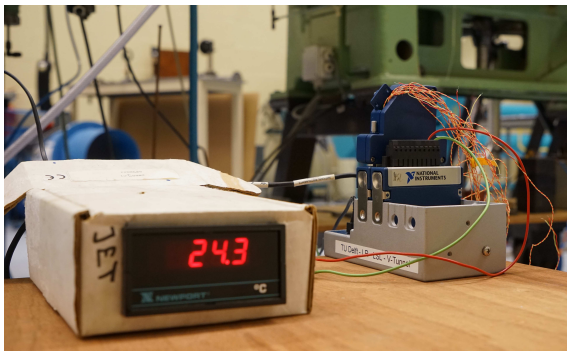

FIGURE 4.32: Thermocouple acquisition tray, incl. Newport controller.

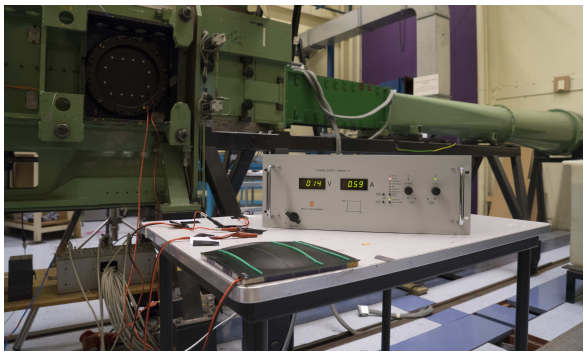

FIGURE 4.33: Delta Electronika SM600-10 power supply.

As a result, all thermocouples are connected to the same NI acquisition tray which is controlled from a single LabView program. Through this program, the acquisition box was set

to a *high accuracy mode* which limited the acquisition frequency to 2 *Hz* whilst obtaining an average accuracy of 0.365°C. As the primary goal of this setup is to offer quantitative insights, this improved accuracy is favorable to a higher recording frequency of ~10 *Hz*.

The electric power is delivered to the PCBs by a Delta-Electronika SM600-10 laboratory power supply (Figure 4.33), which is capable of delivering $600V$ and $10A$. Prior to each wind tunnel measurement, the desired current output is set by using a spare model as reference. Once the flow conditions of the wind tunnel test section have stabilized (± 5 sec), the power supply is switched-on using an interlock connector located inside the control room (Figure 4.34). Then, right before the end of the experiment, the power supply is switched-off prior to ceasing the wind tunnel flow; preventing the model from overheating.

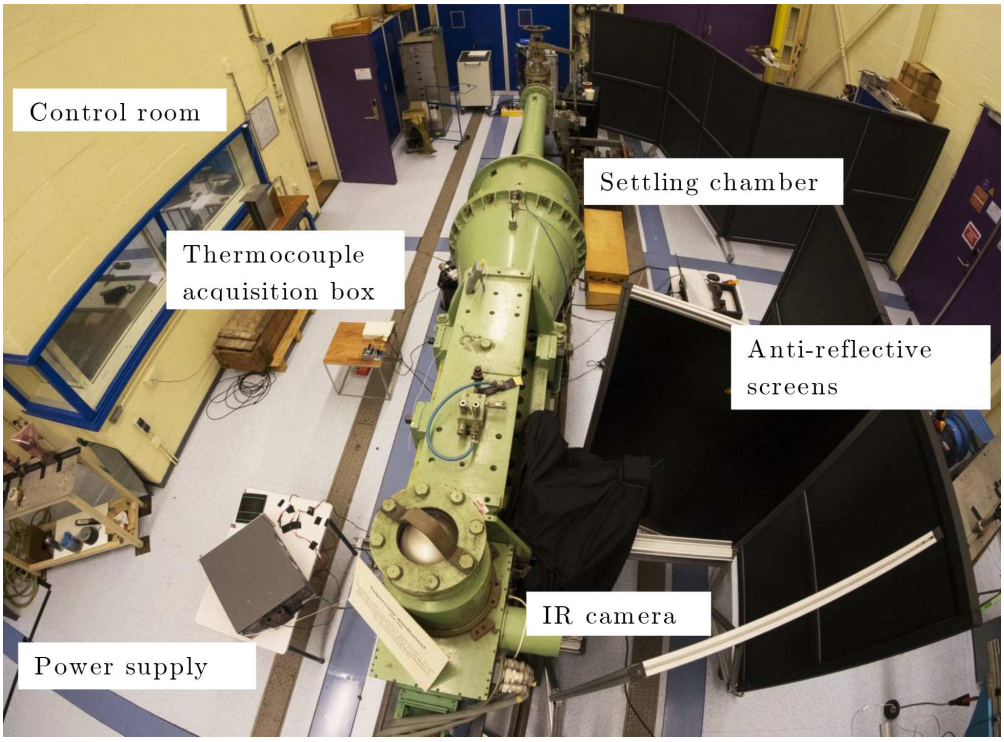

FIGURE 4.34: Upper view of the entire QIRT setup.

Both primary and secondary campaigns utilized the experimental setup depicted in Figures 4.31 and 4.34. The sole differences lie in the usage of the type of IR camera, and inclusion of the reference thermocouples (Section 4.2.2).

Initial operations The main uncertainty revolving around the usage of the QIRT experimental setup was to obtain a steady thermal state. Therefore, during the initial operations, some investigations were required as to which power levels would result in the desired steady-state conditions. These conditions were based on the reference flat plate model, which should obtain an appropriate temperature contrast, $\Delta T_{con} \geq 10\ K$ within a steady-state time, $t_{ss} \leq 50$ sec. The initial estimate for the necessary power levels, $q_{el.est}$ was found by the preliminary, semi-infinite solid analysis discussed in Section 4.1.1. The resulting $q_{el.est}$ was found equal to 742.9 W, however for safety, the starting electrical current level was limited to 2.63 A; providing 156.3 W of power ($q_{el.sft}$). As expected, this initial power setting proved to be too low for reaching a steady thermal condition. During measurements, the effect of which was shown by a continuous decline in surface temperatures whilst displaying no sign of leveling-out or stabilizing. To counteract this, small increments were made

to the output of the laboratory power supply. The latter was conducted up to the point where a steady-state was reached sufficiently fast and provided a relatively high temperature contrast. This influx point from continuous cooling to stable heating was found to be at approximately +225% of the limited flat plate estimate, $q_{el.sft}$; equal to 507.9 W. It is the latter value which is used as a starting point for all test plates ($q_{el.base}$) and is obtained by tailoring the current output, I to the base resistivity, R_0.

By later analysis, it was found that the flat plates operating at this minimal $q_{el.base}$ obtained a steady state within an average t_{ss} of 23 seconds whilst having an estimated ΔT_{con} of approximately 37.3 K. It is observed that these characteristics are not too far from the previously estimated t_{ss} of 27 seconds and ΔT_{con} of 35.6 K. However, the minimal required $q_{el.base}$ is significantly lower than the previously estimated $q_{el.est}$ at 742.9 W. This difference can be explained by the lower average convective heat transfer coefficient, h of 510.1 W/m^2K obtained by the flat plate measurements (Appendix Q). As this measured h is only 65% of the Dittus-Boelter estimate and ΔT_{con} is relatively similar, a lower convective heat transfer (q_{conv}) develops. This q_{conv} can be estimated by $\Delta T_{con} \times h$, which is found to be equal to 2.91×10^4 and 1.90×10^4 W/m^2 for respectively the 1D estimate and flat plate measurement. In correspondence, the total required q_{el} to counteract the convection logically becomes smaller as well. This discrepancy in power set points is expected to be caused by an error in the simplified h computation (Section 4.3.5). Most likely, the estimated Reynolds number was underestimated for the Dittus-Boelter relation. With the freestream conditions known, Re is estimated to be 1.6 $\times 10^8$; providing the same flat plate h ($\pm$ 5%).

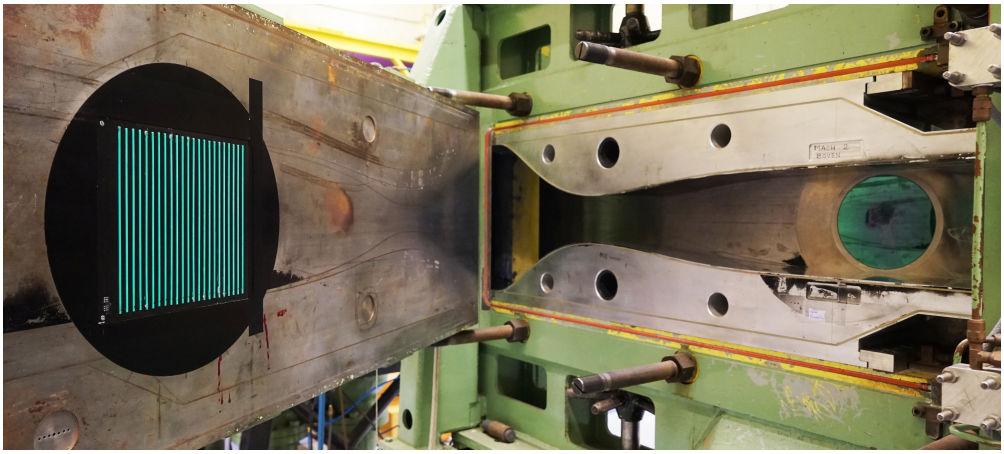

FIGURE 4.35: Heated model setup at ST-15 wind tunnel.

With the correct $q_{el.base}$ defined, it is possible to determine the exact required power output settings for each QIRT measurement. These settings are defined by the respective base resistivities, R_0 of each of the test plates. By the etching process of the PCBs, local discrepancies in copper thickness are formed. As a result, quite substantial differences in R_0 exist between the PCBs used to construct the test models (Appendix N). Therefore, by knowing the exact resistivities specific to each test plate, the required amperage output, I can be computed. It is decided to conduct three measurements on each test plate, starting at the $q_{el.base}$ (i.e. +225%). In turn, depending on the magnitude resulting surface temperatures, two consecutive measurements are conducted at power level increments of respectively 5, 10 or 12.5%.

During the experimental campaigns, a lot of experience was gained in terms of wind tunnel operation for QIRT. The final checklist used to properly conduct an experiment is indicated in Appendix M. In turn, a complete list of wind tunnel runs and adjoining (power supply)

settings is provided in Appendix G. It can be seen that mostly the same power levels are used, meaning that the emerging flow features hardly affected the steady-state capabilities of the QIRT setup. The remaining aspects of the QIRT operation sequence are discussed in relation to the data reduction procedure, provided in the following section.

4.3 Data reduction procedure

The goal of conducting QIRT is to accurately quantify the convective heat transfer properties of each ribbed geometry. Various data reduction techniques are available through which the convective heat flux is derived from measured time-transient temperature distributions. Two main types can be distinguished, based on respectively unsteady, transient and steady heat transfer conditions.

Transient heat transfer According to Scott and Walker (1998), data reduction techniques for unsteady or transient heat transfer can be grouped in three classes.[77] Practically though, each of these solution classes revolves around solving a particular form of the heat equation. The complete, transient, three-dimensional heat equation is given by:

$$\frac{\partial T}{\partial t} = \frac{1}{\alpha}\left(\frac{\partial^2 T}{\partial x^2} + \frac{\partial^2 T}{\partial y^2} + \frac{\partial^2 T}{\partial z^2}\right) \tag{4.21}$$

Where α is the *thermal diffusivity* (Equation 4.5) and $T(x, y, z, t)$ corresponds to the temperature variable within three-dimensional space and time. Depending on the physical problem which is to be approached, appropriate assumptions are applied to Equation 4.21 to accommodate the situation. Three classes of solution types are identified. Class 1 methods solve the unsteady one-dimensional (1D) heat conduction equation in closed form, which allows the derivation of an analytical solution for the convective heat flux (q_{conv}) as function of the surface temperature (Section 4.1.1). Well-known examples of this type of method are the approaches from Liepmann et al. (1962) and Kendall et al (1967).[78,79] Although robust and fast, these approaches assume the physical problem to be a 1D semi-infinite slab with constant material properties along two dimensions. As a result, it is not possible to take non-uniform thicknesses, varying material properties (i.e. $\alpha(x, y, z) = \alpha$) nor the effect of lateral conduction into account. Class 2 methods are performed through the computation of convective heat fluxes from a direct numerical solution of the unsteady two- (2D) or three-dimensional (3D) heat conduction equation on a discretized model of the wind tunnel test plate. Through the possibility of varying the model's boundary conditions, a class 2 method typically is more flexible. Finally, class 3 methods solve the full-inverse problem, usually via an adjoint-type solution (Ozisik and Necat, 2000). Such a solution method is highly computationally intensive, but does inherently provide the sensitivities of the solution.[80]

Steady heat transfer The previously mentioned classes revolve around solving the single- or multidimensional, transient representation of the heat equation. In the steady case, it can be assumed that the (surface) temperature of the wind tunnel model becomes invariant. As a result, $\partial T/\partial t$ = 0 meaning that Equation 4.21 becomes equal to:

$$\frac{1}{\alpha}\left(\frac{\partial^2 T}{\partial x^2} + \frac{\partial^2 T}{\partial y^2} + \frac{\partial^2 T}{\partial z^2}\right) = 0 \tag{4.22}$$

For which the temperature variable T consequently is solely dependent on the physical dimensions x, y and z. Therefore, with $T = T(x, y, z)$, the time-independent thermal energy balance holds for the wind tunnel model, as:

$$q_{in} = q_{conv} + q_{cond} + q_{rad} \tag{4.23}$$

Where q_{in} is the input heat flux into the test model (i.e. q_{el}), and q_{conv}, q_{cond} and q_{rad} represent respectively the convective, conductive and radiated heat flux out of the test model. The current data reduction technique revolves around solving the local convective heat transfer properties ($q_{conv}(x, y)$). By rewriting Equation 4.23, and substituting the definition of the convective heat transfer (Equation 2.12). It is found that the *convective heat transfer coefficient* (h) can be directly solved through the energy balance with:

$$h = \frac{q_{el} - q_{cond} - q_{rad}}{(T - T_{aw})} \tag{4.24}$$

Where $h = h(x, y)$, $T(x, y)$ is the surface temperature and T_{aw} is the adiabatic wall temperature. Finally, through the computation of the heat transfer coefficient h, the Stanton number (St) of each configuration is computed using Equation 2.11. It is thus seen that the primary convective output $h(x, y)$ is directly solvable provided each heat flux term is known.

4.3.1 Overview data reduction routine

The self-made data reduction program represents a steady-state approach in which multiple input sources are used to finally obtain the convective heat flux (Equation 4.24). The flow chart of the complete reduction routine is presented in the following figure:

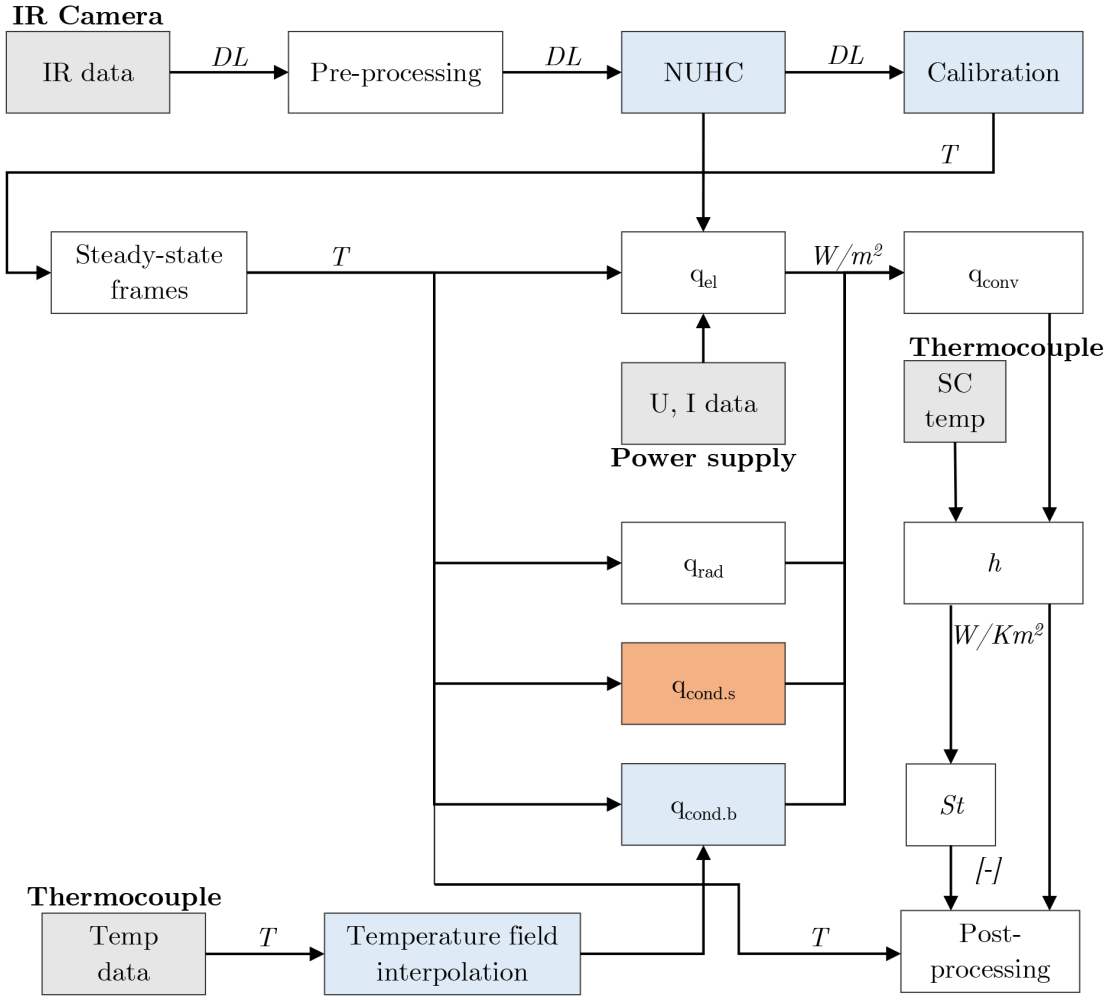

FIGURE 4.36: Flowchart of IRT data reduction routine.

Where each gray box indicates a specific input obtained from one of the measurement sources, and a white box displays a process or computation. The arrows in Figure 4.36 represent the interrelations between each component of the reduction program, where the unit of each input is indicated on top. It has to be noted that the exact working of the program is mostly equal for both *primary* and *secondary* campaign. However, due to the qualitative character of the secondary campaign, the NUHC, Calibration and $q_{cond.b}$ are discarded. As a result, the programming blocks specific to the primary campaign are indicated with blue. Even though originally considered, it is decided to exclude the $q_{cond.s}$ computation from the analysis (orange box). The exact reasoning behind this is provided in Section 4.3.7. The following explanation considers the primary campaign.

The data reduction routine is programmed into a MatLab function, which roughly works as follows. The raw infrared images in *DL* from the Cedip IR camera are imported, and are pre-processed to solely resemble the PCB's heated, copper area (Figure 4.2). For each wind tunnel run, the following infrared measurements are conducted:

1. Unheated, empty measurement (UEM): mitigate camera reflection.
2. Heated, empty measurement (HEM): non-uniform heating correction (NUHC).
3. Wind tunnel measurement (WTM): regular experimental conditions.

Where, per test case, the WTM is conducted at three distinct power levels in order to quantify the repeatability and sensitivity of the measurement technique (Section 5.2.1). The first two measurements are conducted prior to the WTMs, and are performed only once to quantify respectively the camera and PCB heating signatures. Once the pre-processing is done, the NUHC is computed. This correction matrix is then applied to the temperature fields of each WTM frame. In turn, these corrected WTM frames are converted from DL to T through the optimized calibration curve (Figure 4.28). By analyzing the transient temperature variations of these consecutive frames in T, those frames which are at steady-state are maintained whilst remaining frames are discarded. The resulting steady-state frames are used for the computation of the three heat flux terms q_{el}, q_{rad}, q_{cond}, where the conductive heat flux is subdivided in a surface and body term; respectively $q_{cond.s}$ and $q_{cond.b}$. It is seen that additional input of the power supply settings ($U(V)$, $I(A)$) and reference thermocouples are used for the computation of respectively, electric heat flux and conductive heat transfer into the body. By combining all heat flux terms, the convective heat flux q_{conv} is obtained (Equation 4.24). This q_{conv} is then converted to the convective heat transfer coefficient (h) and Stanton number (St). To this end, the temperature in the settling chamber (SC) is used to accurately estimate the value for the adiabatic wall temperature (Equation 4.41). Finally, through a post-processing routine, the h, St and T fields are time-averaged over 50 steady-state frames (Section 4.3.6). By then performing a spatial-averaging routine the h-, St- and T-profiles are formed which are either limited to a single cavity or the whole FOV.

In the following sections, more precise explanations on the functioning of each block of the MatLab routine are provided. It is noted though that primarily those features are touched upon which are unique to the current data reduction routine.

4.3.2 Pre-processing

Prior to converting the WTM in DL to K, a pre-treatment is applied to the raw IR camera data. It is decided to first subtract the unheated empty measurements (UEM) from the heated empty measurements (HEM) and the wind tunnel measurements (WTM) such to

obtain IR images without camera reflection. The latter is performed as the relatively large FOV requires the IR camera to stand close to the window, under a nearly normal angle (i.e. $\theta = 0°$, Figure 4.20). Therefore, the reflections are quite severe and should be accounted for.

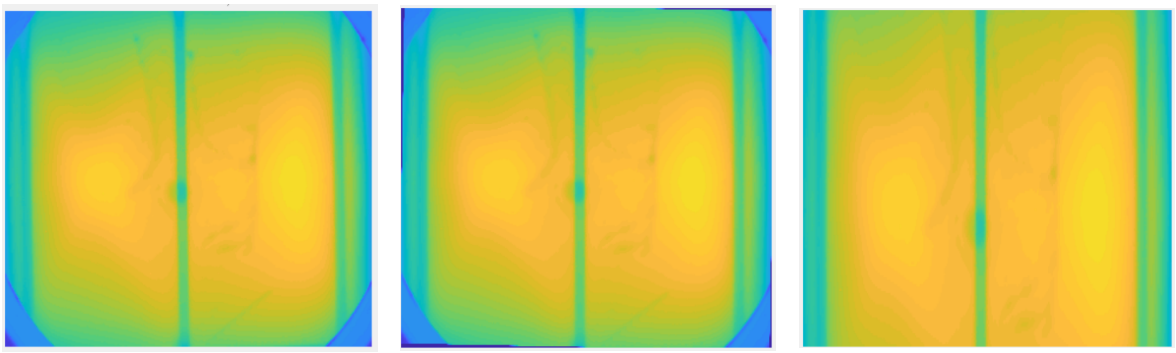

(A) BPR treated figure. (B) Rotated IR image. (C) Limited to copper area.

FIGURE 4.37: Primary actions performed during the pre-processing routine.

Even though a bad-pixel replacement routine was also applied to the acquisition settings using Cirrus, still some discrepancies showed in the images. Therefore, once the subtractions are completed, a self-made bad-pixel replacement function is conducted (Section 4.2.3). After this, the IR images are rotated with respect to their center by using a two-dimensional rotation matrix. The angle of rotation is arbitrary and can be selected by the user. Finally, the fully-treated IR images are limited to the PCB area.

The primary components of the image pre-treatments are indicated in Figures 4.37a – 4.37c. For the remainder of the data reduction routine, only the data limited to the PCB region is considered. As a result, the non-dimensionalized coordinates are also scaled with respect to this limited region.

4.3.3 Non-uniform heating correction

The production process of PCBs involves untreated epoxy plates covered with a thin layer of copper (t_c ~35 μm) to be immersed in an acid bath (i.e. etching). By covering the plates with a stencil, only the uncovered copper areas are fully dissolved in the bath; leaving only the copper tracks. In this process, minor fluctuations in acid exposure have caused copper thickness variations to occur across the surface area of each PCB. Since the local resistance of the copper tracks is linearly dependent on the surface area of the wire (Equation 4.8), local temperature variations occur once Ohmic heating takes place. This temperature variation is directly quantified by observing heated PCBs under natural convection. These heated empty measurements (HEMs) are used to devise a custom correction matrix for each PCB, which reestablishes the radiation intensity of the PCB to represent uniform heating.

By heating a test plate under natural convection (20 W, ~5 min) up to a steady-state, it is found to comply with the heat balance equation:

$$q_{in} = q_{conv} + q_{cond.b} + q_{rad}$$

An order of magnitude analysis shows that for these HEM, q_{rad} ~93.1%, q_{conv} ~2.4% and q_{cond} ~4.5%. The radiative term is estimated through Equation 4.40, using an averaged temperature observed from the PCB surface. The convective term is found by using Equation

4.2, where h for stagnant air is set equal to 5 W/m^2K.[63] (Kreith, 2012) Part of the conductive term, $q_{cond.s}$ is found to be negligible compared to $q_{cond.b}$ (< 1%). The latter of which is computed under the assumption of a linear temperature profile (Equation 4.39). This is allowed, considering that the tested models are observed during a steady-state (Figure 4.3b).

From the order of magnitude analysis, it becomes clear that both q_{conv} and $q_{cond.b}$ are negligible compared to q_{rad}. Even though the conductivity into the body is relatively large in terms of overall magnitude, it displays a negligible variance (< 2%). Therefore, the effect of excluding $q_{cond.b}$ would be equal to a near constant subtraction across the entire surface, which has hardly any effect on the relative proportionality between the local values of the PCBs. As a result, it is stated that for a stagnant, heated measurement:

$$q_{el} \sim q_{rad} \tag{4.25}$$

Which implies that – as the IR camera acquires the levels of radiation (Section 4.2.2) – the relative magnitude of local Ohmic heating can be directly related to the registered digital levels (DL). In turn, by the etching process, variations in copper thickness arise which are directly related to the resistance of the test plates. As a result of this, PCB properties become local properties such that $R = R(i,j)$ and $q_{el} = q_{el}(i,j)$, for which:

$$R(i,j) = \frac{L}{\kappa\, w_c\, t_c(i,j)} \quad \text{and,} \tag{4.26}$$

$$q_{el}(i,j) = R(i,j)\, I^2 \tag{4.27}$$

By the relations of Equations 4.26 and 4.27, it is concluded that the thickness variation is directly related to the local heating properties such that:

$$q_{el} \sim t_c^{-1} \tag{4.28}$$

As a result, combining the relations from Equation 4.25 and 4.28, it can be stated that:

$$q_{rad} \sim t_c^{-1}$$

Which effectively implies that the local variations in copper track thickness can be directly correlated to the DL registered by the IR camera. The non-uniform heating correction, *NUHC* is based on this principle and is computed through the the following steps:

1. Average radiation intensity E (in DL) over all HEMs (25 frames), to mitigate noise.
2. Compute the average radiation intensity E_{avg} over the entire surface area (excl. ribs).
3. Determine the local scaling matrix:

$$NUHC(i,j) = \frac{E_{avg}}{E(i,j)} \tag{4.29}$$

4. Smoothen the correction matrix through a MatLab-based cubic interpolation.

An example of a resulting NUHC matrix is shown in Figure 4.38, which represents the 4.8/5 geometry. It is seen that the NUHC merely represents a localized scaling factor in [-], based on the average radiation intensity of the entire PCB in DL. In determination of each NUHC, the rib locations are excluded based on a predefined geometrical configuration. These NUHC matrices are created for each test model, as each PCB has its own faults in copper thickness variation and thus specific radiative signature. These NUHCs, in turn, are applied to correct for these inevitable production faults. The latter is done by (1) multiplying the WTM in *DL* by the NUHC, and (2) by multiplying the average copper thickness t_c by the NUHC such that $t_c \rightarrow t_c(i,j)$.

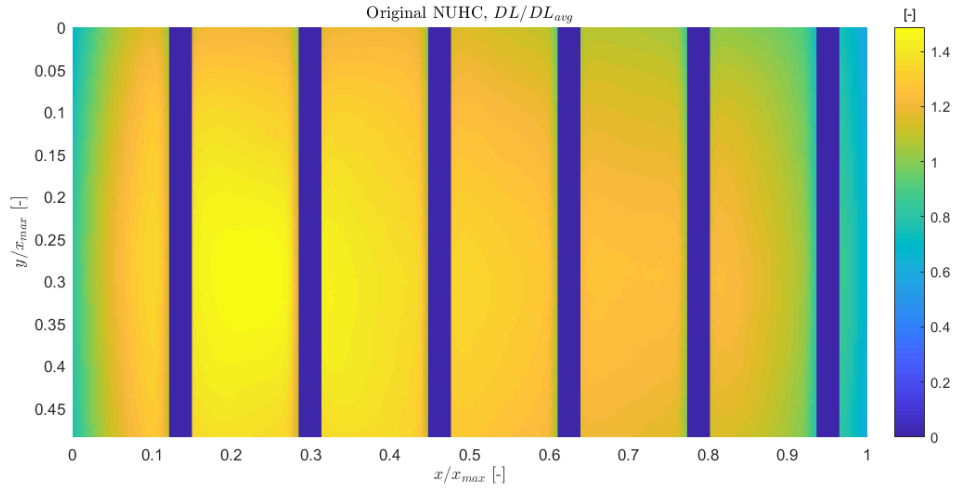

FIGURE 4.38: NUHC obtained for the 4.8/5 configuration.

It is seen in Figure 4.38 that the local variance of the radiative intensity can be up to 40% higher than the computed average. If this would not be done, measured variations during WTMs could not be directly assigned to flow effects. However, now that this is corrected for, DL and T differences can be safely assigned to flow phenomena.

4.3.4 Transient temperature analysis

Once the NUHC is applied to all WTMs, the calibration function is used to convert the WTM frames from DL to T (K). With these WTMs in terms of temperature, a temperature transient analysis is performed such to quantify which frames are at steady-state. To this end, six points are chosen which lie at distinct locations along the longitudinal and lateral centerline (Figure 4.39). By their dispersion, these points are representative of the entire model surface.

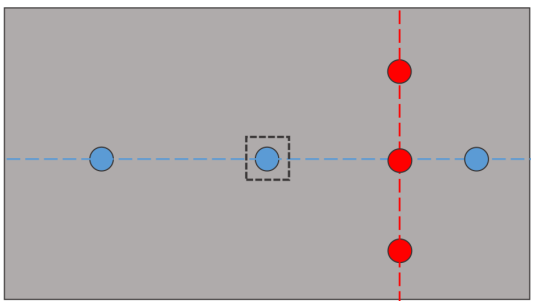

FIGURE 4.39: Locations on FOV used for transient temperature analysis.

In order to prevent the implementation of outliers in the transient, the mean values are taken from squared regions surrounding each point. In turn, the resulting six mean transient curves are computed for each recorded WTM (i.e. 2125 frames or 85 sec). It was mentioned in Section 4.2.3 that both IR cameras encompass some inherit measurement noise, quantified by the noise equivalent temperature difference (NETD). This NETD is observed in Figure 4.40 by the data oscillations. To avoid the inclusions of this NETD, it is decided to construct an 8th-order polynomial fit trough each transient. In turn, the steady-states are based on these fit curves for which the following steady-state criterion is used:

$$T_{max} - \Delta T_{ss} \leq T \leq T_{max} \tag{4.30}$$

Where ΔT_{ss} is set to 20 mK, equal to the NETD of the Cedip Titanium 530L IR camera. This criterion is equal to the one seen for the one-dimensional semi-infinite solid analysis (Section 4.1.1), where its usage was verified by the notion that a data reduction procedure cannot transcend the accuracy of this NETD. Therefore, it is safe to assume that the model is at steady-state once the average T is within the bounds of the NETD.

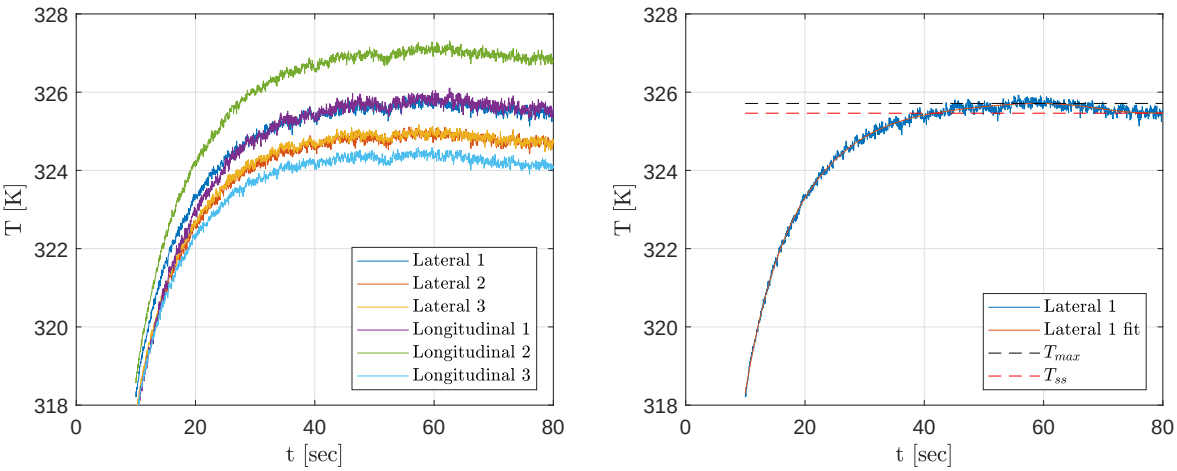

(A) Transient response all positions.

(B) Steady-state qualification.

FIGURE 4.40: Transient temperature analysis for steady-state definitions.

Figure 4.40b displays how the steady-state criterion works. Since each transient has an step-wise response to the triggering of the power supply (i.e. delivery of electric power), each curve transcends up to a maximum after which it seems to slowly decay with the temperature in the settling chamber and thus test section. However, a continuous, completely inter-dependent decay of the surface temperatures with the settling chamber temperature could not be identified. Therefore, only those images between the maximum T and the lower limit with NETD are said to be at steady state (Equation 4.30). Once all six transients fall within this temperature range, the complete model is said to be at steady-state. In the remainder of the reduction program, only those frames are used which abide with the combined steady-state criterion; typically 300 out of 2125 frames (~12 sec).

4.3.5 Heat flux computation

At this stage of the data reduction, the gathered images have been pre-processed, adjusted for non-uniform heating and limited for the steady-state criterion. The remaining WTM frames are used for the actual computational part where, through additional input data, each of the heat flux terms is computed (Figure 4.36). In order to comply with the definition of q_{conv}, it is chosen to compute each of the heat flux components in terms of W/m^2.

Electric heat flux

The electric heat flux q_{el} is the only thermal input to the PCBs, the settings of which are tailored to the PCB-specific resistances of the test models (Appendix G.3). From the definition of electric power, it is possible to compute q_{in} multiple ways. Due to the fact, however, that the significance of the voltage meter of the power supply is low (i.e. $\epsilon_{ps} \pm 0.5V$), it is decided to use the following form:

$$q_{el} = I^2 R_{PCB} / A_{PCB} \tag{4.31}$$

Where the PCB-specific resistance, R_{PCB} is corrected for local temperature effects and variances in copper thickness, by:

$$R_{PCB} = R(i,j) = R_{PCB,0}(1 + \alpha_{cu}(T_s(i,j) - T_{test})) \times NUHC \tag{4.32}$$

Where $R_{PCB,0}$ is the base resistance defined at a testing temperature T_{test} of 21.1°C. In turn, the delivered current setting, I is registered for each wind tunnel run, the surface temperature $T_s(i,j)$ is derived from the data analysis and the PCB surface area A_{PCB} and temperature coefficient for copper α_{cu} are known constants.

The variation in base PCB resistance is a direct cause of the etching process; equal to the copper thickness variations. The distinct variation in R_{PCB} is displayed in Appendix N. For the current discussion, it is important to know that those PCBs are used which were closest to one another in terms of their resistance Ω. As a result, the PCBs considered were within a maximum range of ± 10.5% from the mean equal to, $\overline{R}_{PCB}$ = 22.6 Ω. Fortunately, it is seen that $\overline{R}_{PCB}$ exactly matches the estimate stated in Section 4.3.5. For the data reduction, the $R_{PCB,0}$ are loaded for the specific model and matched with additional measurement inputs.

Conductive heat flux

The conductive heat flux arises from temperature differences between adjacent, connected segments of the test models. In three-dimensional space, its equation is given by the following representation of the Fourier law:

$$q_{cond}(x,y,z) = -\frac{1}{A_{PCB}}\left(k_{xx}\frac{\partial^2 T_s}{\partial x^2} + k_{yy}\frac{\partial^2 T_s}{\partial y^2} + k_{zz}\frac{\partial^2 T_s}{\partial z^2}\right) \tag{4.33}$$

Where in Equation 4.33 k_{xx}, k_{yy} correspond to the equivalent thermal conductivities respectively parallel and normal to the flow, whereas k_{zz} is directed perpendicular to the test surface (into the model). For each Cartesian coordinate, the respective conductive heat flux term is a function of k_{eq} and the second-order temperature derivative. By the linearity of Equation 4.33, each conductive flux can be solved separately as:

$$q_{cond}(x,y,z) = -\underbrace{\frac{1}{A_{PCB}}\left(k_{xx}\frac{\partial^2 T_s}{\partial x^2} + k_{yy}\frac{\partial^2 T_s}{\partial y^2}\right)}_{q_{cond.s}} - \underbrace{\frac{1}{A_{PCB}}\left(k_{zz}\frac{\partial^2 T_s}{\partial z^2}\right)}_{q_{cond.b}} \tag{4.34}$$

Where $q_{cond.s}$ corresponds to the conductive heat flux across the surface, and $q_{cond.b}$ is equal to the heat flux into the body of the test models. Both terms depend on different measurement inputs, and are solved using varying methods and assumptions. Their respective implementation into the data reduction program are listed next.

Surface conductivity The PCBs consists of an epoxy-based support surface (i.e. FR-4) topped with copper wires of varying thickness (Figure 4.2). As a result of the copper wire layout and height variance, the thermal properties of this copper surface are anisotropic. This means that, prior to using the expression for $q_{cond.s}$, equivalent conductivity terms $k_{eq.xx}$ and $k_{eq.yy}$ should be derived to generalize Equation 4.34. This is done by using the dimensional definitions of the PCB, displayed in Figure 4.41.

By the definition of the Cartesian coordinate system, the x- and y-axes are directed respectively normal and parallel to the copper tracks. This means that the conductive heat flux along the y-axis is the sum of two mechanisms in parallel; one due to the copper tracks,

the other by the FR-4 support. Through this, the equivalent conductivity in y, $k_{eq.y}$ can be defined for a square region sized $w_f \times w_f$, such that:

$$k_{eq.yy} = \gamma^* t_c k_c + t_f k_f \tag{4.35}$$

Where the parameter $\gamma^* = w_c/w_f$ is equal to the width ratio between respectively the copper tracks w_c and corresponding FR-4 base material w_f, and k_f and k_c indicate the considered material-specific thermal conductivities in $W/(mk)$.[81] (Astarita and Cardone, 2000)

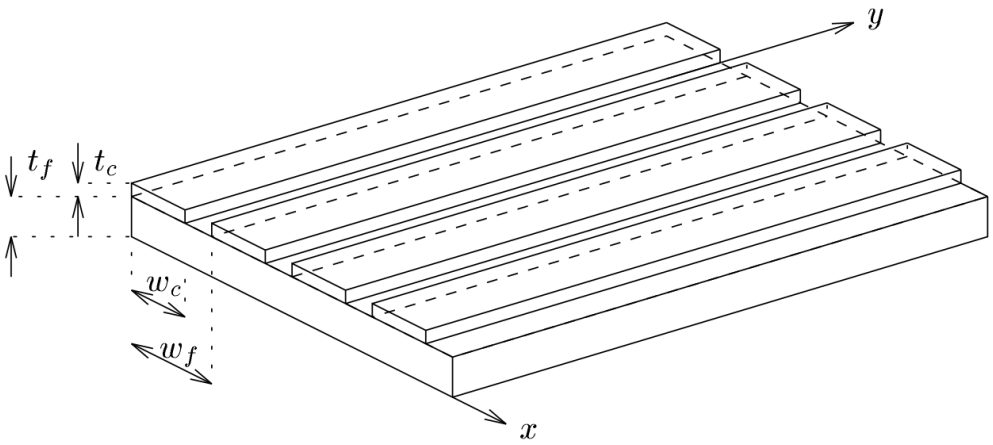

FIGURE 4.41: Sketch of a printed circuit board.

The implementations of anisotropic thermal properties is slightly more complicated for the x-coordinate, directed normal to the copper tracks (Figure 4.41). At the copper gap, only the epoxy-base allows conductive heat transfer to take place, whilst, in the copper track region, both materials contribute to thermal conduction. Therefore, in this case, the $k_{eq.xx}$ is estimated through both a series and a parallel process. The resulting equation is given by:

$$k_{eq.xx} = 1/\Big\{ \frac{1-\gamma^*}{t_f k_f} + \frac{\gamma^*}{t_f k_f + t_c k_c} \Big\} \tag{4.36}$$

Where t_f and t_c correspond to respectively the thickness of the copper tracks and FR-4 base, and γ^* indicates the previously defined width ratio.

With the equivalent conductivity terms known, it remains to derive the second-order spatial temperature derivatives $\partial^2 T/\partial x^2$ and $\partial^2 T/\partial y^2$, such to compute the complete conductive heat flux terms. In the MatLab code, these terms are approximated by a higher-order central differencing scheme, given by:

$$\left.\frac{\partial^2 u}{\partial (x,y)^2}\right|_{(x,y)_i} = \frac{-u_{i+2} + 16u_{i+1} - 30u_i + 16u_{i-1} - u_{i-2}}{12\Delta(x,y)^2} + \frac{\Delta(x,y)^4}{90} \left.\frac{\partial^6 u}{\partial (x,y)^6}\right|_{(x,y)_i} + ... \tag{4.37}$$

Where the values for $u(x,y)$ are equal to the surface temperature fields as obtained by the IR cameras, and the spacing terms Δx and Δy correspond to the non-dimensionalized physical spacing per pixel, equal to a constant of 0.0032 [-].

Body conductivity The equivalent thermal conductivity in z-direction or $k_{eq.zz}$, is defined by the sum of four mechanisms in series; respectively (1) copper tracks, (2) PCB base (FR-4), (3) Epoxy-based glue and (4) Makrolon insulation. The interrelations of these adjoined materials is given by the sketch of the test plate's cross-section in Figure 4.42. The resulting expression for the body-equivalent thermal conductivity is given by:

$$k_{eq.zz} = \left(\frac{t_c}{k_c w_c w_f} + \frac{t_f}{k_f w_f^2} + \frac{t_g}{k_g w_f^2} + \frac{t_m}{k_m w_f^2} \right)^{-1} \tag{4.38}$$

Where each term is based on the thermal resistance R_k given by t/kA, which is dependent on the material thickness (t), area (A) and material-specific thermal conductivity (k). For the derivation of Equation 4.38, the contact resistance is assumed to be completely encompassed by the specific thermal resistance of the glue layer. The latter is allowed, considering that the two surfaces were cured whilst being under high pressure.[63] (Kreith et al., 2012)

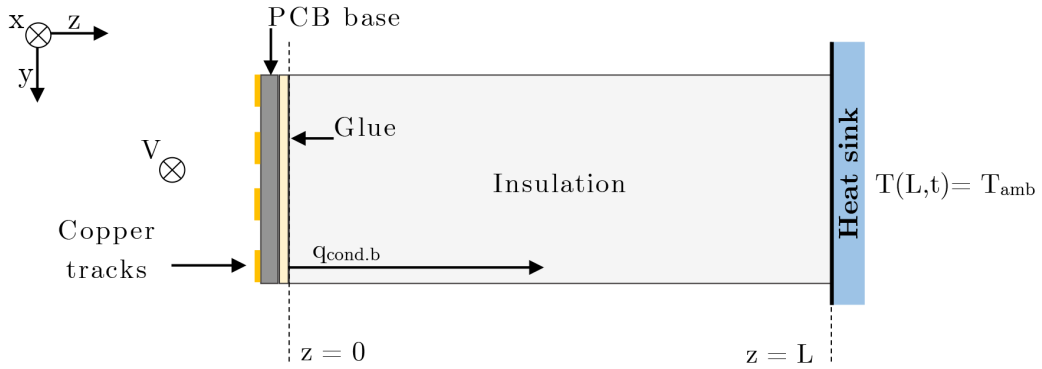

FIGURE 4.42: Cross-sectional view of the PCB model.

Applying the material properties to Equation 4.38, the average thermal conductivity of the test plate cross-section is estimated to be 1.62 W/K. The contribution of each material to this total is given by 2.0 $\times 10^{-4}$, 7.9, 0.7 and 91.5% for respectively copper, FR-4, glue and Makrolon insulation. As such, it is substantiated to neglect the effects of the variance of both the glue and copper thickness. In fact, the insignificance of their influence on $k_{eq.zz}$ contributes to the overall predictability of the model as the thickness estimation for both materials belong to the most uncertain components of the one-dimensional analysis.

During the evaluation of the conductive heat fluxes, the entire test model is assumed to operate under steady-state conditions. Therefore, the temperature profile in z-direction can be assumed to be linear (Section 4.3.5) and, as such, the thermal body conductivity flux is given by:

$$q_{cond.b} = -\frac{k_{zz}}{A_{PCB}} (T(i,j) - T_{tk}(i,j)) \tag{4.39}$$

Where $T(i,j)$ is the surface temperature, registered by the IR camera, and $T_{tk}(i,j)$ corresponds to the temperature field of the rear segment of the insulation, obtained by the reference thermocouples. The QIRT experimental setup was constructed such that 16 K-type thermocouples could be placed strategically along the rear and sides of each model (Figure 4.9). The resulting zero-dimensional data points are used for reconstructing the temperature fields. This is done through a second-order surface interpolation, as this approximate has the same order as the original conductivity equation; preventing the possibility of non-physical interrelations (Equation 4.34).

An example of such a temperature field reconstruction is provided in Figure 4.43, where the dots indicate the original locations of the thermocouple tips. By synchronizing the thermocouple data with the IR camera frames, the associated temperature data points are matched from both measurement sources. In turn, thermocouple temperature field reconstructions are made for each steady state frame, such that the the $T(i,j)$ values are matched spatially

and temporally. As a result, both T and T_{TK} can be implemented directly in Equation 4.39 such that the $q_{cond.b}$ is derived for each steady-state IR frame.

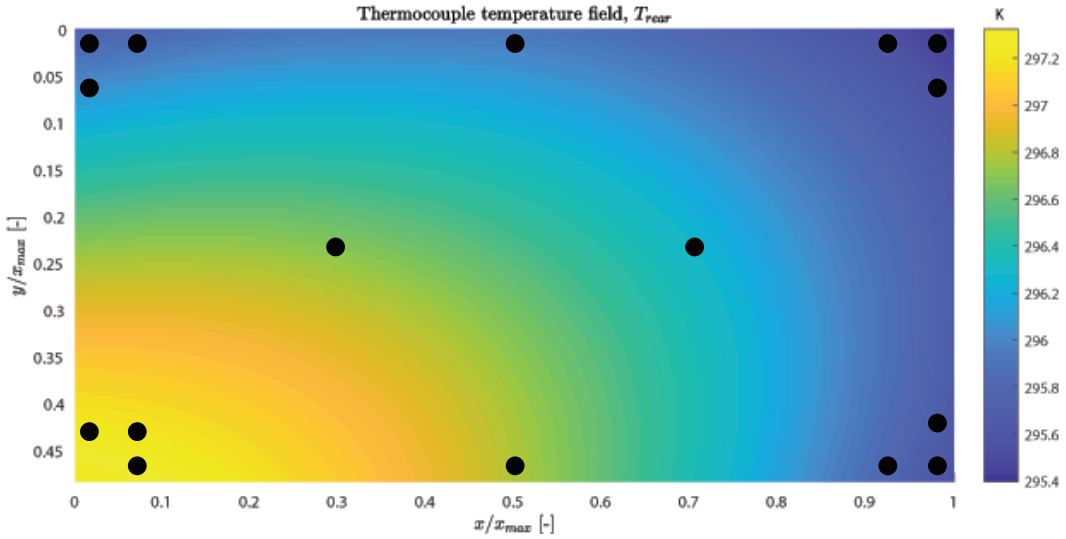

FIGURE 4.43: Interpolated thermocouple temperature field.

Radiative heat flux

The last flux term to be determined for the thermal equilibrium equation (4.23) is the radiative heat flux, q_{rad}. As explained before, any object with a temperature above absolute zero emits a certain amount of radiation. Part of this radiation – primarily in the IR spectrum (Section 4.2.1) – correlates to a specific amount of heat, which is equated through:

$$q_{rad} = \frac{\epsilon\sigma}{A}(T^4 - T_{aw}^4) \tag{4.40}$$

Where $\epsilon = \epsilon_{model}$ equal to 0.88 [-], σ the Stefan-Boltzmann constant equal to 5.67 W/K^4 and T_{aw} the adiabatic wall temperature in the test section (K). The latter temperature is derived through the following relations:

$$T_{aw} = T_{sc}\frac{(1 + rM_e^2(\gamma - 1)/2)}{(1 + M_e^2(\gamma - 1)/2)} \tag{4.41}$$

Where T_{sc} is the static temperature measured in the settling chamber, M is the freestream Mach number, γ the expansion coefficient of air and r the recovery factor based on the turbulent boundary layer:

$$r = Pr^{1/3} \tag{4.42}$$

For which Pr is equal to 0.71, making r equal to 0.89.[9] (White, 2006) During the initial phases of QIRT testing, it was attempted to measure the T_{aw} values directly from the test plates. This was done by operating the wind tunnel, whilst not heating the flat plate model. In turn, the test plate would simply cool down up to the adiabatic conditions. Unfortunately, even within 5 minutes of runtime, no unheated steady-state and associated T_{aw} were measured. As a result, the aforementioned method is used during this data reduction.

From the PIV results (Section 5.1), it was found that a Mach-defect was formed compared to previous experiments conducted by Sun et al. (2012). The reason for this was that the leading edge insert of the PIV test plates resulted in the formation of a strong oblique shock wave (Figure 3.3). As a result, it seems that for a complete computation of the T_{aw}, the

isentropic and the oblique shock wave relations should also be included here (Appendix O). Nevertheless, as the LE insert is absent for the QIRT experiments, no interfering OSW is formed prior to the models. This means that the resulting Mach defect and corresponding relations only play a role for the freestream Mach number estimation during PIV. As a result, Equation 4.41 suffices for this data reduction technique where M remains equal to 2.0.[5]

4.3.6 Post-processing

Finally, with each flux component know, the convective heat flux, q_{conv} is computed by using an expanded form of the steady heat balance equation (4.23):

$$q_{conv} = q_{el} - q_{cond.s} - q_{cond.b} - q_{rad}$$

Through which the heat transfer coefficient, h and Stanton number, St are computed through Equations 2.12 and 2.11. For these, u_∞ and ρ_∞ are estimated through the air properties in the settling chamber (T_{sc} and P_{sc}) and the isentropic relations at M of 2.0. Once again, the stagnant temperature is measured by the thermocouple located inside the settling chamber, whereas the stagnant pressure is monitored by a gauge located in the control room (~2 *bar*). As such, St is not computed through a constant scaling factor, but by an experiment-specific set of variables.

Time- and spatial averaging By the implementation of the previous equations, the data reduction program delivers the surface representations for each geometry in terms of T, q_{conv} and h. Even though the resulting images are esthetically pleasing, one is convoluted to draw explicit conclusions based on them. Therefore, during the post-processing phase, it is decided to temporally and spatially average the datasets such to obtain 1D profiles.

The spatial region considered for planar-to-profile averaging is formed by the data located on the longitudinal centerline and pixel lines radially outward (Figure 4.44). It is decided to use 15 pixel lines on both sides of the indicated centerline, as this is representative of the flow (~20% PCB width) whilst avoiding possible the wall effects.

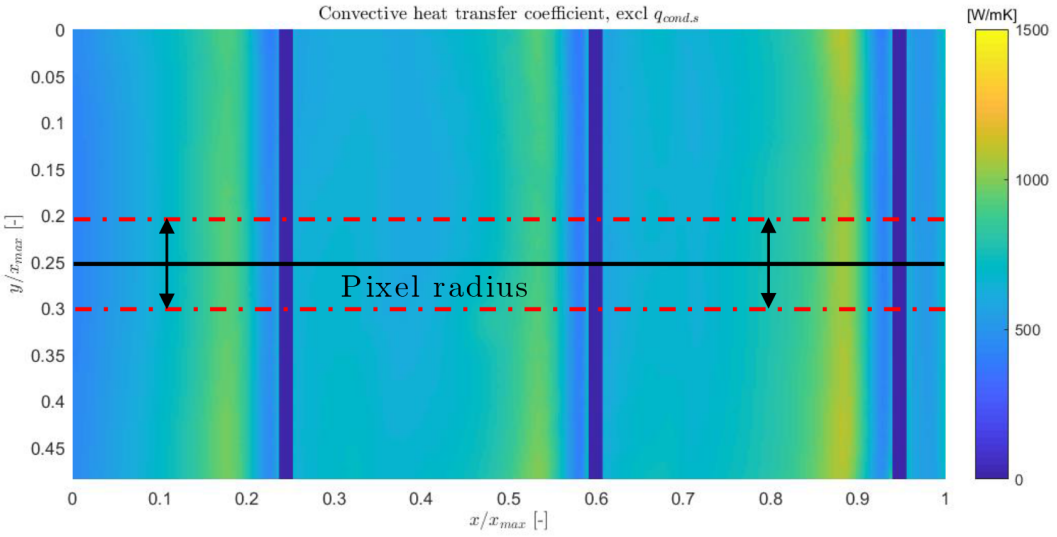

FIGURE 4.44: Indication of the spatial region used for profile computation.

The temporal or transient data averaging encompasses the number of IR frames at steady-state required to obtain a converged solution. To this end, a transient data convergence

study is done over a sequence of IR frames using only the cropped region indicated by Figure 4.44. The results of the convergence study is provided in the Figure 4.45, where the data on the y-axis represents the percentile difference in sum-averaged convective heat transfer coefficient (i.e. $\sum \Delta h(i)/h(i)$). From this sum-averaged profile, it is seen that an extremely small percentile variance exists between the IR frames at steady-state conditions. As such, it is decided to use 50 frames for the transient averaging of h. At this number of frames, the average uncertainty is estimated to be approximately 0.0018% which means that negligible discrepancies are introduced. This averaging forms the end of the overall data reduction program. The results of the QIRT methodology are shown in Chapter 5.2, where there is primarily focused on the cavity profiles of h and St.

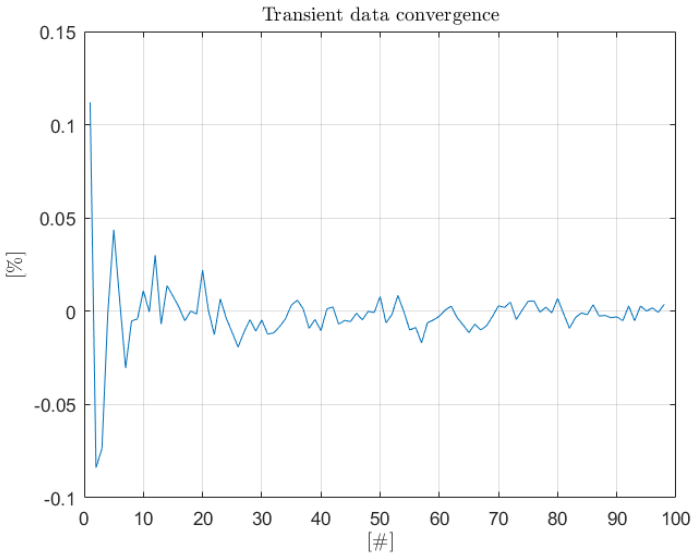

FIGURE 4.45: Transient convergence study.

4.3.7 Order of magnitude analysis

The utilization of both the QIRT setup and the corresponding data reduction technique is performed for the first time. Therefore, it should be decided with which settings the data reduction is most reliable and under what conditions the data should be obtained. This is done through an adjoined order-of-magnitude (OM) and signal-to-noise (SNR) analysis, where each of the computed heat flux terms is assessed in relation to the final output (i.e. q_{conv}, h and St). It is decided to start the investigation to the final settings by a computation of q_{conv}, for which each indicated heat flux term is used (Equation 4.3.6).

An example of a resulting planar computation is given in Figure 4.46, which displays a largely pixelated, coarse convective heat transfer field. It is seen that this effect is progressively worse for regions with high temperature gradients (i.e near the rib faces, reattachment regions etc.), which aims at inaccuracies of the $q_{cond.s}$ computation. Prior to investigating this specific term, the relative magnitude and overall influence of each flux term is assessed. The contribution of each heat flux term – averaged over all conducted measurements – as a percentage of q_{el}, is 100% for respectively q_{el}, 91.25% for q_{conv}, 7.92% for $q_{cond.s}$, 0.83% for q_{rad} and 4.44×10^{-5}% for $q_{cond.b}$, where the average q_{el} is equal to $2.04 \times 10^4\ W/m^2$. This order of magnitude division displays the limited effect which both q_{rad} and $q_{cond.b}$ have on the overall computation of q_{conv}. Recalling the results of the one-dimensional analysis in Section 4.3.5, it was estimated that $\leq$ 0.1% of the q_{el} would convert into $q_{cond.b}$. The current order

of magnitude analysis thus proves that the estimated property is valid. This implies that, in the end, the reference thermocouples functioned more as a setup performance validation method than a data improvement tool. Therefore, for future measurements, the application of these reference thermocouples can be disregarded such that the turn-around of the QIRT technique is highly improved. Even though it turns-out that these reference thermocouples are not vital to the QIRT data reduction, conclusions like these are important to the proof of operation (Chapter 7).

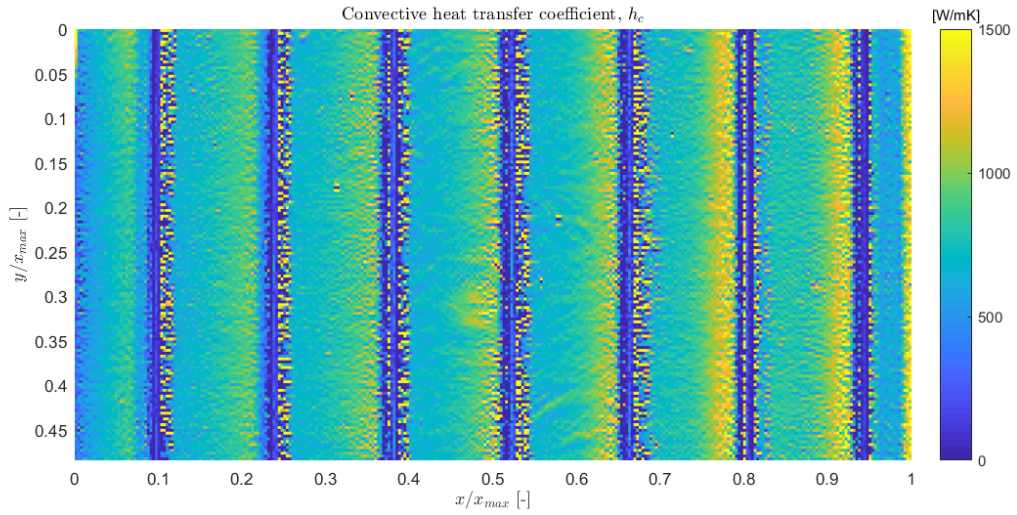

FIGURE 4.46: Heat transfer coefficient field, including $q_{cond.s}$.

By the exclusion of q_{rad} and $q_{cond.b}$, no improvement to the coarse data representation was found (Figure 4.46). Actually, it turns out that the initial impression regarding the implementation of $q_{cond.s}$ was valid. The computation of $q_{cond.s}$ relies on the usage of discrete double spatial derivatives of raw temperature data (Equation4.37). The resulting temperature gradient fields are highly sensitive, and directly affect the stability of the q_{conv} data. An example of a planar q_{conv} field excluding $q_{cond.s}$, is given in the following figure:

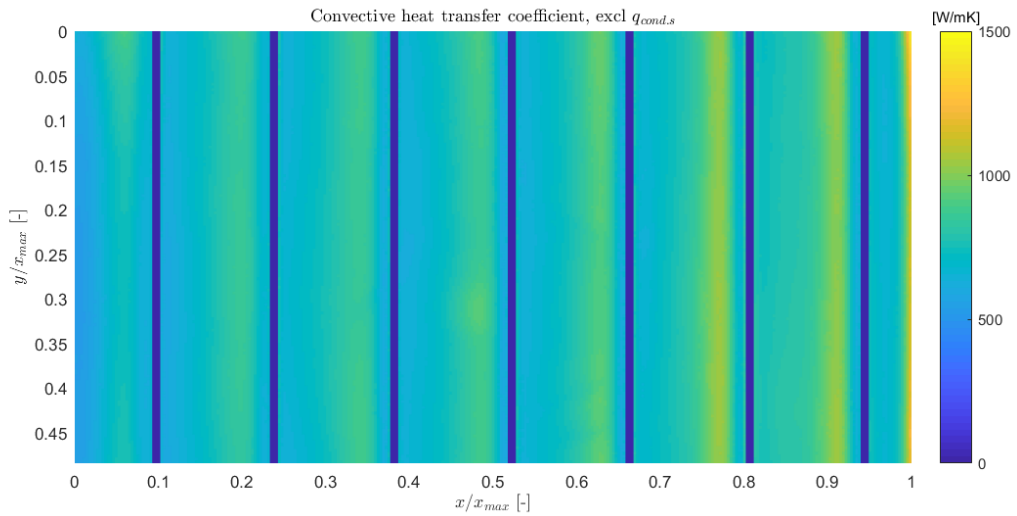

FIGURE 4.47: Heat transfer coefficient field, excluding $q_{cond.s}$.

From which it is clearly seen that the overall FOV is less coarse. In addition, the data at each pixel location seems nearly unaffected regardless of the relatively high order of magnitude of $q_{cond.s}$ relative to the signal (i.e. h). This feature is supported by the h-profiles of the final cavities, an example of which is given by following figure:

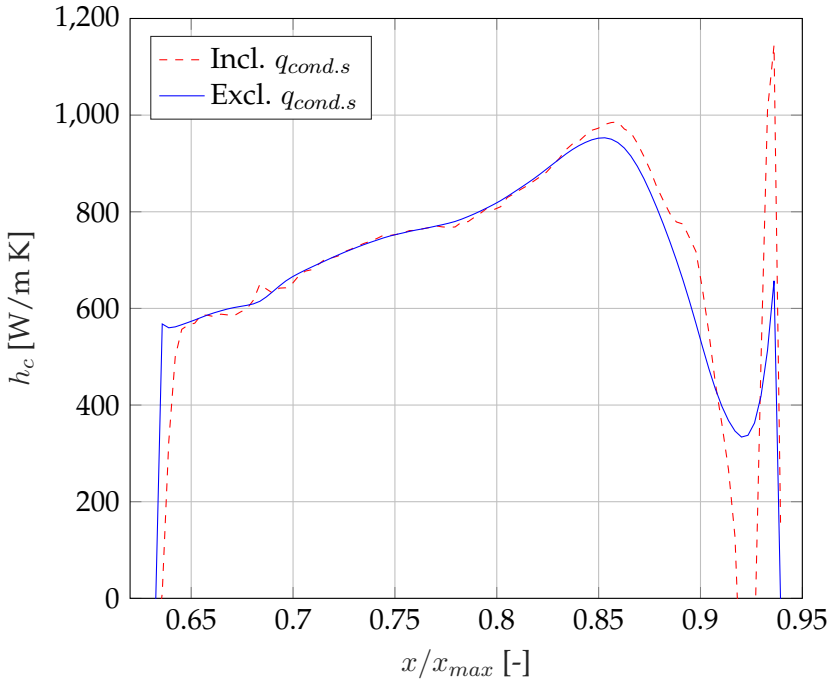

FIGURE 4.48: h cavity profile for 3.6/15 model, incl. and exlc. $q_{cond.s}$-term.

Where the h-profiles are shown for computations respectively including or excluding $q_{cond.s}$. On average, the overall percentile change between the two h-profiles is 3.52%. Of this difference, the majority (3.0%) is limited to the regions within the vicinity of the rib faces (i.e. 0.025 x/x_{max}), whereas the remainder is found at the regions affected by discontinuities. Each of these indicated regions is characterized by temperature gradients which are significantly higher than adjoining flow regions. By the non-physical h-profile additions of including the $q_{cond.s}$-term, it seems that mostly noise is added to the overall solution. Actually, the inaccuracy of the T_{xx} and T_{yy} computations are found to provide more noise than overall output improvement. IT has been attempted to mend these deficiencies via:

1. Higher-order central differencing scheme.
2. Interpolation of the raw data, prior to numerical derivation.
3. Smoothing polynomial through the existing $q_{cond.s}$-fields.
4. Measures 1–3 simultaneously.

Even though ts was observed that the the third measure slightly improved the data. The large downside was that this procedure introduced an artificially altered dataset. This, in turn, led to the elimination of several important features from the h-profiles by smoothening-out several more slight flow effects. In order to avoid both the introduction of non-physical solutions, none of these measures are considered for the final data reduction procedure. Instead, the $q_{cond.s}$ flux terms are discarded for the computation of q_{conv}.

The decision to exclude the $q_{cond.s}$ due to worsened SNR, is supported by a sensitivity analysis of the h-profiles, where variations between measurements at consecutive power settings are compared. An example of such an analysis is provided in the following figure:

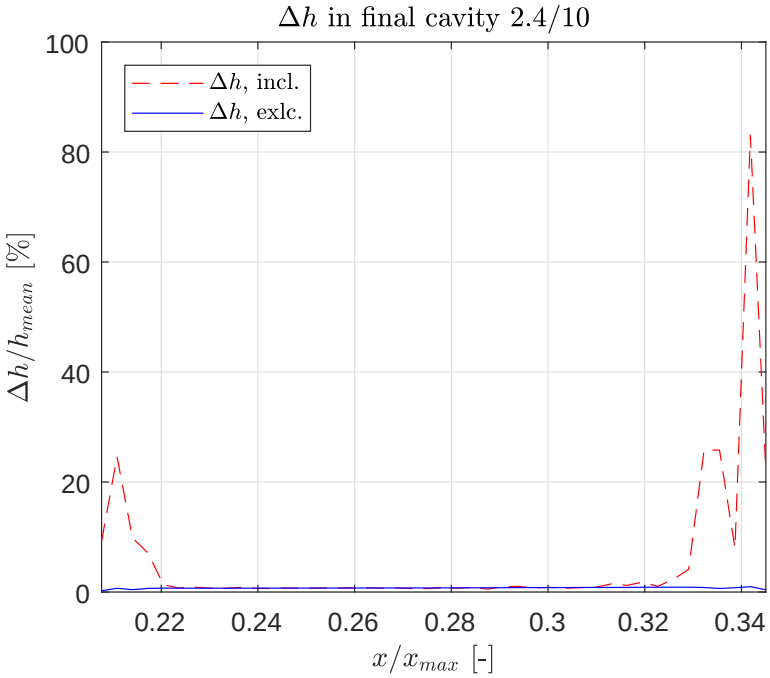

FIGURE 4.49: Variance of the convective heat transfer coefficient, incl. and excl. $q_{cond.s}$.

In which the variance of the h-profiles is shown for the final cavity of the 2.4/10 model, respectively including and excluding $q_{cond.s}$. Figure 4.49 clearly shows that regions near the edges of the cavities are significantly more divergent for computations including $q_{cond.s}$, whilst center regions of the cavities remain largely unaffected. Actually, analyzing the variance curves of all roughness models, it is found that on average Δh_{incl} and Δh_{excl} display average variances of respectively 35% and 2.6% near the ribs. In contrast, regions within the cavity center remain relatively equal at an average variance of 1.24%. Converting this variance into a signal (h) to noise (Δh) ratio, it is found that the SNR is ~3.2 in the center whilst being ~1.05 near the ribs. As such, the decision to improve the reliability and stability of the solutions by excluding the $q_{cond.s}$ terms is valid. Therefore, all cavity profiles of this report correspond to those excluding $q_{cond.s}$.

4.3.8 Uncertainty analysis

As no severe data augmenting schemes were used during the data reduction routine (smoothing, interpolation etc.), the most dominant uncertainties originate from the equipment utilized during the experiments. The uncertainties encountered for the QIRT methodology are subdivided in three main categories: (1) measurement uncertainties, (2) calibration uncertainty and (3) material property variance. By combining the resulting errors, a complete a priori, systematic uncertainty estimate is made (ϵ_{sys}).

Measurement uncertainties The described data reduction method relies on various measurement inputs, which are obtained through respectively the IR camera, thermocouples and laboratory power supply. Each of these measurement devices encompasses an inherit

level of uncertainty. Over the complete IRT methodology, five measurement devices are identified. To each, the following errors are assigned by their respective manufacturers:

- Cedip 630L IR camera = 0.025 K
- Optris PI 640 IR camera = 0.075 K
- NI/TB-9214 thermocouple acquisition = 0.365 K
- Black body homogeneity = 0.245 K
- SM600-10 power supply = 0.005 A
- Fluke 116 true RMS multimeter = 0.9% + 0.2 Ω

Which affect the inputs of respectively T, T_{tk}, T_{aw}, I, R_0 and the calibration procedure. Apart from the latter, each error margin can be readily implemented into the respective equations. However, the calibration error requires some additional considerations.

Calibration error The description of the calibration procedure (Section 4.2.4) indicates that three distinct measuring devices are involved at the determination of the calibration curve: the IR camera, K-type thermocouples and NI thermocouple acquisition modules. In addition to this equipment, the blackbody itself contains some inherit, non-homogeneous temperature variance (Appendix P). The calibration curve is defined by simultaneously logging both temperatures (K) and digital levels (DL), where the temperature is defined as:

$$T_{bb} = (T_{tk.1} + T_{tk.2})/2 + \epsilon_{bb} + \epsilon_{tk}$$

Equal to the average thermocouple temperature registration within the blackbody, including the blackbody (ϵ_{bb}) and thermocouple uncertainties (ϵ_{tk}). On the other end of the calibration curve the DLs were obtained by the IR camera, which suffers from a temperature-independent measuring uncertainty. This NETD is equal to 0.025 *K* for the Cedip IR camera used during the primary campaign. Combining the uncertainties involved, the overall calibration uncertainty is defined by:

$$\epsilon_{cal} = (\epsilon_{IR}^2 + \epsilon_{tk}^2 + \epsilon_{bb}^2)^{\frac{1}{2}} \tag{4.43}$$

Which correlates to an estimated ϵ_{cal} of 0.44 K for the primary campaign, whereas the built-in calibration for the secondary campaign is ~$2K$.[71] (Cedip, 2016) In the data reduction routine, the ϵ_{cal} is assigned to the uncertainty of the surface temperatures, T. During the reduction, this ϵ_{cal} is combined with the variables to obtain the systematic error estimate.

Material variance Unlike metals and other conductors, the thermal conductivity and diffusivity of polycarbonate materials are known to vary as much as 8% within a limited temperature range of $50K$.[82] (Zhang et al., 2002) During the experiments, it was seen that along streamwise direction the PCB surface temperatures may vary as much as $70K$. As the Makrolon slab equates to over 90% of the entire cross-sectional area of each test model (Section 4.1.1), this uncertainty should be investigated.

In Section 4.3.5, it was determined that the resistance of the Makrolon slab (R_{mk}) accounts for an estimated 91.5% of the total resistance. In turn, R_{FR4}, R_g and R_c correspond to respectively 7.9, 0.7 and 2.0 $\times 10^{-4}$. This implies that it is safe to neglect the influence of slight thickness and material property variances for both the epoxy-based glue and the copper tracks with regards to k_{zz}. The order-of magnitude analysis of each heat flux term, however,

has proven the insignificance of the $q_{cond.b}$ with regard to the q_{conv} altogether (Section 4.3.7). As $q_{cond.b}$ accounts for 4.4 $\times 10^{-5}$ of the complete heat flux balance, any variance in the polycarbonates Makrolon and FR-4 remains negligible compared to the final output. Therefore, the material variance effects are not included into the current uncertainty analysis.

Systematic uncertainty estimate The complete ϵ_{sys} is found by assigning each of the previously defined uncertainties to its corresponding variables within the data reduction routine (i.e. T, I, R_0 etc.). In turn, the uncertainty propagations are computed through the interrelations (equations) in which these variables occur. To make sure that a representative dataset is used for this uncertainty estimate, all heat flux components and temperature fields are represented by the steady-state average of all experiments. As such $\overline{T}$ = 315.6 K, $\overline{T}_{aw}$ = 277.1 K, $\overline{T}_{tk}$ = 294.5 K, q_{conv} = 20299 W/m^2, $\overline{q}_{el}$ = 22561 W/m^2, $\overline{q}_{cond.s}$ = 2053 W/m^2, $\overline{q}_{cond.b}$ = 0.013 W/m^2 and $\overline{q}_{rad}$ = 204 W/m^2. In addition, the average electrical current $\overline{I}$ = 4.85 A, whereas the base resistivity $\overline{R}_0$ is set to 22.77 Ω. The values of each of the variables listed are used to non-dimensionalize each uncertainty, making that the systematic uncertainty estimate ϵ_{sys} is given in %.

With both the uncertainty levels and representative data in place, it is possible to compute the complete systematic uncertainty. In general, the interrelations are formed by the equations belonging to each heat flux term of the thermal balance equation:

$$q_{conv} = q_{el} - q_{cond.s} - q_{cond.b} - q_{rad}$$

the definition of the convective heat transfer coefficient:

$$h = \frac{q_{conv}}{(T - T_{aw})}$$

and Stanton number:

$$St = \frac{h}{(\rho_e u_e c_p)}$$

Once the heat flux specific error margins have been computed, the weighted-average is taken to obtain the uncertainty estimate for q_{conv}, h and finally St. The uncertainty estimates per heat flux are equal to 3.28 %, 0.14 %, 2.75 % and 0.13 % for respectively q_{el}, $q_{cond.s}$, $q_{cond.b}$ and q_{rad}. This equates to a complete, systematic error estimation of 4.6% for the primary campaign. In turn, a similarly conducted uncertainty analysis of the secondary campaign provides a systematic error of 7.3%. The relative error listing shows that the largest uncertainty originates from the q_{el}, which encompasses the measurement of power output and base resistivity. Looking back at the methodology, this inaccuracy could have been bypassed completely by incorporating a continuous read-out of the power supply output in both I (A) and U (V) through the LabView program. This way, the R_0 estimate would have been obsolete such that a prominent measurement error is avoided. The complete QIRT uncertainty estimate is made by combining the ϵ_{sys} with the inherit experimental sensitivity or randomized variance, ϵ_{var}. The latter is described in Section 5.2.1.

Chapter 5

Results

The setup of the current thesis required Schlieren and PIV to respectively visualize and quantify the turbulent, supersonic boundary layers, subjected to large, ribbed roughness elements. In turn, through QIRT, direct temperature measurements lead to the computation of heat transfer data. As PIV serves both as flow quantification and validation tool, the derived flow fields are assessed for both mean flow and turbulence properties. In this Chapter, the results obtained by Schlieren, PIV and QIRT are provided. In order to comply with the structure of the thesis, it is decided to subdivide the results in a visualization and a QIRT section, where respectively the results from Schlieren and PIV (Section 5.1), and QIRT (Section 5.2) are provided.

5.1 Flow visualization

Through Schlieren visualization, it was possible to illuminate the entire flow field of each roughness model. Unfortunately, by the limited accessibility of the ST-15 test section, this did not hold for PIV (Appendix H). As such, it is required to combine the observations from both visualization techniques in order to substantially conclude upon the effects of various flow phenomena occurring amongst the test plates. The latter is done in this section, by providing spark-Schlieren images, mean flow and turbulence flow fields; segregated according to pitch and height effects.

5.1.1 Nomenclature for discontinuities

A substantial portion of the observations are directly found at the hand of the spark-Schlieren visualization results (Section 3.3). Therefore, prior to the discussion on the flow phenomena, the appearing discontinuities and corresponding nomenclature are clarified. In assistance of this, Figure 5.1 is provided; depicting a spark-Schlieren image of the flow field which result from the 2.4/30 model (Section 3.3). Each number corresponds to a specific discontinuity, which either originates from interfering elements of the wind tunnel or from the geometry itself. The oblique shock wave (OSW), at the most upstream portion of the test section is one of such interfering discontinuities. This OSW (1) is formed by the leading edge insert used for the Schlieren and PIV setup (Figure 3.3), which discontinues the curvature of the Mach block. As a result, the flow is turned into itself and causes this compression wave to occur; degrading the freestream Mach number from 2 to ~1.8 (Appendix O). This OSW reflects from the top portion of the test section, and forms a weaker shock depicted by (2). The final interfering set of SWs is indicated by (3), and originates from the screw holes used to fix the leading edge insert. Within these SWs, respectively an expansion wave (EW), OSW and another EW are seen. From a preliminary analysis, it was seen that (3) is relatively weak and negligibly influences the downstream flow fields. In addition, by covering-up these screw holes, the flow either hardly improved or worsened. Therefore, it was decided not to cover the screw holes such to keep the interference minor and identical amongst all experiments.

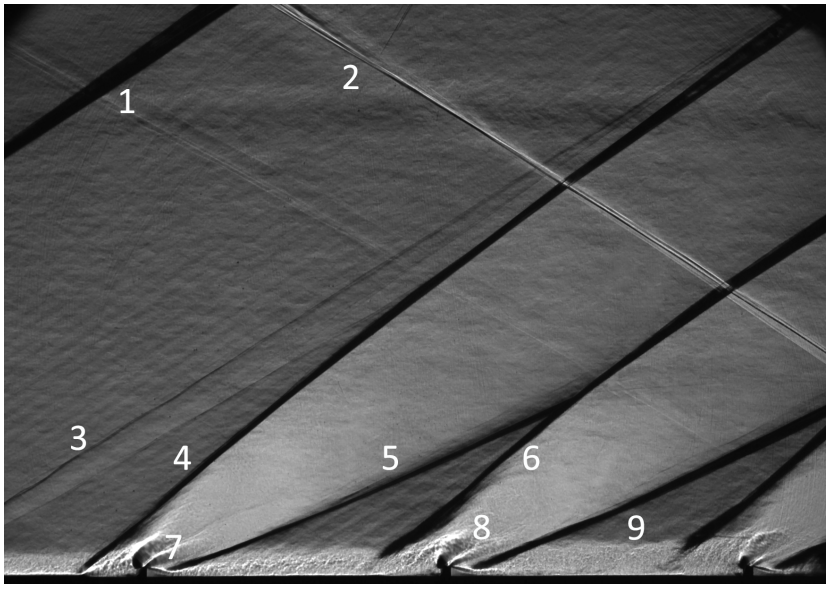

FIGURE 5.1: Discontinuity types occurring in the ST-15.

The remaining discontinuities are all assigned to the geometry itself, and correspond to respectively a blockage shock wave (4), impingement shock wave (5), recurring blockage or deflection wave (6), shear layer (7) and expansion wave (8). From the description in the following section, it becomes evident to what extent each discontinuity occurs for the respective models. It has to be noted though that waves 1 – 4 appear for every single model as each is tested with the same wind tunnel configuration and flow conditions. As the primary aim is to optimize the heat transfer properties of the flow, there is focused on the development of the boundary layer (9). Therefore, the Schlieren images depicted further in this chapter are cropped to primarily display this feature. As a result of this, the Schlieren images are approximately equal to the FOV utilized for PIV (Figure 3.10). Complementary to these FOVs, the reflected OSW (2) is excluded from the investigated flows and does not interfere with the results.

5.1.2 The effect of pitch

In Section 3.2.1, the geometrical definitions of all fifteen models were described based on respectively the relative height (e/δ) and pitch (p/e). From these models, four testing sequences can be defined where: (1) p/e is constant at 5, (2) p/e is constant at 15, (3) p/e is constant at 20 and (4) p/e is variant at e/δ = 0.4 [-]. Each of these sequences can be identified from Table 3.1 and are chosen based on their height effect at constant pitch (1–3), and pitch effect at constant height (4). In this section, observations regarding the fourth sequence are described for which primarily the cavity type flows are found to vary. The resulting observations, in turn, are used to isolate the height effects at varying e/δ.

Description of the flow fields In Section 2.4, it was concluded that most flow phenomena resulting from the influence of large-ribbed roughness elements in subsonic flows are directly ascribed to certain cavity-type flows. From the Schlieren images in Figures 5.2a – 5.2f, it is observed that this is largely the same for the supersonic flow fields. As a result, the characterization of the boundary layer developed remains *repeated cavity flows*.

Generally, the p/e is observed to primarily control the occurrence of specific supersonic cavity flow types. However, as each interaction of the boundary layer (BL) with the ribs enhances the turbulence levels near the wall (and degrades the mean KE), slight changes in these cavity type flows occur moving downstream (Figure 5.5). Nevertheless, as the cavity flows remain relatively unaltered, the respective cavity flow classifications are discussed by focusing on the first rib pair. During the current discussion, the mechanisms of open – transitional – closed cavity are considered to be known to the reader. If this is not the case, one is advised to study the material in Section 2.3.

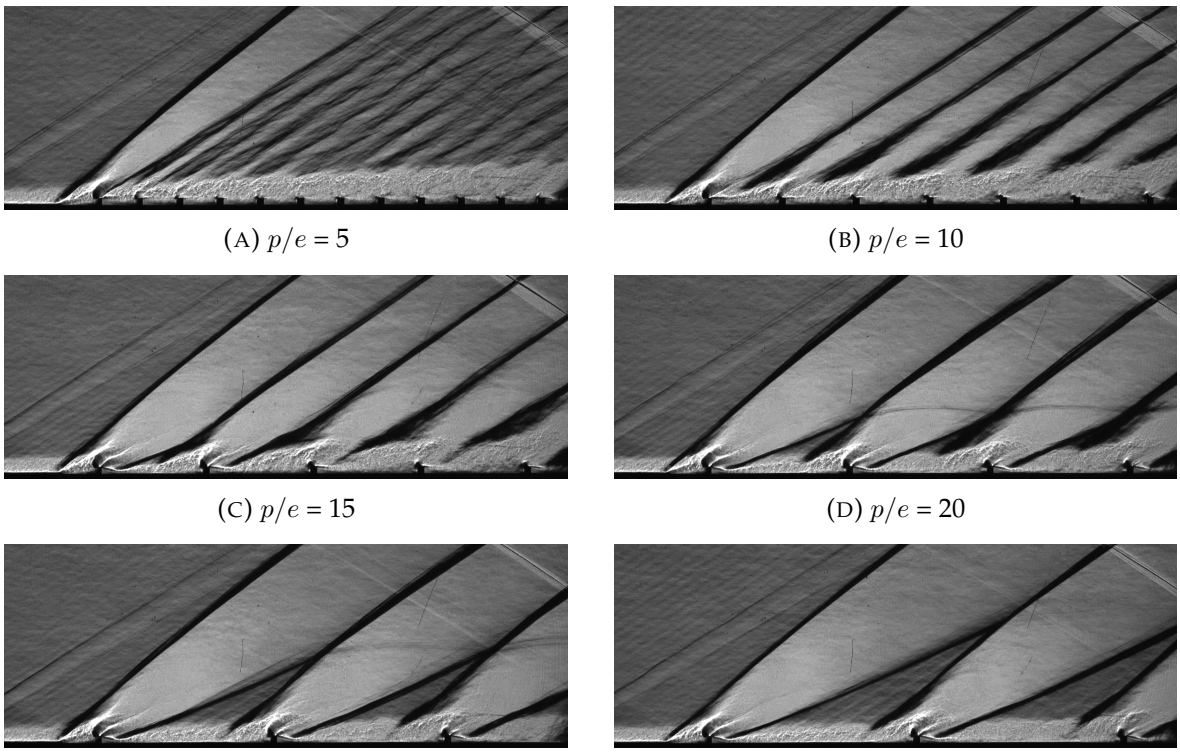

(A) p/e = 5 (B) p/e = 10

(C) p/e = 15 (D) p/e = 20

(E) p/e = 25 (F) p/e = 30

FIGURE 5.2: The effect of pitch at constant rib height $e = 2.4mm$ or $e/\delta = 0.4$.

Supersonic cavity research conducted by Stallings and Wilcox (1987) and Zhang et al. (2002) resulted in roughly the same cavity classifications, where $p/e \leq 10$ is considered *open*, $10 < p/e < 14$ *transitional* and $p/e > 14$ as *closed*.[34,13] Between their researches, a minor discrepancy existed regarding the latter classification where $(p/e)_{cr}$ = 13 for Stallings and Wilcox, and 14 for Zhang et al. The latter effect was assigned to the influence of a limited width-over-height ratio (w/e) of 5, which introduced wall effects onto the centerline for Stallings and Wilcox. Figure 5.2c displays the first occurrence of a delta-wave formation, common to closed cavity flows. As in this case w/e = 62.5, Zhang's conclusion regarding $(p/e)_{cr}$ seems correct; a $w/e \geq 10$ prevents the interference of wall effects to the centerline characteristics. These absence of wall effects in the ST-15 is proven by the QIRT measurements shown in Section 5.2. As a result, Zhang's cavity classification is found parallel to the current flow fields.

It is known that the transition between cavity flows is nearly exclusively defined by the p/e-ratio, which determines whether the shear layer bridges or impinges the cavity. The first model of the sequence (Figure 5.2a) depicts the formation of open cavity flows in between each rib pair. As a result, stable vortices are formed within each cavity such that – after the

initial impingement or blockage shock – a boundary layer is formed continuously on top of the crest of the ribs; insulating the floor. This semi-no-slip condition on top of the cavities is clearly depicted by Figure 5.3a, where a slightly concave shear layer is seen to bridge each rib pair. Judging by these flow fields, it is expected that these should be avoided when considering heat transfer maximization.

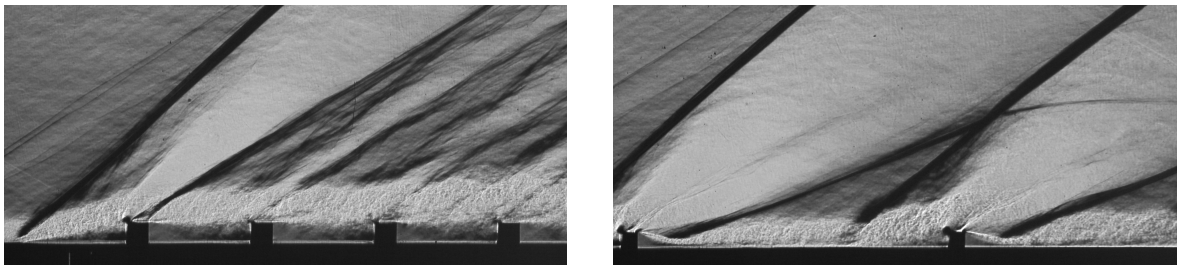

(A) e/δ = 0.8, p/e = 5 (B) e/δ = 0.8, p/e = 15

FIGURE 5.3: Zoomed spark-Schlieren representation of open- and closed cavity flow.

By extending the p/e-ratio, the shear layer is developed for a longer distance. As the shear layer grows thicker, it approaches the floor gradually. The presence of the floor hinders the free development of the lower part of the shear layer and pushes it upward. As a result, the main flow is deflected, producing a compression fan over the rear portion of the cavity. The latter is known as transitional cavity flow and is depicted by the 2.4/10 model in Figure 5.2b. Further increasing the p/e, the shear layer suddenly impinges onto the floor, completely cutting the backflow into two separate recirculations; i.e. closed cavity flow. This deprivation of air causes the pressure near the front part to drop to a minimum. To compensate for this, a strong expansion fan replaces the weak SW at the upstream rib and forces the boundary layer to enter the cavity and re-establish itself. Due to the lack of backflow towards the front of the cavity and the blockage of the downstream rib, large pressure increments are formed at the rear portion of the cavity. As a result of this, the BL at the floor is deflected and a second OSW is formed. This OSW transcends the crest of the ribs, where it collides with the initial impingement wave; forming a delta wave.

Equal to the cavity flow research conducted by Zhang et al. (2002), the final transition to closed cavity flow occurs once $p/e > 14$.[13] Therefore, the first closed cavity flow pattern is seen for the model at p/e equal to 15 (Figure 5.4c). The described flow field is shown in more detail for the 4.8/15 model in Figure 5.3b, proving the invariance of the cavity type flows with e/δ. Once a closed-cavity flow is reached, the characteristic distances between the upstream rib face and impingement shock (Ld1), as well as that between the deflection shock and downstream rib (Lf1) remain unchanged (Appendix B). The latter is caused by the invariance of the strengths of each discontinuity for a constant rib height. This feature is illustrated nicely by the vertical velocity fields obtained through PIV on the 2.4/5 – 2.4/30 models in Figures 5.4a – 5.4d. Each of these flow fields depicts an equally strong blockage shock at the most upstream position, followed by an expansion fan. Once this initial rib is passed and the model encompasses a $p/e \geq 14$, a strong EW is formed at the upstream rib accompanied by a delta-wave structure. As these discontinuities do not vary strength or position relative to the ribs, the p/e effectively only controls the distance over which the boundary layer remains reattached (Figures 5.2c – 5.2f). Therefore, it is expected that larger cavities will result in relatively more heat transfer, contrary to the notion made by Liou and Hwang (1992).[8] The latter effect is proven from the analysis shown in Section 5.2.

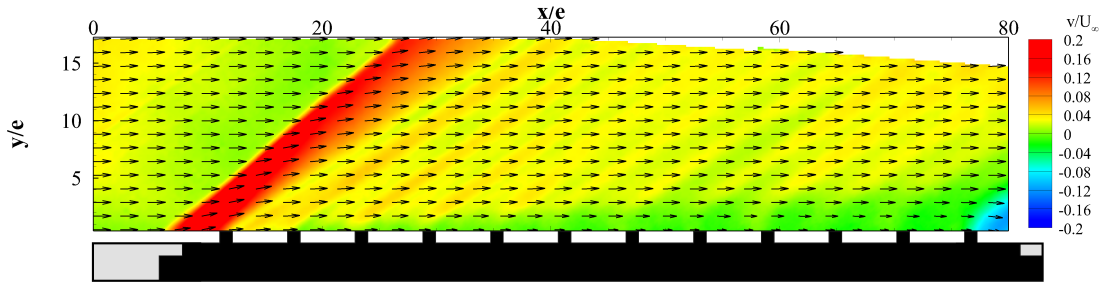

(A) $e/\delta = 0.4$, $p/e = 5$

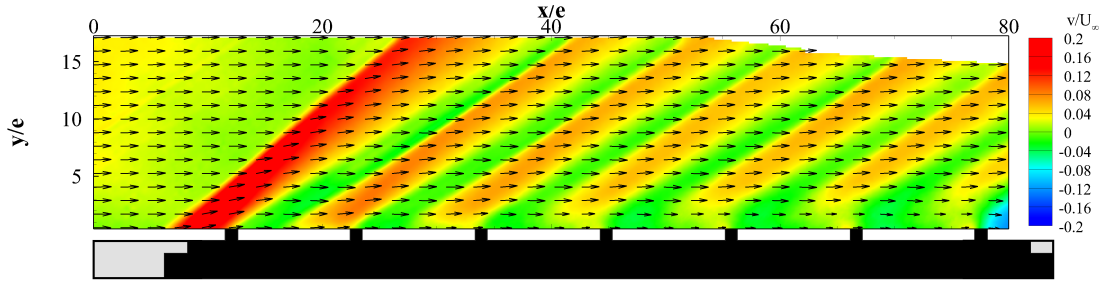

(B) $e/\delta = 0.4$, $p/e = 10$

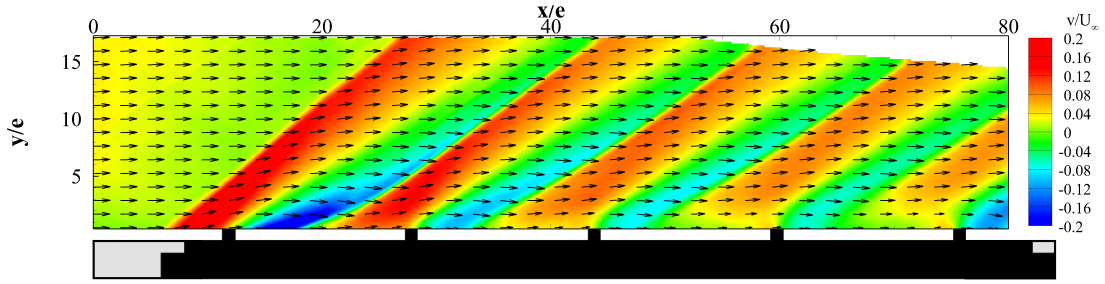

(C) $e/\delta = 0.4$, $p/e = 15$

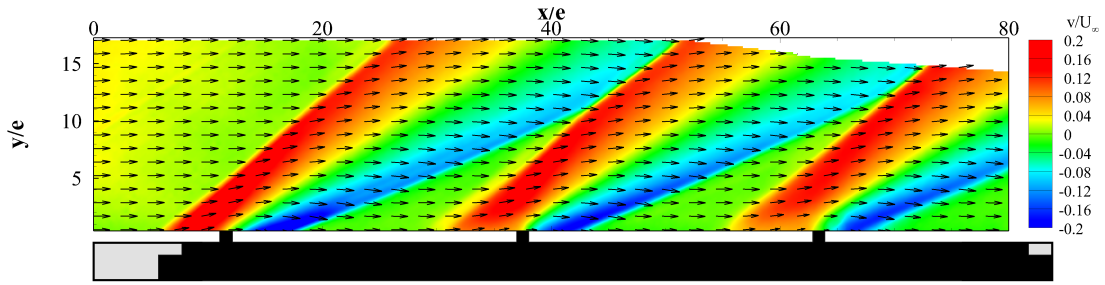

(D) $e/\delta = 0.4$, $p/e = 30$

FIGURE 5.4: Selected planar v/U_∞ – fields, for $e/\delta = 0.4$ and $5 \leq p/e \leq 30$.

The vertical velocity fields obtained through planar PIV (Figure 5.4), accurately indicate the transition from open – transitional – closed cavity flows. In contrast to the Schlieren images, however, the PIV fields clearly display a streamwise decreasing strength of the discontinuities. Whereas the strength of the initial blockage shock remains constant, the strength of

the discontinuities clearly degrade moving downstream. The rate at which this reduction occurs is seen to deteriorate with increasing p/e-ratios. From the Schlieren images (Figures 5.2a – 5.2f), this effect can be assigned to the transition from a discontinuous to continuous boundary layer. Whereas flow fields for $p/e \leq 10$ have continuous BLs, those for $p/e \geq 15$ become increasingly discontinuous. As a result, BL from open or transitional cavity flows develop continuously moving downstream, become thicker and scavenge more kinetic energy (KE) from the freestream. This is in contrast to the closed cavity flows, that redevelop again and again by re-impingement with the cavity floors.

Turbulence promotion The quickened deterioration of the discontinuity strengths as a result of the continuous boundary layer should be supported by an increase in turbulence level. This is, as a decrease in KE, $\overline{u^2}$ transfers into TKE and $\tau_{i,j}$, $\overline{u'v'}$. In Section 5.2.2 it is concluded that the heat transfer coefficients (h, St) correlate well with the Reynolds stress for turbulent mixing ($\overline{u'v'}$), this flow parameter is also used in this section.

The planar Reynolds stress fields in $\overline{u'v'}/u_{ref}^2$ in Figures 5.6a – 5.6c clearly display the increasingly limited turbulence levels for increasing p/e. In the subsonic research conducted by Liou and Hwang (1992), it was observed that an optimized heat transfer should exist for geometries at a p/e equal to 10. This was concluded upon by comparison with the prior results from Han (1984), which displayed a slight maximum in heat transfer for the same geometry. Han's research, however, was based on direct heat transfer measurements (i.e. temperature), whereas Liou and Hwang conducted measurements in velocity fluctuations, u' at 1 mm above the rib tops.[6,29] In the current research, a similar approach is taken and is summarized in the following figure:

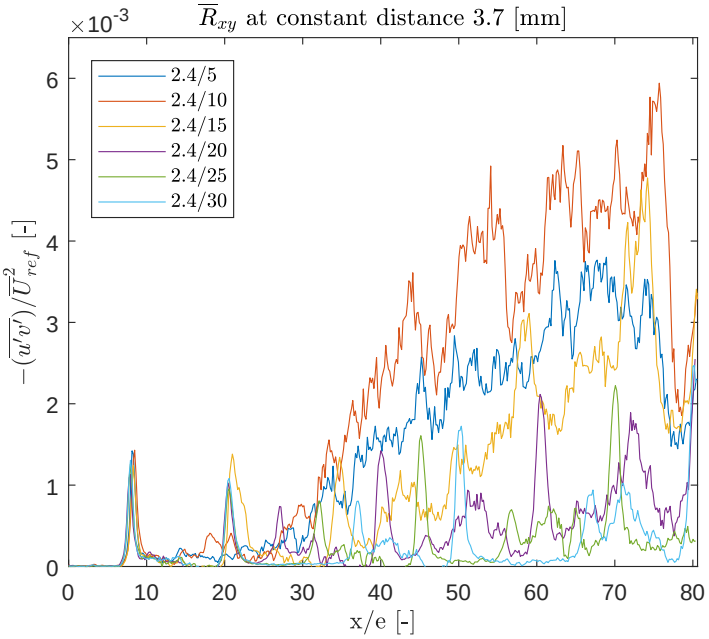

FIGURE 5.5: Development of Reynolds stress, sequence 4.

Which represent the development of the Reynolds stress for the complete FOVs at a fixed height from the rib tops of 3.7 *mm*. This height is chosen as it prevents the inclusion of outliers into the turbulence analysis, and as such makes observations more reliable. Figure 5.5 clearly depicts the increase of turbulence into the boundary layer for the open and transitional cavity flow models, i.e. 2.4/5 and 2.4/10. The latter is also illustrated by the

Schlieren images (Figures 5.2a and 5.2b), which both depict increasingly small turbulence structures (i.e. eddies) within their continuous BLs.[17] (Pope, 2012) These increasingly small turbulence structures are also observed by the Schlieren images of the closed cavity flows (Figures 5.2c – 5.2f). The corresponding $\overline{u'v'}$-profiles, however, do not necessarily represent the improved turbulence structures from their BLs. The reason for this is that the discontinuous BL and smaller eddies remain at the cavity floors, whereas the turbulence levels are registered above the crest of the ribs. Actually, for each closed cavity structure, primarily the BL impingements with the downstream rib faces are observed by PIV as here the turbulence effects do protrude into the PIV measurement regions.

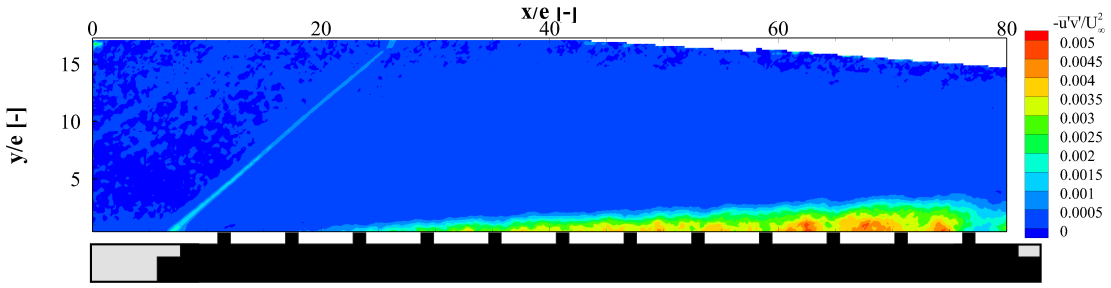

(A) $e/\delta = 0.4$, $p/e = 5$

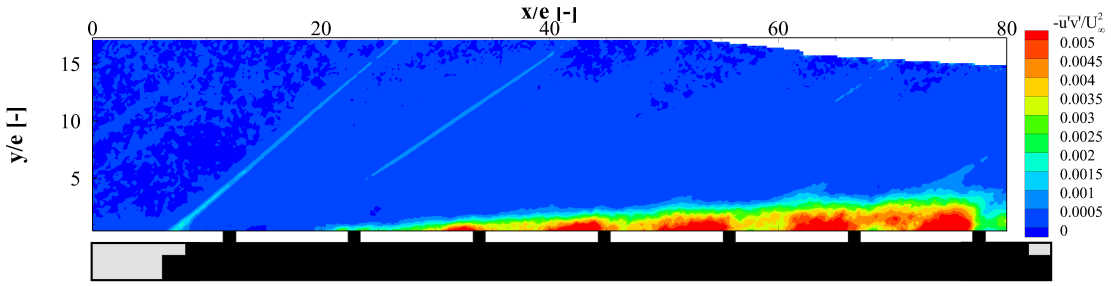

(B) $e/\delta = 0.4$, $p/e = 10$

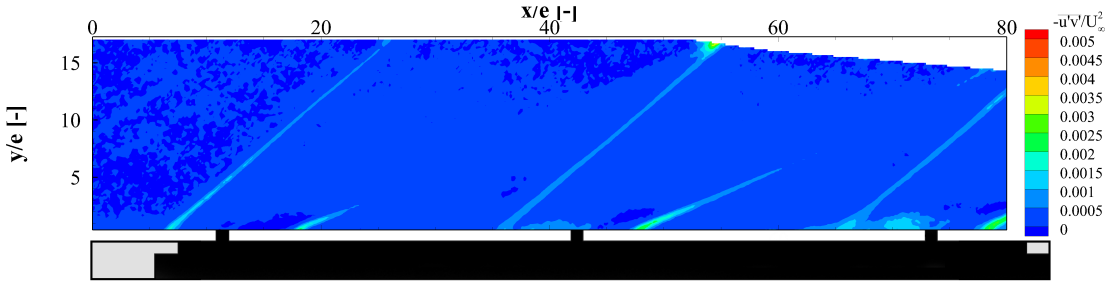

(C) $e/\delta = 0.4$, $p/e = 30$

FIGURE 5.6: Planar $\overline{u'v'}/U_\infty^2$ – fields, for $e/\delta = 0.4$ and $p/e \leq 30$.

In terms of heat transfer optimization, there should be as much high turbulent interaction with a surface as possible. As a result, it is expected that the $\overline{u'v'}$-profiles from Figure 5.5 are not representative for the heat transfer properties of the models. In contrast, these results are more a measure for BL turbulence enhancement than heat transfer enhancement. This means that the conclusions made by Liou and Hwang (1992) regarding the similarity in turbulence and heat transfer measurements may not hold in supersonic flows.[8] The fact that

a high level of turbulence exists right above the rib crest does not mean that a lot of heat transfer takes place, there should also be an improved wall interaction. These hypotheses are proven through the correlations in Section 5.2.

Cavity measurements To solve the uncertainties from the primary PIV campaign with regard to turbulent mixing estimations (i.e. validation of QIRT), it was decided to conduct a secondary campaign. For this campaign, there was focused on measuring inside the cavities of a select set of geometrical models. By the limitations of the wind tunnel setup (Section 3.4.4), however, only limited portion of each cavity could be illuminated by the laser sheet. As a result, each geometry was chosen based purely on position and the size of their most downstream cavities such to introduce sufficient light. The test plates which met this illumination criterion were the 2.4/15, 2.4/30, 3.6/20 and 4.8/15 geometries. The clearest, most reliable example is given by the 2.4/30 model:

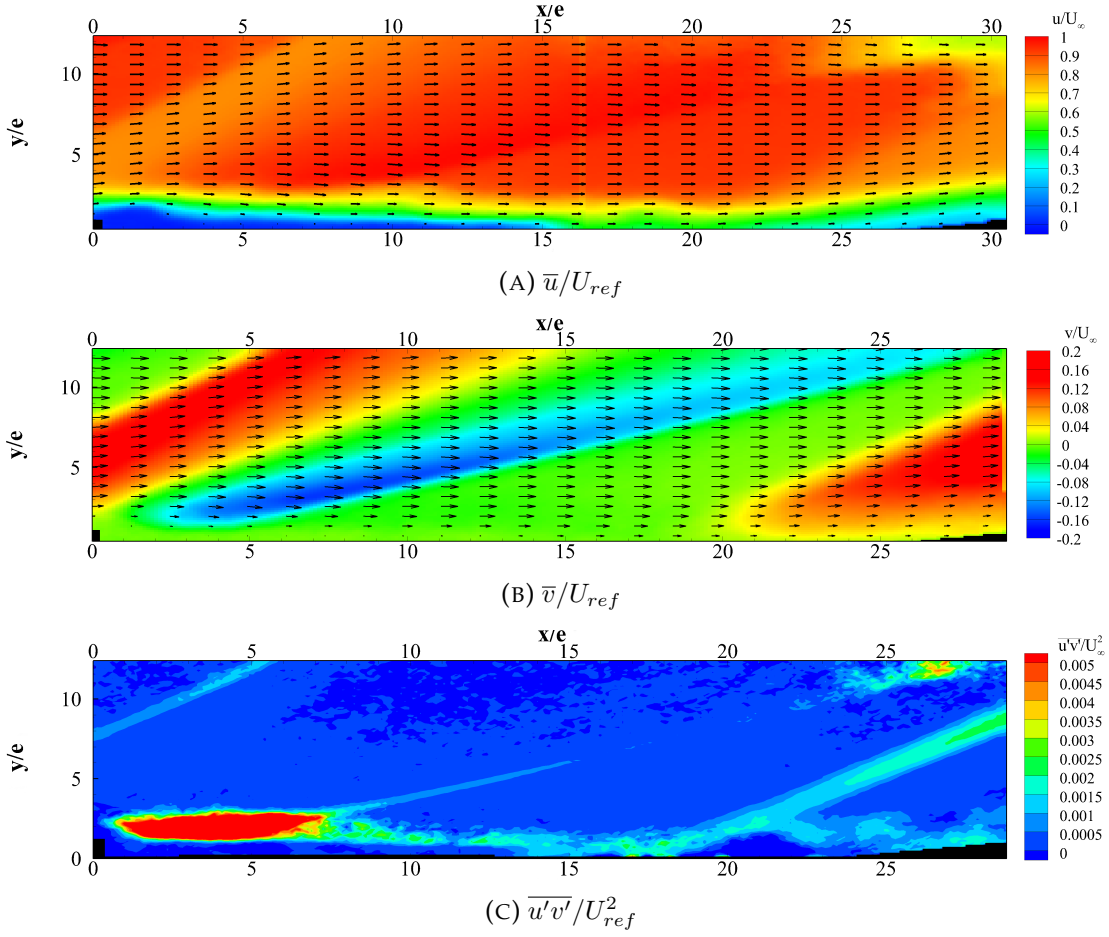

(A) $\overline{u}/U_{ref}$

(B) $\overline{v}/U_{ref}$

(C) $\overline{u'v'}/U^2_{ref}$

FIGURE 5.7: Planar flow fields for the final cavity of the 2.4/30 model.

For which, in Figure 5.7, respectively the non-dimensionalized horizontal (A) and vertical velocities (B), as well as the Reynolds stress (C) are shown. Comparing these flow fields with their counterpart from respectively the Schlieren (Figures 5.2f) and primary PIV campaign (Figures 5.4d and 5.6c), it is seen that these are largely in agreement. Due to the relative buoyancy of the DEHS particles with respect to the airflow, however, there were a significantly lower number of particles protruding the cavity.[51] (Ragni et al., 2009) As a result, it was seen that the signal-to-noise ratios (SNR) within DaVis were reasonable around the crest of the ribs, whereas this became unacceptably low near the cavity floors. The latter effect is seen to become progressively worse for models with larger the rib heights (Appendix

S) or closely-spaced ribs (Figure 5.8). As a result, most image pairs did not make the SNR required to obtain reliable, quantitative data. The goal of these measurements was to quantify the cavity flow fields, and observe the flow phenomena at the floor of closed-cavity type flows. As the measurement quality is insufficient, only marginal observations are made.

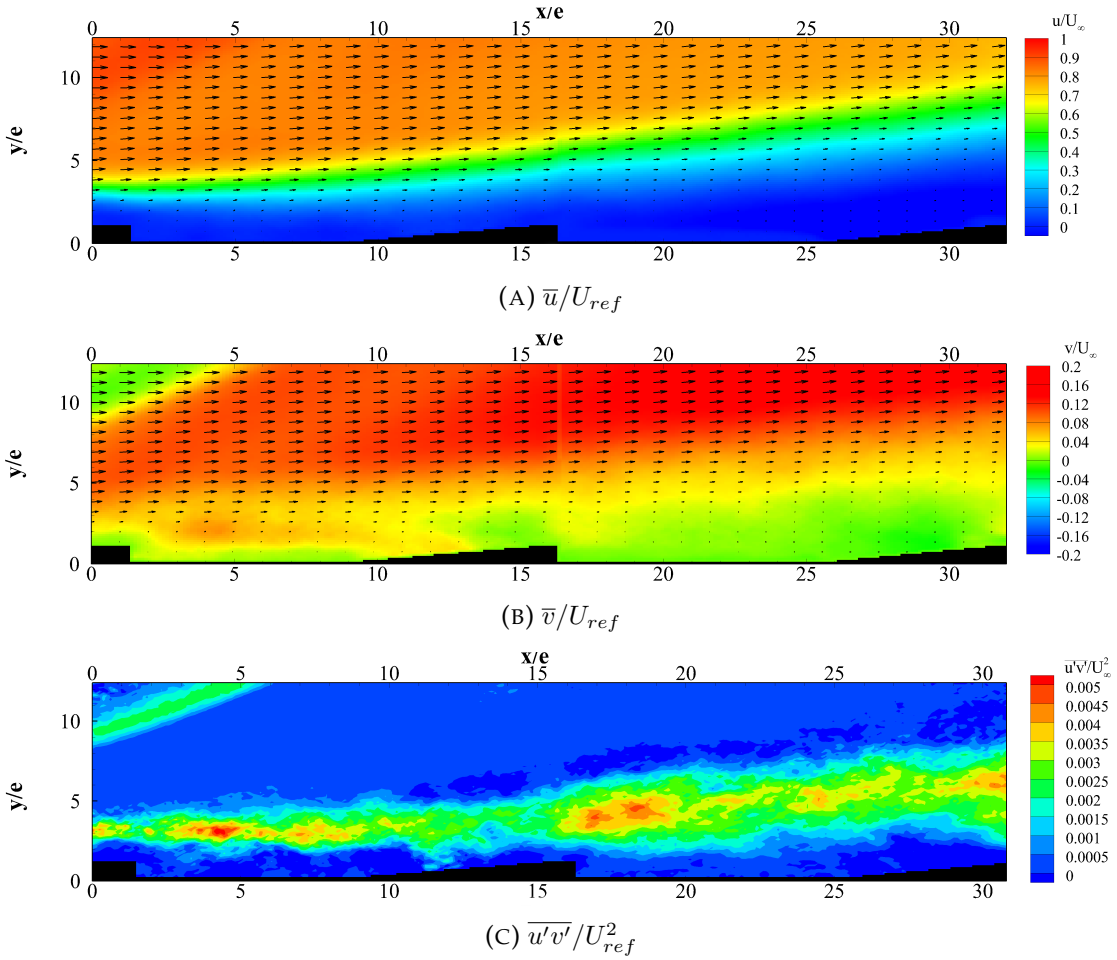

(A) $\overline{u}/U_{ref}$

(B) $\overline{v}/U_{ref}$

(C) $\overline{u'v'}/U_{ref}^2$

FIGURE 5.8: Planar flow fields for the final cavity of the 2.4/15 model.

Even though the 2.4/30 model resulted in the most reliable flow representation of all secondary PIV measurements, even here the buoyancy deficiencies are seen clearly by comparing the $\overline{u}$ field (Figure 5.7) to the boundary layer development shown in the Schlieren image (Figure 5.2f). Where the Schlieren image shows a upstream recirculation regions of approximately two rib heights wide, its PIV counterpart resembles a completely different boundary layer development. Thus, the measurements obtained in the direct vicinity of the floor are not used to draw explicit quantitative conclusions nor operate as a QIRT validation.

At the crest of the ribs, however, the results are sufficient. As such, it can be observed that there does exist an increased Reynolds stress within the cavity of the 2.4/30 model (Figure 5.7c). This implies that indeed most of the turbulent mixing and interaction takes place directly at the floor for closed cavity flows, in contrast to the transitional and open cavity flows. In addition, turbulence enhancing phenomena originating from discontinuities do impinge the rib crest in the direct vicinity of their origin. As such, these discontinuities should have a correlating counterpart for both Reynolds stress and heat transfer coefficient. It is this feature which is used to validate the QIRT results with PIV and (Section 5.2).

5.1.3 The effect of height

In the previous section, it was concluded that the p/e ratio determines which types of cavity flow are formed in between the consecutive ribs. This means that – regardless of the actual value of rib height e – similar overall flow topologies are formed once the p/e ratios remain fixed. In this section, the effect of roughness height e is investigated for respectively open- and closed cavity type flows. Once again, a qualitative view of the resulting flow fields is provided by spark-Schlieren images which are depicted in the following figures:

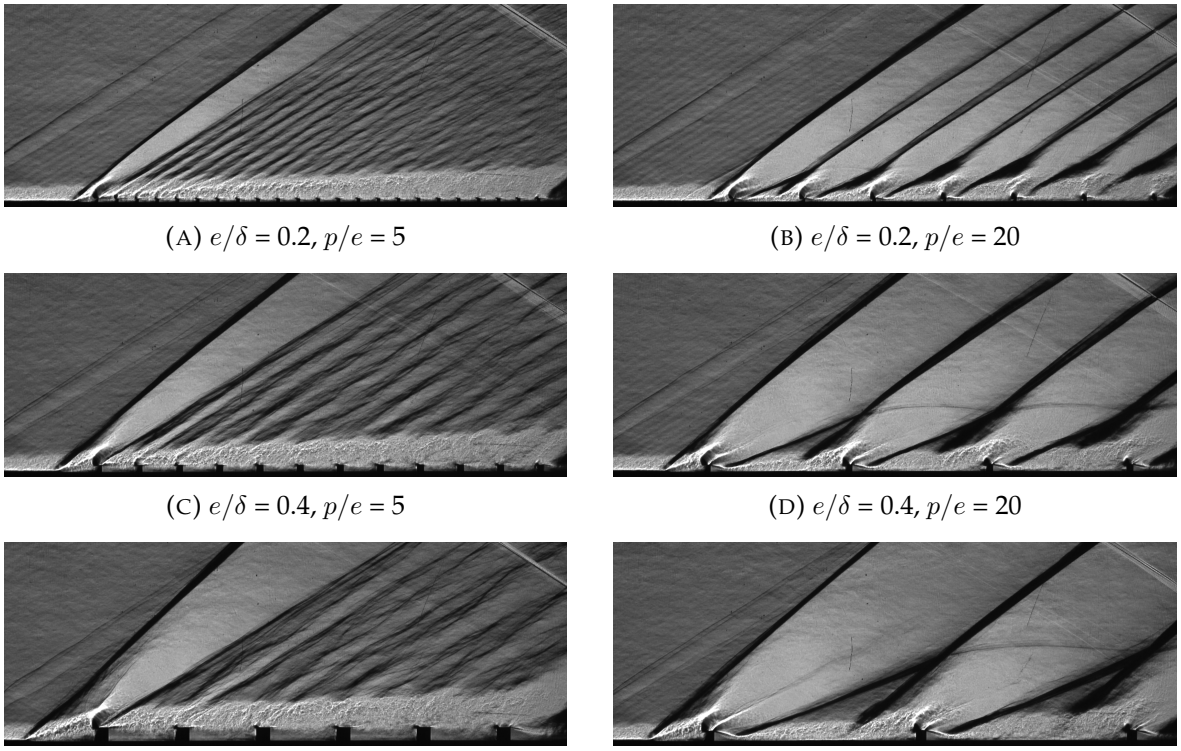

(A) e/δ = 0.2, p/e = 5 (B) e/δ = 0.2, p/e = 20

(C) e/δ = 0.4, p/e = 5 (D) e/δ = 0.4, p/e = 20

(E) e/δ = 0.6, p/e = 5 (F) e/δ = 0.6, p/e = 20

FIGURE 5.9: The effect of rib height for open (L) - and closed-cavity (R) type flows.

Where it is seen that respectively geometrical sequence 1 (p/e = 5) and 3 (p/e = 20) are used for this discussion. It is decided to use these sequences such to identify the effects which roughness height have for respectively continuous (Figures 5.9a, 5.9c and 5.9e) and disrupted boundary layers (Figures 5.9b, 5.2d and 5.9f). Both the open and closed cavity flow fields display the invariant flow topologies, relative to their respective rib height, e. As such, the variance of w/e-ratio (i.e. 31.25 – 125 [-]) is assumed to be negligible for the current discussion. This is in-line with the observations made by Zhang et al. (2002), who found that no variance in cavity classifications should occur once $w/e \geq 10$.[13]

Open cavity flows The closely spaced geometries produce a repeated open cavity flow field, for which a continuous boundary layer is developed over the crest of the steady vortices located in between the ribs. The primary difference between each BL is that for each increment in roughness height (e/δ), the final thickness of the BL increases as well; i.e. from ~9.0 to 13.7 mm. After the initial blockage OSW emanating from the most upstream rib, the boundary layer starts to develop from the same position. However, once the rib height is larger, a more substantial portion of the boundary layer is blocked and a stronger SW is formed (Figure 5.10). This means that, even though the BLs develop similarly from the same streamwise location, the starting conditions are different as $\overline{u}$ is lower and $\overline{u'v'}$ is higher. As

a result, more KE of the freestream is converted into turbulence which continues along the complete geometry of each model. This fact is illustrated well by the FOV profiles depicted in the following figures:

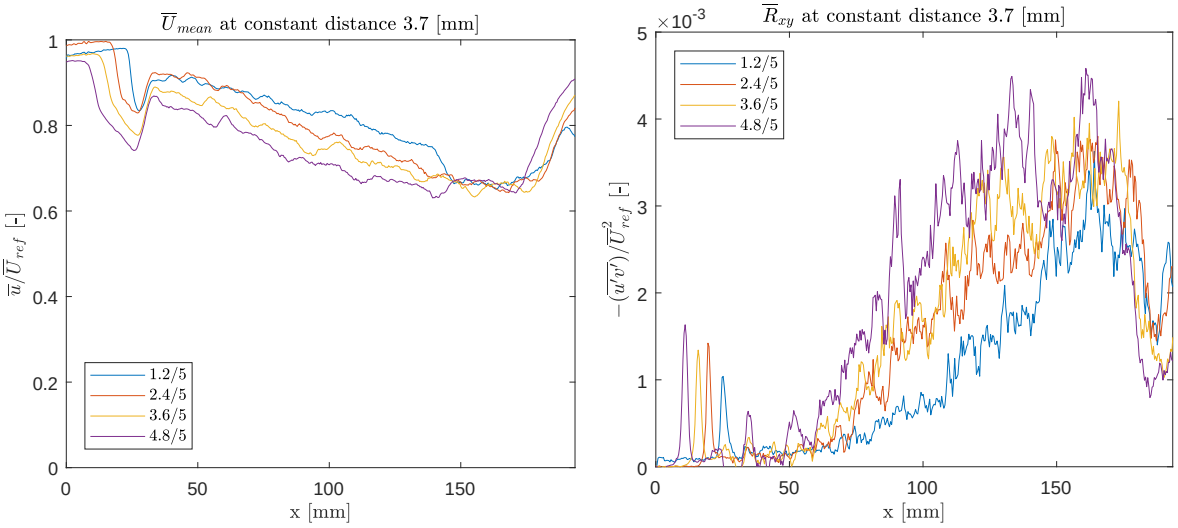

FIGURE 5.10: Development of mean flow (left) and turbulence properties (right), sequence 1.

Where the $\overline{u}/u_{ref}$ profiles in Figure 5.10 show an increasing mean velocity deficit at the initial blockage shock, whereas the $\overline{u'v'}/u^2_{ref}$ profiles in display a growing initial turbulence peak for an increase of e/δ. These initial turbulence peak excitations are followed by a continuous turbulence growth, which is the result of the increasing height of the continuously developing boundary layer. As the top of the BL increases, it meets decreasingly disturbed portions of the freestream. These higher regions of the flow, in turn, have an inherently higher velocity which makes a collision more fruitful in terms of turbulence production. This also explains the steepened growth in turbulence levels by larger rib heights (Figure 5.10, right). The BLs develop similarly undisturbed over the crest of these closely spaced rib geometries, whilst starting at a higher portion within the BL. Therefore, over the coarse of the BL development, relatively more energetic flows are encountered. As a result, a larger velocity deficit $\Delta\overline{u}/u_{ref}$ and a higher turbulence intensity increment $\Delta\overline{u'v'}$ are established.

The turbulence profiles depicted in Figure 5.10 have been derived from the planar PIV analyses on the complete FOVs of the primary campaign. Two examples of which are shown in Figure 5.12, displaying the FOVs resulting from geometries with a p/e of 5 at e/δ equal to respectively 0.2 (A) and 0.6 (B). From the planar FOVs, it becomes clear that around the crest of the geometries the turbulence production stays relatively unaffected by the presence of the ribs. This implies that – apart from the initial upstream blockage impingement – no strong impingement occurs downstream due to the continuous, (semi-)no slip conditions. The latter effect is in direct contrast with closed cavity flows (Figure 5.13), where turbulence excitations are forming by the interaction with each of the rib impingements.

In terms of heat transfer optimization, it is expected that the improved turbulence levels for $p/e < 10$ provide an adverse view of reality. Even though the turbulence levels rise for increments in e/δ, these useful mixing properties remain distant from the cavity floors. In fact, at larger roughness heights, these improved turbulence levels are even more distant from the floor and actually prevent more heat transfer from taking place. The latter is proven by the direct heat transfer measurements conducted through QIRT (Section 5.2).

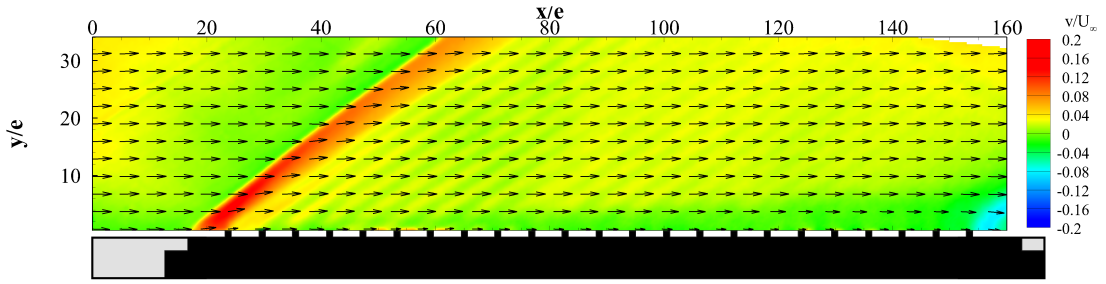

(A) $e/\delta = 0.2$, $p/e = 5$

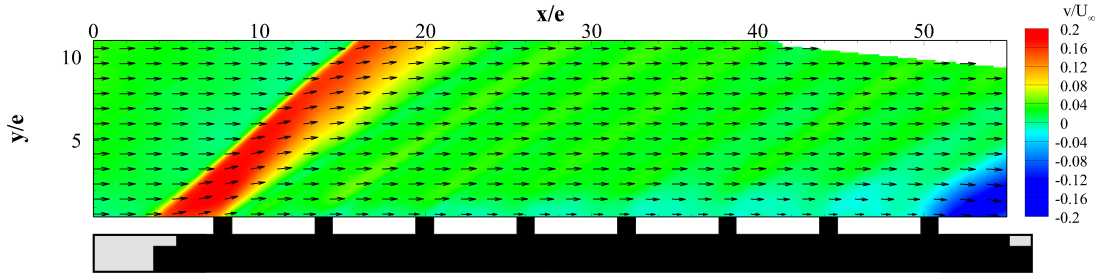

(B) $e/\delta = 0.6$, $p/e = 5$

FIGURE 5.11: Planar v/U_∞ – fields, for $p/e = 5$ and respectively $e/\delta = 0.2, 0.6$.

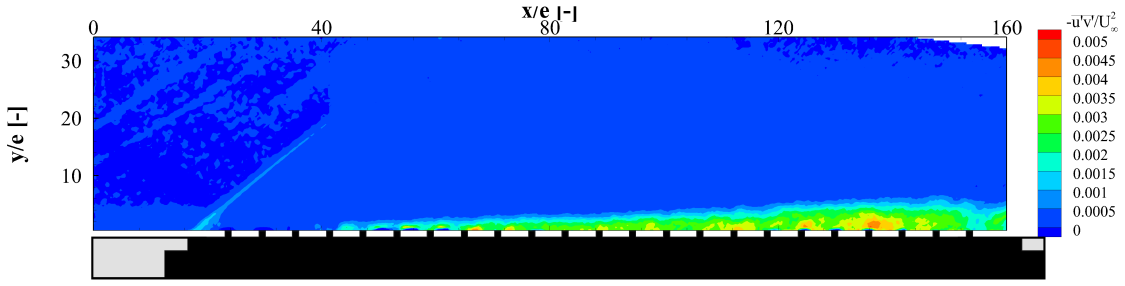

(A) $e/\delta = 0.2$, $p/e = 5$

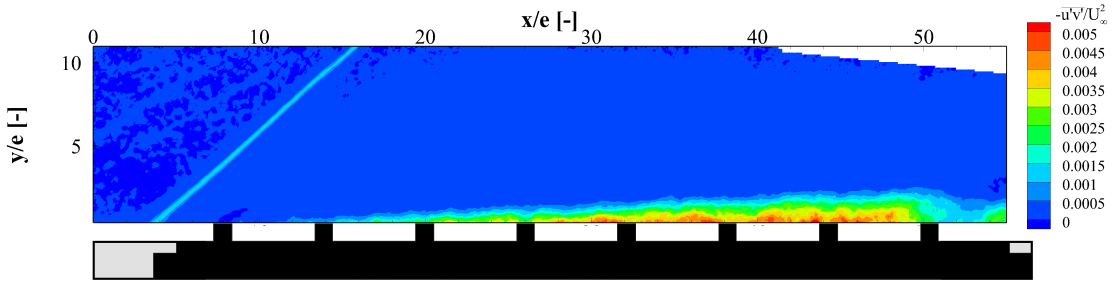

(B) $e/\delta = 0.6$, $p/e = 5$

FIGURE 5.12: Planar $\overline{u'v'}/U_\infty^2$ – fields, for $p/e = 5$ and respectively $e/\delta = 0.2, 0.6$.

Closed cavity flows In contrast to the repeated open cavity flows, the boundary layers for closed cavity flow fields ($p/e \geq 14$) are disrupted for each rib interaction. This is caused by the fact that for such flow fields, a series of strong EWs is formed at the upstream positions

of each repeated cavity (Figures 5.15a and 5.15b). As a result, the BLs reattach in the cavities and redevelop themselves prior to the downstream ribs. In turn, the BLs collide with these ribs and cause instantaneous turbulence enhancements by means of the blockage effect (i.e. impingement effects, Section 2.4). The result of this is that after each rib interaction, a more turbulent BL interacts with the floor of a downstream cavity. As the turbulence interaction primarily takes place inside these cavities, the thermal exchange is optimized. This is confirmed by Reynolds stress fields depicted in the following figures:

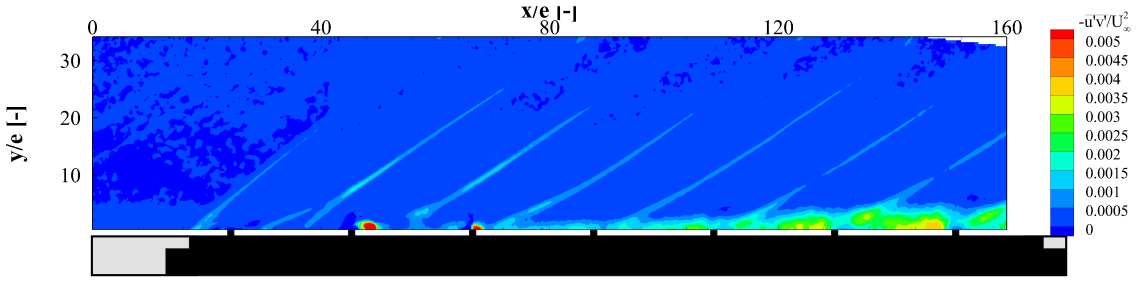

(A) e/δ = 0.2, p/e = 20

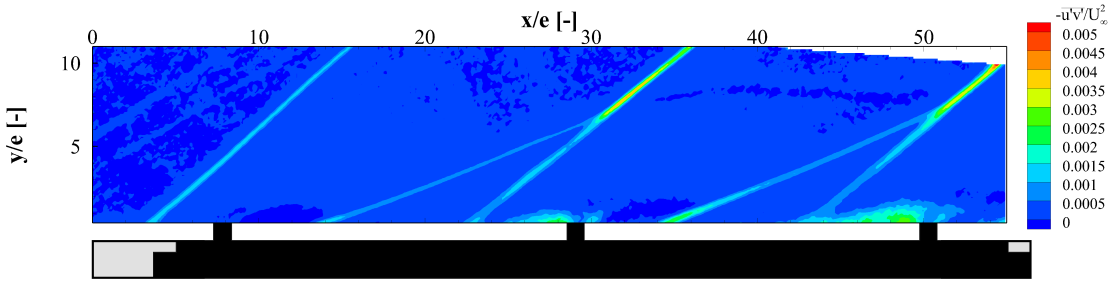

(B) e/δ = 0.6, p/e = 20

FIGURE 5.13: Planar $\overline{u'v'}/U_\infty^2$ – fields, for $p/e = 20$ and respectively $e/\delta = 0.2, 0.6$.

Where Figure 5.13a corresponds to the geometry at a p/e of 20 with a e/δ of 0.2, and Figure 5.13b depicts the same geometry at e/δ of 0.6. As indicated during the discussion on the effects of pitch, it becomes clear that the $\overline{u'v'}$ effects only protrude the crest of the ribs once a discontinuity or rib interaction takes place. By comparing the respective test models though, it is observed that these impingements and discontinuities become more energetic for larger rib heights. This is understandable, considering that larger rib faces bring about more blockage. Nevertheless, the increased levels of turbulence for each rib collision may give an adverse view of the heat exchange capabilities of each model.

This notion is confirmed by the horizontal velocity and $\overline{u'v'}$-profiles, indicated in respectively Figure 5.14. For each increment in roughness heights, more energetic but isolated turbulence enhancements take place; indicated by the increased $\overline{u'v'}$-peaks. Still, it is only the 1.2/20 geometry which effectively produces a semi-continuous increment in turbulent mixing along the length of the geometry. The same is seen for the corresponding u/u_{ref} profiles, for which merely the 1.2/20 geometry shows a continuous velocity deficit; indicating a conversion of KE to TKE. By comparing the Reynolds stress fields with their Schlieren counterpart (Figures 5.9b and 5.9f), it is found that each geometry provides an equal, yet scaled interaction of the BL with the cavity floor. Therefore, it is expected that – for closed cavity

flows – the geometry with the smallest e/δ would result in the most heat transfer. The latter notion is justified by the direct heat transfer measurement results shown in Section 5.2.

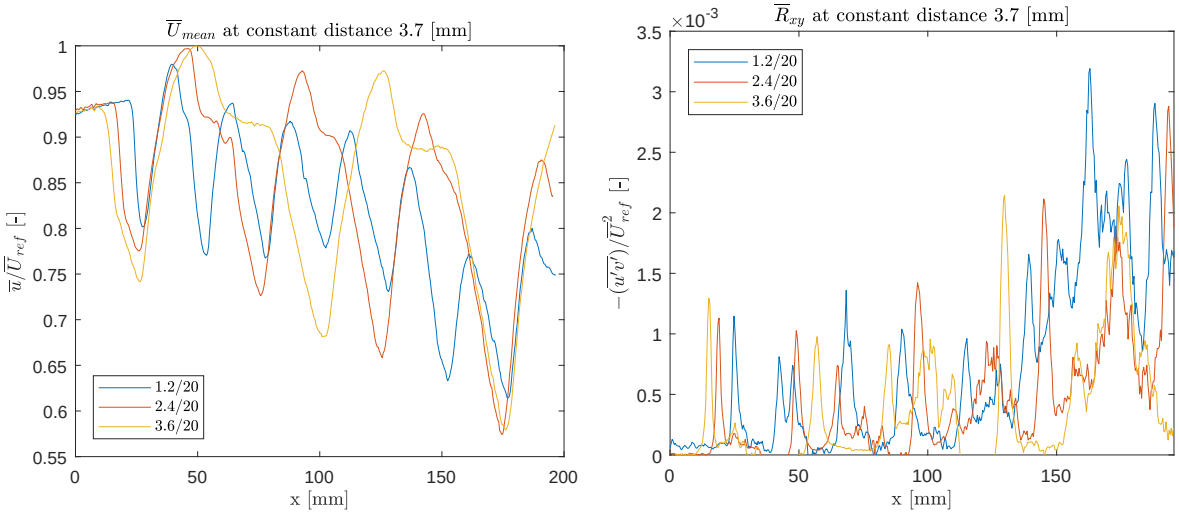

FIGURE 5.14: Development of mean flow (left) and turbulence properties (right), sequence 3.

Interestingly, this negative trend with respect to rib height is similar to that seen for the open cavity flow fields. In this case, however, it is not the cavity flow topology which causes this effect (i.e. insulation) but the absence of rib repetition which limits the improvement in heat exchange. This observation suggests that for closed cavity flows, the repetition of ribbed roughness elements weighs more than the roughness height in terms of turbulence promotion. This is in contrast to the repeated open cavity flows, which required the e/δ to be larger such to excite the BL more strongly. As a result, the turbulence production of open cavity flows is a direct cause of the external flow, whereas the turbulence enhancements of the closed cavity flow correlates with individual rib impingements. Relating this observation with regard to rib height to the heat transfer results found in Section 5.2.2, one can say that the resulting isolated impingements have a greater magnitude. However, contrary to smaller roughness elements, these flow excitations disperse from the cavity floors into the freestream; the exact opposite from where needed for heat transfer promotion.

This redistribution of turbulence into the freestream is a consequence of the increased intensities of the discontinuities at larger e/δ. By comparing the horizontal velocity fields (Figure 5.14) with the planar FOVs of respectively the 1.2/20 and 3.6/20 geometries (Figures 5.15a and 5.15b), the effects of discontinuity isolation become more evident. Along with the rib height increment from 1.2 – 3.6 mm, a significantly stronger EW is formed at the upstream ribs of the latter geometry. In addition, even the second EW is strong enough to completely resettle the boundary layer. This is in contrast to the 1.2/20 geometry, which only displays a delta-wave structure for the first rib pair followed by weak EWs progressing downstream the roughness geometries.

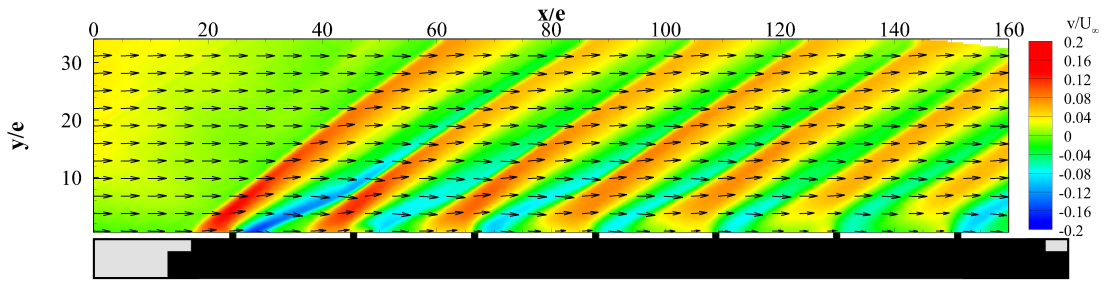

(A) e/δ = 0.2, p/e = 20

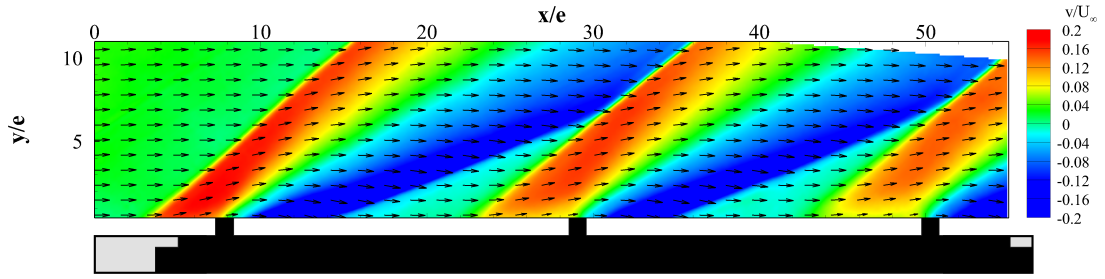

(B) e/δ = 0.6, p/e = 20

FIGURE 5.15: Planar v/U_∞ – fields, for $p/e = 20$ and respectively $e/\delta = 0.2, 0.6$.

The discussion on the effects of height (e/δ) for respectively open- and closed cavity type flows has indicated that the disruption of the BLs give rise to completely opposite mechanisms of turbulence enhancements. Where the open-cavity flow displays a boundary layer development equal to that of a regular flat plate, the closed-cavity flows re-establish themselves with increasingly strong turbulence levels. Aliaga et al. (1993) have mentioned that either flow fields should be fully developed from the third rib downstream, resulting in similar velocity and heat transfer profiles.[10] The latter can also be observed from the various mean flow profiles in this section. In the following section, it is investigated whether actually a self-similar boundary layer is formed.

5.1.4 Boundary layer profiles

To accommodate the investigation to the existence of self-similarity for repeated cavity flows, the development of the boundary layers is assessed through the BL profiles (i.e. $\overline{u}/u_{ref}$) of a select set of test plates. The supersonic roughness research from Latin and Bowersox (2000) has shown that these profiles should scale properly with the boundary layer thickness, δ.[11] For the current investigation, this thickness is defined by the local coordinate in y where the horizontal velocity matches the freestream velocity, u_{ref} within 99%; i.e. δ_{99}. Equally to the previous discussion, it is decided to check the influence of both continuous and discontinuous boundary layer topologies. Therefore, four geometries were chosen at respectively a pitch of 5 (i.e. open cavity) and a pitch of 20 (i.e. closed cavity).

In order to allow an equal comparison between roughness geometries, the locations of the BL profiles were defined to be exactly at the center of each rib top. The results of which are shown in Figure 5.16 for the open cavity, and Figure 5.17 for the closed cavity flows. Interestingly, both open cavity flow geometries display a collimated set of boundary layer profiles, whereas the closed cavity flow fields display the complete opposite; implying that

self-similarity only occurs for open cavity flows. This was to be expected, considering that BLs of the open cavity flows were formed continuously by the semi-no slip conditions at the crest of the ribs. In contrast, each closed cavity flow is forced to redevelop itself after each rib impingement.

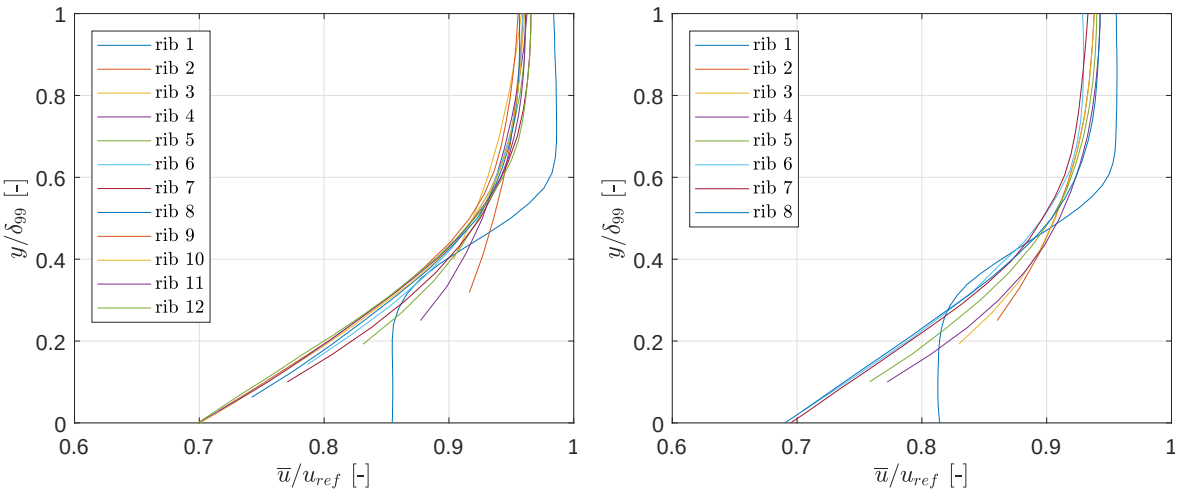

FIGURE 5.16: BL development across open cavity geometries, 2.4/5 (left) and 3.6/5 (right).

A more in-depth analysis shows that these self-similar conditions hold from the fourth rib downstream; in between the fourth and fifth rib. This is in contrast to the observation made by Aliaga et al. (1993), who found similar cavity flow conditions from the third rib.[10] One has to be aware of the difference between the similarity mentioned in their research, and the self-similar boundary layer.[9] (White, 2006) Consequently, it takes one more rib interaction before self-similarity is obtained. In addition, contrary to cavity profile similarity, self-similarity is only formed for open or transitional cavity flow fields. In Section 5.2, similarity between repetitive cavity flow fields are discussed through the heat transfer data.

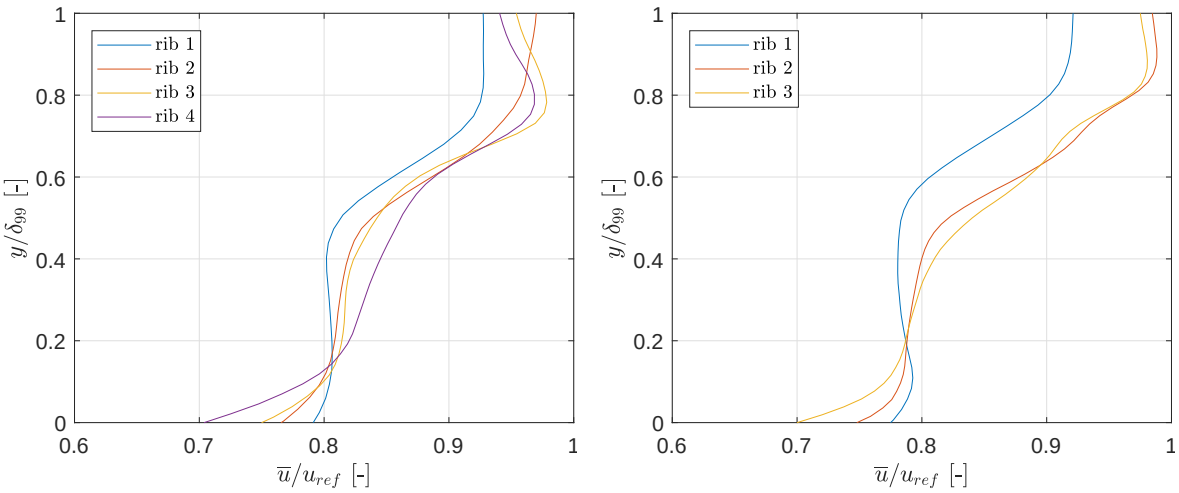

FIGURE 5.17: BL development across closed cavity geometries, 2.4/20 (left) and 3.6/20 (right).

An example of transitional cavity flow similarity is given by Figure 5.18, where the boundary layer profiles are shown to merge nicely from the fourth rib. It appears that the boundary layer development of this model is stable enough for the boundary layer to develop continuously. The latter is supported by the semi-continuous BL depicted by the spark-Schlieren image in Figure 5.2b, and the velocity field displayed by the PIV data in Figure 5.4b.

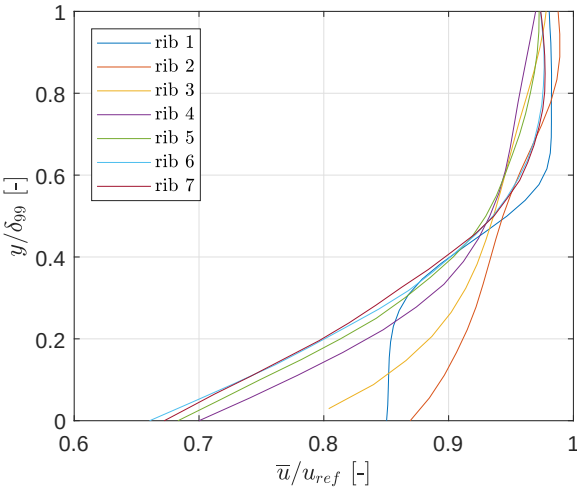

FIGURE 5.18: Transitional BL profiles.

Apart from the differences in boundary layer (profile) development, two critical similarities do exist between the progress of the BL development between open, transitional and closed cavity flows. All geometries show roughly the same BL profile for the first rib, which corresponds to the severely retarded flow field right after the initial impingement shock. In addition, the larger the relative rib height (e/δ), the more velocity deficit ($\Delta\overline{u}/u_{ref}$) occurs within the vicinity of the rib crest. It is due to these equal rib interaction effects that – regardless of the strength of the initial SW – the profiles have nearly the same shape relative to each rib. The latter is observed particularly well between the BL profiles of ribs 3 for respectively the 2.4/20 and 3.6/20 models (Figure 5.17). Comparing the velocity deficit for various rib heights between open and closed cavity flows, however, it is seen that significantly more momentum is lost for the closed cavity models. This, again, is assigned to the more severe rib impingements, which occur as a result of the reattached boundary layers.

5.1.5 Summary

Prior to discussing the findings obtained through QIRT, it is decided to shortly summarize the primary findings combined through the Schlieren and PIV techniques. The PIV technique was used in order to both visualize and quantify the flow fields, particularly the turbulence properties. As this technique is relatively cumbersome, and the ST-15 experimental setup was insufficient for proper inner cavity measurements, spark-Schlieren visualization was conducted beforehand. The latter technique proved to be quite useful in visualizing the exact developments of the BLs inside the cavities; assisting the PIV technique for assigning specific flow phenomena to profile variations. The discussions were subdivided into the effects of relative pitch (p/e) and roughness height (e/δ), where there was of a focus on the turbulence properties as a measure of heat transfer.

The investigations on the relative pitch ratio were conducted on the basis of finding an optimum roughness configuration; equal to Han (1984).[6] After this, the isolated effects of height could be derived. The main observations which can be made from the investigation of relative pitch p/e, are:

- The cavity flow types and accompanying flow features resemble the same as those seen in pure, supersonic cavity flow research (independent of w/e):

    1. $p/e \leq 10$: open cavity flows, stable vortices.

2. $10 < p/e < 15$: transitional cavity flows, centralized compression wave.
3. $p/e \geq 15$: closed cavity flows, delta wave structure.

- The turbulent mixing $\overline{u'v'}$ is maximal for p/e = 10, equal to Liou and Hwang (1992).[8]
- The maximum heat transfer is found by a combination of enhanced $\overline{u'v'}$ and prominent surface interaction; one of the closed cavity geometries.

The effects of roughness height were determined for geometries which resulted in respectively open and closed cavity type flows. This was done in order to isolate the effects of flow topology, and purely focus on the variations in BL development as a result of relative roughness height e/δ. The main observations made during the adjoined discussions are:

- The $\overline{u'v'}$ of open cavity flow geometries increase with the roughness height, e/δ.
- The $\overline{u'v'}$ of closed cavity flow geometries decrease with the roughness height, e/δ.
- Either geometrical models result in less overall turbulence interaction with the wall, caused by:
  - Open cavity: More distance between the crest of the ribs and the cavity floor.
  - Closed cavity: Less turbulence enhancement and more shedding into the freestream.
- Turbulence enhancement is determined by different flow mechanisms, the magnitude is depending on the rib height ,where for:
  - Open cavity: More energetic impacts results between the BL and the freestream, by regions which are located higher within the freestream.
  - Closed cavity: Turbulence is enhanced more by increased blockage effects.
- Self-similarity is found from the third rib downstream for the open cavity flows, independent of the rib height.

The results from the PIV measurements were gathered to function as a validation tool for the QIRT results. This is necessary, considering that the QIRT design, construction, testing and data reduction are all performed for the first time at the ST-15. Generally, it is expected that the Stanton number, $\overline{St}$ and Reynolds stress, $\overline{u'v'}$ display roughly the same trends for the developed cavity flows. However, as the PIV data does not relate the heat transfer measurements to the situation directly at the cavity floors (Figure 5.22), it is expected that these correlations hold mostly for closed cavity flows. For open cavity flows, there are no impingement effects or discontinuities which protrude the crest of the ribs. As a result, these flow fields are expected to display an adverse turbulence mixing effect than the actual heat transfer interaction. Still, in terms of validation, it should be possible to correlate the rib crest protruding turbulence effects with the heat transfer data. Fortunately, this is the case, as described in Section 5.2.2.

5.2 QIRT

The flow visualization techniques have shown that the flow fields correlate well with the predefined *repeated cavity flow* representations, as described in Section 2.4. In this section, the results obtained through the quantitative infrared thermography technique (QIRT) are assessed for repetitiveness, validated and then discussed. The validation is conducted by a comparison with turbulent mixing properties of the flow (i.e. $\overline{u'v'}$), derived through PIV.

This way, it is made sure whether the results are correct and to which level of detail (i.e. error margin) one is allowed to draw conclusions on the derived results. The results obtained by QIRT are mostly represented as $\overline{h}$- and $\overline{St}$-profiles, which are computed through the data reduction procedure described in Section 4.3. As a result, all profiles are computed using the settings defined prior, meaning that for each q_{conv} is derived excluding the $q_{cond.s}$-term.

5.2.1 Repeatability of QIRT

During the assembly of the test plates, it was decided to produce the fifteen primary geometries with those PCBs which had closest resistivity of all test plates (Appendix N). This was done in order to avoid as much experimental variation as possible and maximize similarity between the tests. In addition to these main models, three reference flat plate and two additional 2.4/10 test plates were made. Through the main models, the primary goal was to quantify the heat transfer properties of each cavity geometry and define their interrelations. In turn, the reference models were constructed such to analyze the coherence between the measurements and check the repeatability of the complete measurement technique.

In order to properly research the sensitivity and repeatability of the QIRT technique, each test plate is experimented upon at three distinct power levels, q_{el} varying at least 5% from one another. Regardless of the power setting and resulting surface temperatures, h should be independent and equal for each experiment (Appendix G). The following table displays the maximum variance (%) on the h-profiles between such consecutive measurements, which are computed using the data reduction routine discussed in Section 4.3:

TABLE 5.1: Maximum variance of the h measurements within the cavity of each model for consecutive experiments.

Test plates	Max. dev., Δh (%)	Test plates	Max. dev., Δh (%)
1.2/5	0.76	2.4/30	0.41
1.2/15	0.69	3.6/5	0.78
1.2/20	0.78	3.6/15	0.34
2.4/5	1.3	3.6/20	1.05
2.4/10	0.68	4.8/5	2.22
2.4/10 (low)	1.26	4.8/15	3.01
2.4/10 (high)	1.44	FP (BG)	-
2.4/15	3.13	FP (ref)	1.70
2.4/20	0.68	FP (ref2)	1.59
2.4/25	0.58		

The data from Table 5.1 shows that the overall Δh between experiments on the same model is of desired insignificance. For IRT experiments at steady-state, such variance levels are not uncommon. Aliaga et al. (1993) indicated that variance between two measurements could be as low as 0.3%.[10] Actually, on average, the outcome of h-profiles within cavities of test plates varies merely 1.24%, regardless of the power input. In addition, the percentile variances are completely incoherent with the stepwise changes in power settings or surface temperatures. This means that those experiments for which ΔP was at a maximum (i.e. 25%), did not necessarily result in the maximum variance in Δh (%). As a result, the indicated data variance estimates represent a randomized overall error of the QIRT technique and methodology (i.e. ϵ_{var}).

The correct functioning of the complete QIRT procedure, including the assembly process (i.e. insulation mounting, rib placement etc.), varying PCB resistivity and resulting adaptations to power supply settings, is proven by comparing the results from the three 2.4/10 models. These models were assembled completely separately, whilst the resistivities of the reference models were as far apart as possible (ΔR_0 = 9 Ω). As such, a comparison amongst these three represents the most severe experimental variation within the scope of the current experimental technique. The average $\overline{h}$-profiles of the final cavity of each model are provided in the following figure:

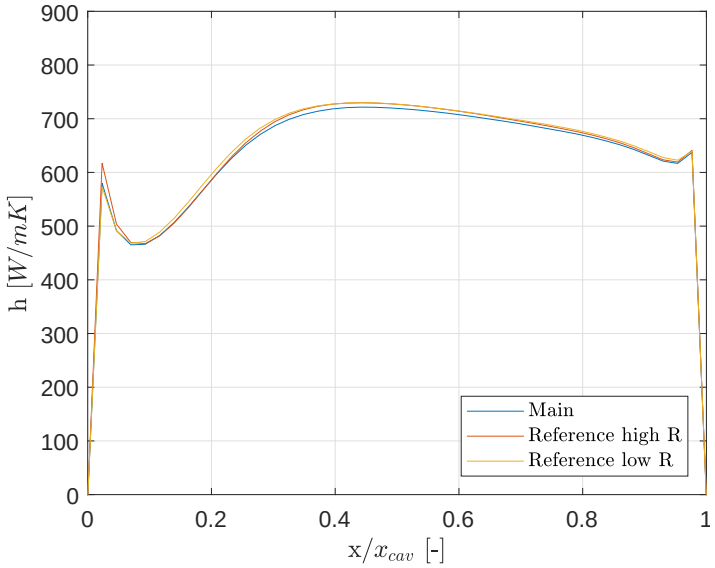

FIGURE 5.19: h-comparison between three 2.4/10 models.

Which directly displays the coherence between the three models, which were investigated upon separately at three distinct power levels. Their similarity is quantified by determining the average and maximum variance amongst the three experimental results, which are equal to respectively 0.67 and 1.00%. The closeness of this data is a direct proof of the correct functioning of the utilized methods form assembly to post-processing. As a result, one can conclude that the design, construction, experimentation and data reduction of this QIRT technique are both accurate and reliable. The complete uncertainty estimate of the current experimental technique is the summation of the systematic a priori error estimate (ϵ_{sys}) described in Section 4.3.8), and the indicated average variance (ϵ_{var}):

$$\epsilon_{QIRT} = \sqrt{\epsilon_{sys}^2 + \epsilon_{var}^2} = 4.74\% \tag{5.1}$$

Which is a very acceptable error margin for a QIRT technique. For the secondary campaign, only one power setting was used for each test plate. As such, it is impossible to conduct a variance computation equal to that shown in Table 5.1. Still, by comparing the primary with the secondary data, a variance estimate is made; being equal to 3.5% (Section 5.2.4). This means that the overall ϵ_{sys} for the secondary campaign, is equal to 8.1%.

In previous research, Han (1984) and Aliaga et al. (1994) estimated an average error margin of approximately 9.1 and 7.8%.[6,14] The equipment advancement made within the years between their research and the current thesis are likely what have caused the error reduction with regard to the primary campaign. As an example, the 600L Inframetrics IR camera utilized by Aliaga et al. had a NETD $\leq 0.1K$ which is four times higher than that seen for

the Cedip IR camera, utilized during the primary campaign. As a result, the complete error estimate, ϵ_{QIRT} is found to be to be realistic and valid.[83] (American Infrared, 1989)

5.2.2 QIRT validation

The fact that each separate measurement displays a low level of variance, does not necessarily mean that the represented data is correct. To accommodate this, the derived heat transfer data is compared directly to the obtained turbulence data.

Previous experimental research has shown that the average turbulent mixing properties ($\overline{u'}$, $\overline{v'}$ and $\overline{u'v'}$) of the boundary layer correlate directly with the heat transfer properties (h, St).[6,11] (Han, 1984; Latin and Bowersox, 2000) Actually Liou and Hwang (1992) found that an analysis of heat transfer optimization through turbulence properties ($\overline{u'}$) resulted in the same conclusions as direct temperature measurements made by Han et al., 1985.[7,8] Within this thesis, the same principle is used to validate the self-designed QIRT setup and data reduction technique. Through PIV, turbulence properties have been obtained at a fixed height above the crest of the ribs (i.e. $\pm 3\ mm$). By placing these profiles next to the heat transfer measurements, correlating trends are used as a proof of operation.

The validation is made through a comparison of respectively St from QIRT, and respectively $\overline{u'}$ and $\overline{u'v'}$ from PIV. Previously, Liou and Hwang (1992) were limited to observing the variations in streamwise standard deviation $\overline{u'}$. As a prior coherence has been proven between this flow property and heat transfer, this fact is duplicated first.

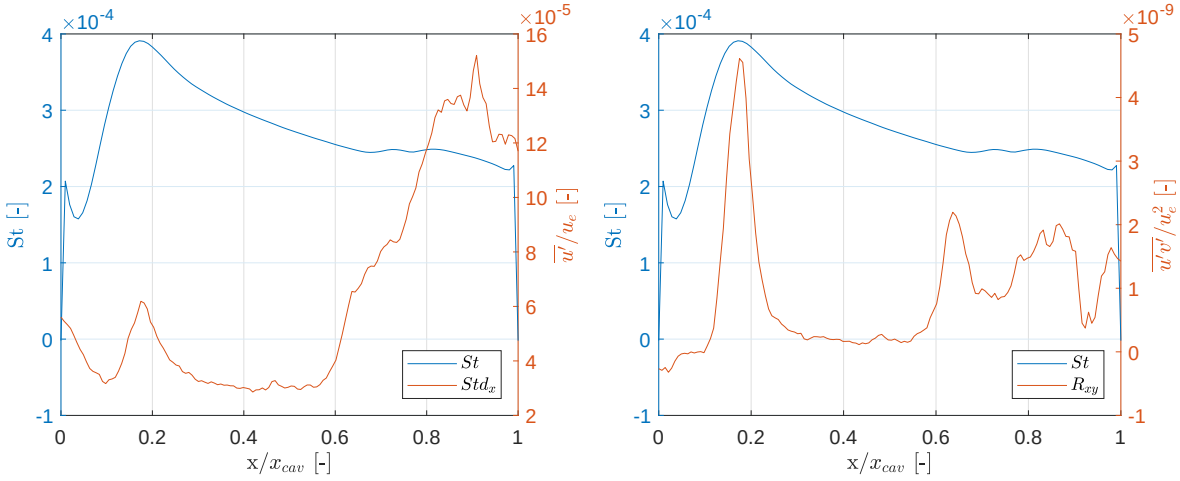

FIGURE 5.20: Comparison of turbulence and heat transfer profiles for 2.4/25 model.

Figure 5.20 does display a certain level of similarity with respect to the turbulence properties and St-profiles. From the Schlieren images in Section 5.2e, it is known that the 2.4/25 model produces a closed cavity type flow. As a result, BL reattachment, development and separation follow-up one another corresponding to respectively a heat transfer peak, near-linear decline, slight increment and decline in St. As seen in Figure 5.20, the St-profiles represent these features nicely. In contrast, the $\overline{u'}$ only partially displays these features and primarily correlates to the St-peaks. The same was found to hold for turbulent kinetic energy profiles during preliminary investigations. Opposite to the prior turbulence properties, the Reynolds stress curve does correlate more accurately with the heat transfer data by demonstrating nearly each flow feature with a $\overline{u'v'}$-counterpart.

Actually, most of the comparisons between St-profiles, and respectively $\overline{u'}$ and $\overline{u'v'}$ display a similar trend; whereas the standard deviation in x matches most heat transfer peaks with turbulence peaks, the more refined flow features do not stand out. In contrast, the Reynolds stress does more narrowly match the trends of each flow feature. This is logical, as the Reynolds stress is a direct measure of the complete turbulent mixing properties of a boundary layer. As it was proven prior that the $\overline{u'v'}$-data is converged, the conclusions derived from which are assumed to be reliable (Section 3.4.6). An exception to the rule is embodied by the measurements obtained for the open cavity flows:

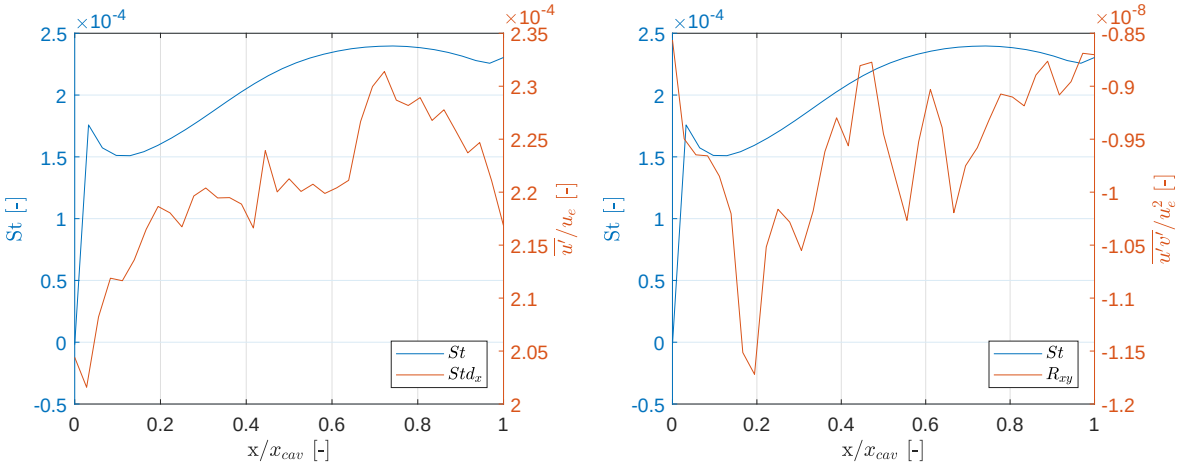

FIGURE 5.21: Comparison of turbulence and heat transfer profiles for 3.6/5 model.

Where the $\overline{u'}$ and $\overline{u'v'}$ profiles provided in respectively Figure 5.21 provide a significantly coarser representation of the relatively stable boundary layer formation. The latter is a direct effect of the distinct measurement locations of the temperature and velocity properties by respectively QIRT and PIV. This is illustrated by the following Schlieren image:

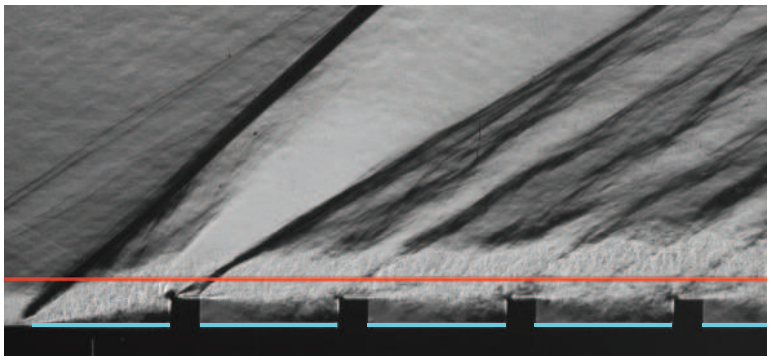

FIGURE 5.22: Measurement locations used for combined profile analysis; PIV (red), QIRT (blue).

Where an increasingly turbulent boundary layer transcends each cavity by the presence of a stable vortex below the crest of the ribs. As a result of this, the temperatures measured directly from the cavity bottom do not necessarily match the turbulence properties within the boundary layer itself. In fact, this feature holds for the St and $\overline{u'v'}$ profile comparisons of each model. However, the discontinuity effects of the closed cavity type flows typically impinge the region above the rib tops. As such, these features are also caught by the $\overline{u'v'}$ measurements and function sufficiently for comparative and complementary purposes. It is concluded that – apart from the open cavity flows – each Reynolds stress profile accurately

matches the qualitative trends of the St. This is in-line with the observations made in Section 5.1, where an adverse trend is seen between turbulence maximization and boundary layer – cavity floor interaction. The latter implies that it is expected that these $\overline{u'v'}$-trends are sufficient for qualitative purposes. However, for quantitative purposes, significant variances in turbulence and heat transfer are anticipated. The latter statement is confirmed by the integrated cavity correlations and trends in Section 5.2.5. Fortunately in Section 4.2.5, the measured levels of St were validated between the approximate flat plate solution (Equation 2.26) and the direct heat transfer measurements on the flat plate models (Appendix Q). As these values remained within $\pm$ 5% from one another, the St-levels are validated.

The qualitative observations made with regard to the turbulence and heat transfer profiles, in combination with the flow fields found prior, allow to conclude that the QIRT technique functioned as desired. Finally, including the relatively low systematic errors and randomized operational variance (ϵ_{QIRT} = 4.74%), it can be stated that the currently utilized QIRT setup performed both reliably and accurately.

5.2.3 Heat transfer profiles

Now that the obtained QIRT data is assessed for repeatability and accuracy, it is known to what level of detail the results can be evaluated. These combined results are presented in the form of heat transfer profiles in $\overline{St}$, along the cavities of each test plate. From the real-life application of these roughness elements, it is known that as much heat transfer should take place within a limited streamwise length. In order to get a reliable view of the heat transfer properties per geometry, the final cavities of each test plate are chosen. It is at these locations, where the boundary layers are developed the most and optimally indicate the difference in performance between the geometries. Even though the current supersonic flow regime is completely different to the subsonic conditions utilized by Aliaga et al. (1993), qualitatively the St-profiles are largely similar.[10]

Previously, it was seen that the obtained turbulence profiles (i.e. $\overline{u'v'}$) have a clear counterpart in terms of heat transfer. Most of the components of these profiles can be directly related to specific flow phenomena and discontinuities. In this section, the effects of these flow phenomena are identified by their relative effect on local heat transfer. This is, once again, performed at the hand of the isolated effects of relative pitch (p/e) and height (e/δ). For the discussions on heat transfer, however, it is assumed that the reader has studied the material described in Section 5.1. Therefore, knowledge regarding the occurrence and general effects of each mentioned flow phenomenon is assumed known such that there is focused on their respective effects on heat transfer. Each of the heat transfer profiles is displayed by including the complete error margins; custom to their measurement variation. In contrast to the data in Table 5.1, these variations are not fixed but vary over the position within the cavities, i.e. $\epsilon(x)$. This way, specific effects within the $\overline{St}$-profiles can be assessed in correspondence to their local error margin.

The effect of pitch In Figure 5.23, the $\overline{St}$-profiles are shown corresponding to the geometries of sequence 4; varying merely in p/e at a constant e/δ of 0.4 (Section 5.1). Overall, the transition from open – to – transitional – to – closed cavity flows is observed by the appearance of more profound heat transfer peaks which corresponds to flow reattachment.

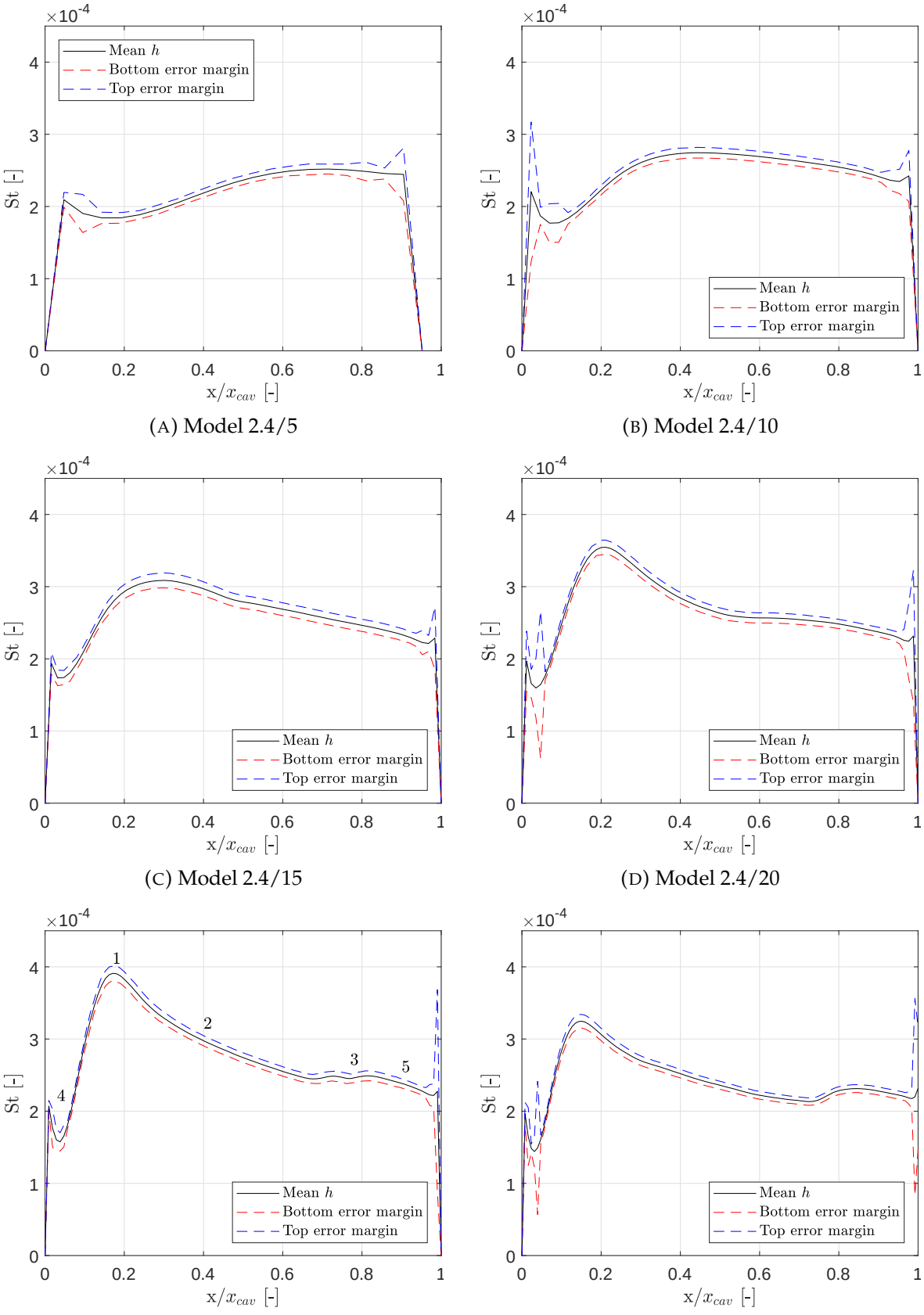

(A) Model 2.4/5

(B) Model 2.4/10

(C) Model 2.4/15

(D) Model 2.4/20

(E) Model 2.4/25

(F) Model 2.4/30

FIGURE 5.23: Comparison of the final cavity profiles, $e/\delta = 0.4$

Generally, it can be said that the characteristics of the flow phenomena belonging to respective cavity type flows can be clearly identified. At a p/e of 5, an open cavity flow profile is formed across the cavities of the entire test plate geometry. For such cavity flow fields, a stable vortex prevents the turbulent BL from interacting with the cavity floor. From the $\overline{St}$-profile in Figure 5.23a, though, it is seen that after the upstream recirculation, more heat transfer and thus more BL interaction takes place. This is in-line with the growing thickness of the shear layer, as identified from the Schlieren image in Figure 5.2a. For the most downstream cavity of the transitional cavity flow topology (i.e. p/e = 10), the BL barely impinges the cavity floor after a region of flow recirculation. This impingement is directly followed by a strong redirection of the, flow which disperses the BL into the freestream (Figure 5.2b). These flow phenomena have a clear counterpart in terms of heat transfer; where the recirculation acts isolating and a slight $\overline{St}$-peak follows due to BL impingement. In turn, the modest decline in heat transfer is a direct effect of the downstream blockage, which forces the enhanced turbulent flow out of the cavity.

Even though the closed cavity flows are defined to occur from $p/e \geq 15$, the effects of the complete set of related flow features (i.e. delta wave) are only observable from the profiles of the geometries with $p/e \geq 25$. Such typical delta wave structures consist of two OSW due to respectively BL reattachment and separation, which are disjointed by a developing BL. As indicated in Figure 5.23e, reattachment strongly increases the $\overline{St}$ (1), whereas the growing BL insulates the floor (2); reducing the level of heat transfer. Finally, a decline in $\overline{St}$ aims at the flow separation location (3), equivalent to the origin of the downstream OSW. The delta wave structures are surrounded by an upstream recirculation (4), and a downstream blockage region (5) which both decline potential heat transfer. The first does this by the formation of a stable vortex region, whereas the latter dilutes the BL into the freestream. Either effects insulate the cavities, but only affect a marginal portion of the complete cavities. For each closed cavity geometry (Figures 5.23c – 5.23f), strength of reattachment is seen to improve between the geometries at $15 \leq p/e \leq 25$, together with a more dominant effect of the BL. By the increase of the pitch, this BL development embodies a growing portion of the complete cavity length; improving the overall heat transfer characteristics. Interestingly, there is a decline in both heat transfer peak and overall $\overline{St}$ levels between the 2.4/25 and 2.4/30 models. Judging by the similarity in cavity flow topologies (Figures 5.2e and 5.2f), this is not the result of weaker BL reattachment. In contrast, this decline in $\overline{St}$ suggests that there is a decrease in turbulence enhancement by the enlarged cavity length. The latter is enforced by the turbulence levels depicted in Figure 5.5, and thus aims at the existence of an optimized heat transfer for geometries at a p/e of 25.

The effect of height It is clear that the characteristic cavity flow phenomena have a counterpart in heat transfer. The respective appearance of these phenomena is determined by the pitch, p/e. As such, it is expected that each cavity type flow encounters different effects from changes in relative rib height, e/δ. These effects are investigated by displaying the $\overline{St}$ cavity flow profiles for respectively, open (p/e = 5) and closed (p/e = 15, 20) cavity type flows.

In general, two primary effects can be distinguished by the increase of e/δ, namely; (1) cavity flow topology (in)variance, and (2) overall increment or decrement in heat transfer. As expected from the spark-Schlieren images, it is observed that the open cavity flow profiles are largely invariant to changes in e/δ (Figure 5.24). In contrast, the closed cavity flow profiles are heavily affected by the increments in rib height. Actually, this variation is seen to become progressively dominant, the larger the p/e becomes (Figures 5.25 and 5.26). This enforces the idea that, for closed cavity flows, the number of ribs transcended affects the BL

more prominently than the height of the elements. During the discussion on the turbulence levels, this effect was observed by the strength of the downstream rib impingements. In the current analysis, this same observation can be made by the relatively strong decline in $\overline{St}$ downstream of the cavities with $p/e \geq 15$, and a relatively insignificant decrement for geometries at $p/e \leq 10$; correlating with the absence of a blockage effect.

The overall levels of heat exchange are found to decline with e/δ, regardless of the p/e. The reasons behind this, though, are completely different for each cavity type flow. For the open cavity flows, it was seen that the BL freely transcends the crest of the ribs whilst tremendously increasing overall turbulence levels (Figure 5.10). Still, regardless of the improved turbulence levels, the distance between the turbulent BL and cavity floors increases as well. In the following figures, the resulting decline becomes evident:

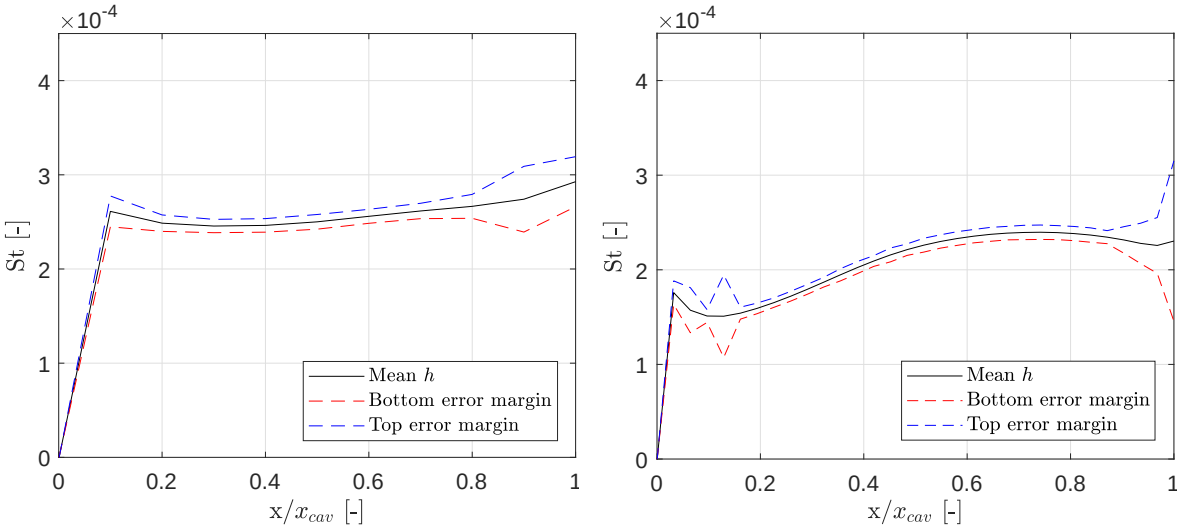

FIGURE 5.24: Final open cavity profiles, p/e = 5 at 1.2 mm (left) and 3.6 mm (right).

Where either $\overline{St}$-profiles of the 1.2/5 (left) and 3.6/5 (right) models display an insulating effect, which slightly decreases traveling downstream. This decrement is caused by the thickening of the shear layer, which results in more cavity floor interaction. The minor difference between the profiles shapes is caused by the limited resolution of the IR system (~1.6 pixels/mm). As such, approximately four data points are obtained for the 1.2/5 cavity, whereas 12 data points are found for the 3.6/5 cavity. Nevertheless, it is expected that either models would result in the same cavity profiles once more data points were available. Therefore, both profiles display a limited blockage effect by the slight decline of $\overline{St}$ at the most downstream position of the open cavities (Section 5.2.4).

The closed cavity profiles also contain differences in flow profiles. These, however, are not the result of a limited IR resolution but actual variations in flow topology. As mentioned previously, the strong impingements of the reattached BLs with each rib forces the BLs to become more turbulent. Inherently, this means that kinetic energy of the freestream is converted into turbulence such that the discontinuities become weaker. Between the profiles of the geometries with a p/e of 15 and 20, at respectively e/δ of 0.2 and 0.8 (Figures 5.25 and 5.26), this is seen by the strong upstream decrease in $\overline{St}$; corresponding to the recirculation zone. For geometries at larger rib heights, less rib impingements have occurred prior to the final cavity. In addition, by the pure increment in rib height, a stronger expansion wave is

formed for such geometries. As a result, the BL reattachment is more defined which subsequently gives rise to the maintenance of the unique closed cavity type flow fields. It should be noted, however, that – regardless of the rib height e/δ – cavity profiles similarly to those for the 1.2/15, and 1.2/20 models would form (Figures 5.25). This is, once a sufficient number of ribs is passed for a geometry with $p/e \geq 15$. Another way to judge the closed cavity profiles, is to see the models at e/δ of 0.2 as fully-developed whereas the larger geometries are within the BL development phase.

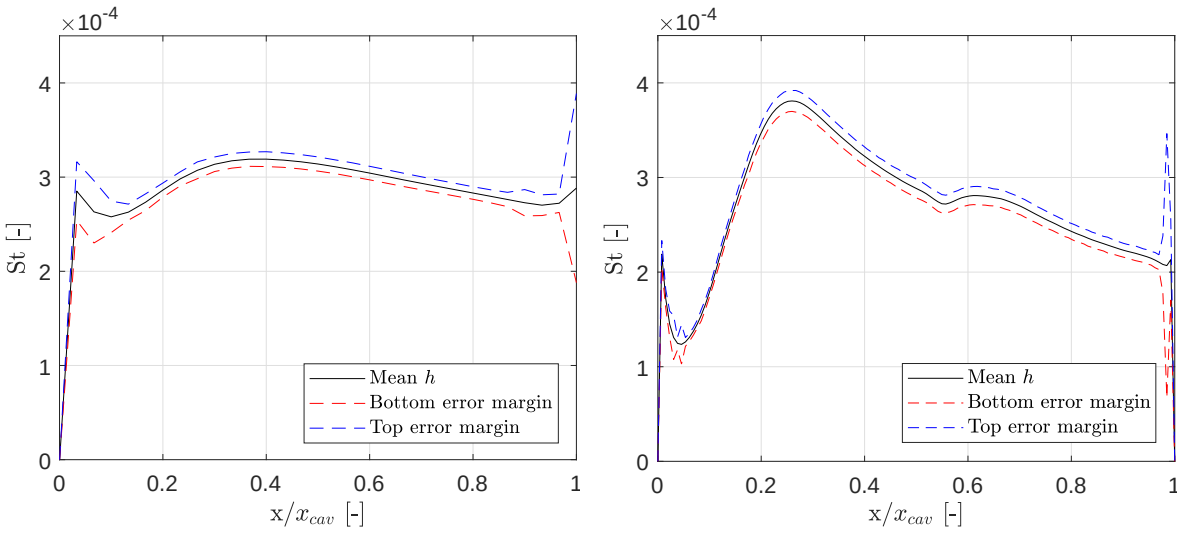

FIGURE 5.25: Final closed cavity profiles, p/e = 15 at 1.2 mm (left) and 4.8 mm (right).

Either geometry depicts largely similar $\overline{St}$-profiles at respectively the same roughness heights or rate of BL development. Still, the primary difference lies in the fact that for larger p/e, a proportionally larger part of the cavity is covered by an attached BL. This feature is key to the optimization of heat transfer for flow regions which are substantially longer than the currently investigated test plates (i.e. nozzle length).

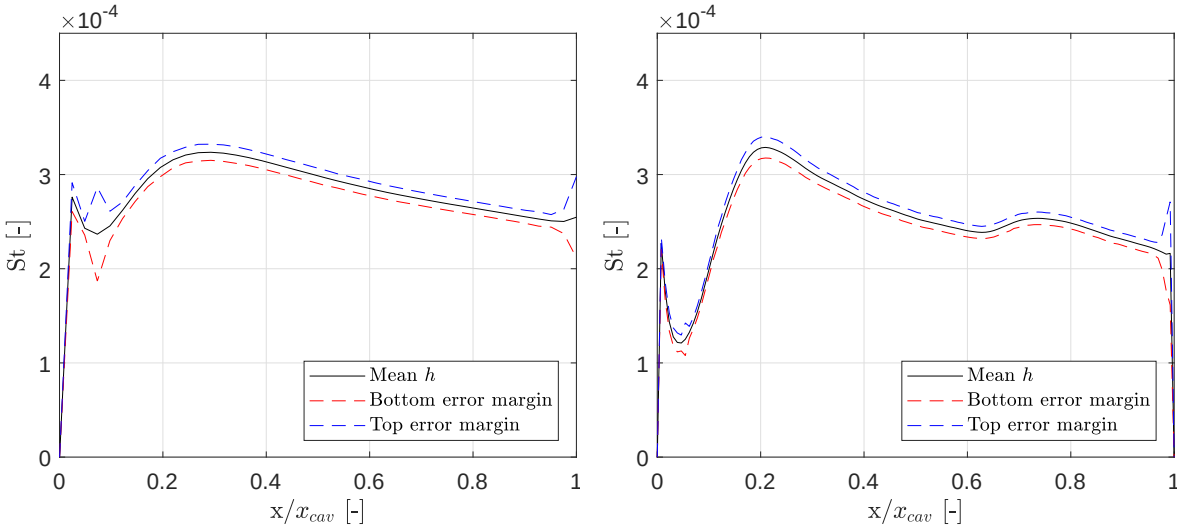

FIGURE 5.26: Final closed cavity profiles, p/e = 20 at 1.2 mm (left) and 3.6 mm (right).

For all the displayed heat transfer profiles, it is seen that within the cavities the total error margins (ϵ_{QIRT}) remain relatively small, whereas the inverse occurs near the edges of the cavities. This is a repeating pattern for all heat transfer profiles computed for the primary

campaign, and is likely to have two causes: (1) unsteadiness of the flow near the rib faces, and, (2) inaccuracy of the IR camera by the presence of the ribs. At the edges of each cavity, either flow stagnation or recirculation occurs. These flow phenomena are a lot more unsteady than their more centered counterparts such as compression fans and delta waves. This unsteadiness is likely to cause more flow variance, and thus more temperature variance; affecting the stability of the heat transfer data. Another origin of increased data variance, is the measurement inaccuracy of the IR camera itself. Within the vicinity of the ribs, these surfaces form a straight corner. As a result, thermal radiation interacts with the IR sensor either directly from the PCB surface or indirectly through reflections. In turn, variation between the acquisition of (in)direct radiation could affect the stability of the temperature data.

Which of the two effects most dominantly affects the heat transfer computations, is not exactly known. Nevertheless, it is chosen to maintain the more highly varying data for qualitative purposes and only base quantitative conclusions on the less variant, more centered cavity measurements. This fact is used for the computations of the trends and correlations in Section 5.2.5, where the heat transfer is based on the averaged or integrated cavity values excluding the highly variant data near the edges of the cavities.

5.2.4 Primary vs. secondary campaign

Up to now, the presented heat transfer profiles have been based on the results from the primary campaign. This campaign is characterized by highly accurate temperature data at a limited resolution. It has previously been concluded by the a priori data reduction and the complete error estimations in Sections 4.3 and 5.2.1 that the secondary campaign provides significantly less accuracy. Nevertheless, this drawback could be moderately counteracted by the increase in system resolution (i.e. 1.6 $\rightarrow$ 7.4 pixels/mm, Section 4.2.2).

In Section 5.2.3, it was briefly touched upon that for the smallest geometrical profiles (i.e. 1.2/5) on average merely 4 data points were obtained per cavity. As a result, it was found that the resulting cavity profiles displayed a significant variance with their larger counterparts (Figure 5.24). In order to prove the remark of qualitatively invariant cavity profiles for open cavity flows, it was decided to observe these small cavity flows by means of the high resolution Optris IR camera. Select results of which are shown in the following figure:

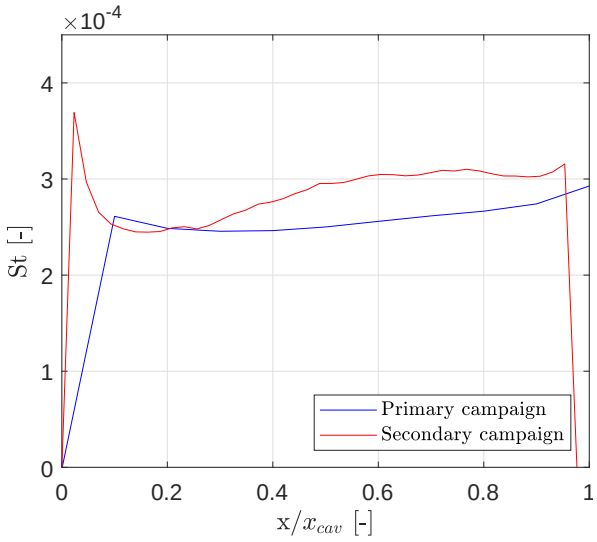

FIGURE 5.27: Cavity profile for 1.2/5 geometry.

Where, respectively the $\overline{St}$-profiles from the primary and secondary campaign are displayed. The profiles from Figure 5.27 prove that qualitatively, by the increased number of pixels, this 1.2/5 cavity profile is relatively similar to its geometrically larger counterparts. Between the primary and secondary profiles, there even seems to be a quantitative similarity as well. Unfortunately though, this observation is considered more a coincidence than an actual feature of the secondary campaign. In Section 4.3, it was explained that the Optris IR camera continuously re-calibrated itself by unknown calibration curves derived from its built-in sensors. The effect of which is that, depending on the measurement time and environmental factors, acquired temperature data correlated well or poorly with that of the primary campaign. This varying quality is illustrated nicely within the following figures:

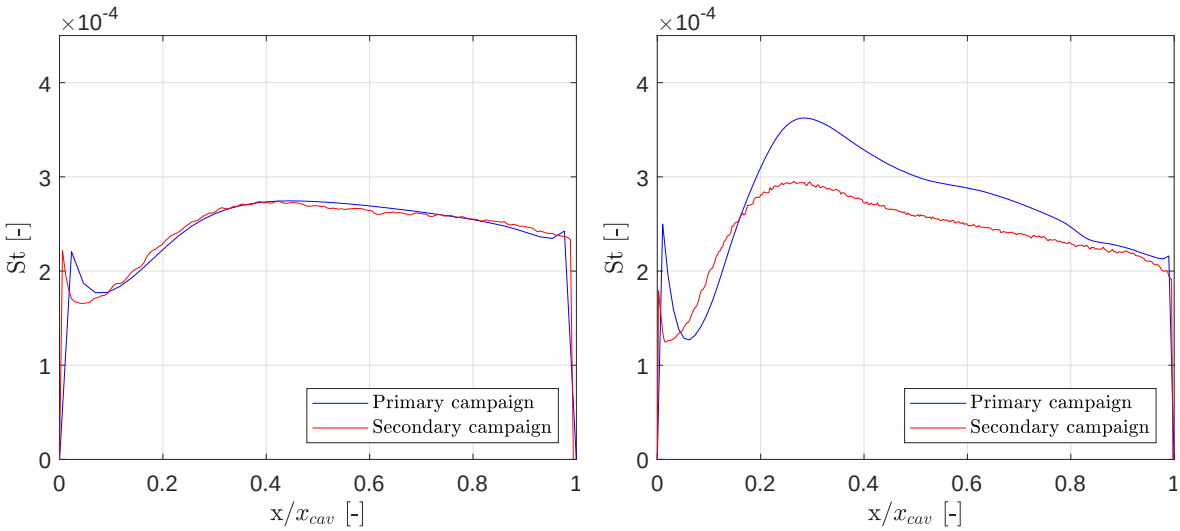

FIGURE 5.28: St-profiles over two campaigns; 2.4/10 (left) and 3.6/15 (right) models.

Where respectively the $\overline{St}$-profiles are shown for respectively the 2.4/10 (left) and 3.6/15 (right) models. The relative similarity of the 2.4/10 data shown in Figure 5.28 is truly unique, as it accurately approximates the data from the primary campaign. Nevertheless, most investigations of the secondary campaign only qualitatively approximated the results derived through the primary campaign. A typical example of which is displayed in 3.6/15 data, where the effects of the flow features are identified relatively equally whilst, in contrast, the assigned quantities are distinct. This effect is found to become progressively worse for geometries which have larger roughness elements. The latter seems to be a direct effect of the larger temperature variances, which emerge by the more powerful discontinuities along the streamwise direction of the cavity. In turn, as the NETD of the Optris IR camera is relatively abundant, these sudden variances become more difficult to record.

From the comparative analysis, it becomes clear that the Optris IR camera system should only be used for qualitative purposes. Even though it is capable of grasping some key flow features from the cavity flow fields, most derived datasets are found to be highly variant in relation to data from the primary campaign. Knowing the differences in camera performance, it is said that the large increase in NETD effectively cancels-out the improved resolution of the Optris IR camera. In addition, the varying performance of unavoidable self-calibration makes this system unscientific and unpredictable. Nevertheless, the secondary system was useful in proving the invariance of open-cavity flow fields where it is expected that the IR camera performed adequately.

5.2.5 Trends and correlations

In their research, Liou et al. (1992) described the existence of a turbulence peak in $\overline{u'}/u_{ref}$ for geometries with constant e, at a relative pitch ratio of 10 [-].[8] They related this result directly to the experimental results form Han (1984), who observed a maximum heat transfer peak $\overline{St}$ for the same configuration. In turn, Liou et al. concluded that a geometry with a relative pitch of 10 should result in an optimum heat transfer. Whether these correlations are reproduced, is treated in this section. The latter is conducted by combining the integrated heat transfer and turbulence properties from the final cavities of each geometry, derived through respectively PIV and QIRT techniques.

In Section 5.2.2, it was shown that both $\overline{u'}$ and $\overline{u'v'}$ correlate well with either heat transfer coefficients $\overline{h}$ and $\overline{St}$. From these correlations, however, it was found that the most favorable coherence exists between the Stanton number, St and the Reynolds stress, $\overline{u'v'}$. As the trends for turbulence and heat transfer are inherently different, it is first proven whether the interrelations between these physical processes are maintained.

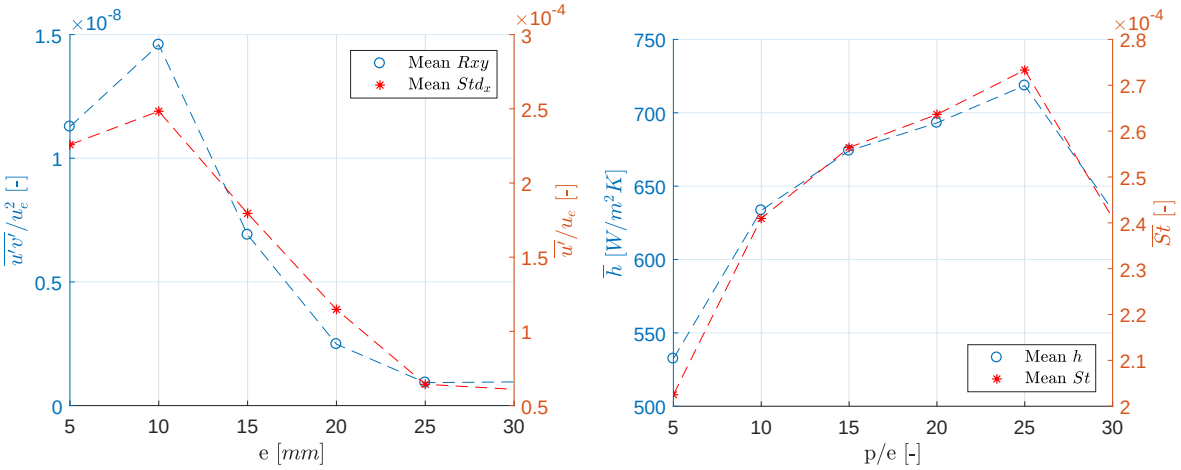

FIGURE 5.29: Correlations for the heat transfer and turbulence properties, sequence 4

These interrelations of the related physical values are assessed in Figure 5.29, where the averaged cavity results are displayed for respectively the turbulence (left), or heat transfer properties (right). From these correlation curves, it becomes evident that – regardless of the minor differences – the general trends remain constant amongst these variables. Therefore, it is decided to continue with comparing the trends between $\overline{u'v'}$ and St. The resulting trends and correlations are displayed in Figures 5.30 and 5.31, which are first compared amongst their sequences. After this, the appropriate datasets are combined with the research by Han (1984) such to check coherence with subsonic research.[6]

Previous discussions on the geometry-specific turbulence enhancement in Section 5.1 has indicated that the turbulence properties of the cavity flows are more sensitive than their heat transfer counterparts. Nevertheless, it is seen that the averaged-cavity turbulence properties are representative of their mixing properties. A good example of this is provided in Figure 5.30, where a strong increment in (freestream) turbulence between e/δ = 0.4 – 0.6, has an opposite effect for the heat transfer. It is known from the PIV results that, for closed cavity flows, larger rib heights result in more severe impingement effects. By these collisions, however, turbulence is enhanced yet diluted into the freestream by the effects of blockage; denying the heat transfer improvements. Interestingly though, this adverse effect of turbulence expulsion occurs at different roughness heights for each of the closed cavity flows; i.e.

0.6 for p/e = 15, and 0.4 for p/e = 20. It is expected that these differences are more the cause of lesser rib interactions than the roughness height itself (Section 5.2.3).

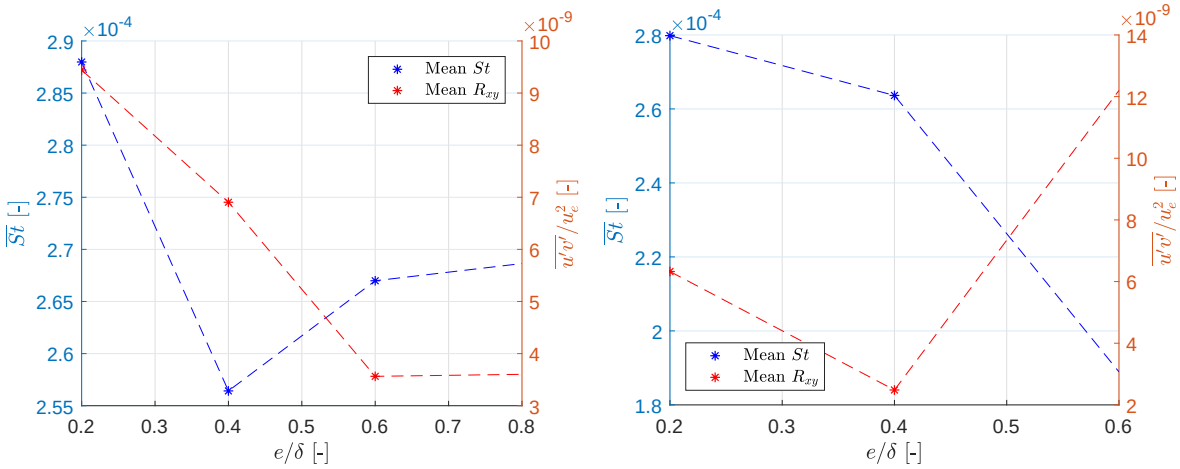

FIGURE 5.30: Correlated trends between $\overline{u'v'}$ and St for sequence 2 (left) and 3 (right).

Even though the averaged St cavity profiles in both Figure 5.30 are found to have an inflection point at e/δ = 0.4, each has a completely opposite effect. This is seen by an increment in St for the geometry at a p/e of 15, and a decline for test plates with p/e equal to 20. Actually, the latter of which has quite a severe decline in average heat transfer, contradictory to the relatively slight improvement in St for the smaller pitched cavity geometry. This is a direct result of the respective flow phenomena by the relative rib heights and number of rib interactions (Section 5.1). Apart from all these differences in flow effects, a general equivalence does exist by by the effects of rib height, e/δ. Namely that – regardless of the cavity flow types – a maximum St is found for the geometry with the smallest rib height. Proof of which is additionally provided by the sequence 1 correlation curve in Figure 5.31, where the data is displayed for geometries with a constant p/e of 5.

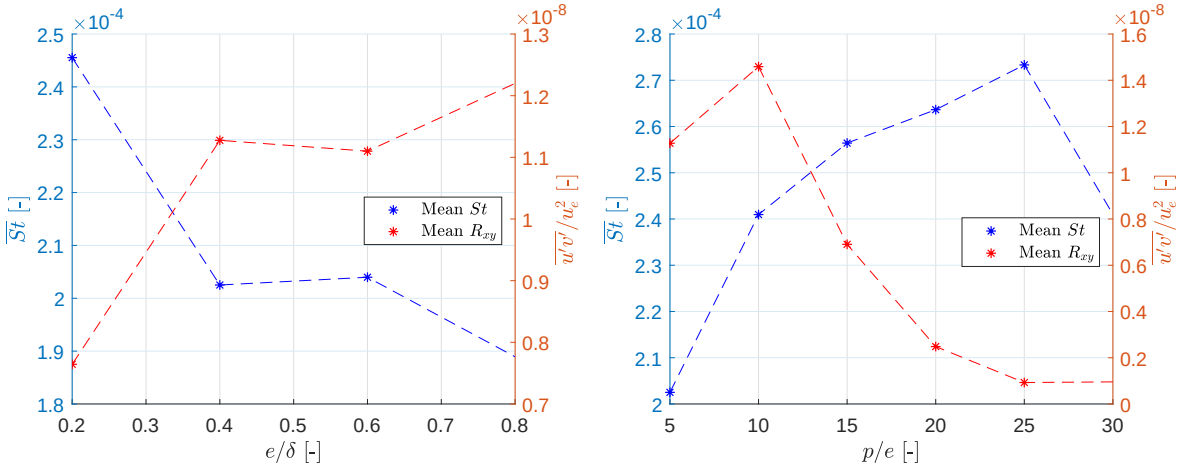

FIGURE 5.31: Correlated trends between $\overline{u'v'}$ and St for sequence 1 (left) and 4 (right).

Contrary to the the closed cavity flows, the St-profile data of sequence 1 does encompass a semi-continuous decline in heat transfer. The reason for this is that – simultaneously to the improvements in turbulence levels ($\overline{u'v'}$) – the enhanced BLs become more separated from the cavity floors. As a result, a decline in St and an increase $\overline{u'v'}$ are found. The latter is depicted nicely by the opposite response for respectively the $\overline{u'v'}$-, and $\overline{St}$-profiles.

With the general height effects discussed, it remains to identify the respective trends with regard to the variance in relative pitch. To this end, the averaged turbulence and heat transfer data are combined in Figure 5.31. From the clear turbulence peak at p/e = 10, it can be concluded that the $\overline{u'v'}$-profile does correlate perfectly with the observations made by Liou and Hwang (1992).[8] Even though they drew there conclusions with regard to $\overline{u'}$, the same peak exists for the currently derived $\overline{u'v'}$-profiles as depicted in Figure 5.20. In contrast to subsonic research, however, no such heat transfer peak is found at the same geometry. However, this does exist for a the geometry at a p/e of 25. The latter was already expected from the discussions of the turbulence data (Section 5.1), where the combination of closed cavity floor interaction and turbulence enhancement was foreseen to results in the highest heat transfer coefficient. In turn, it was found that a maximally enhanced BL exists for p/e of 10 which interacted minimally with the cavity floor (Figure 5.2b).

It can be summarized that the displayed heat transfer correlations relate logically to the observations made previously from the flow descriptions from Schlieren, the turbulence data from PIV and cavity profiles gathered through IRT. Nevertheless, there are many differences with respect to the subsonic trends obtained by Han (1984). The expected reasons for which are due to the differences in experimental setup. As discussed in Section 2.2.3, Han only obtained temperature data within the fully-developed flow field at fixed locations behind a heated duct. In his case, a minimum of 20 ribs was passed prior to the thermocouple measurements. As seen in this thesis, the cavity flows vary significantly by the number of rib passes; depending on the p/e. Thus, the conclusions drawn here with respect to flow optimizations are said to count for a limited streamwise length. The latter explains why none of the trends displayed in this section could equate with the relatively simplistic correlations derived by Liou and Hwang (1992) nor Han (1984). As a result it is stated that, in order to conclude upon which geometry is optimal for a geometry at length of a rocket nozzle, additional experiments should be performed (Appendix A). Nevertheless, the IR data is found to be accurate and reliable. In addition, both cavity profiles and height effects are seen to be highly equivalent to the subsonic data shown by Aliaga et al. (1993).[10]

5.2.6 Summary

The QIRT technique was designed, constructed and utilized to obtain direct surface temperature measurements for the same flow fields investigated through Schlieren and PIV. By gaining exact knowledge on the temperature propagations of various sources (settling chamber, PCB and insulation surface), it was possible to define the exact heat transfer profiles of each respective geometry.

Prior to analyzing these profiles, it was decided to assess each experiment for variance and repeatability (Table 5.1). This was done by computing the maximum difference from the mean of three consecutive measurements, conducted at three distinct power levels. By comparing the experiments from each test plate, an overall variance of 1.2% was found. As a result, it was assumed that the current QIRT methodology is fully repeatable and reliable in terms of operation. The substantiation of this technique was done by interrelating the effects of certain flow phenomena in turbulence, $\overline{u'v'}$ to heat transfer levels, $\overline{St}$. As expected from the PIV discussions in Section 5.1, this qualitative assessment was primarily possible for closed cavity flows. Since the flow phenomena related to open cavity flows do not transcend the crest of the ribs, it is relatively difficult to distinguish their effect on either turbulence or heat transfer. Nevertheless, it is concluded that either results correlate logically with the flow field descriptions from Schlieren, as well as the turbulence data from PIV. In addition, by the fact that an analytical flat plate solution closely approximated the average

flat plate estimates, quantitative equivalence is proven as well (Appendix Q). As such, this IRT technique is said to be both reliable and quantitatively sound; i.e. QIRT.

Each $\overline{St}$-profile has been displayed in parallel to its custom error margins, as function of non-dimensionalized cavity length, x/x_{cav}. Generally, it was found that each heat transfer profile correctly displayed the effects of its associated cavity flow phenomena. Importantly though, most of these effects remained well within the defined error bounds. The only exceptions to this, however, were given by the the profiles at the edges of the cavities. It is at these locations where the results became relatively variant ($\epsilon_{QIRT} \geq 6\%$), causing that no conclusions are drawn regarding their local magnitudes of $\overline{St}$. Qualitatively though, it is found that the shear layer growth, boundary layer impingement and blockage effect improve the overall heat transfer, whereas, recirculation, flow stagnation, boundary layer reattachment and BL development insulate the cavity floors. The latter two are identified as recurring effects for all closed cavity flows, and become progressively dominant with p/e.

The effects of all cavity flow phenomena were summarized by their averaged heat transfer coefficients, excluding the cavity edge portions at ~0.5 e/δ. From these averaged cavity values, the trends regarding heat transfer variations by respectively the rib height and pitch were found by combining the values into sequence-specific graphs. From these graphs, it was concluded that across all p/e-ratios an increase in e/δ results in a decrease in $\overline{St}$. However, judging by the simultaneously limited number of ribs transcended, it is expected that this trend would decline for closed cavity flows once it has more repetitions. In contrast to the turbulence data, no maximum $\overline{St}$ was found at a p/e of 10. However, this maximum occurred for a geometry at p/e of 25. Actually nearly all the trends were found to propagate oppositely to turbulence, $\overline{u'v'}$-profiles. This was expected by the difference in effective measurement locations between PIV and QIRT (Figure 5.22). From all tested geometries, it is expected that a 1.2/25 geometry would provide the most optimal combination of turbulence enhancement and cavity floor interaction. In order to extend this observation to a full-scaled flow at the length of a rocket nozzle, however, additional QIRT investigations should be performed. Fortunately, for these future experiments, a working, validated QIRT setup is available.

Chapter 6

Conclusions

The inner surface of a rocket nozzle is exposed to an extremely harsh environment. By the process of a rocket engine, strongly accelerated, supersonic air (M ~2.0) exits the launch vehicle at high temperatures (1100 K). In order to survive such an exposure for a sufficiently long duration of time, the inner surface of nozzles is commonly covered by cooling channels. These consist of hollow tubes through which fuel is pumped, prior to entering the combustion chamber. By this process, the inner surface of the nozzle remains at appropriate temperatures whilst the fuel is properly pre-heated. The geometries of these cooling channels are most dominantly defined by relative pitch and height as design features. Contradictory to the subsonic flow regime, the investigations on the effects of such roughness elements in supersonic flows is relatively underrepresented. Therefore, it is decided to conduct a parametric study on large roughness elements in supersonic flow conditions, where M = 2.0 and p/e and e/δ are the only design variables.

In order to keep the current study fundamental and not only tailored to a specific roughness geometry (i.e. cooling channels), it is decided to investigate the heat transfer effects of large, square-ribbed roughness elements. From previous investigations, it is known that – regardless of the flow regime – an element can be assigned as *large* provided its effect on the flow is discrete. According to Jimenez (2004), the latter occurs for $e/\delta \geq 0.2$.[12] As such, each investigated geometry possessed a height which abides this requirement. In addition, the relative pitch ratios, p/e were varied between 5 and 30 such to encounter each of the cavity flow types which could possibly affect the characteristics of the flow.[34,41] (Stallings and Wilcox, 1987; Zhuang et al., 2006)

QIRT design and operational validation The implementation of ribbed roughness elements is mostly ascribed to the enhancement of turbulence and the optimization of heat transfer. For any sub- or supersonic application, this implies that a maximum thermal exchange should exist within a limited streamwise length (i.e. turbine blades, rocket nozzle or nuclear reactor). As a result, it was decided to conduct direct temperature measurements such that geometry-specific heat transfer estimations could be made. To this end, it was chosen to conduct an infrared thermographic measurement campaign as this technique is non-intrusive and has proven capabilities in both sub- and hypersonic flows.[10,33] (Aliaga et al., 1993; Carlomagno and Cardone, 2010) The most reliable and accurate heat transfer estimations are made on test surfaces, which operate at a steady-thermal state.[15] (Astarita et al., 2012) Unfortunately though, no such system was available for the ST-15 wind tunnel. As such, it was required to design, construct and utilize an active IRT setup for which all thermal in- and outputs could be accurately monitored. To accommodate this, a heat flux sensor was constructed which consists of a printed circuit board, insulation plate and wind tunnel cavity door; where the latter effectively functioned as a heat sink.

As operation with this IRT setup is unfamiliar, its functioning should be validated from related datasets obtained by a known measurement technique. By comparisons made in subsonic research on the same ribbed geometries, it is known that turbulence ($\overline{u'}$, $\overline{u'v'}$) and heat transfer properties ($\overline{St}$) correlate well with one another. (Han, 1984 and Liou and Hwang, 1992) As such, it is decided to perform PIV experiments on the geometries; providing both qualitative insight into the flow fields and quantitative knowledge on flow properties such as $\overline{u}$, $\overline{u'}$ and $\overline{u'v'}$. Since PIV is relatively cumbersome, it was decided to conduct a spark-Schlieren investigation prior in order to get a feel for the occurring supersonic flow fields. From these investigations, it was found that each geometry affected the boundary layer such to form *repeated cavity flows*. This means that each flow phenomenon and discontinuity can be directly related to a p/e-dependent cavity flow field. As such, supersonic observations made prior by Latin and Bowersox (2000) are found to hold for larger rib heights.[11]

The operational reliability of the IRT methodology is proven by testing each wind tunnel model at three consecutive power levels and, in turn, quantifying the variance in h between consecutive measurements.[63] (Kreith, 2012) By then combining the overall variance of the 22 test models, the average ϵ_{var} was found to be merely 1.2%. In turn, the total error margin is found by combining this variance to the inherent methodological uncertainty. The latter was found to be approximately 4.7%. As such, the overall QIRT technique was found to be reliable and to operate within acceptable error bounds. Nevertheless, the accuracy of the data itself was not assessed yet. The latter is done by means of the turbulence data from PIV and the analytic flat plate Dittus-Boelter equation. It turns out that $\overline{St}$-profiles generally correlate well with the $\overline{u'v'}$ data of crest protruding events, whilst the average flat plate $\overline{St}$ remained within acceptable error bounds from the approximate solution (i.e. 5%). From subsonic research, this was known to be sufficient proof. Judging by the level of resemblance, the same is concluded with regard to the current experimental campaigns; allowing for the title quantitative infrared thermography, or QIRT.

PIV and QIRT results From the fact that the QIRT data is steady, invariant to external conditions and correlates well with proven experimental techniques, it is concluded that the data is both reliable and accurate. As such, it is allowed to draw conclusions regarding the heat transfer data up to a reasonably small level of detail. The latter is done by means of either St cavity profiles or fixed quantities averaged over the cavity lengths. The same was done for the Reynolds stress components, which allowed for a combined turbulence and heat transfer characteristic assessment. From subsonic research on the fully-developed, ribbed-roughness induced flow fields, it was found that both a turbulence and heat transfer optimum should exist for geometries at a p/e of 10.[6,8] (Han, 1984; Liou and Hwang, 1992) The latter was indeed confirmed by the turbulence levels, $\overline{u'v'}$ measured through PIV. However, this feature was not duplicated by the $\overline{St}$ data from QIRT; demonstrating a maximum St at p/e of 25. In addition to this, the average cavity St was found to decline with regard to rib height, e/δ; opposite to the subsonic IRT research conducted by Aliaga et al. (1993).[10] Nevertheless, it was observed that the complete St cavity profiles were qualitatively similar to those obtained within the latter research and logically followed the flow fields depicted by both Schlieren visualization and PIV. Therefore, it is expected that these variations with respect to the subsonic research are the result of differences in experimental setup and the occurrence of (strong) discontinuities.

With the utilization of three different experimental techniques, a multitude of observations has been made. In order to provide clarity to the totality of data, it is decided to merge these results into a single qualitative representation. This is displayed in the following figure:

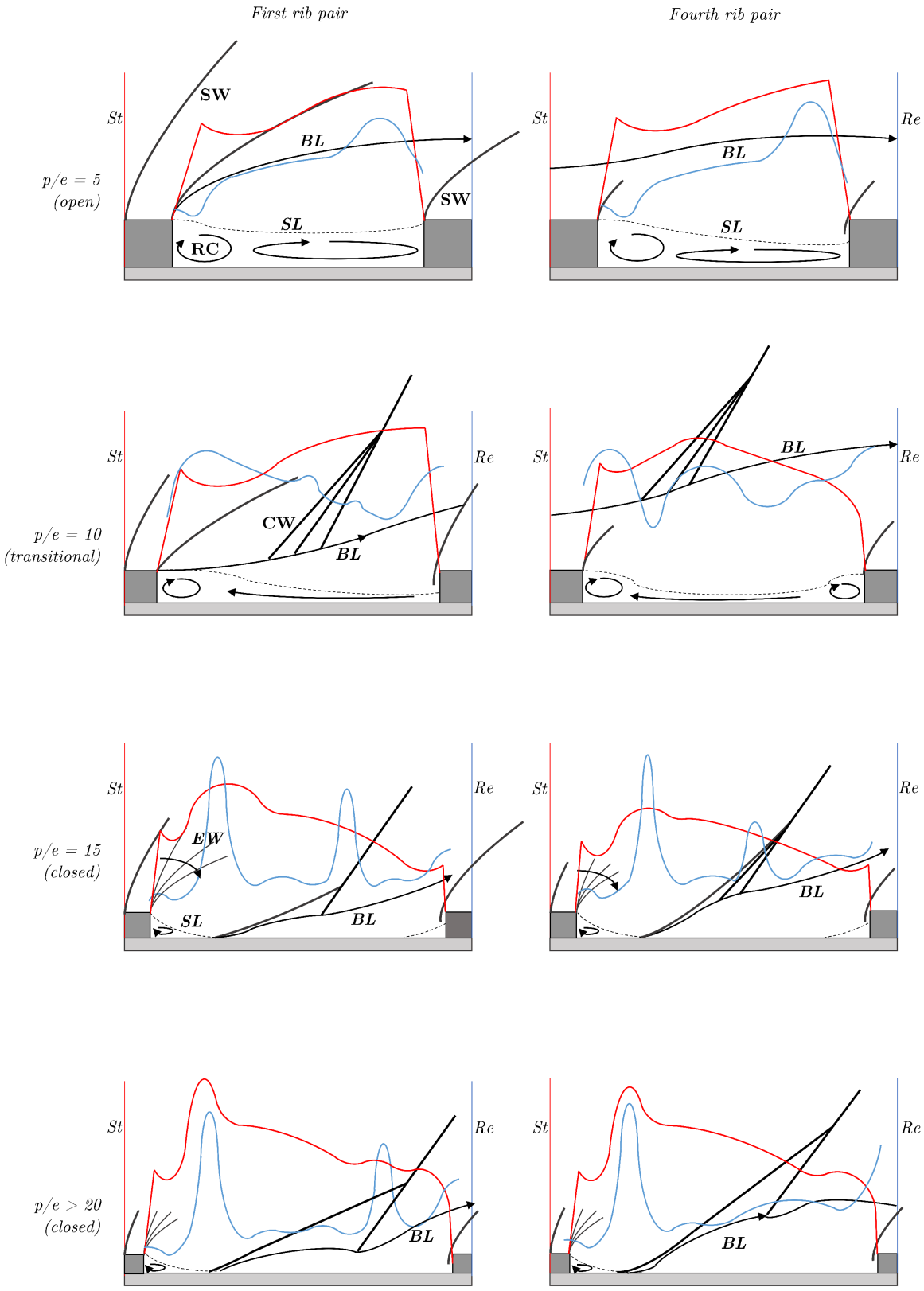

FIGURE 6.1: Schematic representation of flow field development and corresponding heat transfer and turbulence profiles.

Where qualitative heat transfer, St and turbulence, $\overline{u'v'}$-profiles are listed for four roughness geometries, representing respectively *open*, *transitional* and *closed* repeated cavity flows. In addition, by approximating the development of the boundary layer (BL), shear layer (SL) and discontinuities for the first rib pair and fourth rib pair, the effects of flow development are visualized. As a note, the St and $\overline{u'v'}$-profiles displayed in Figure 6.1 represent those derived by the measurement techniques. As such, the St profile relates to the cavity floor, whilst the $\overline{u'v'}$-profile corresponds to data at ~3 mm from the rib tops.

Across the cavity flow types, it becomes clear that the flow is fully developed from the fourth rib (pair) downstream. This is seen by relatively unchanging St- and $\overline{u'v'}$-cavity profiles, regardless of the flow topologies. Differently though is the (dis)continuous development of the BL for respectively open and closed cavity flows. By the semi-no slip condition for geometries with $p/e \leq 10$, a continuously developing BL results on top of the crest of the ribs; resulting in similarity conditions. In contrast, for $p/e > 10$, the boundary layer reestablishes itself at each rib interaction, which contributes to the overall heat transfer capabilities. More generally though, the following conclusions can be drawn:

- The maximum heat transfer rates are found for geometries which embody an optimal combination of the turbulence enhanced boundary layer and surface interaction.
- Insulating flow phenomena, declining $\overline{St}$: *BL thickening*, *BL development*, *flow separation* (at delta-wave) and *recirculations* (RC).
- Enhancing flow phenomena, increasing $\overline{St}$: *expansion waves* (EW), *thinning shear layer* (SL), *rib impingements/blockage*.
- Geometrically, surface interaction is solely defined by the relative pitch, where:
  1. $p/e \leq 10$: open cavity flows, stable vortices.
  2. $10 < p/e < 15$: transitional cavity flows, centralized compression wave.
  3. $p/e \geq 15$: closed cavity flows, delta wave structure.
- The effect of an increment in relative roughness height, e/δ causes that:
  1. Turbulent mixing, $\overline{u'v'}$ is enhanced, independent of the cavity type flows.
  2. Heat transfer, $\overline{St}$ is declined, independent of cavity type flows.
- The opposite response in $\overline{u'v'}$ and $\overline{St}$ are directly caused by the variance in measurement location by respectively PIV and QIRT. As a result, PIV did function as a possible quantitative justification tool for heat transfer, but missed the observation of varying boundary layer-wall interaction.

It is concluded that the turbulence and heat transfer profiles, trends and correlations are paralleled logically amongst the PIV and QIRT methods. In addition, by the analogous usage of each measurement technique, turbulence and heat transfer effects were directly assigned to flow features. With the gained knowledge, designers of future supersonic (nozzle) cooling channels can more adequately avoid the occurrence of flow phenomena associated with wall insulation. In terms of heat transfer optimization for supersonic cooling geometries, it is recommended to employ a geometry has a p/e equal to 25, and e/δ of 0.2. In addition, in the case of limited space in streamwise direction, a geometry having a minimal p/e of 15 should be used. However, this should be proven by a future parametric study in which a longer test section is used. As a result, it is possible to investigate the effects of prolonged rib impingements for geometries encompassing the more ideal closed cavity type flows. Fortunately, for these future tests, a usable, accurate and reliable QIRT setup is available.

Chapter 7

Recommendations

The setup of the current thesis was to conduct a parametric study to heat transfer optimization of ribbed roughness geometries in supersonic flow conditions. This experimental investigation required the design and construction of an active thermographic IRT setup, capable of delivering steady state conditions. According to the results and conclusions, the resulting QIRT setup functioned accurately and reliably. The quantitative justification used to prove operation was done through PIV. However, by the differences in measurement location (Figure 5.22), merely the crest-protruding flow events could be correlated with QIRT. Even though the latter is seen as sufficient proof of accuracy, improvements remain for both measurement techniques.

Improvements to PIV The spark-Schlieren images have displayed the occurrence of three distinct cavity type flows depending purely on the value of p/e. From the clarity of the respective boundary layer development and parallel PIV measurements at the crest of the ribs, the PIV results were found to solely represent the turbulence levels of the BL; excluding improvements of BL-wall interaction. As a result, it was not surprising to obtain adverse averaged cavity profile correlations by respectively PIV and QIRT.

In order to provide clarity on the inner cavity turbulence of the BL, the secondary PIV campaign was conducted. It turned out, however, that the buoyancy of the DEHS particles and the restricted laser sheet accessibility greatly limited the signal-to-noise ratio (SNR) of the image pairs. As such, these secondary PIV measurements could merely be used qualitatively and did not provide any means of correlating cavity floor measurements to QIRT data. In the case these experiments are to be revised, it is recommended to:

- Utilize an illumination path, which allows laser light to protrude the cavities normal to the floor; optimizing illumination and minimizing the occurrence of shadowing.
- Manufacture transparent test models, allowing the researcher to use the same illumination path whilst maximizing laser light from entering the cavities.
- Exchange the DEHS for TiO_2 particles. As this seeding material is slightly less buoyant, it is more likely to protrude the cavities.

Taking into account the image pairs obtained currently for the secondary PIV campaign, it is seen that both entry of particles and full illumination of cavities are an issue. Considering the relative ease of the utilized illumination path, it is advised to first use different seeding material and check the SNR. If this is insufficient, attempt the usage of the adjusted illumination path. This can be done by aiming the laser sheet onto a mirror located at the top of the test section, reflecting the light straight into the cavity; preventing shadows to form. As a final option, the transparent models can be constructed.

Logistical improvements to QIRT The primary QIRT setup was devised such to provide the most accurate means of computing the convective heat transfer, q_{conv} and its corresponding coefficients, h and St. To accomplish this, reference thermocouples were placed strategically at the back of the insulation. Through these thermocouples, the conductive heat transfer, $q_{cond.b}$ was estimated. Equally to the initial semi-infinite, one-dimensional estimate, it was found that $q_{cond.s} < 0.1\%$ of the electric power input, q_{el}. On the other side, though, the average q_{el} required for steady-state was approximately 2.4 times higher than the safety estimate. By the redundancy of the PCB design, however, this increase in I was accounted for. Still, the actual QIRT setup was validated for the estimated thermal leakage to be insignificantly small. Logistically though, this implies that the usage of the thermocouples does not have to be repeated for future measurements; provided the same heat flux sensor and cavity door are used. Actually, apart from abstaining the future use of these thermocouples, the following improvements should be made to the QIRT setup:

- A continuous read-out of the power supply, incorporated into the LabView program.
- Synchronized triggering of the IR camera and settling chamber thermocouple.
- Utilize another glue type, being more predictable in terms of operational limits.



(A) Insulation plate and thermocouples. (B) Damaged Germanium window.

FIGURE 7.1: Damage to test model and Germanium window after PCB shear-off.

Failures of QIRT testing Even though the data obtained through QIRT was shown to be both reliable and accurate, some operational failures have occurred during the initial testing of the technique. There have been two occurrences where the PCBs sheared of the insulation plates; badly damaging the Germanium window (Figure 7.1). The reasons for this revolve around the uncertainty of the limitations of the epoxy-based glue. By the method of curing, this glue should be able to withstand local temperatures up to ~95°C. Still, even with power supply settings resulting in maximum local surface temperatures of only ~75°C, PCBs were found to shear-off. It is found that this glue can indeed withstand these maximum temperatures. However, by prolonged exposures to slightly less intense temperatures, already some degree of glue evaporation takes place. As a result, the overall glue properties degrade and the PCB model is loosened. During the testing phase of QIRT, the following ground-rules were set to prevent these shear-offs from happening once more:

- Set power supply such that local T do not surpass 70°C, for flat plate $q_{el} \leq 665$ W.
- Never preheat the models past a surface temperature of 40°C, for any plate $q_{el} \leq 15$ W.

- Place tape over the entire leading edge ridge separating the window from the PCB.

Where the latter is used as a measure in the case the glue does still fail, and the PCB is technically loosened from the insulation. By the implementation of tape, no air can reach underneath the PCB. As a result, the PCB is not lifted from the insulation such that it will not fly off. After the two occurrences of shear-off, none reoccurred by following these ground rules. For future experiments, though, it is advised to look into the usage of a different kind of glue. This glue should be characterized by extremely high durability and withstand high operating temperatures for an extended amount of time. As it is known that most of the heat is lost through convection, it is valid even to use a glue type whose thermal conductivity, k does not match either FR-4 or Makrolon.

Design improvements to QIRT The discussion of the results has shown that – apart from some operational uncertainties – the currently designed QIRT methodology provided sufficiently accurate data at a high repeatability. As such, possible design improvements should neither affect the thermal properties significantly nor change the methods of operation. Still, if the possibility arises, design adaptations can be made which improve the reliability of operation and minimize the intervention of data altering schemes such as the NUHC.

Previously, the PCB was setup such to be able to safely provide a deliberately over-designed amount of thermal power to its surface. The serpentine copper layout was set such to retain an average base resistivity, R_0 of 22.4Ω and adopt a current, I of up to 7.2A. From all the 78 wind tunnel tests performed by QIRT, it is known that the maximum required q_{el} for a steady-state was 704.1 W; only 60% of the designed maximum q_{el}. With this knowledge at hand, it is a lot easier to develop a more suitable PCB layout. From the PCB manufacturing analysis of the producer (i.e. Eurocircuits), it is known that the relatively small-scaled copper wires of 0.75 *mm* required a longer etching treatment. This is likely to have aggravated the discrepancies in copper thickness across the area of the PCB. Knowing the exact design requirements, it is definitely possible to develop the PCBs such to have wider copper wires and cope with even higher amperages. In turn, the enlarged wires would greatly reduce the etching time, and limit variations in copper thickness. As a result, the NUHC may become obsolete allowing the heated empty measurements to be avoided. This would make the QIRT methodology less cumbersome and increase reliability of the gathered data.

The application of the reference thermocouples has proven the negligibility of thermal conductivity into the body ($q_{cond.b}$), compared to the remaining heat fluxes. Therefore, for future IRT data reduction, their application can be avoided which greatly speeds-up the turn-around time of the experimental process. Since these thermocouples do not have to be placed any more, the accommodative small spacings between the insulation and the cavity walls become obsolete. Thus, in the case additional insulations are being manufactured, the outer dimensions of which should be increased by 2 *mm*. Therefore, no small cavities exist underneath the PCBs, which prevents air from becoming trapped. As such, the chances of a PCB shear-off are reduced tremendously. Intermediate to ordering a new outline of these insulation slabs, the existing small cavities should be filled with clay.

Future investigations The QIRT setup was designed in such a way that numerous roughness elements could be mounted on top of the heated surface. This means that, provided equivalent flat plate models are available, any type of roughness induced flow field can be investigated within confinements of the ST-15 test section. One could think of investigations on the heat transfer properties of micro ramps, isolated or other repeated roughness

elements. To accommodate such research, it is recommended to devise a gluing process which is fully outsourced and automated. For the current thesis, approximately two weeks were spend in optimizing the gluing process. Regardless of the fact that most of the gluing operations were successful, it remained laborious, tedious and somewhat unpredictable. Since the future insulation outlines and PCB designs are known to detail, minor design alterations can be implemented to allow automation. Considering that the gluing of two synthetic material-based slabs are quite common, operations such as these should be outsourceable. One example of which is true assembly-line work, where each surface is UV cured (sanded) after which the two plates are bonded by unsaturated polyesters.[84] (Dvorchak, 1995) Once this is done, multiple PCB-insulation slab combinations can be ordered and used for any type of heat transfer investigation. One could simply take one of these models, mount the preferred roughness element and conduct their experiments.

In terms of research regarding the effects of repeated, large-scale roughness elements in supersonic flows, it is interesting to investigate the heat transfer properties fully-developed closed cavity flow fields. During the discussions of the results, it was found that roughness height correlations are not completely sound in the sense of number of interacted ribs. For repeated closed cavity flows, the number of rib interactions is vital to the overall heat transfer characteristics. Therefore, it is important to compare the flow fields of several geometries having an equal and minimal number of rib impingements of 5, at $p/e \geq 15$. As a result, the uncertainty of rib interactions can be circumvented and more equal comparisons can be made regarding each geometry's performance. Even though many flow development observations and heat transfer characteristics can be estimated for a longer streamwise geometry (such as a rocket nozzle), definite proof is not yet available. Therefore, for the sake of heat transfer optimization at nozzle length, such research would be very useful.

Bibliography

[1] ESA, "Ariane 5 Launch vehicle", 2016.

[2] H. A. Youssef, H. A. El-Hofy, and M. H. Ahmed, *Manufacturing technology: materials, processes, and equipment*. CRC Press, 2011.

[3] *SpaceX's Grasshopper: Reusable Rocket Prototype*, `https://www.space.com/26042-spacex-grasshopper.html`, Accessed: 06-10-17.

[4] B. Church, "THERMAL ANALYSIS OF LIQUID ROCKET ENGINES", 2015.

[5] Z. Sun, F. F. J. Schrijer, F. Scarano, and B. W. van Oudheusden, "The three-dimensional flow organization past a micro-ramp in a supersonic boundary layer", *Physics of Fluids*, vol. 24, no. 5, pp. 1–22, 2012.

[6] J. C. Han, "Heat Transfer and Friction in Channels With Two Opposite Rib-Roughened Walls", *Journal of Heat Transfer*, vol. 106, no. 4, p. 774, 1984.

[7] J. C. Han, J. S. Park, and C. K. Lei, "Heat Transfer Enhancement in Channels With Turbulence Promoters.", *Journal of Engineering for Gas Turbines and Power*, vol. 107, no. 3, pp. 628–635, 1985.

[8] T. M. Liou and J. J. Hwang, "Turbulent Heat Transfer Augmentation and Friction in Periodic Fully Developed Channel Flows", *Journal of Heat Transfer,ASME*, vol. 114, no. February 1992, pp. 56–64, 1992.

[9] F. M. White, *Viscous fluid flow*, 3. New York: McGraw-Hill, 2006.

[10] D. A. Aliaga, D. E. Klein, and J. P. Lamb, "Heat Transfer Measurements on a Ribbed Surface At Constant Heat Flux Using Infrared Thermography", *Experimental Heat Transfer*, vol. 6, no. 1, pp. 17–34, 1993.

[11] M. latin Robert and D. W. Bowersox Rodney, "Flow Properties of a Supersonic Turbulent Boundary Layer with Wall Roughness Introduction", *AIAA journal*, vol. 38, no. 10, pp. 1804–1821, 2000.

[12] J. Jimenez, "Turbulent Flows Over Rough Walls", *Annual Review of Fluid Mechanics*, vol. 36, no. 1, pp. 173–196, 2004.

[13] J. Zhang, E. Morishita, T. Okunuki, and H. Itoh, "Experimental investigation on the mechanism of flow-type changes in supersonic cavity flows", *Transactions of the Japan Society for Aeronautical and Space Sciences*, vol. 45, no. 149, pp. 170–179, 2002.

[14] D. A. Aliaga, J. P. Lamb, and D. E. Klein, "Convection heat transfer distributions over plates with square ribs from infrared thermography measurements", *International Journal of Heat and Mass Transfer*, vol. 37, no. 3, pp. 363–374, 1994.

[15] T. Astarita and G. M. Carlomagno, *Infrared thermography for thermo-fluid-dynamics*. Springer Science & Business Media, 2012.

[16] L. Prandtl, "Uber flussigkeitsbewegung bei sehr kleiner reibung", *Verhandlungen des dritten internationalen Mathematiker-Kongresses in Heidelberg 1904*, no. 3, 1904.

[17] S. B. Pope, *Turbulent flows*, 2001.

[18] A. H. Shapiro, *The dynamics and thermodynamics of compressible fluid flow*. John Wiley & Sons, 1953.

[19] Q. Li, Y Xuan, and J Wang, "Investigation on convective heat transfer and flow features of nanofluids", *Journal of Heat transfer*, vol. 125, no. 2003, pp. 151–155, 2003.

[20] J. Nikuradse, "Stromungsgesetze in Rauhen Rohren", *Forschung Arb. Ingenieurwesen*, no. 361, 1933.

[21] A. E. Perry, W. H. Schofield, and P. N. Joubert, "Rough wall turbulent boundary layers", *Journal of Fluid Mechanics*, vol. 37, no. 02, p. 383, 1969.

[22] H. Schlichting, *Boundary layer theory*. New York: McGraw-Hill, 1955.

[23] B. Hodge and R. Taylor, "Application of the Discrete-Element Surface Roughness, Model to Rocket Nozzle Heat Transfer Computation", *AIAA-91-2435*, vol. 27, 1991.

[24] H. Liepman and F. Goddard, *Note on the mach number effect upon the skin friction of rough surfaces*, 1957.

[25] R. M. Latin, "The influence of surface roughness on supersonic high reynolds number turbulent boundary layer flow", DTIC Document, Tech. Rep., 1998.

[26] E. R. Van Driest, "Turbulent boundary layer in compressible fluids", *Journal of the Aeronautical Sciences*, 1951.

[27] S. Corrsin and A. Kistler, "Free-stream boundaries of turbulent flows", *NACA Technical Report*, no. 1244, 1996.

[28] G. Christoph and A. Fiore, "Numerical simulation of flow over rough surfaces, including effects of shock waves.", DTIC Document, Tech. Rep., 1983.

[29] T. M. Liou, Y. Chang, and D. Hwang, "Experimental and Computational Study of Turbulent Flows in a Channel With Two Pairs of Turbulence Promoters in Tandem", *Journal of Fluids Engineering*, vol. 112, no. 3, p. 302, 1990.

[30] C. Kao, "Symmetric and asymmetric turbulent flows in a rectangular duct with a pair of ribs", *Journal of fluids engineering*, vol. 110, p. 373, 1988.

[31] W. M. Rohsenow, J. P. Hartnett, and E. N. Ganic, "Handbook of heat transfer applications", *New York, McGraw-Hill Book Co., 1985, 973 p. No individual items are abstracted in this volume.*, vol. 1, 1985.

[32] M. Hishida and J. Hwang, "Heat transfer coefficients of the ribbed surface", *Proceedings of the ASME/JSME Thermal Engineering Conference*, vol. 3, pp. 103–110, 1991.

[33] G. M. Carlomagno and G. Cardone, "Infrared thermography for convective heat transfer measurements", *Experiments in fluids*, vol. 49, no. 6, pp. 1187–1218, 2010.

[34] R. L. Stallings Jr. and F. J. Wilcox Jr., "Experimental cavity pressure distributions at supersonic speeds", 1987.

[35] H. H. Heller, D. Holmes, and E. E. Covert, "Flow-induced pressure oscillations in shallow cavities", *Journal of sound and Vibration*, vol. 18, no. 4, 545IN9547–546IN10553, 1971.

[36] K. Ahuja and J. Mendoza, "Effects of cavity dimensions, boundary layer, and temperature on cavity noise with emphasis on benchmark data to validate computational aeroacoustic codes", 1995.

[37] M. Tracy and E. Plentovich, "Cavity unsteady-pressure measurements at subsonic and transonic speeds", 1997.

[38] D. P. Rizzetta and M. R. Visbal, "Large-Eddy Simulation of Supersonic Cavity Flowfields Including Flow Control", *AIAA Journal*, vol. 41, no. 8, pp. 1452–1462, 2003.

[39] W. Auxer, D. Nestler, and A. Saydah, "Heat transfer to steps and cavities in hypersonic turbulent flow.", *AIAA Journal*, vol. 7, no. 7, pp. 1368–1370, 1969.

[40] J. Rossiter, "Wind tunnel experiments on the flow over rectangular cavities at subsonic and transonic speeds", Ministry of Aviation; Royal Aircraft Establishment; RAE Farnborough, Tech. Rep., 1964.

[41] N. Zhuang, F. S. Alvi, M. B. Alkislar, and C. Shih, "Supersonic Cavity Flows and Their Control", *AIAA Journal*, vol. 44, no. 9, pp. 2118–2128, 2006.

[42] Z. Sun, "Micro ramps in supersonic turbulent boundary layers: An experimental and numerical study", 2014.

[43] F. Donker Duyvis, "Laser sheet probe design for piv in high speed wind tunnels", in *Proc. PIVNET II International Workshop on the Application of PIV in Compressible Flows, Delft, the Netherlands*, 2005.

[44] L. Robert, J. Stallings, J. Floyd, and J. Wilcox, "Experimental Cavity Pressure Distributions at Supersonic Speeds", *NASA Technical Paper*, no. 2683, p. 77, 1987.

[45] G. Settles, "Schlieren and shadowgraph techniques- visualizing phenomena in transparent media(book)", *Berlin, Germany: Springer-Verlag GmbH, 2001.*, 2001.

[46] LaVision, *High-speed controller product-manual*, 2013.

[47] M. Raffel, C. E. Willert, S. Wereley, and J. Kompenhans, *Particle image velocimetry: a practical guide*. Springer, 2013.

[48] R. Giepman, A. Srivastava, F. Schrijer, and B. van Oudheusden, "The effects of mach and reynolds number on the flow mixing properties of micro-ramp vortex generators in a supersonic boundary layer", *AIAA*, 2015.

[49] D. Ragni, "Piv-based load determination in aircraft propellers", 2012.

[50] C. Tropea and A. L. Yarin, *Springer handbook of experimental fluid mechanics*. Springer Science & Business Media, 2007, vol. 1.

[51] D. Ragni, F. Schrijer, B. W. van Oudheusden, and F. Scarano, "Particle tracer response across shocks measured by PIV", *Exp Fluids (2011) 50:53–64*, vol. 2, 2009.

[52] P. M. Hext, J. A. Tomenson, and P. Thompson, "Titanium dioxide: Inhalation toxicology and epidemiology", *Annals of Occupational Hygiene*, vol. 49, no. 6, pp. 461–472, 2005.

[53] Lavision, "Imager intense, Lavision", 2016.

[54] L. Benedict and R. Gould, "Towards better uncertainty estimates for turbulence statistics", *Experiments in fluids*, vol. 22, no. 2, pp. 129–136, 1996.

[55] R. Humble, F Scarano, and B. Van Oudheusden, "Unsteady flow organization of a shock wave/turbulent boundary layer interaction", in *IUTAM Symposium on Unsteady Separated Flows and their Control*, Springer, 2009, pp. 319–330.

[56] R. Hain, S. Scharnowski, N. Reuther, C. J. Kähler, A. Schröder, R. Geisler, J. Agocs, A. Röse, M. Novara, M. Stanislas, *et al.*, "Coherent large scale structures in adverse pressure gradient turbulent boundary layers", 2016.

[57] D Ragni, F Schrijer, B. Van Oudheusden, and F Scarano, "Particle tracer response across shocks measured by piv", *Experiments in fluids*, vol. 50, no. 1, pp. 53–64, 2011.

[58] F. Schrijer and F. Scarano, "Effect of predictor–corrector filtering on the stability and spatial resolution of iterative piv interrogation", *Experiments in fluids*, vol. 45, no. 5, pp. 927–941, 2008.

[59] R De Kat and B. Van Oudheusden, "Instantaneous planar pressure determination from piv in turbulent flow", *Experiments in fluids*, vol. 52, no. 5, pp. 1089–1106, 2012.

[60] K. Lynch and F. Scarano, "Material acceleration estimation by four-pulse tomo-piv", *Measurement Science and Technology*, vol. 25, no. 8, p. 084 005, 2014.

[61] R. Haberman, "Applied partial differential equations with fourier series and boundary value problems", *Mathematics and Computer Education*, vol. 46, no. 1, p. 72, 2012.

[62] W. L. McCabe, J. C. Smith, and P. Harriott, *Unit operations of chemical engineering*. McGraw-Hill New York, 1993, vol. 5.

[63] F. Kreith, R. M. Manglik, and M. S. Bohn, *Principles of heat transfer*. Cengage learning, 2012.

[64] *Eurocircuits manufacturing limits*, `https://www.eurocircuits.com/STANDARD-pool-your-default-choice-for-your-PCB/`, Accessed: 2016-12-12.

[65] *Sikablock m940 – tooling board*, 2016.

[66] W. Sieber, "Zusammensetzung der von werk-und baustoffen zurückgeworfenen wärmestrahlung", PhD thesis, 1939.

[67] E. Schmidt and E. Eckert, "Über die richtungsverteilung der wärmestrahlung von oberflächen", *Forschung im Ingenieurwesen*, vol. 6, no. 4, pp. 175–183, 1935.

[68] R. Mayer, "Orientation on quantitative ir-thermography in wall-shear stress measurements", *Delft University of Technology, Faculty of Aerospace Engineering, Report LR-812*, 1996.

[69] *Titanium user manual*, 2008.

[70] *Optris pi 640 – technical data*, 2015.

[71] CEDIP, *Lens Specification Sheet*. 2008.

[72] *Optris pi series – operators manual*, 2015.

[73] "Altair engineering manual", 2008.

[74] "Cirrus manual", 2008.

[75] T. Astarita and G. M. Carlomagno, *Infrared Thermography for Thermo-Fluid-Dynamics*, 11. 2013, vol. 7, pp. 956–963, ISBN: 978-3-642-29507-2.

[76] F. Schrijer, F. Scarano, and B. van Oudheusden, "Transient heat transfer measurements on a blunted cone-flare model in a short duration hypersonic facility using quantitative infrared thermography", in *7th Triennial International Symposium on Fluid Control, Measurement and Visualization*, 2003.

[77] D. G. Walker and E. P. Scott, "Evaluation of estimation methods for high unsteady heat fluxes from surface measurements", *Journal of thermophysics and heat transfer*, vol. 12, no. 4, pp. 543–551, 1998.

[78] H. Liepmann, R. Narashimha, and M. Chahine, "Reduction of data from thin-film heat-transfer gages: A concise numerical technique", *vacuum*, vol. 12, pp. 394–408, 1962.

[79] D. N. Kendall, W. P. Dixon, and E. H. Schulte, "Semiconductor surface thermocouples for determining heat-transfer rates", *IEEE Transactions on Aerospace and Electronic Systems*, no. 4, pp. 596–603, 1967.

[80] M. Ozisik, *Inverse heat transfer: fundamentals and applications*. CRC Press, 2000.

[81] T. Astarita and G. Cardone, "Thermofluidynamic analysis of the flow in a sharp 180° turn channel", *Experimental Thermal and Fluid Science*, vol. 20, no. 2, pp. 188–200, 2000.

[82] X Zhang, W Hendro, M Fujii, T Tomimura, and N Imaishi, "Measurements of the thermal conductivity and thermal diffusivity of polymer melts with the short-hot-wire method", *International Journal of Thermophysics*, vol. 23, no. 4, pp. 1077–1090, 2002.

[83] *Inframetrics 600l*, http://www.americaninfrared.com/ProductDetail.asp?ID=11, Accessed: 2017-12-09.

[84] M. J. Dvorchak, "Uv curing of pigmented high-build wood coatings based on non-air-inhibited unsaturated polyesters", *Journal of Coatings Technology*, vol. 67, pp. 49–49, 1995.

[85] X. Zhang, "Compressible cavity flow oscillation due to shear layer instabilities and pressure feedback", *AIAA journal*, vol. 33, no. 8, pp. 1405–1411, 1995.

[86] A. Charwat, J. Roos, F. Dewey, and J. Hitz, "An investigation of separated flows—part i: The pressure field", *Journal of aerospace Sciences*, vol. 28, no. 6, pp. 457–470, 1961.

[87] J. D. Anderson Jr, *Fundamentals of aerodynamics*. Tata McGraw-Hill Education, 2010.

Appendix A

Heat transfer and skin friction correlations

Perry et al (1969), derived boundary layer models through which an estimate could be made on the effect of wall geometries with either 'k-' or 'd-type' roughness elements.[21] Through these models, however, the effects on the heat transfer are only roughly quantifiable and cannot be considered accurate. Therefore, the main goal of Han's experimental research was to obtain correlations with which heat transfer and skin friction properties could be estimated precisely and accurately.[6] In Section, 2.2.3 it was mentioned that Liou and Hwang's (1992) derived similar correlations on $\overline{St}$ and $\overline{f}$. As the latter correlations have a higher accuracy and compact representation, these are preferred over those derived by Han. Still, as reference, Han's correlations and estimation method is summarized here.

Han's prediction equations are derived for the following range of design (i.e geometrical) and freestream parameters, respectively:

- Relative pitch: $10 \leq p/e \leq 40$
- Relative height: $0.021 \leq e/D_e \leq 0.063$
- Reynolds number: $7 \cdot 10^3 < Re < 9 \cdot 10^4$

Where the considered wind tunnel is represented by a rectangular duct with width A and height B. The derived correlations for the friction factor require estimates for both the rough and smooth wall, respectively $\overline{f_r}$ and $\overline{f_s}$ (Equations A.1 and A.2). These estimates can in turn be combined to compute the complete, average friction factor $\overline{f}$ (Equation A.6). The prediction equation for the rib-roughened wall is given by:

$$\overline{f}_r = \frac{2}{\left[0.95(p/e)^{0.53} - 2.5\ln\frac{2e}{D_e} - 2.5 - 2.5\ln\frac{2B}{A+B}\right]^2} \tag{A.1}$$

for which, opposite to Liou and Hwang (1992), both relative pitch p/e and relative height e/D_e are included in this single relation.[8] In turn, the prediction equation for the smooth wall is given by:

$$\frac{1}{\sqrt{\overline{f}_s}} = 4\log_{10}(\mathrm{Re_{D_e}}\sqrt{\mathrm{f_s}}) - 0.4 + 4\log_{10}\left(\frac{2\mathrm{R_{av}}}{\mathrm{D_e}}\right) \tag{A.2}$$

where,

$$\frac{2R_{av}}{D_e} = \frac{1.156 + (B/A - 1)}{B/A} \tag{A.3}$$

$$= 1.156 \text{ for square ducts} \tag{A.4}$$

and, Re_{De} is the Reynolds number based on the equivalent duct diameter D_e equal to:

$$D_e = \frac{2AB}{A+B} \tag{A.5}$$

Finally, the complete average friction factor can be found by combining the results from Equations A.1 and A.2:

$$\overline{f} = \frac{A\overline{f}_s + B\overline{f}_r}{A+B} \tag{A.6}$$

In the following figure, the average complete friction factor (Equation A.6) is compared to the experimental data obtained by Han:

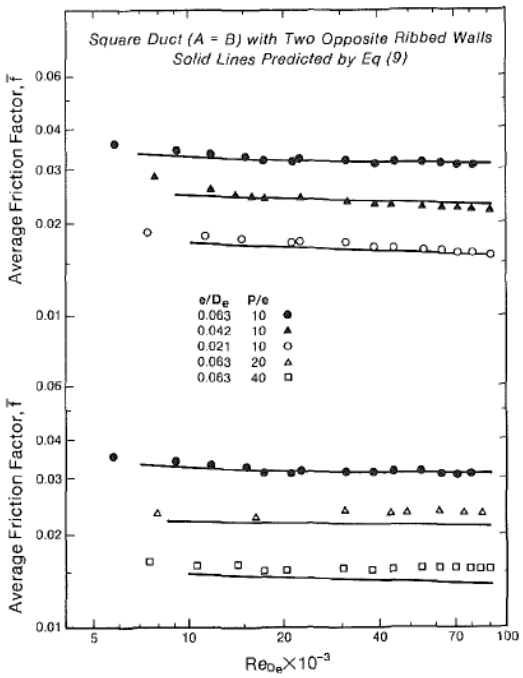

FIGURE A.1: Comparison of prediction methods with present friction data.[6] (Han, 1984).

Where the for each displayed geometrical design combination of e/D_e and p/e, mostly an acceptable agreement is derived between the correlations and measurement data. However, minor discrepancies exist for the predicted friction factor for p/e ratios ≥ 10 which is up to 10 percent lower than the measured data at p/e of 20 and 40. It has to be noted though that these errors solely occur at high Reynolds numbers.

A similar approach as for $\overline{f}$ is taken to derive the prediction method for the heat transfer coefficient ($\overline{St}$); based the same geometrical set. Once more two separate prediction methods are defined for a roughened and a smooth wall, respectively Equations A.7 and A.10. In turn, the average $\overline{St}$ is computed by combining the results of the two in Equation A.11.

The Stanton number for the roughened duct wall is predicted through the following equation:

$$\overline{St}_r = \frac{2}{1+\sqrt{\overline{f}_r/2}[G_H(e^+, Pr) - R_m(p/e)]} \tag{A.7}$$

where G_H is a function of relative roughness height, $e^+ = e/D_h$, and Prandtl number, Pr:

$$G_H(e^+, Pr) = 4.5(e^+)^{0.28} Pr^{0.57};\ \ e^+ \geq 25 \tag{A.8}$$

and, R_m a function of relative pitch p/e:

$$R_m(p/e) = 0.95(p/e)^{0.53} \tag{A.9}$$

In turn, the Stanton number for the smooth wall is determined from the modified Dittus-Boelter relation (2.24):

$$\overline{St}_s = \frac{0.023}{Re_{D_e}^{0.2} Pr^{0.6} (2R_{av}/D_e)^{0.2}} \tag{A.10}$$

Where the Reynolds number is substituted by Re_{D_e}, and $2R_{av}/D_e$ given by Equation A.3. Finally, the rough wall and smooth wall predictions are combined to form the total, average Stanton number, using:

$$\overline{St} = \frac{A\overline{St}_s + B\overline{St}_r}{A + B} \tag{A.11}$$

Equal to the prediction method of the average friction factor, the predicted average Stanton numbers are considerably close to data measured for the entire geometrical set. However, for the St correlations, once more an error margin is encountered of as much as 10 percent for a p/e of 40. From the following figure, it can be seen that this offset with respect to the data only occurs at large Reynolds numbers:

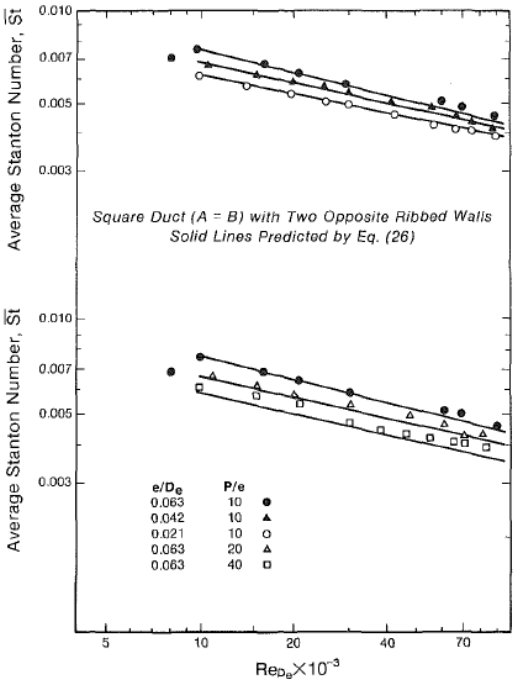

FIGURE A.2: Comparison of prediction methods with present heat transfer data.[6] (Han, 1984).

From the correlations displayed in Figures A.1 and A.2, it can be concluded that Han's estimation method works well for the indicated set of geometries. Even though discrepancies emerge at high end of the considered freestream conditions (i.e.Re), these correlations still provide better results than previously existing estimation methods. Nevertheless, the current thesis topic considers supersonic flow conditions at even higher Re. Therefore, it is chosen to consider only the format and method of derivation of Han's technique, whereas the correlations of Liou and Hwang are preferred.

Appendix B

Mechanisms of open – transitional – closed cavity flow transition

The general classifications of the types of cavity flow have been defined to be either *open* (l/h < 10), *transitional* (10 < l/h < 14) or *closed* ($l/h \geq 14$). In turn, both free stream as well as geometrical characteristics were proven to have a negligible effect on these classifications; provided that wind tunnel tests are conducted under turbulent, supersonic conditions, and $w/h > 10$. As a result, the aerodynamic mechanisms which form the respective cavity flow types can be assumed to be a direct cause of changes in l/h. In this chapter, these mechanisms associated with each cavity type as well as the transition between these types, are explained in relation to the centerline pressure distributions.

Generally, the main flow features which are ascribed to *open*, *transitional* and *closed* cavity flows are governed by the discontinuities associated with compressible flow. From Figure 2.26, it is concluded that for:[34,13]

- *Open cavity flow*: a relatively weak leading edge shock and a stronger trailing edge shock exists, separated by a cavity bridging shear layer.
- *Transitional cavity flow*: a leading and trailing edge expansion fan are formed, separated by a compression wave. The first of which increasingly forces the shear layer towards the cavity floor.
- *Closed cavity flow*: stronger leading and trailing edge expansion fans are found, separated by two compression waves. The latter of which collide into a single shock wave which enters the freestream; forming a delta-wave. Due to the two recirculation zones, separated by a reattached boundary layer, this cavity flow type is commonly called a 'dumbbell flow'.

The flow mechanisms, which are at the base of these compressible flow features, can be described more quantitatively through the pressure coefficient measurements along the cavity centerlines. The changes in pressure coefficient profiles due to the gradual increment in l/h, are shown in the following figures:
Where Figure B.1a displays the gradual change from open–to–transitional–to–closed cavity flows (i.e. $5 \leq l/h \leq 20$), and Figure B.1b focuses on the sudden change between transitional and closed cavity flow for $12 \leq l/h \leq 15$ [-].

Based on the research as conducted by Zhang et al. (2002), the aerodynamic mechanisms behind the transition from open–to–transitional–to–closed can be summarized through the following steps:[13]

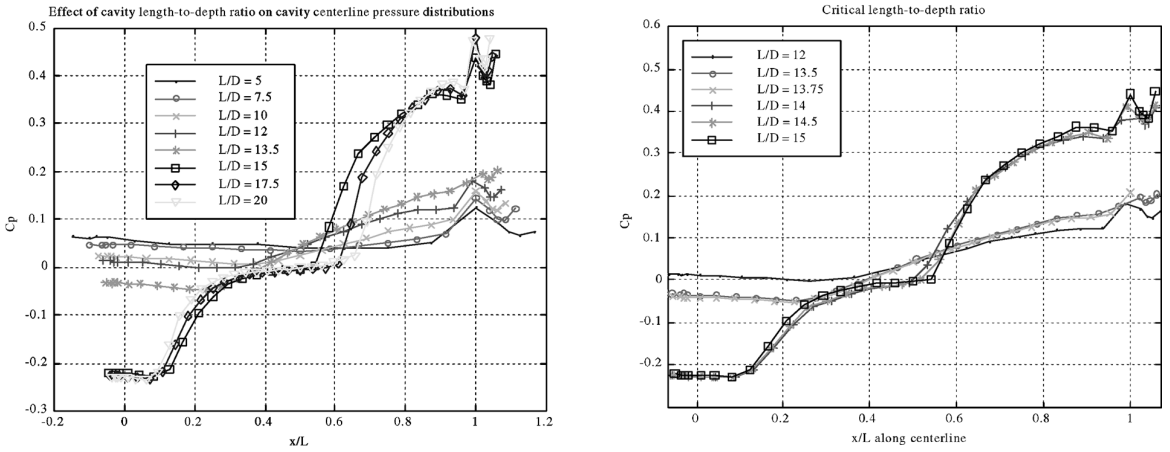

(A) C_p profiles for all l/h. (B) C_p profiles around $(l/h)_{cr}$.

FIGURE B.1: Changes of cavity flow types with l/h. (Zhang et al., 2002)[13]

1. For an open-type cavity flow, the upstream boundary layer separates at the leading edge and entrains some amount of fluid beneath it inside the cavity, forming a mixing layer. The mixing layer becomes thicker as it moves downstream. Through the large velocity difference between the cavity and freestream, the mixing layer is forced to circulate and forms a stable vortex (pair); allowing the outer flow to transcend the cavity relatively undisturbed. This feature is supported by Figure B.1a, for which C_p is nearly uniform for most of the cavity. However, since the l/h of the cavity is small, the separating shear layer strikes the trailing edge of the cavity, forming a shock wave. As a result, this trailing edge impingement shock compresses the cavity air relatively strongly and noticeably increases the pressure. This is seen in Figure B.1a as the sudden C_p peak at $x/L \approx 1.0$. A weak shock wave emanating from the leading edge is generated to adapt the freestream to the high pressure over the cavity. In contrast to the trailing edge shock, this weak leading edge shock hardly effects the flow as no clear ΔC_p can be observed.

2. At an increased value of $10 < l/h < 12$, the shear layer gets developed for a longer distance. The momentum with which it strikes the trailing edge increases, resulting in even higher pressure near the rear face of the cavity; seen by the increased C_p peak at $x/L \approx 1.0$ in Figure B.1a. As the shear layer grows thicker, it approaches the floor gradually. The presence of the floor hinders the free development of the lower part of the shear layer and pushes it upward. As a result, the main flow over the cavity gets deflected, producing a compression fan over the rear portion of the cavity (Figure 2.26). On the other hand, as the space between the shear layer and the floor diminishes, and the momentum of the fluid flowing downstream in the shear layer increases, it becomes more and more difficult for the high-pressure fluid at the rear part of the cavity to travel upstream (i.e. recirculation). In fact, the streamlines inside the cavity, as predicted from numerical simulation, reveal that the backflow is squeezed at the mid portion into a dumbbell-like shape by the shear layer and the floor.[85] In the meantime, the air at the front part of the cavity is continuously scavenged by the shear layer above it, causing the local pressure there to decrease. As a result, the shock wave at the leading edge weakens, and the size of the recirculation near the front corner shrinks. This effect is indicated by the local C_p drops between the curves for respectively L/D = 10, and 12 [-] at $0 < x/L < 0.2$ [-] in Figure B.1a.

3. Further increasing the value of 12 < l/h < 13.75, the shear layer approaches so close to the floor that the backflow is essentially separated into two parts. In turn, two new recirculations, embedded in the backflow and linked by only a thin layer of fluid, are formed. Because of reduced air supplement, the pressure near the front corner decreases below that of the freestream. To compensate the pressure decrement, an expansion fan replaces the weak shock wave at the leading edge, and the external flow begins to deflect into the cavity; initiating the transitional-open type cavity flow. This change in flow discontinuity at the leading edge is also resembled between curves L/D 12 – 13.75 in Figure B.1b, where a slightly negative C_p is formed for $0 \leq x/L \leq 0.4$. After this shallow slope of negative C_p, a relatively strong positive C_p follows; representing the larger, second recirculation. This implies that the compression fan over the rear portion of the cavity becomes strengthened.

4. At a critical value of $13 < l/h \leq 14.0$ [-], the shear layer suddenly impinges onto the floor, completely cutting the backflow into two separate recirculations. The deprivation of air supplement through backflow from the rear part of the cavity causes the pressure near the front part to drop to a minimum. To compensate for this, a strong expansion fan is formed at the leading edge. Due to the lack of backflow towards the front of the cavity, large pressure increments are formed at the rear portion of the cavity. As a result of this pressure, the main flow at the floor is deflected. At this deflection, a single shock is formed, marking the transitional-closed type cavity flow. As this transitional–closed type cavity is extremely sensitive to l/h, it is not explicitly shown in Figure B.1b. However, the corresponding C_p profile is expected to be similar to curve L/D 14 [-] with only one sharp ΔC_p (+) located at the position of the single shock wave. The flow fields belonging to this highly sensitive cavity flow transition, are provided in the following figure:

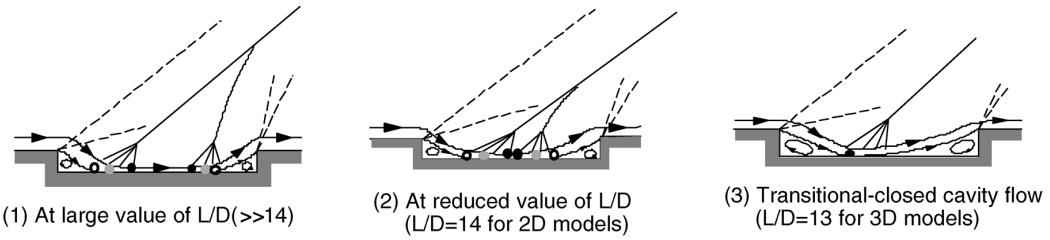

FIGURE B.2: Sketches of flow fields during the opening of closed-type cavity flow.[13] (Zhang et al., 2002)

Where B.2 (3) correlates with the currently described cavity flow type. The final transition from transitional- to closed-type cavity flow requires the formation of two separate, consecutive compression fans. In order to achieve this, sufficient spacing between the shear layer impingement location and the downstream cavity face is required.

5. Thus, moving beyond $(l/h)_{cr}$, it is seen that the distance between the shear layer separation and floor impingement location (Ld_1) as well as the pressure length between the exit shock and trailing edge (Lf_1) decrease. The result of this is that the two compression fans (and two shocks) are increasingly spaced from one another, allowing a longer reattached boundary layer development in the center of the cavity. Additionally, due to increasingly strong expansion waves at the leading and trailing edge of the cavity, the recirculation wakes are increasingly shorter as well. The closed-type cavity flow is thus characterized by two relatively short recirculations, separated by a reattached boundary layer which is enclosed by two compression fans (Figure B.2, (1)). The C_p graphs $15 \leq L/D \leq 20$ from Figure B.1a, accurately display these flow features by:

(a) Recirculation, $0 < x/L < 0.1$: Minimal, negative C_p directly after LE.
(b) Compression fan, $0.1 < x/L < 0.3$: Rapid increment in C_p.
(c) Boundary layer, $0.3 < x/L < 0.6$: Gradual increase in C_p.
(d) Compression fan, $0.6 < x/L < 0.9$: Rapid increment in C_p.
(e) Recirculation, $0.9 < x/L < 0.95$: Sudden C_p slope decrement.
(f) Impingement Shock, $0.95 < x/L < 1.0$: Sudden peak in C_p.

It has to be noted, though, that the characteristic distances (i.e. x/L) of each of these closed cavity-type flows is not necessarily fixed for all $l/h \geq (l/h)_{cr}$. Zhang et al. (2002) concluded that for $l/h > 14$ [-], both recirculation lengths (Ld_1 and Lf_1) remain constant at respectively 7 and 4 [-].[13] In contrast, the pressure lengths associated with the distance from the cavity walls (Ld_3 and Lf_3) to the compression fans do vary; implying the extension of the reattached boundary layer. The definitions of the indicated characteristic lengths are provided in the following figure:

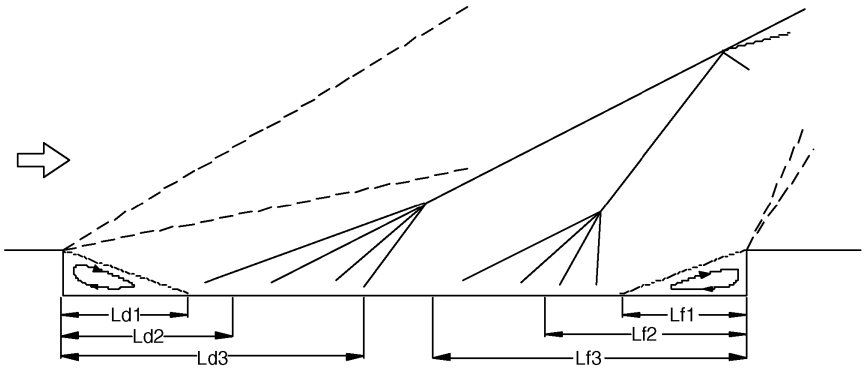

FIGURE B.3: Characteristic lengths for closed cavity flows.[13]
(Zhang et al., 2002)

For which Ld_1 and Lf_1 correspond to respectively upstream and downstream recirculation lengths, Ld_2 and Lf_2 to the deflection lengths and Ld_3 and Lf_3 to the pressure lengths. From their research, Zhang et al. (2002) concluded that – based on their experimental results – that the critical length–to–depth ratio may be predicted with the following equation:[13]

$$(L/D)_{cr} = (Ld_3 + Lf_3)/D \tag{B.1}$$

Which predicts $(L/D)_{cr}$ to be equal to 13.65 [-], relative to 14.00 [-] as measured directly from C_p profiles and Schlieren imaging. As the percentile difference is merely 2.6%, the proposed Equation B.1 seems promising. However, there is no other research yet which supports this equation. Therefore, no definite arguments are stated further on this observation.[86] (Charwat et al., 1961)

Appendix C

Technical drawings

C.1 Schlieren and PIV

In this section, the schematics of an exemplary test model and corresponding wind tunnel placement inserts specific to Schlieren and PIV are provided. All indicated measurements are in mm, whilst each of these models is made of anodized aluminum.

C.1.1 Leading edge insert

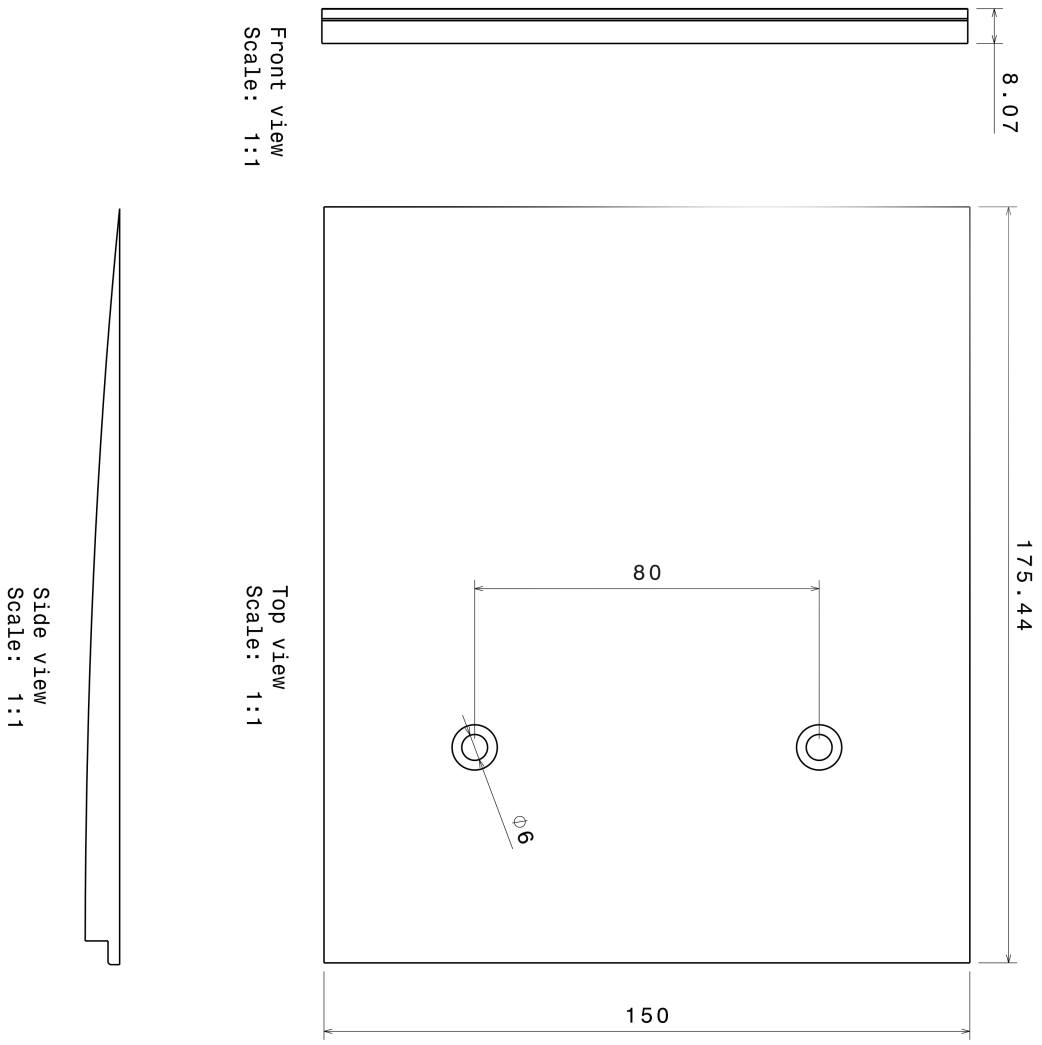

C.1.2 Trailing edge insert

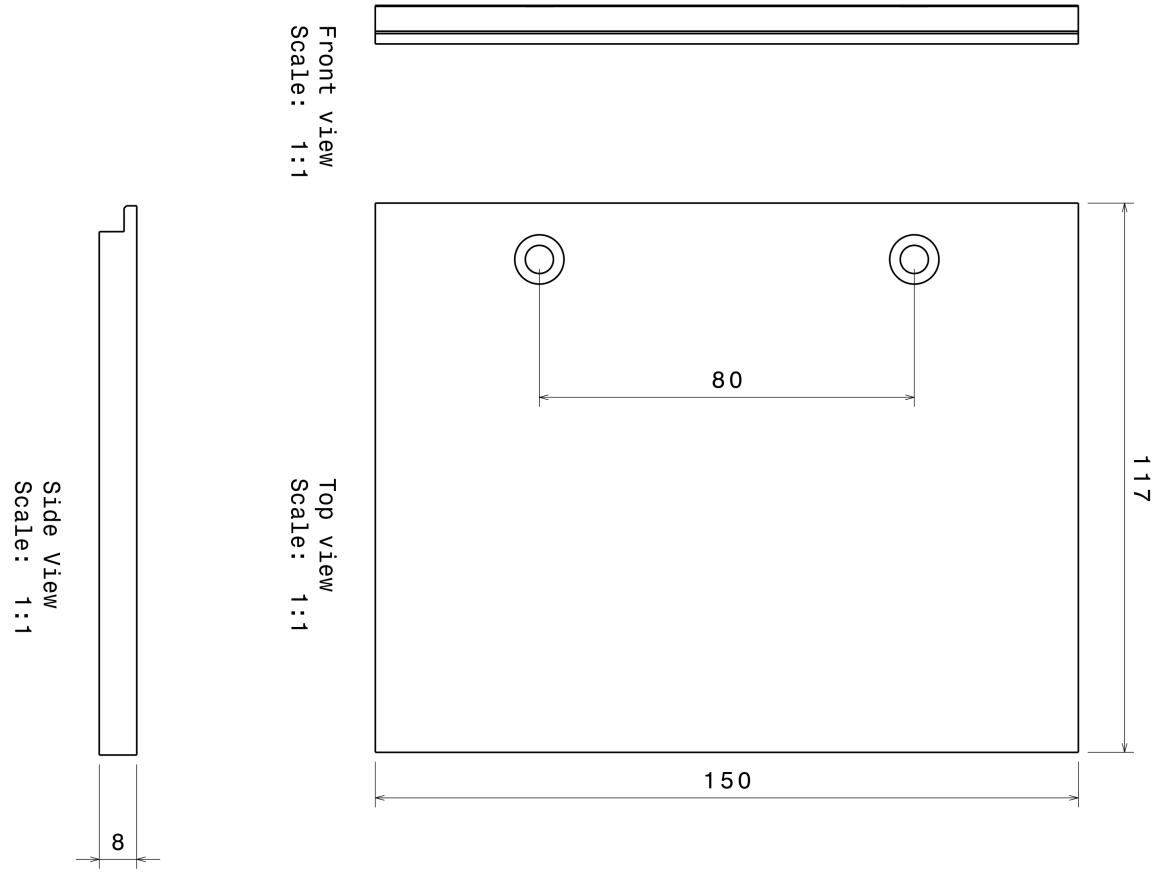

C.1.3 Exemplary wind tunnel model

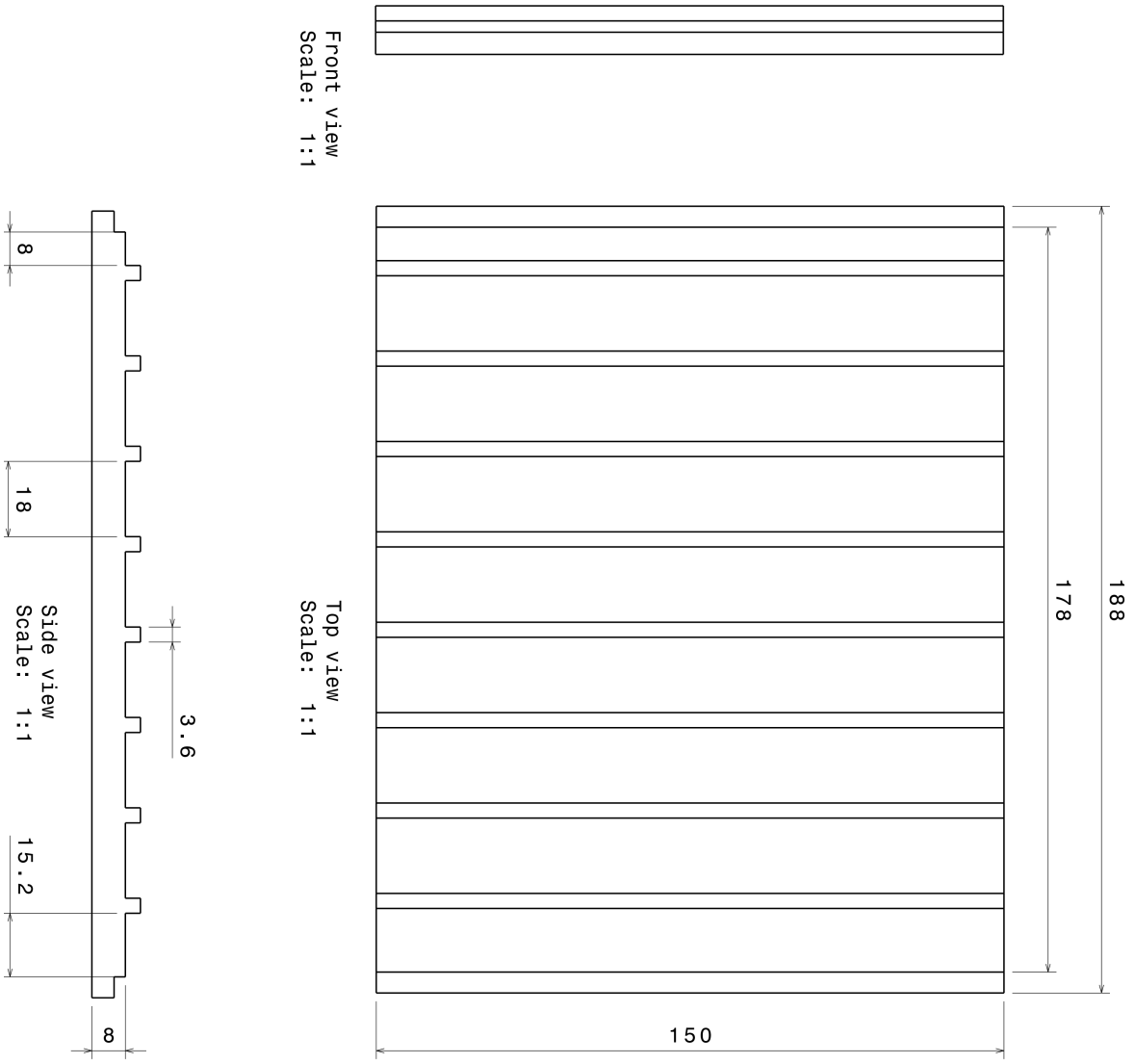

C.2 QIRT

In this section, the schematics of the PCB, insulation plate and cavity door are provided. Together, these three primary components build-up most of the QIRT setup.

C.2.1 Printed circuit board

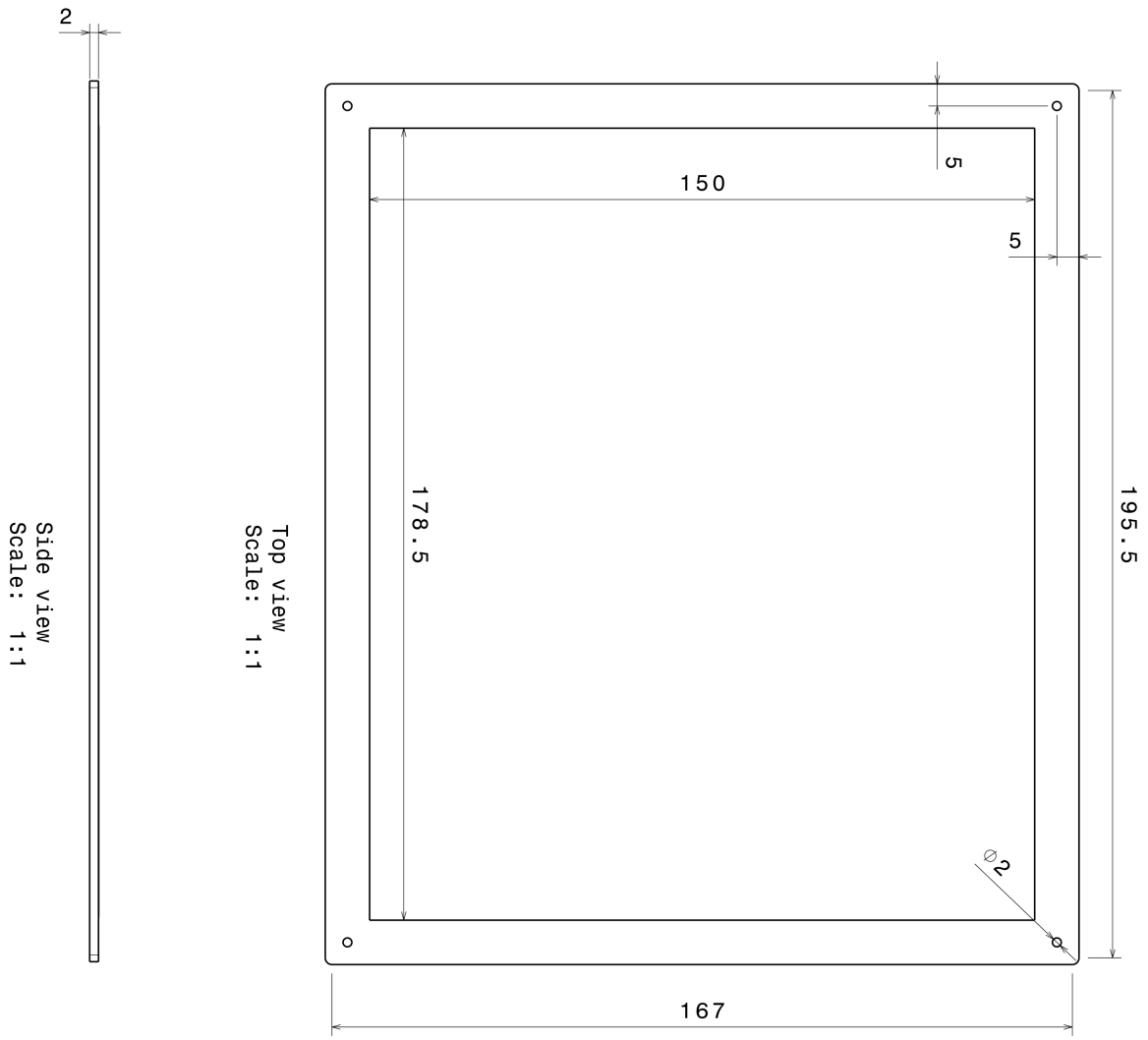

C.2.2 Insulation plate

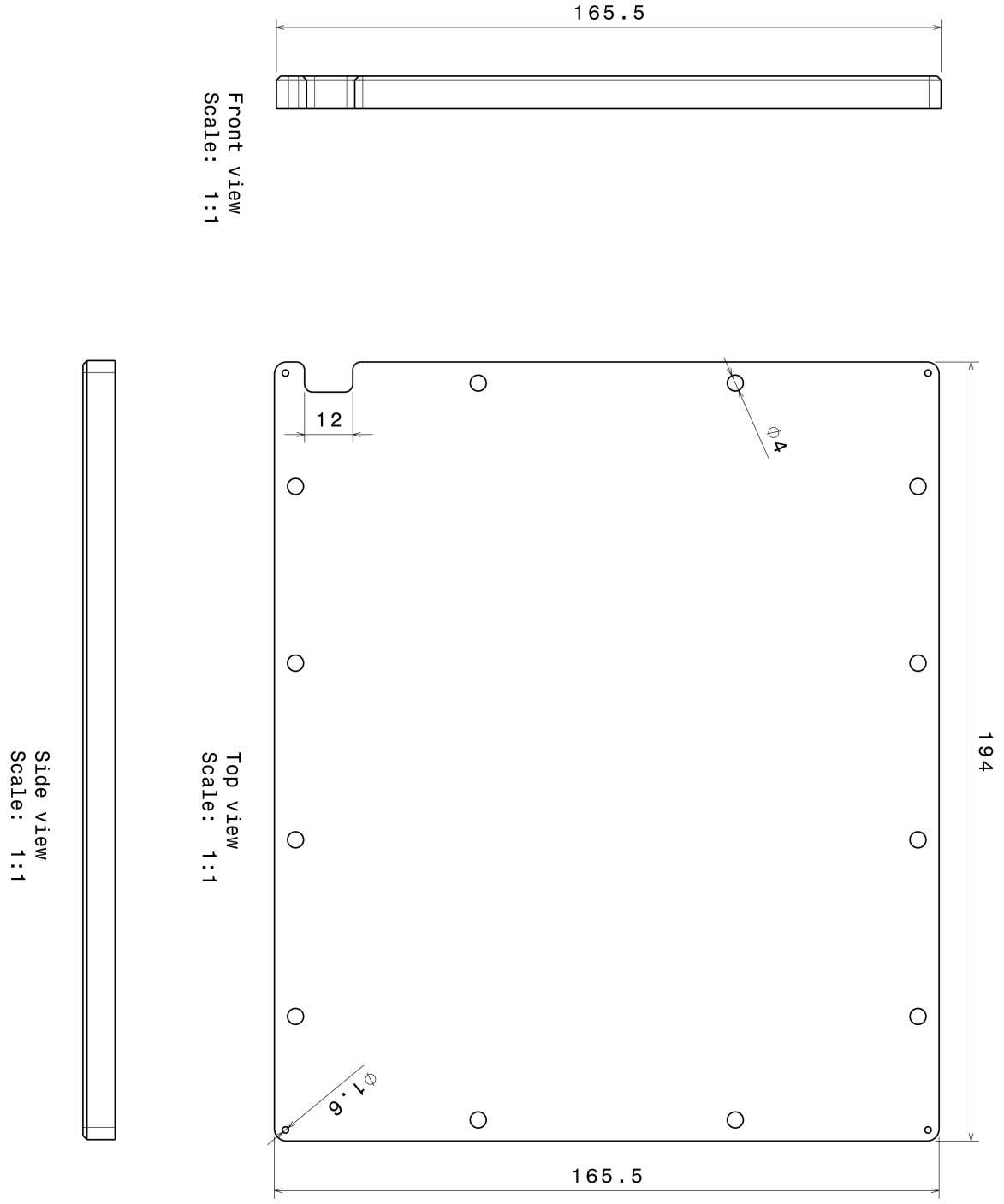

C.2.3 Cavity door

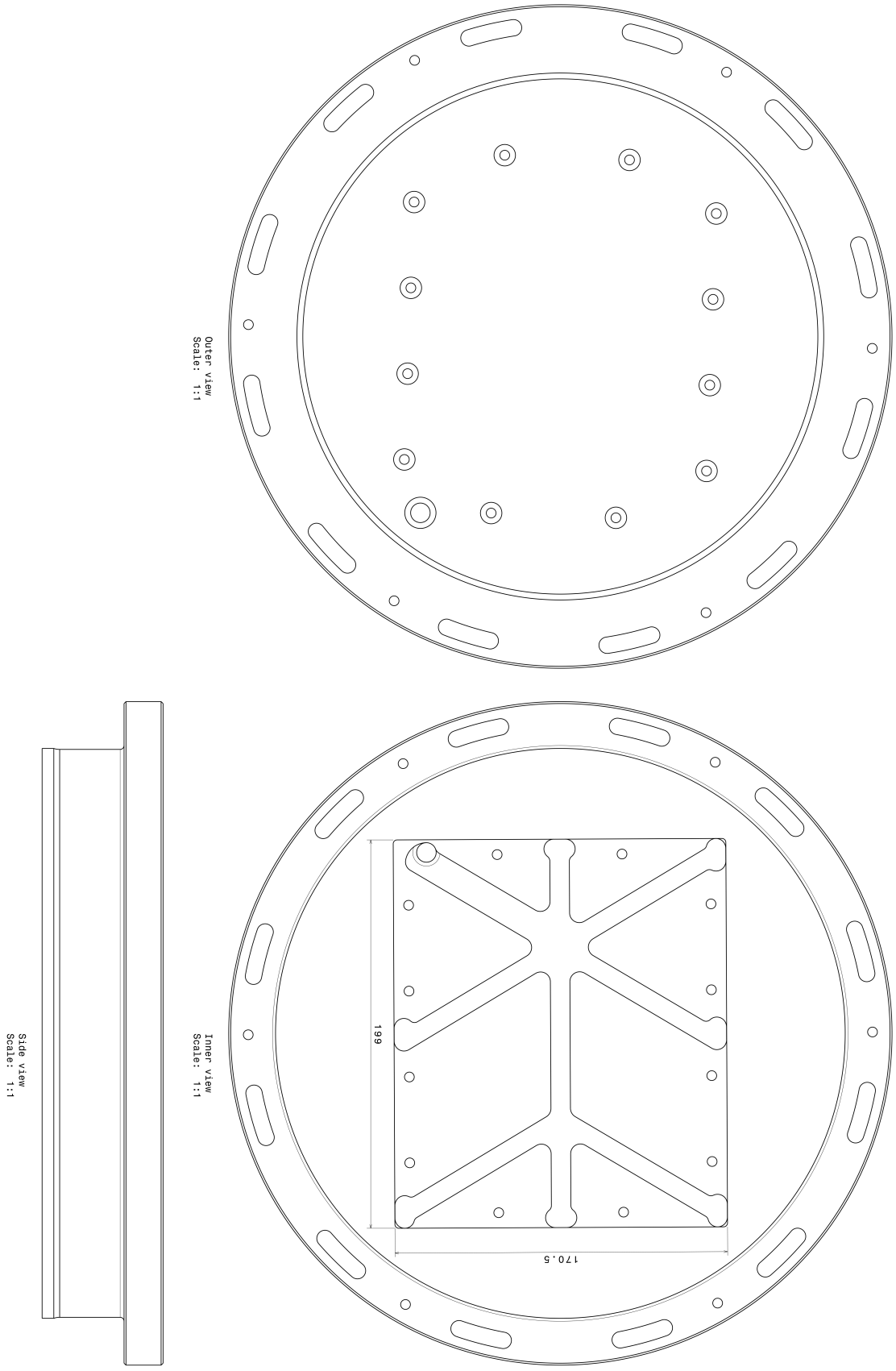

Appendix D

IR camera description - CEDIP 530L

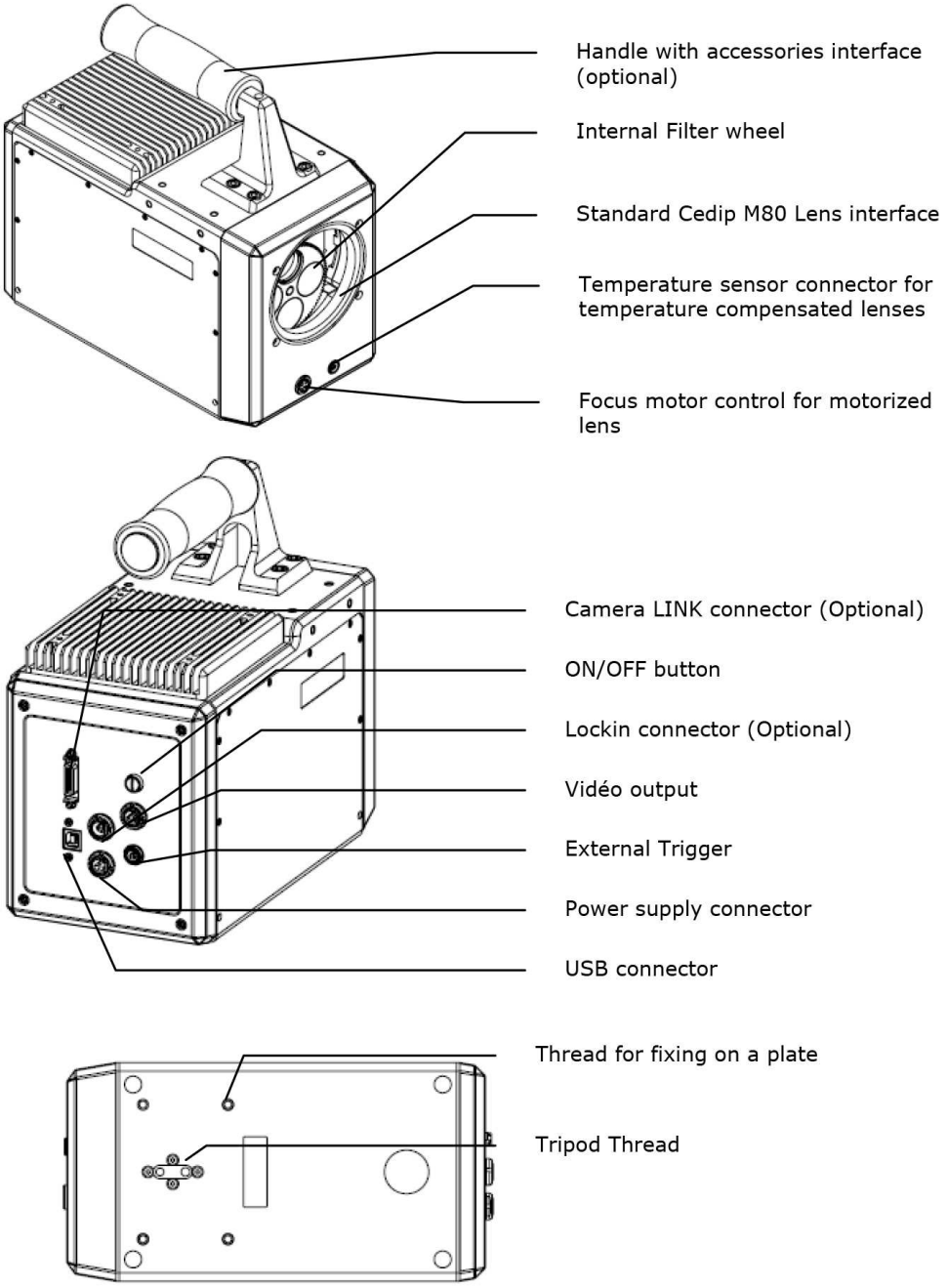

Appendix E

IR lens design - LW 25mm 2.0 Jade

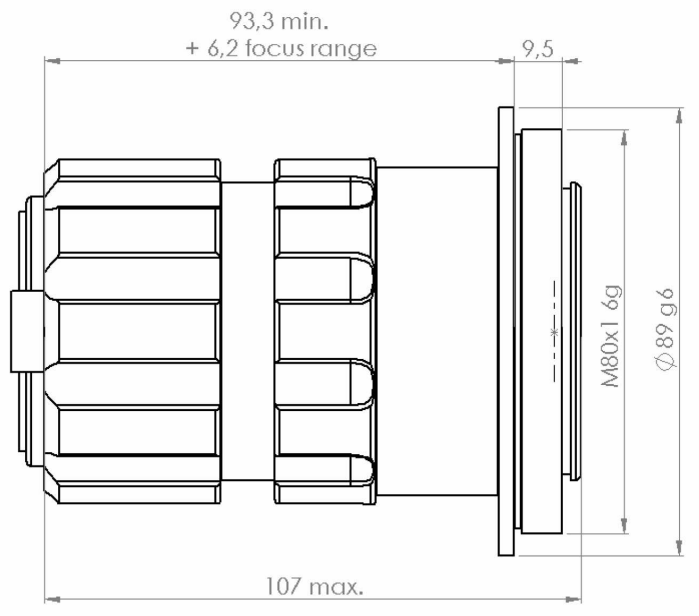

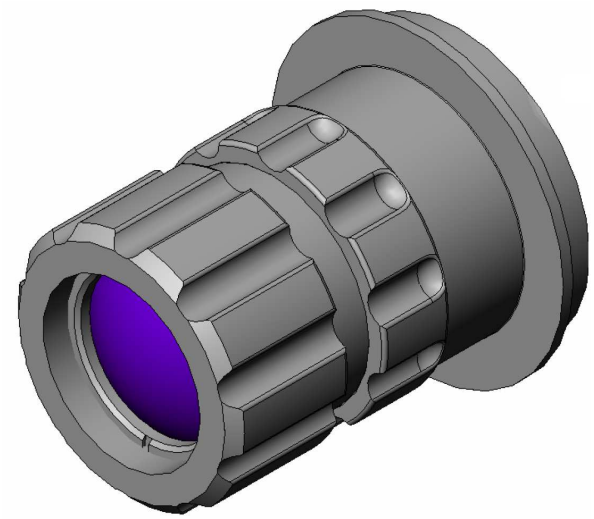

Appendix F

IR camera description – Optris PI 640

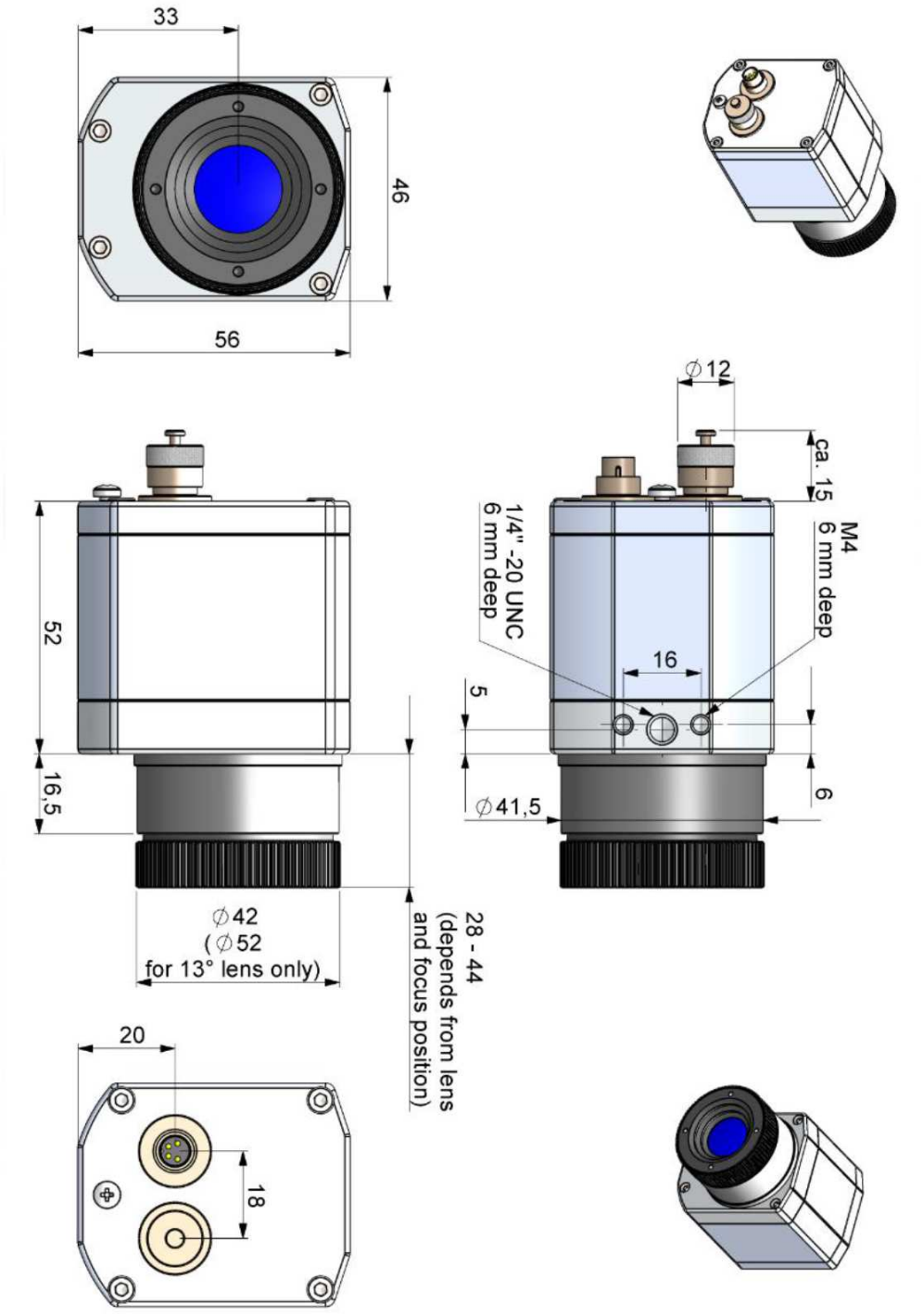

Appendix G

List of experiments

During the research, a multitude of experimental (sub-) campaigns have been conducted. In this section, the labels and characteristics of these wind tunnel tests are listed to provide a detailed overview for the whole thesis. Based on the mentioned labels, future researchers can easily look-up the datasets from the database which is left behind. Note that, in reality, even more experiments were conducted than shown here. Actually, only those tests on which a data reduction or analysis was performed, are specified.

G.1 Schlieren

TABLE G.1: Test matrix Schlieren, incl. knife positions (1/2).

Wind tunnel run	Test plate	Schlieren type	Knife position
31	Flat plate	Continuous	Horizontal, down
32	Flat plate	Continuous	Horizontal, down
33	1.2/15	Continuous	Horizontal, down
34	2.4/15	Continuous	Horizontal, down
35	3.6/15	Continuous	Horizontal, down
36	4.8/15	Continuous	Horizontal, down
37	1.2/20	Continuous	Horizontal, down
38	2.4/20	Continuous	Horizontal, down
39	3.6/20	Continuous	Horizontal, down
40	1.2/5	Continuous	Horizontal, down
41	2.4/5	Continuous	Horizontal, down
42	3.6/5	Continuous	Horizontal, down
43	4.8/5	Continuous	Horizontal, down
44	2.4/10	Continuous	Horizontal, down
45	2.4/25	Continuous	Horizontal, down
46	2.4/30	Continuous	Horizontal, down
47	4.8/15	Spark	Horizontal, down
48	4.8/5	Spark	Horizontal, down
49	3.6/20	Spark	Horizontal, down
50	3.6/15	Spark	Horizontal, down
52	3.6/5	Spark	Horizontal, down
53	2.4/30	Spark	Horizontal, down
54	2.4/25	Spark	Horizontal, down
55	2.4/20	Spark	Horizontal, down
56	2.4/15	Spark	Horizontal, down
57	2.4/10	Spark	Horizontal, down
58	2.4/5	Spark	Horizontal, down

TABLE G.2: Test matrix Schlieren, incl. knife positions (2/2).

Wind tunnel run	Test plate	Schlieren type	Knife position
59	1.2/20	Spark	Horizontal, down
60	1.2/5	Spark	Horizontal, down
61	1.2/15	Spark	Horizontal, down
62	Flat plate	Spark	Horizontal, down
66	Flat plate	Spark	Clockwise
67	Flat plate	Spark	Counter-clockwise
68	4.8/5	Spark	Counter-clockwise
69	3.6/20	Spark	Counter-clockwise
70	2.4/10	Spark	Counter-clockwise
71	1.2/5	Zoomed Spark	Horizontal, down
72	1.2/15	Zoomed Spark	Horizontal, down
73	1.2/20	Zoomed Spark	Horizontal, down
74	2.4/5	Zoomed Spark	Horizontal, down
75	2.4/10	Zoomed Spark	Horizontal, down
76	2.4/15	Zoomed Spark	Horizontal, down
77	3.6/5	Zoomed Spark	Horizontal, down
78	4.8/5	Zoomed Spark	Horizontal, down
79	2.4/20	Zoomed Spark	Horizontal, down
80	2.4/25	Zoomed Spark	Horizontal, down
81	2.4/25	Zoomed Spark	Horizontal, down
82	2.4/30	Zoomed Spark	Horizontal, down
83	3.6/15	Zoomed Spark	Horizontal, down
84	3.6/20	Zoomed Spark	Horizontal, down
85	4.8/15	Zoomed Spark	Horizontal, down

G.2 PIV

TABLE G.3: Test matrix PIV, incl. FOV characteristics. (1/2)

Run (#)	Test plate	FOV type	FOV size	ΔT (μs)	Cams (#)	Res. (pxl/mm)
8	2.4/10-I	Above ribs	198×42	1	4	30
9	2.4/10-II	Above ribs	198×42	1	4	30
13	2.4/5-I	Above ribs	198×42	1	4	30
14	2.4/5-II	Above ribs	198×42	1	4	30
15	2.4/15-I	Above ribs	198×42	1	4	30
16	2.4/15-II	Above ribs	198×42	1	4	30
17	2.4/20-I	Above ribs	198×42	1	4	30
18	2.4/20-II	Above ribs	198×42	1	4	30
19	2.4/25-I	Above ribs	198×42	1	4	30
20	2.4/25-II	Above ribs	198×42	1	4	30
21	2.4/30-I	Above ribs	198×42	1	4	30
22	2.4/30-II	Above ribs	198×42	1	4	30
24	3.6/5-I	Above ribs	198×42	1	4	30
25	3.6/5-II	Above ribs	198×42	1	4	30
27	3.6/15-I	Above ribs	198×42	1	4	30
28	3.6/15-II	Above ribs	198×42	1	4	30

TABLE G.4: Test matrix PIV, incl. FOV characteristics. (2/2)

Run (#)	Test plate	FOV type	FOV size	ΔT (μs)	Cams (#)	Res. (pxl/mm)
30	3.6/20-I	Above ribs	198×42	1	4	30
31	3.6/20-II	Above ribs	198×42	1	4	30
35	Flat plate	Above ribs	198×42	1	4	30
36	Flat plate	Above ribs	198×42	1	4	30
37	1.2/5-I	Above ribs	198×42	1	4	30
38	1.2/5-II	Above ribs	198×42	1	4	30
39	1.2/15-I	Above ribs	198×42	1	4	30
40	1.2/15-II	Above ribs	198×42	1	4	30
41	1.2/20-I	Above ribs	198×42	1	4	30
42	1.2/20-II	Above ribs	198×42	1	4	30
43	4.8/5-I	Above ribs	198×42	1	4	30
44	4.8/5-II	Above ribs	198×42	1	4	30
48	4.8/15-I	Above ribs	198×42	1	4	30
49	4.8/15-II	Above ribs	198×42	1	4	30
68	2.4-30-cavity-I	Final rib pair	76.8×28.4	1.5	2	40.5
69	2.4-30-cavity-II	Final rib pair	76.8×28.4	1.5	2	40.5
70	2.4-30-cavity-I	Final rib pair	72×30	1.5	2	40.5
71	2.4-30-cavity-II	Final rib pair	72×30	1.5	2	40.5
72	2.4-15-cavity-I	Final rib pair	36×20	1.5	2	67.5
73	2.4-15-cavity-II	Final rib pair	36×20	1.5	2	67.5
75	2.4-15-cavity-I	Two rib pairs	79.2×20	1.5	2	40.5
76	2.4-15-cavity-II	Two rib pairs	79.2×20	1.5	2	40.5
77	3.6-20-cavity-I	Final rib pair	72×30	1.5	2	40.5
78	3.6-20-cavity-II	Final rib pair	72×30	1.5	2	40.5
79	4.8-15-cavity-I	Final rib pair	72×30	1.5	2	40.5
80	4.8-15-cavity-II	Final rib pair	72×30	1.5	2	40.5

G.3 QIRT

TABLE G.5: Test matrix primary QIRT, incl. power supply settings and reservoir pressure (1/2).

Wind tunnel run	Test plate	PCB (#)	±% BM	I (A)	U (V)	P (pre)	P (post)
FP_17_heated_325	FP	17	325	5.17	128.6	37	34.1
FP_17_heated_300	FP	17	300	5.01	124.8	34.1	31.1
FP_17_heated_350	FP	17	350	5.32	132.5	31.1	29
1205_11_heated_225	1.2/05	11	225	4.74	107.2	33	30.2
1205_11_heated_237	1.2/05	11	237.5	4.83	109.2	31	27.5
1205_11_heated_250	1.2/05	11	250	4.92	111.2	27.2	23
1215_17_heated_225	1.2/15	17	225	4.52	112.5	29.3	26
1215_17_heated_237	1.2/15	17	237.5	4.60	114.6	27.1	24.5
1215_17_heated_250	1.2/15	17	250	4.69	116.7	26	22.9
1220_09_heated_225	1.2/20	9	225	4.95	102.6	31	27.8
1220_09_heated_237	1.2/20	9	237.5	5.05	104.5	28.1	25
1220_09_heated_250	1.2/20	9	250	5.14	106.4	25.5	22.1

TABLE G.6: Test matrix primary QIRT, incl. power supply settings and reservoir pressure (2/2).

Wind tunnel run	Test plate	PCB (#)	±% BM	I (A)	U (V)	P (pre)	P (post)
2405_06_heated_225	2.4/5	6	225	4.81	105.7	24	20.9
2405_06_heated_230	2.4/5	6	230	4.84	106.5	21	18
2405_06_heated_235	2.4/5	6	235	4.88	107.3	18.9	15.9
2410_05_heated_225	2.4/10	5	225	4.88	104.0	32.1	29
2410_05_heated_230	2.4/10	5	230	4.92	104.8	29.6	26.4
2410_05_heated_235	2.4/10	5	235	4.96	105.6	26.9	24.9
2415_13_heated_225	2.4/15	13	225	4.77	106.4	31.2	28
2415_13_heated_230	2.4/15	13	230	4.81	107.3	28.5	25.2
2415_13_heated_235	2.4/15	13	235	4.85	108.1	25.8	22.9
2420_12_heated_225	2.4/20	12	225	4.90	103.8	39	35.2
2420_12_heated_237	2.4/20	12	237.5	4.99	105.8	35.2	33.1
2420_12_heated_250	2.4/20	12	250	5.08	107.7	33.1	30
2420_12_heated_262	2.4/20	12	262.5	5.17	109.6	31	27.8
2425_20_heated_225	2.4/25	20	225	4.87	104.3	39.2	36
2425_20_heated_230	2.4/25	20	230	4.91	105.1	36.5	33
2425_20_heated_235	2.4/25	20	235	4.95	105.9	33.6	30.5
2430_10_heated_225	2.4/30	10	225	4.85	104.8	35.1	32
2430_10_heated_237	2.4/30	10	237.5	4.94	106.8	33	30
2430_10_heated_250	2.4/30	10	250	5.03	108.7	30	27
3605_8_heated_225	3.6/5	8	225	4.73	107.4	31.5	28.5
3605_8_heated_215	3.6/5	8	215	4.66	105.7	29.9	26.2
3605_8_heated_220	3.6/5	8	220	4.69	106.6	28.5	25
3605_8_heated_225_2	3.6/5	8	225	4.73	107.4	26.1	23
3615_22_heated_225	3.6/15	22	225	4.67	108.8	41	38
3615_22_heated_230	3.6/15	22	230	4.71	109.6	38	35
3615_22_heated_235	3.6/15	22	235	4.74	110.5	35	32
3620_07_heated_225	3.6/20	7	219	4.85	102.8	38	35
3620_07_heated_250	3.6/20	7	243.5	5.03	106.7	35	32.1
3620_07_heated_237	3.6/20	7	233.1	4.96	105.7	32.1	30
4805_04_heated_225	4.8/5	4	225	4.69	108.3	28.2	25
4805_04_heated_237	4.8/5	4	237.5	4.78	110.4	25	22.8
4805_04_heated_250	4.8/5	4	250	4.87	112.4	22.8	19.5
4815_21_heated_225	4.8/15	21	225	4.51	112.7	31	28
4815_21_heated_220	4.8/15	21	220	4.47	111.8	29	26
4815v2_21_heated_215	4.8/15	21	215	4.44	110.9	41.4	38
4815v2_21_heated_220	4.8/15	21	220	4.47	111.8	36	32.5
4815v2_21_heated_225	4.8/15	21	225	4.51	112.7	33	30
FLPL_02_heated_275	FP	2	275	4.69	125.1	32.1	29
FLPL_03_heated_300	FP	3	300	5.00	125.0	40	36.4
FLPL_03_heated_275	FP	3	275	4.84	121.1	37.1	34
FLPL_03_heated_325	FP	3	325	5.16	128.9	34.2	31.1
2410_15_heated_225	2.4/10	15	225	5.13	99.0	39	35.6
2410_15_heated_230	2.4/10	15	230	5.17	99.8	36	33
2410_15_heated_235	2.4/10	15	235	5.21	100.5	33.9	30
2410_1_heated_225	2.4/10	1	225	4.34	117.1	31.5	28
2410_1_heated_230	2.4/10	1	230	4.37	118.0	28.6	25.6
2410_1_heated_235	2.4/10	1	235	4.04	118.9	26	23.1

TABLE G.7: Test matrix primary QIRT, incl. power supply settings and temperature readings (1/2).

Wind tunnel run	Test plate	PCB (#)	±% BM	$T_{amb.1}$	$T_{amb.2}$	$T_{cam.1}$	$T_{cam.2}$
FP_17_heated_325	FP	17	325	20.7	20.6	27.4	28.2
FP_17_heated_300	FP	17	300	20.6	20.5	28.3	28.4
FP_17_heated_350	FP	17	350	20.5	20.5	28.4	28.4
1205_11_heated_225	1.2/05	11	225	22.7	22.8	29.7	29.8
1205_11_heated_237	1.2/05	11	237.5	23.2	23.2	29.9	30.1
1205_11_heated_250	1.2/05	11	250	23.5	23.5	30.1	30.2
1215_17_heated_225	1.2/15	17	225	27.2	27.3	33.2	33.3
1215_17_heated_237	1.2/15	17	237.5	27.6	27.6	33.5	33.6
1215_17_heated_250	1.2/15	17	250	27.9	28	33.7	33.8
1220_09_heated_225	1.2/20	9	225	25.1	25.1	32	32.1
1220_09_heated_237	1.2/20	9	237.5	25.1	25	32.1	32.1
1220_09_heated_250	1.2/20	9	250	25.2	25.3	32.1	32.1
2405_06_heated_225	2.4/5	6	225	24.5	24.5	31.4	31.5
2405_06_heated_230	2.4/5	6	230	24.8	24.8	31.5	31.5
2405_06_heated_235	2.4/5	6	235	25.1	25.2	31.5	31.6
2410_05_heated_225	2.4/10	5	225	22.8	23.1	29.7	30.2
2410_05_heated_230	2.4/10	5	230	23.2	23.2	30.3	30.4
2410_05_heated_235	2.4/10	5	235	23.2	23.2	30.4	30.3
2415_13_heated_225	2.4/15	13	225	24.3	24.5	30.9	31.1
2415_13_heated_230	2.4/15	13	230	24.6	24.6	31.1	31.2
2415_13_heated_235	2.4/15	13	235	24.7	24.7	31.2	31.2
2420_12_heated_225	2.4/20	12	225	19.7	19.8	25.5	25.8
2420_12_heated_237	2.4/20	12	237.5	19.8	20	26.2	27.2
2420_12_heated_250	2.4/20	12	250	20	20.1	27.2	27.3
2420_12_heated_262	2.4/20	12	262.5	20	20	27.5	27.5
2425_20_heated_225	2.4/25	20	225	22.3	22.3	29.9	30
2425_20_heated_230	2.4/25	20	230	22.6	22.8	30.1	30.2
2425_20_heated_235	2.4/25	20	235	23.2	23.2	30.2	30.4
2430_10_heated_225	2.4/30	10	225	21.3	21.3	28.8	29.6
2430_10_heated_237	2.4/30	10	237.5	21.4	21.4	28.6	28.6
2430_10_heated_250	2.4/30	10	250	21.4	21.5	28.6	28.6
3605_8_heated_225	3.6/5	8	225	24.5	24.5	30.9	31
3605_8_heated_215	3.6/5	8	215	24.5	24.5	31.1	31.1
3605_8_heated_220	3.6/5	8	220	24.7	24.7	31.1	31.1
3605_8_heated_225_2	3.6/5	8	225	24.8	24.7	31.1	31.1
3615_22_heated_225	3.6/15	22	225	21.4	21.5	28.7	28.9
3615_22_heated_230	3.6/15	22	230	21.6	21.5	28.9	28.9
3615_22_heated_235	3.6/15	22	235	21.5	21.7	28.9	29
3620_07_heated_225	3.6/20	7	219	19.1	19.1	27.2	27.3
3620_07_heated_250	3.6/20	7	243.5	19.1	19	27.3	27.2
3620_07_heated_237	3.6/20	7	233.1	19.1	19.1	27.2	27.1

TABLE G.8: Test matrix primary QIRT, incl. power supply settings and temperature readings (2/2).

Wind tunnel run	Test plate	PCB (#)	±% BM	$T_{amb.1}$	$T_{amb.2}$	$T_{cam.1}$	$T_{cam.2}$
4805_04_heated_225	4.8/5	4	225	18.5	18.6	25.5	25.8
4805_04_heated_237	4.8/5	4	237.5	18.6	18.6	25.9	25.9
4805_04_heated_250	4.8/5	4	250	18.7	18.7	26	26.1
4815_21_heated_225	4.8/15	21	225	24	24	30.4	30.6
4815_21_heated_220	4.8/15	21	220	24	24	30.7	30.7
4815v2_21_heated_215	4.8/15	21	215	24.2	24.3	28.3	28.6
4815v2_21_heated_220	4.8/15	21	220	24.3	24.6	30.5	30.6
4815v2_21_heated_225	4.8/15	21	225	24.7	24.7	30.7	31
FLPL_02_heated_275	FP	2	275	27.1	27.1	33.8	33.9
FLPL_03_heated_300	FP	3	300	25.8	25.8	30.6	30.9
FLPL_03_heated_275	FP	3	275	26	26	32.1	32.2
FLPL_03_heated_325	FP	3	325	26.6	26.6	32.8	32.9
2410_15_heated_225	2.4/10	15	225	22.5	22.7	28.6	29
2410_15_heated_230	2.4/10	15	230	22.8	23.1	29.2	29.6
2410_15_heated_235	2.4/10	15	235	23.2	23.2	29.7	29.9
2410_1_heated_225	2.4/10	1	225	24.3	24.5	31.1	31.1
2410_1_heated_230	2.4/10	1	230	24.3	24.3	31.2	31.3
2410_1_heated_235	2.4/10	1	235	24.3	24.3	31.2	31.1

TABLE G.9: Test matrix secondary QIRT, incl. power supply settings.

Wind tunnel run	Test plate	PCB (#)	Cavity (#)	±% BM	I (A)	U (V)
2405_06_highrs_250	2.4/5	6	4	250	4.99	109.7
2410_10_highrs_235	2.4/10	10	4	235	4.92	106.4
2425_20_highrs_235	2.4/25	20	2	235	4.95	105.9
2430_10_highrs_250	2.4/30	10	3	250	5.03	108.7
2415_13_c34_highrs_235	2.4/15	13	3&4	235	4.85	108.1
2415_13_c2_highrs_235	2.4/15	13	2	235	4.85	108.1
3620_07_highrs_250	3.6/20	7	2	250	5.08	107.7
4815_21_highrs_225	4.8/15	21	2	225	4.51	112.7
1215_17_highrs_250	1.2/15	17	2	250	4.69	116.7
3615_22_highrs_225	3.6/15	22	2	235	4.74	110.5
1205_11_highrs_250	1.2/5	11	23	250	4.92	111.2

TABLE G.10: Test matrix secondary QIRT, incl. reservoir pressure readings.

Wind tunnel run	Test plate	PCB (#)	Cavity (#)	±% BM	P (pre)	P (post)
2405_06_highrs_250	2.4/5	6	4	250	40	38.9
2410_10_highrs_235	2.4/10	10	4	235	42	39.0
2425_20_highrs_235	2.4/25	20	2	235	31.1	28.1
2430_10_highrs_250	2.4/30	10	3	250	33.3	31.0
2415_13_c34_highrs_235	2.4/15	13	3&4	235	37.1	34.9
2415_13_c2_highrs_235	2.4/15	13	2	235	35.1	32.9
3620_07_highrs_250	3.6/20	7	2	250	39.1	36.9
4815_21_highrs_225	4.8/15	21	2	225	41.1	39
1215_17_highrs_250	1.2/15	17	2	250	37.9	35.1
3615_22_highrs_225	3.6/15	22	2	225	29.1	26.9
1205_11_highrs_250	1.2/5	11	23	250	36	33.8

TABLE G.11: Test matrix secondary QIRT, incl. ambient temperature readings.

Wind tunnel run	Test plate	PCB (#)	Cavity (#)	±% BM	$T_{amb.1}$	$T_{amb.2}$
2405_06_highrs_250	2.4/5	6	4	250	23.9	23.9
2410_10_highrs_235	2.4/10	10	4	235	23.8	23.8
2425_20_highrs_235	2.4/25	20	2	235	27.8	27.9
2430_10_highrs_250	2.4/30	10	3	250	28.1	28.1
2415_13_c34_highrs_235	2.4/15	13	3&4	235	27.7	27.7
2415_13_c2_highrs_235	2.4/15	13	2	235	27.9	28.0
3620_07_highrs_250	3.6/20	7	2	250	27.8	27.8
4815_21_highrs_225	4.8/15	21	2	225	27.4	27.4
1215_17_highrs_250	1.2/15	17	2	250	24.0	24.1
3615_22_highrs_225	3.6/15	22	2	225	27.4	27.4
1205_11_highrs_250	1.2/5	11	2&3	250	24.3	24.3

TABLE G.12: Test matrix secondary QIRT, incl. camera temperature readings.

Wind tunnel run	Test plate	PCB (#)	Cavity (#)	±% BM	$T_{cam.1}$	$T_{cam.2}$
2405_06_highrs_250	2.4/5	6	4	250	31.0	31.0
2410_10_highrs_235	2.4/10	10	4	235	30.6	30.8
2425_20_highrs_235	2.4/25	20	2	235	33.2	33.2
2430_10_highrs_250	2.4/30	10	3	250	32.2	32.2
2415_13_c34_highrs_235	2.4/15	13	3&4	235	32.2	32.2
2415_13_c2_highrs_235	2.4/15	13	2	235	32.1	32.1
3620_07_highrs_250	3.6/20	7	2	250	33.3	33.3
4815_21_highrs_225	4.8/15	21	2	225	33.2	33.2
1215_17_highrs_250	1.2/15	17	2	250	30.8	30.8
3615_22_highrs_225	3.6/15	22	2	225	32.8	32.8
1205_11_highrs_250	1.2/5	11	2&3	250	30.7	30.7

Appendix H

Periscope probe placement

To avoid a severe impingement of (part of) the laser sheet onto the tops of the ribbed geometries, a cut-off knife was mounted in between the laser periscope probe and the test section. By physically eliminating the worst of the resulting reflections, the requirement of DaVis pre-processing would be reduced. For the two sub-campaigns of PIV, different periscope positions were defined; respectively the *primary* (Figure H.1) and *secondary* (Figure H.2).

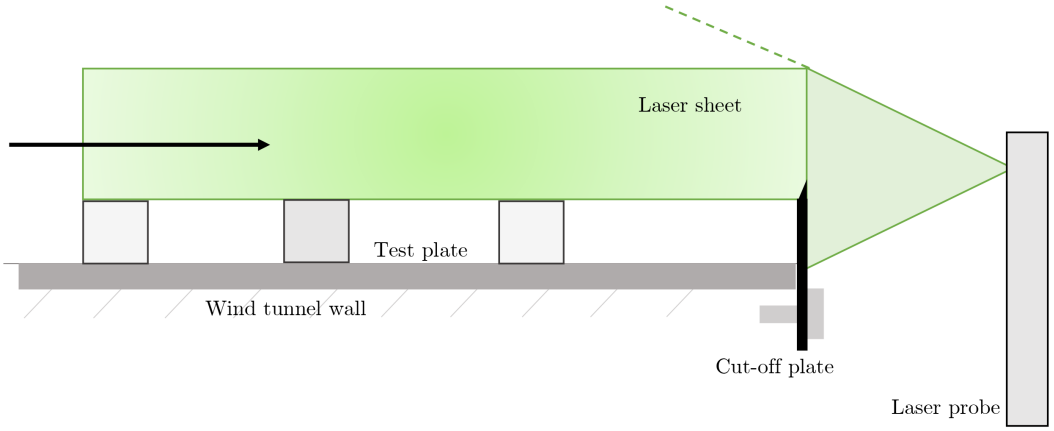

FIGURE H.1: Placement of the laser periscope probe and cut-off plate, primary campaign.

For the primary campaign, it was vital to position both periscope exit and cut-off knife such that the bottom of the laser sheet aligned perfectly with the rib tops (and camera FOV). The resulting setup was found to work correctly during the wind tunnel experiments. A minor defect, however, was that the adjustments to the laser probe had to be conducted in stagnant conditions. This meant that, once the wind tunnel was operated, the probe tilted back slightly; affecting the directionality of the laser sheet. This was corrected for by tiling the probe mirror approximately 2° downward relative to the optimal stagnant setting.

A secondary goal of the PIV campaign was to quantify the flow fields in between the ribs of test plate geometries. Due to the limitations of the laser sheet aiming, however, only the final cavities of specific models could be tested. A schematic of these limitations is indicated in the following figure:

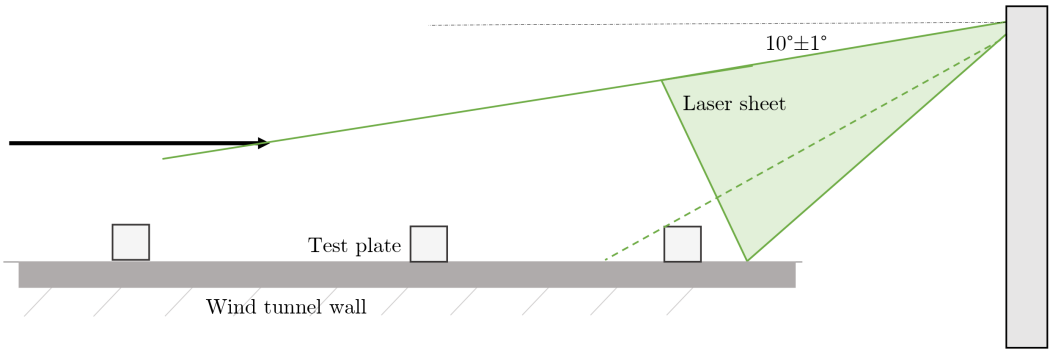

FIGURE H.2: Placement of the laser periscope probe, secondary campaign.

The setup displayed in Figure H.2 was found to work adequately in terms of sufficient cavity illumination. However, by the fact that the high-intense laser light directly interacted with the ribs and cavity floors, many reflections were formed. These, in turn, were prevented as much as possible by decreasing the laser intensity. The final remaining reflections were resolved by applying geometrical masks and filters in DaVis pre-processing.

Appendix I

Optical settings PIV

Complementary to the more general overview of the PIV setup, it is decided to list the exact optical settings used during the PIV campaign. Through the data displayed in Table I.1, a future researcher is enabled to directly copy the equipment, camera settings and DaVis inputs. By combining this knowledge to the descriptions provided in Section 3.4.4, the experiments can be reproduced completely.

TABLE I.1: Optical equipment and settings PIV campaign.

Optical definition	Value
Camera	Bobcat B1610 (4x)
Objective	Nikkor 60mm, f/2.8D (4x)
Camera resolution	1628 $\times$ 1236 pixels
Focal depth	6.0 mm
Planar FOV	198 mm
Panar FOV/camera	54 mm
Overlap FOV	6 mm
Magnification factor (M)	0.132 [-]
Object distance (d_o)	515 mm
Image distance (d_i)	68 mm
Aperture size ($f_\#$)	5.6 [-]
Pulse separation time (Δt)	1.0 μs
V_{maz} (Δt = 1 μs, window = 32 pixels)	270 m/s
V_{min} (Δt = 1 μs, window = 32 pixels)	3.3 m/s
DVR	80 [-]
Laser sheet thickness (Δz_0)	3.0 mm
Capturing frequency	25 *fps*
Image pairs per experiment	250 [-]

Appendix J

Experimental setups

Throughout the report, schematic drawings have been provided such to clarify the workings and placement of the experimental setups which were built for respectively the Schlieren, PIV and QIRT methodologies. In this Chapter, actual pictures of these setups are provided in order to avoid any unclarities which future researchers might have.

J.1 Schlieren

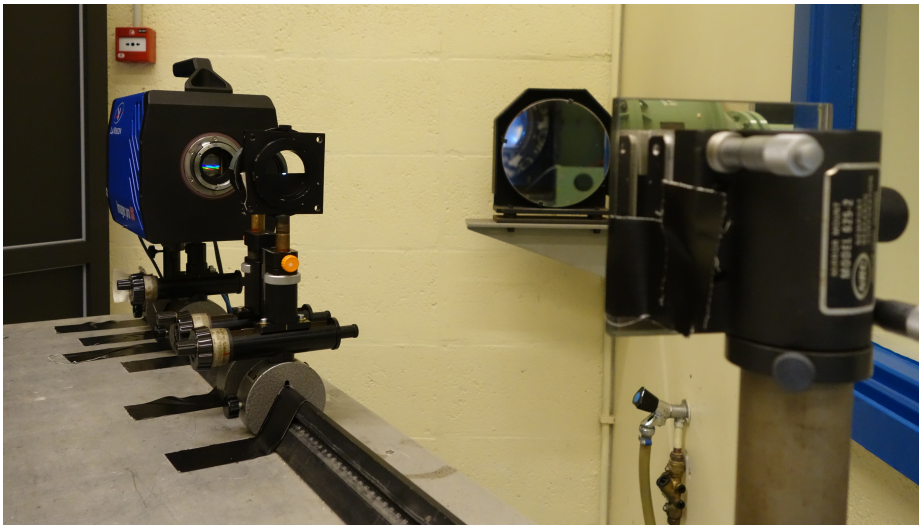

FIGURE J.1: Schlieren-visualization setup: image capturing side.

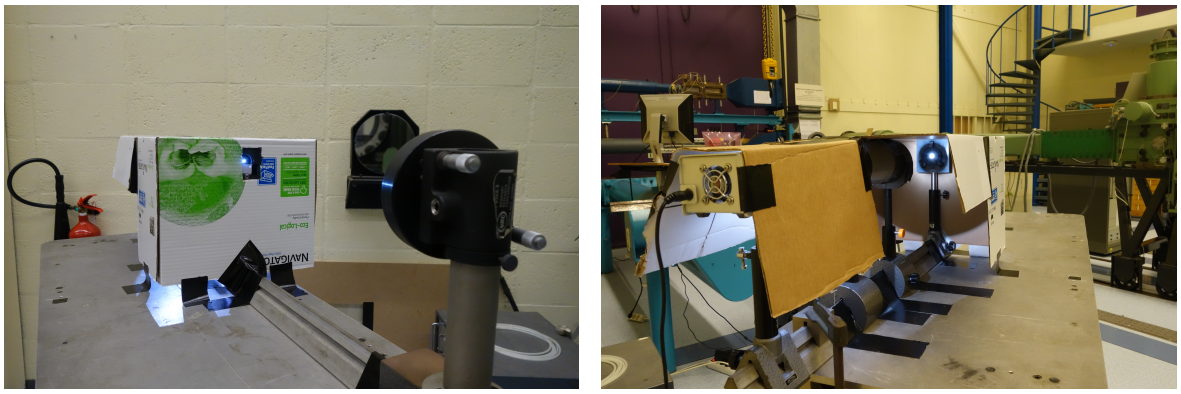

(A) Front view. (B) Rear view.

FIGURE J.2: Schlieren-visualization setup: illumination side.

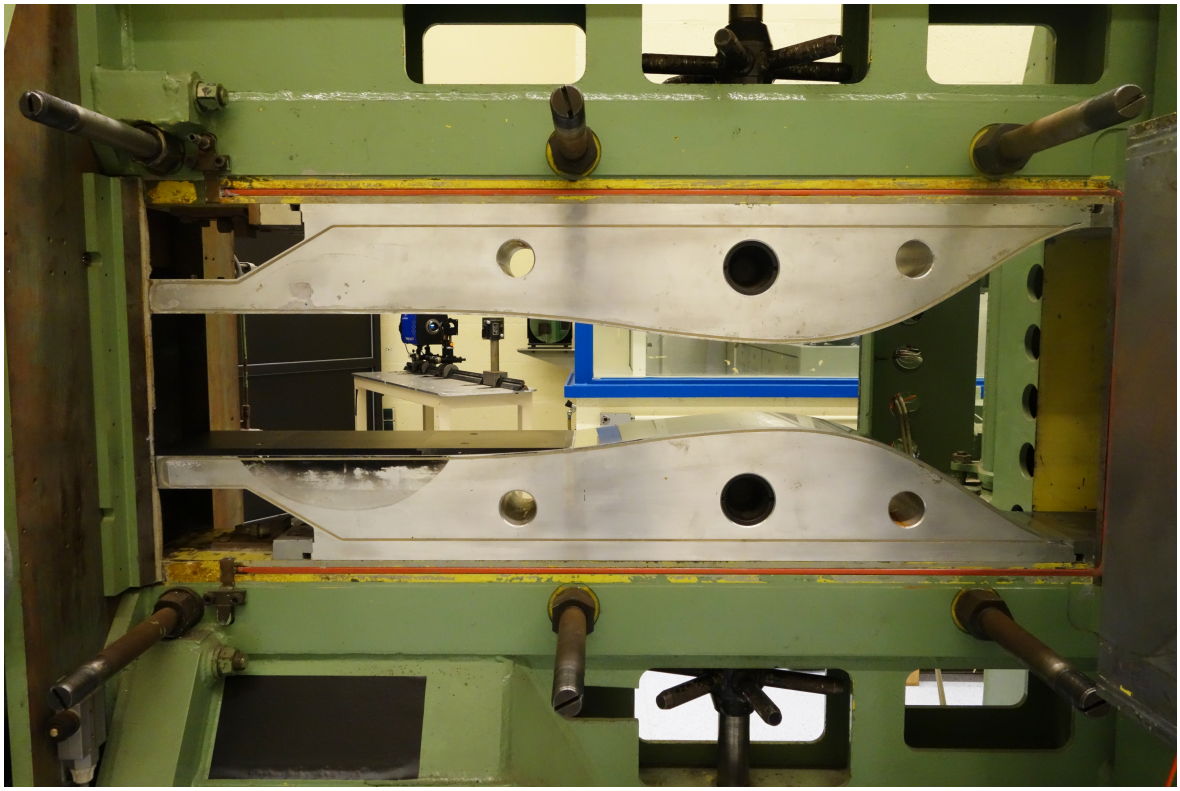

FIGURE J.3: Placement of the test plate and inserts, test section exposed.

J.2 PIV



FIGURE J.4: Complete overview of the ST-15 facility with PIV equipment.

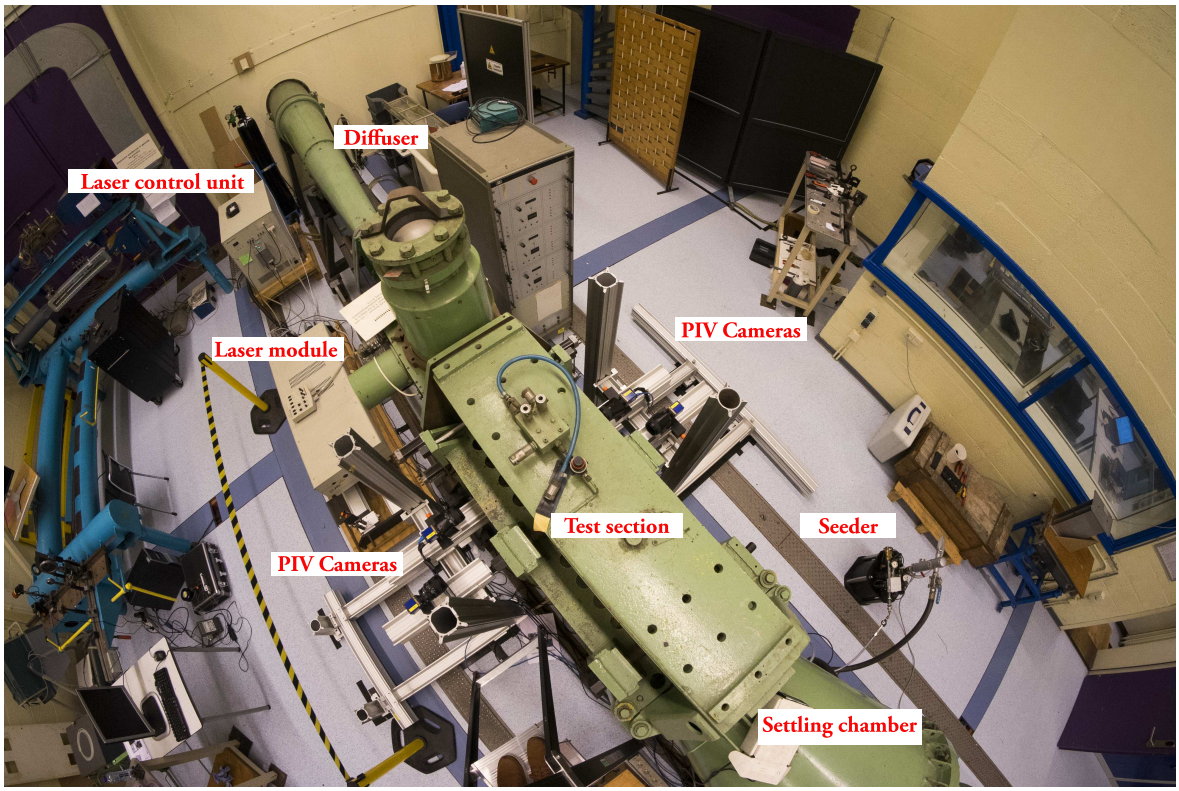

FIGURE J.5: Upper view of PIV setup at the ST-15.

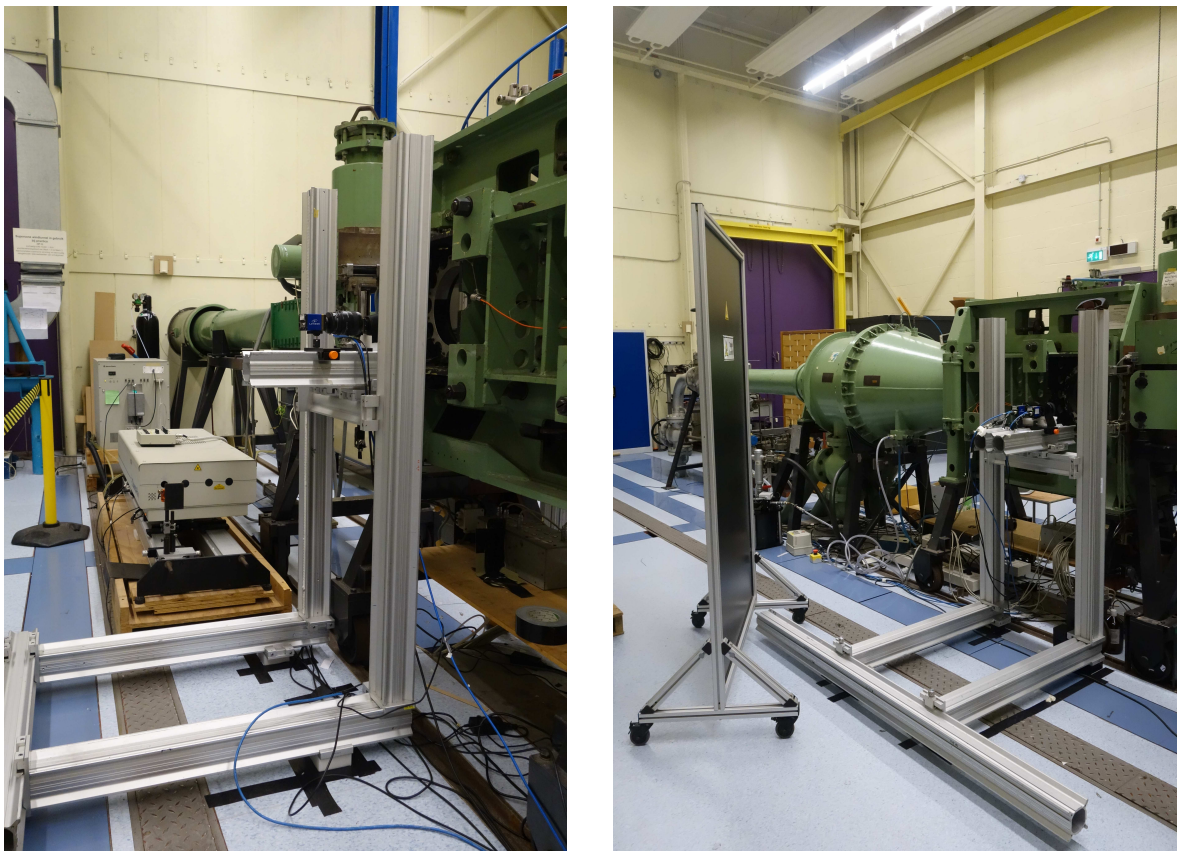

FIGURE J.6: PIV setup: illumination side (left) and imaging side (right).

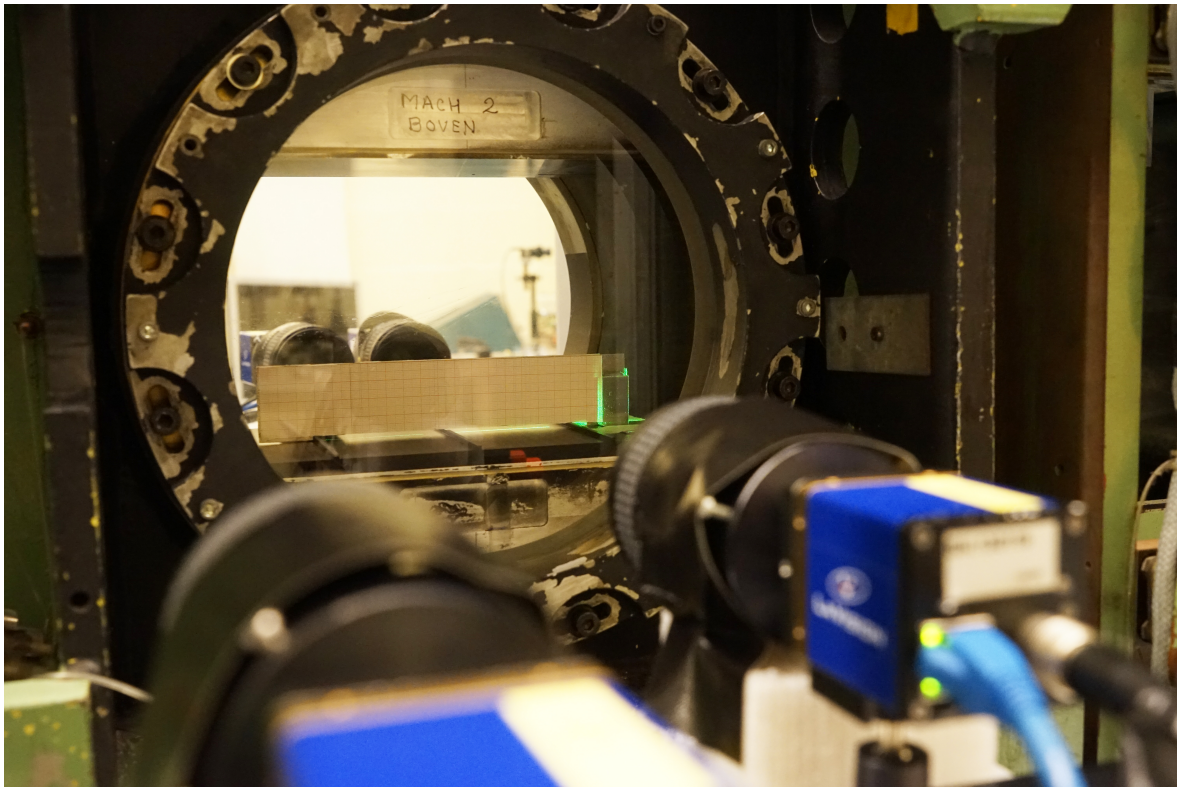

FIGURE J.7: Calibration plate used for image scaling, camera and laser alignment.

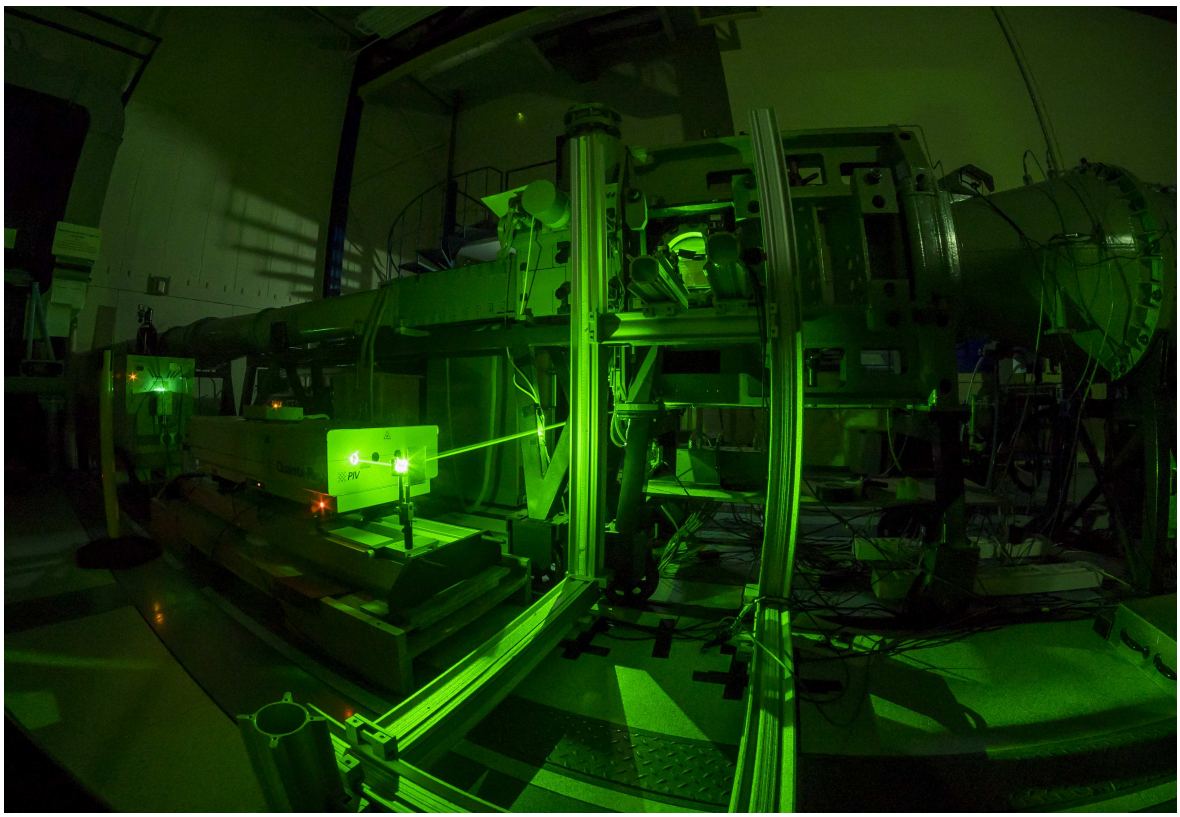

FIGURE J.8: Laser path: traveling from the laser exit to the probe into the test section.

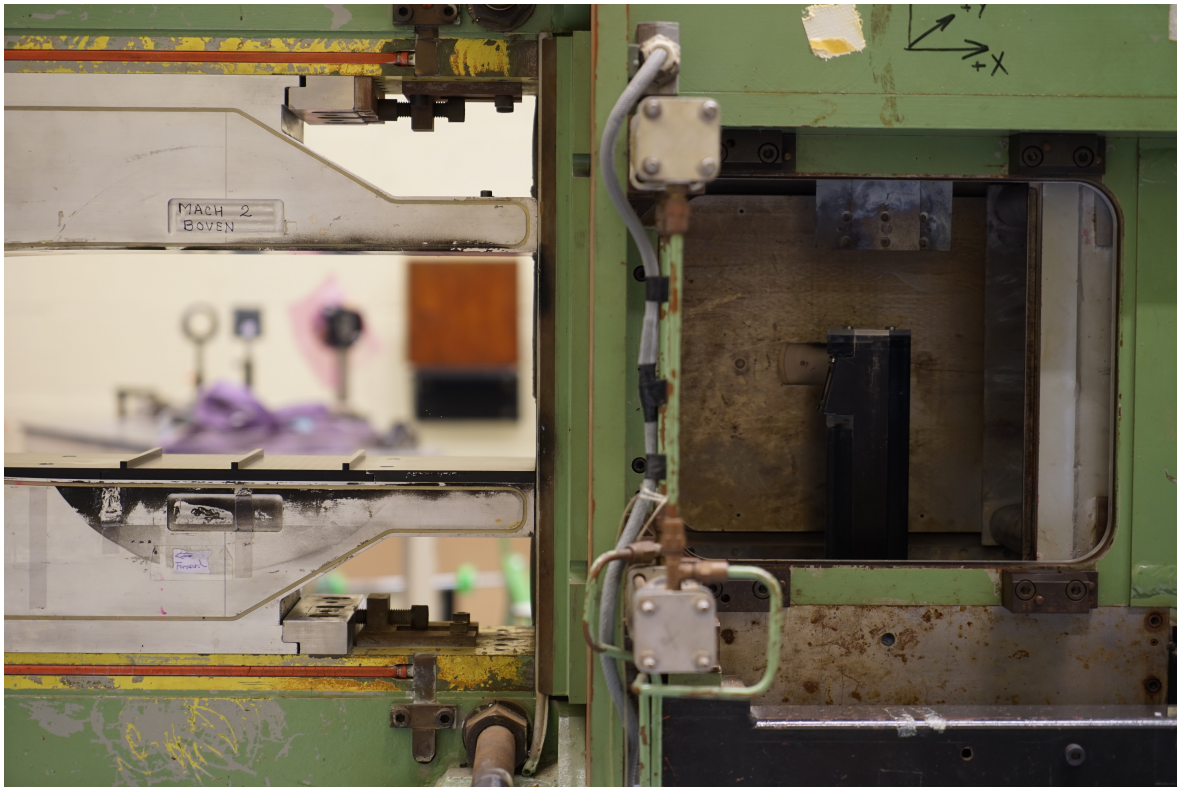

FIGURE J.9: Laser probe located downstream of the test section.

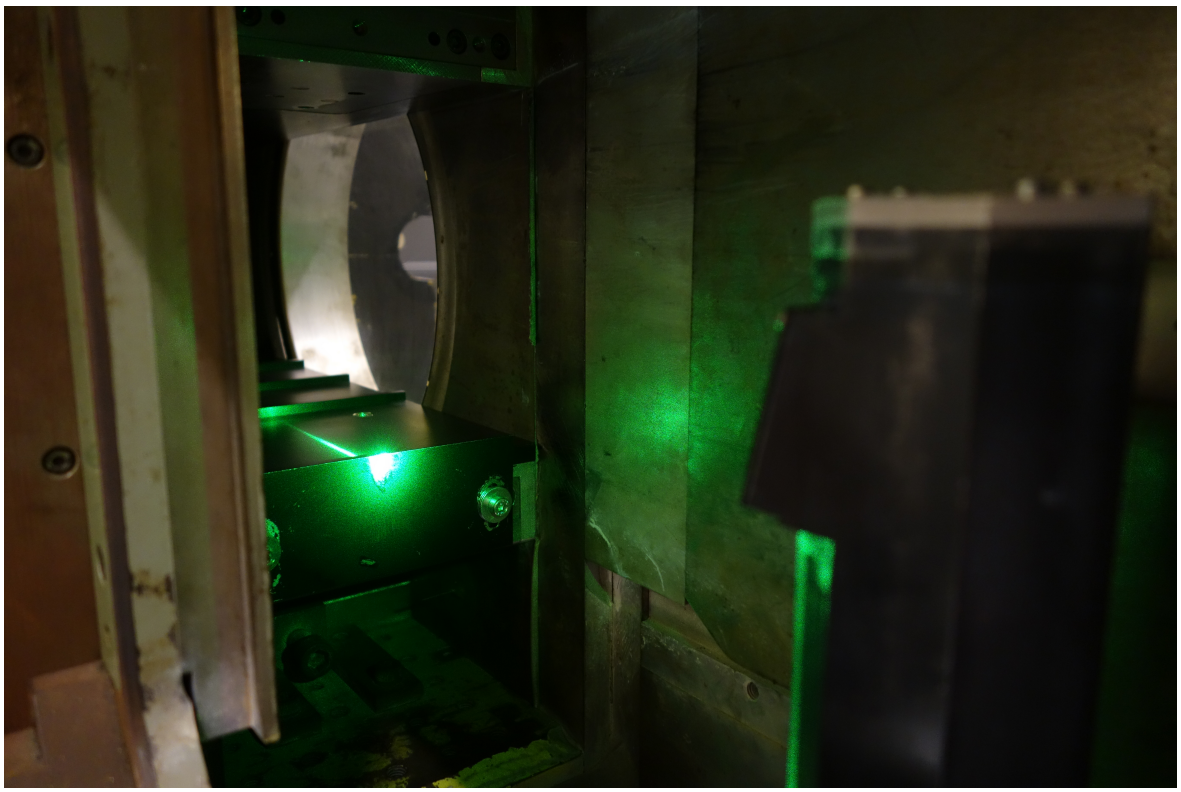

FIGURE J.10: Laser probe and cut-off knife, functionality display.

J.3 QIRT: assembly

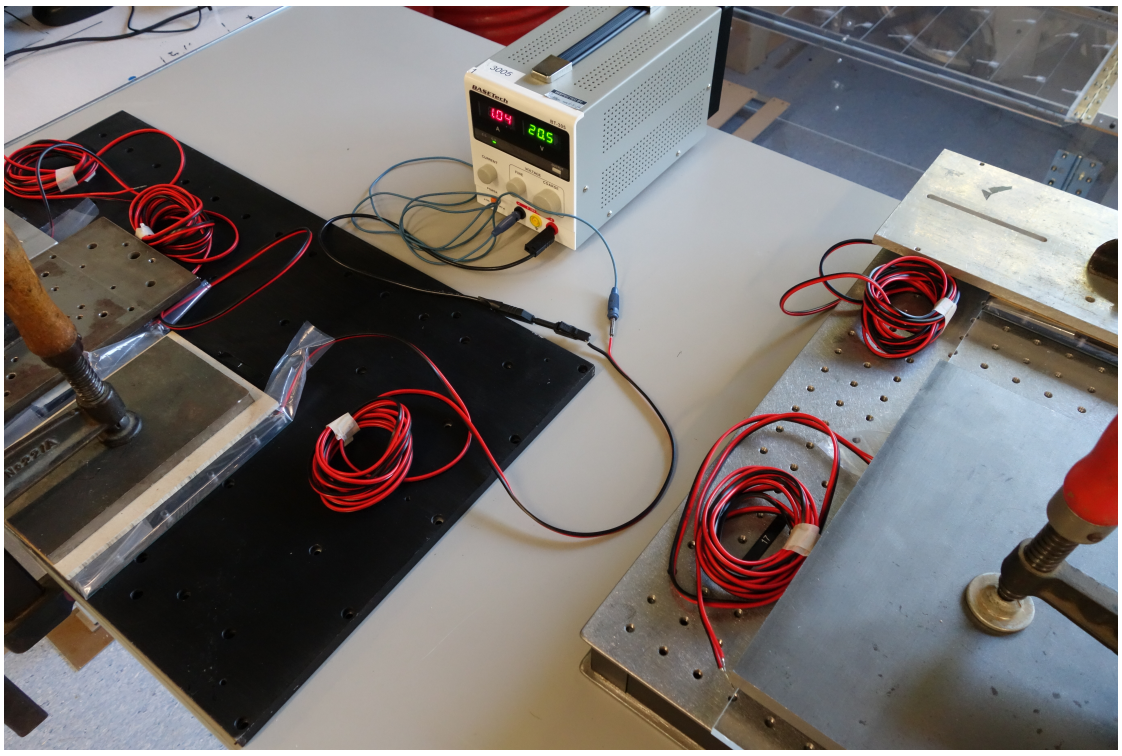

FIGURE J.11: Gluing station, incl. power supply and compression setups.

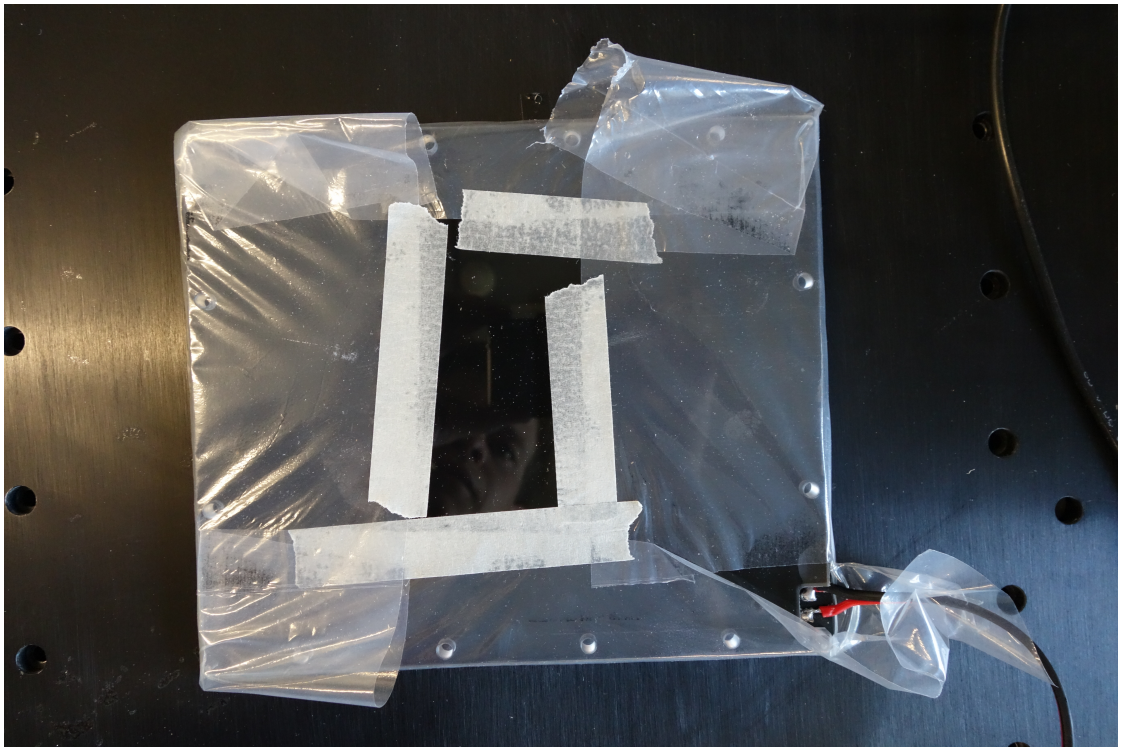

FIGURE J.12: Plastic wrapped test plate right after gluing.

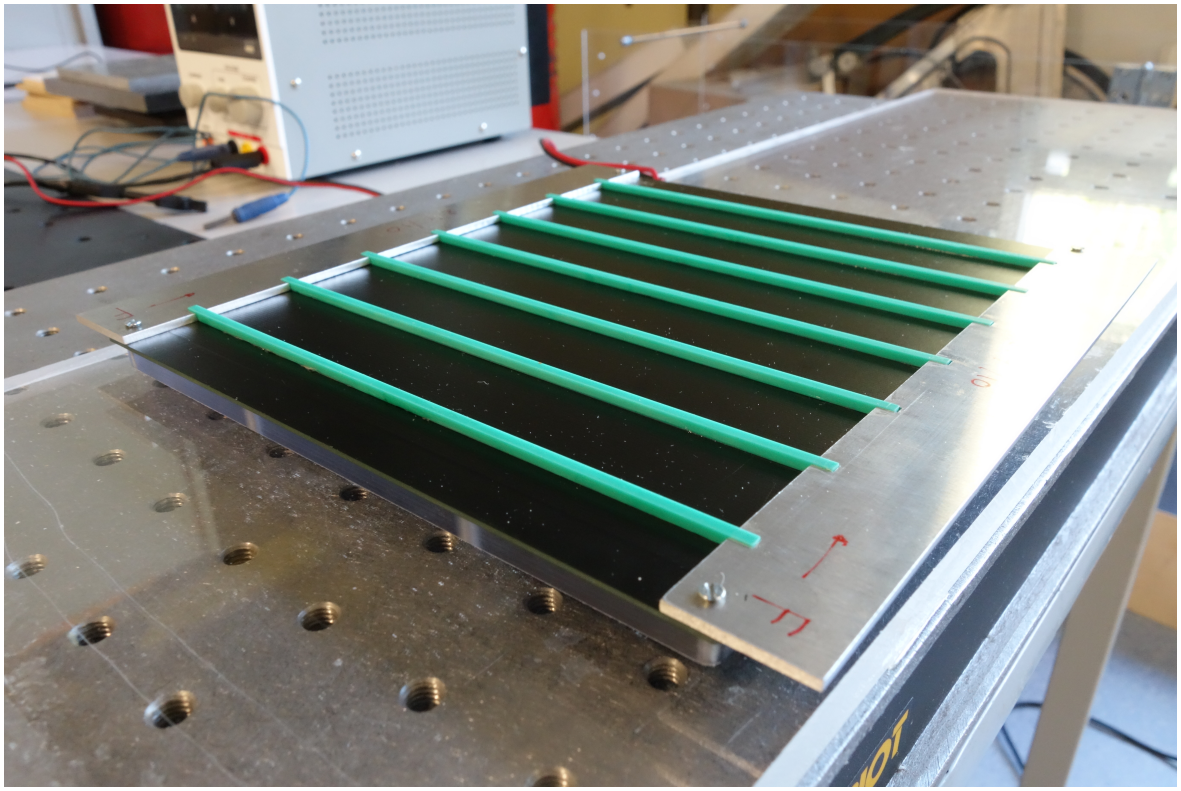

FIGURE J.13: Rib mounting, incl. mounting frame as placement aiding tool.

J.4 QIRT: testing

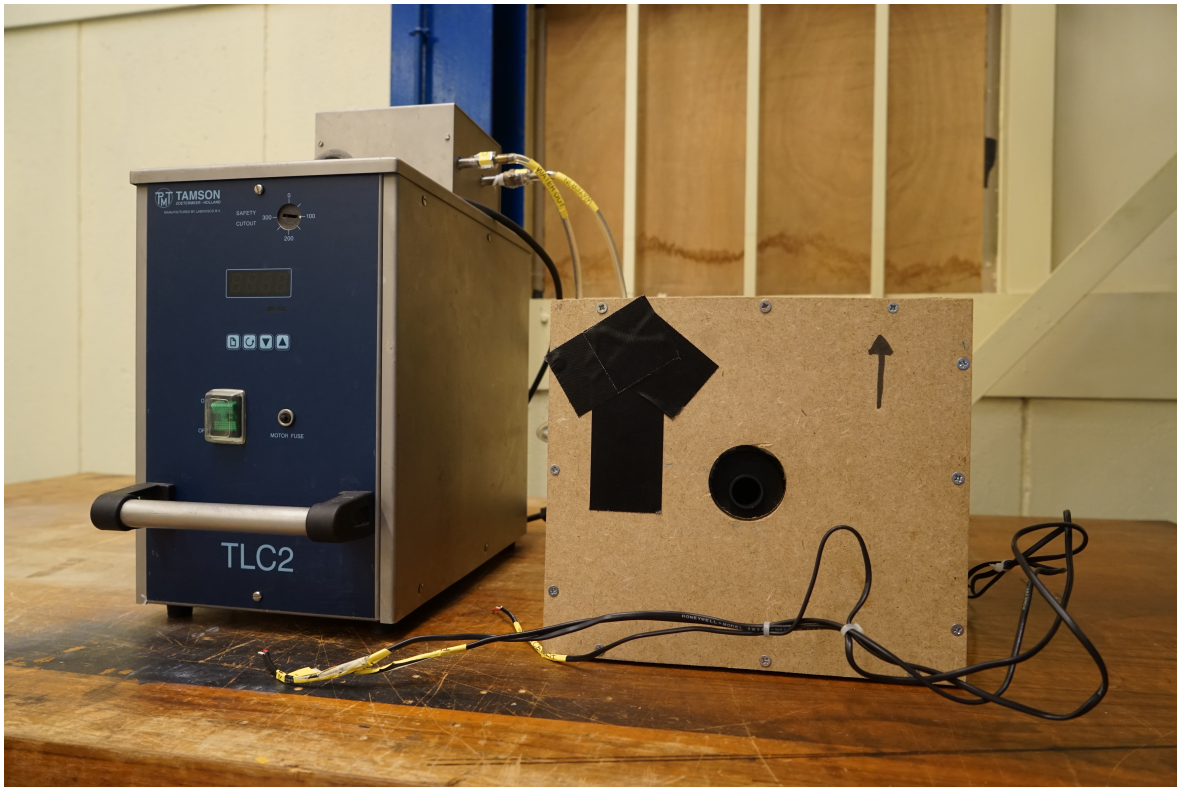

FIGURE J.14: Calibration equipment, incl. thermal bath (left) and blackbody (right).

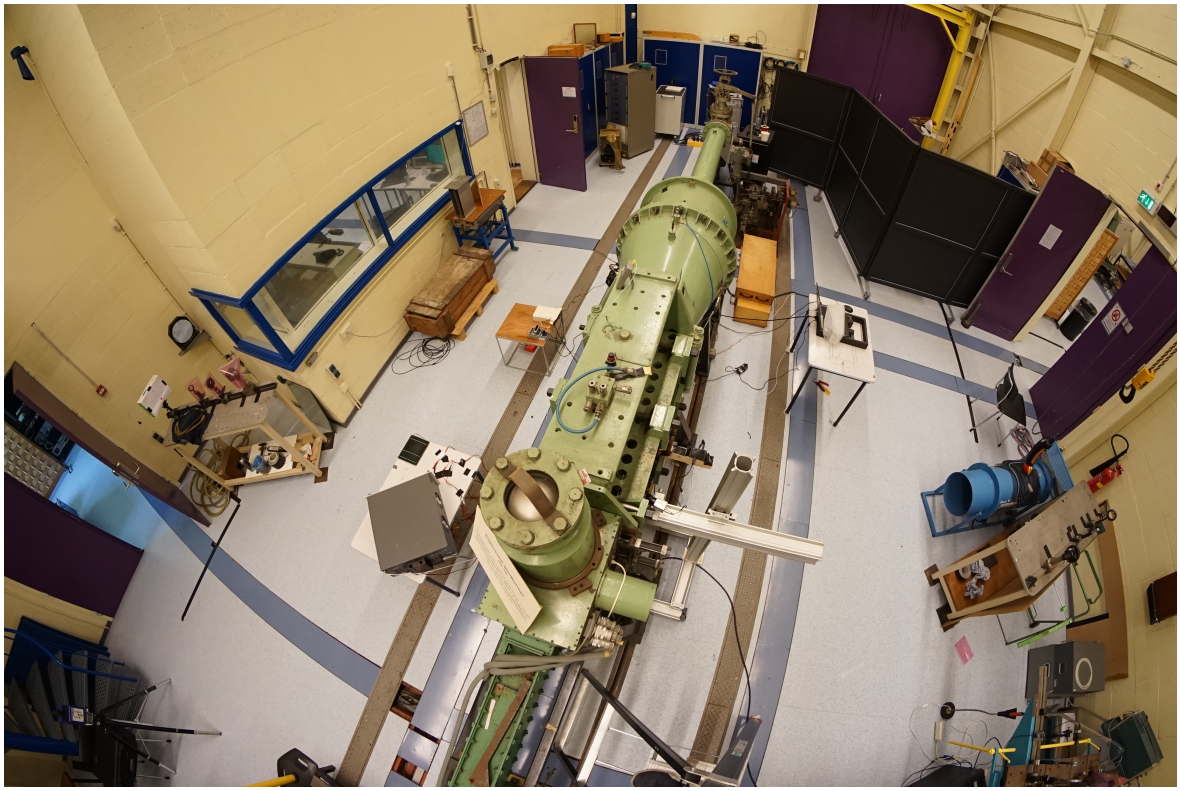

FIGURE J.15: QIRT setup, excl. black cloth and protective screens for clarity.

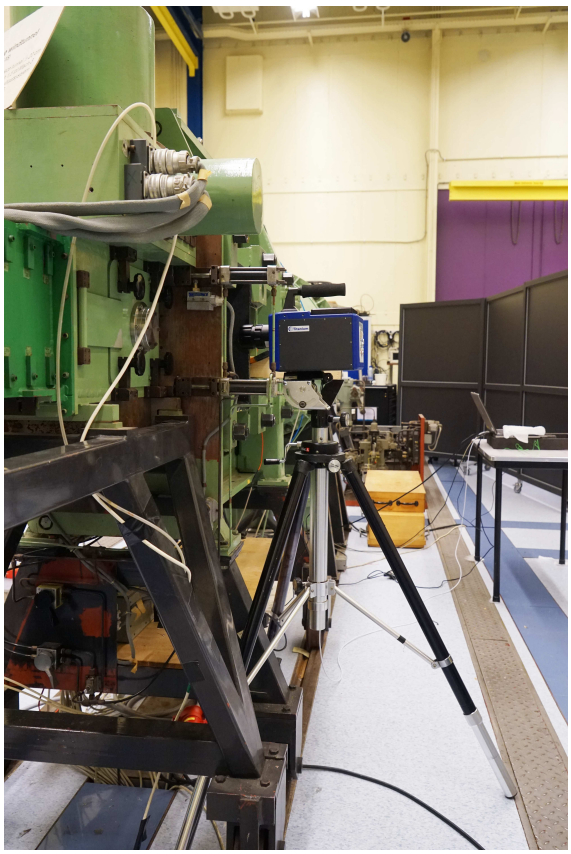

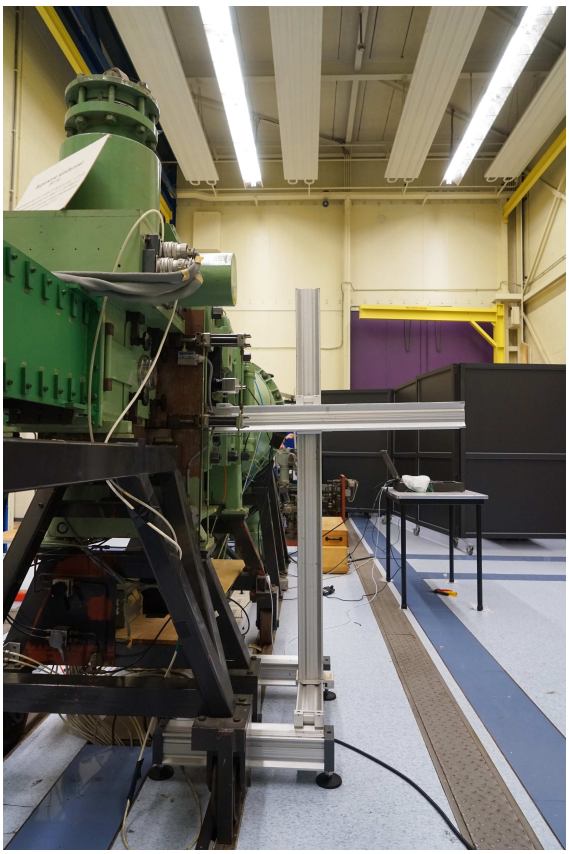

FIGURE J.16: QIRT setup: primary (left) and secondary campaign (right).

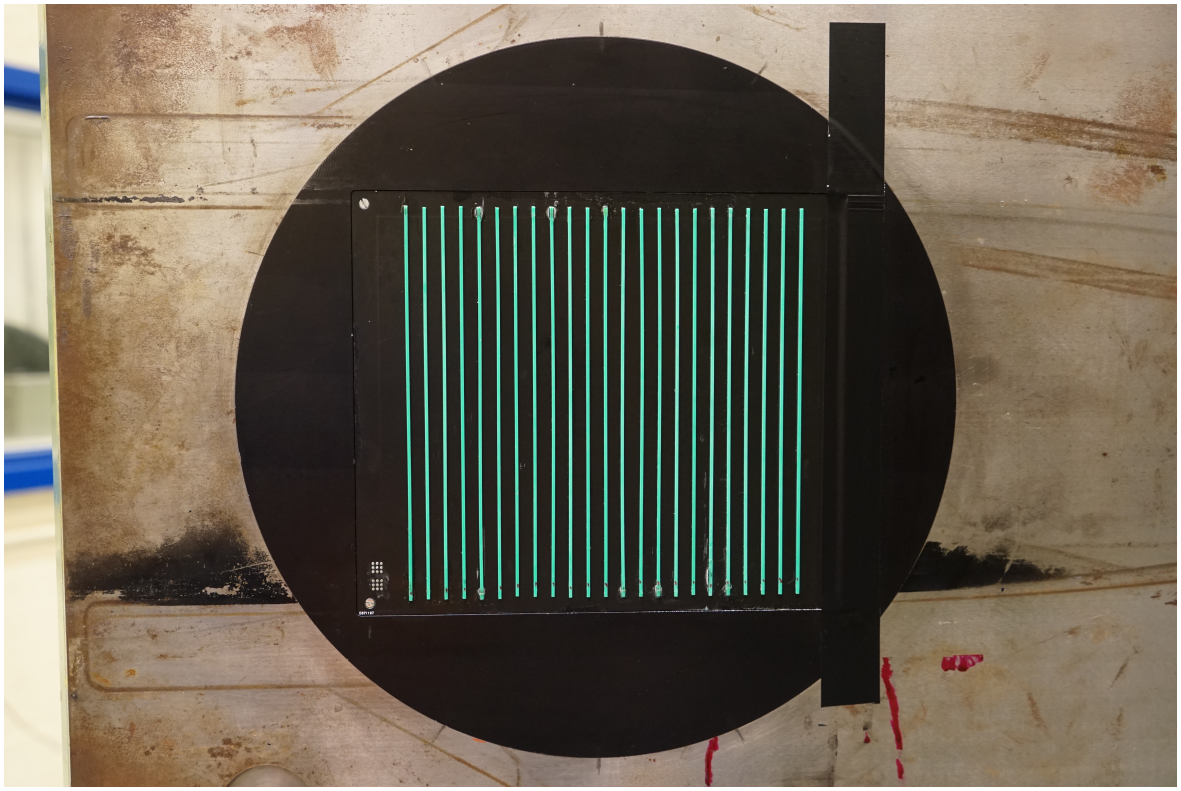

FIGURE J.17: QIRT test plate placement, incl. aerodynamic tape at the leading edge.

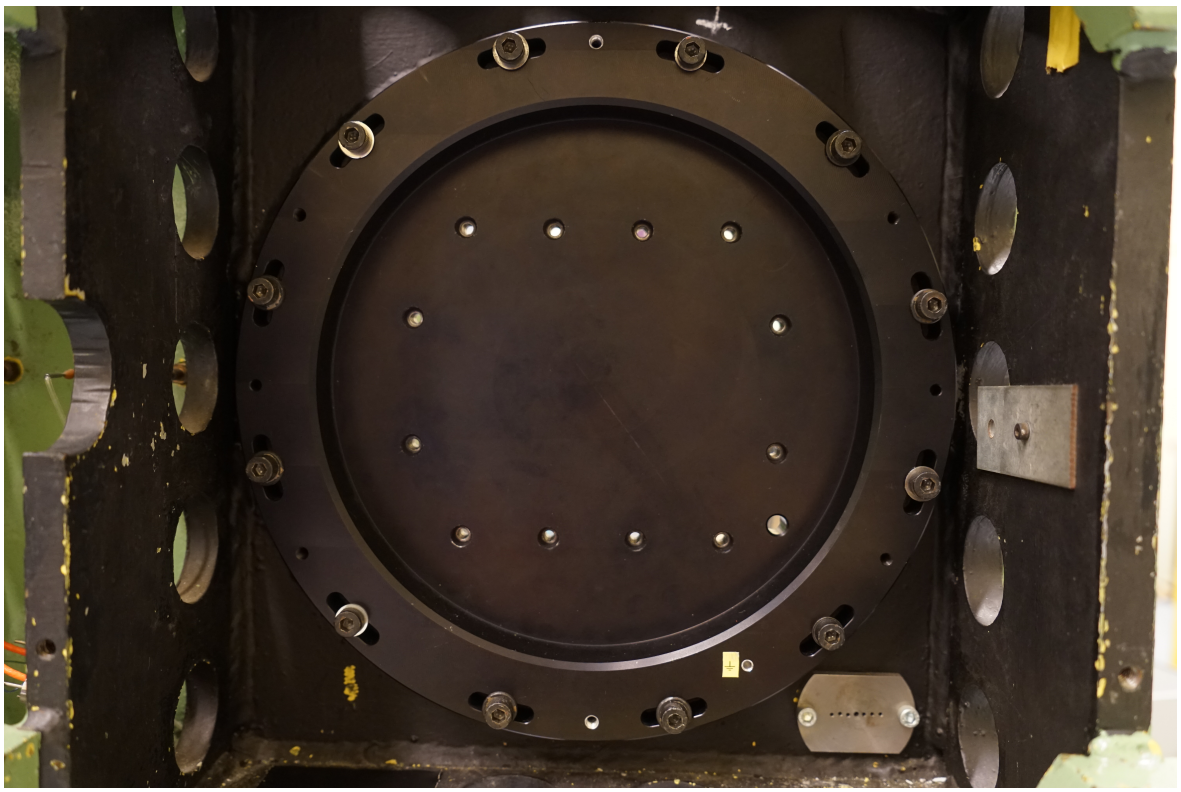

FIGURE J.18: QIRT cavity door, outside view.



FIGURE J.19: Primary QIRT camera cover used for NUC and BPR routines.



FIGURE J.20: Interlock switch and power supply connector.

Appendix K

Derivation one-dimensional heat transfer problem

The simplified heat transfer problem indicated in Section 4.1.1, requires us to solve the non-homogeneous, one-dimensional, transient heat transfer equation. The system of differential equation, boundary conditions and initial condition is given by:

$$\frac{\partial T}{\partial t} = \alpha \left(\frac{\partial^2 T}{\partial z^2} \right) \tag{K.1}$$

with boundary conditions (BCs),

$$(1)\ T(L,t) = T_{amb} \qquad (2)\ -k \left. \frac{\mathrm{d}T}{\mathrm{d}z} \right|_{z=0} = q_{el} - h\left(T(0,t) - T_{aw}\right)$$

and initial condition (IC),

$$T(z,0) = T_{amb}$$

Which can be solved as a closed system, resulting in an analytic solution. Unfortunately though, as the second boundary condition is not typical, this system is solved manually. The derivation is started by dividing the problem $T(z,t)$ into a transient $o(z,t)$ and a steady-state $T_e(z)$ solution:

$$T(z,t) = \overbrace{o(z,t)}^{1} + \overbrace{T_e(z)}^{2} \quad \text{and,} \tag{K.2}$$

$$o(z,t) = T(z,t) - T_e(z) \tag{K.3}$$

In turn, using the interrelations of these solutions, two new systems of equations with BCs and ICs are formed such that they can be solved separately.

(1) Transient, homogeneous problem: Since both $T(z,t)$ and $T_e(z)$ have the same boundary conditions, a transient system is defined for $o(z,t)$ having homogeneous boundary conditions:

$$\frac{\partial o}{\partial t} = \alpha \left(\frac{\partial^2 o}{\partial z^2} \right) \tag{K.4}$$

With boundary conditions (BCs),

$$(1)\ o(L,t) = 0 \qquad (2)\ -k \left. \frac{\mathrm{d}o}{\mathrm{d}z} \right|_{z=0} = 0$$

and initial condition (IC),

$$o(z,0) = f(z) = T_{amb} - T_e(z)$$

The solution to this system is found through the method of separation of variables (Haberman, 20012), where:

$$o(z,t) = \phi(z)\, G(t) \tag{K.5}$$

is used as the assumed solution in product form.[61] In turn, this separated representation of the solution is substituted into the differential equation (K.4):

$$\underbrace{\frac{1}{\alpha G}\frac{\mathrm{d}G}{\mathrm{d}t}}_{\text{function of } t} = \underbrace{\frac{1}{\phi}\frac{\mathrm{d}^2\phi}{\mathrm{d}z^2}}_{\text{function of z}} \tag{K.6}$$

Providing a fully separated solution, in the sense that the left-hand is solely a function of t, whereas the right-hand side only a function of z. From the method of separation of variables, Equation K.6 only holds if both z and t are arbitrary, independent variables which then by definition are equal to the same constant:

$$\frac{1}{\alpha G}\frac{\mathrm{d}G}{\mathrm{d}t} = \frac{1}{\phi}\frac{\mathrm{d}^2\phi}{\mathrm{d}z^2} = -\lambda \tag{K.7}$$

Where λ is the *separation constant*, equal to an arbitrary number. From Equation K.7, two individual differential problems arise, corresponding to respectively a time-dependent ordinary differential equation (ODE) and a homogeneous, eigenvalue problem:

$$\frac{\mathrm{d}G}{\mathrm{d}t} = -\lambda\alpha G \tag{K.8}$$

$$\frac{\mathrm{d}^2\phi}{\mathrm{d}z^2} = -\lambda\phi \tag{K.9}$$

As the first problem is an ODE (Equation K.8), its general solution is directly given by using the characteristic polynomial solution:

$$G(t) = c_1 e^{\lambda\alpha t} \tag{K.10}$$

The second problem corresponds to an eigenvalue problem (Equation K.9), whose solution is required to be found for $\lambda < 0$, $\lambda = 0$ and $\lambda > 0$. From Haberman (2012), it is known that for $\lambda = 0$, only the trivial solution (i.e. ϕ = 0) is found. In addition, for $\lambda < 0$, the solution becomes non-physical.[61] As a result, only physical, non-trivial solutions are found for $\lambda > 0$:

$$\phi = c_2 \cos(\sqrt{\lambda}z) + c_3 \sin(\sqrt{\lambda}z) \tag{K.11}$$

Given the homogeneous BCs, $\phi(0) = 0$ and $\mathrm{d}\phi/\mathrm{d}z$ (0) = 0, the resulting non-trivial solution for ϕ and λ are given by:

$$\begin{aligned} &\phi = c_2 \cos(\sqrt{\lambda}z) \quad \text{where,} \\ &\lambda = \left(\frac{n\pi}{2L}\right)^2 \quad \text{,n} = 1, 3, 5, ... \end{aligned} \tag{K.12}$$

At this stage, solutions are found for both $\phi(z)$ and $G(t)$. Thus, by combining respectively Equations K.10 and K.12, $o(z,t)$ is equal to:

$$o(z,t) = A \cos\left(\frac{n\pi z}{2L}\right) e^{-(\frac{n\pi z}{2L})^2 \alpha t} \tag{K.13}$$

Where the constant A, is equal to the multiple of $c_1 \cdot c_2$. However, an explicit expression for A is still to be resolved. This is done through the implementation of the IC on Equation K.13:

$$T(z,0) = f(z) = \sum_{m=1}^{\infty} A_m \cos\left(\frac{m\pi z}{2L}\right) \quad \text{, m = 1, 3, 5,...} \tag{K.14}$$

Which is solved by multiplying both sides with $\cos\left(\frac{m\pi z}{2L}\right)$, and integrating its result from 0 $\rightarrow L$. The resulting expression is given by:

$$\int_0^L f(z)\cos\left(\frac{m\pi z}{2L}\right) dz = A_m \int_0^L \cos^2\left(\frac{m\pi z}{2L}\right) \tag{K.15}$$

Which is equal to:

$$\int_0^L f(z)\cos\left(\frac{m\pi z}{2L}\right) dz = \frac{L}{2} \quad \text{with, } n = m \neq 0 \tag{K.16}$$

Giving the final expression for A_m as:

$$A_m = A_n = \frac{2}{L}\int_0^L f(z)\cos\left(\frac{n\pi z}{2L}\right) dz \quad \text{for, n = 1, 3, 5,...} \tag{K.17}$$

Where for the current physical problem, $f(z) = T_{amb} - T_e(z)$. Finally, the complete solution for $o(z,t)$ is found by combining the complete expressions for ϕ and G. The resulting solution is given by:

$$o(z,t) = \sum_{n=1}^{\infty} A_n \cos\left(\frac{n\pi z}{2L}\right) e^{-(\frac{n\pi z}{2L})^2 \alpha t} \quad n = 1, 3, 5,...$$

Where, (K.18)

$$A_n = \frac{2}{L}\int_0^L f(z)\cos\left(\frac{n\pi z}{2L}\right) dz \qquad \text{with, } f(z) = T_{amb} - T_e(z)$$

Which represents the entire transient solution of $T(z,t)$. The remaining steady-state solution for $T_e(z)$ is given by the following section.

(2) Spatially dependent, non-homogeneous problem: In turn, $T_e(z)$ represents the steady-state solution of the heat equation which is reduced to the spatially dependent, 1D heat transfer problem:

$$\frac{\partial^2 T}{\partial z^2} = 0 \tag{K.19}$$

With boundary conditions (BCs),

$$(1)\ T_e(L,t) = T_{amb} \qquad (2)\ -k\left.\frac{\mathrm{d}T_e}{\mathrm{d}z}\right|_{z=0} = q_{el} - h\left(T(0,t) - T_{aw}\right)$$

and initial condition (IC),

$$T_e(z,0) = T_{amb}$$

The solution is relatively simple to find, as no separation of variables is required. Instead, Equation K.19 is integrated twice:

$$T_e(z) = c_1 z + c_2 \tag{K.20}$$

Applying the two BCs, it is found that:

$$c_1 = \frac{q_{el} - h}{k}\left(T(0,t) - T_{aw}\right) \tag{K.21}$$

$$c_2 = T_{amb} - \frac{L}{k}\big(q_{el} - h(T(0,t) - T_{aw})\big) \tag{K.22}$$

Resulting in a complete, steady-state solution equal to:

$$T_e = \frac{L - z}{k}\big(q_{el} - h(T(0,t) - T_{aw})\big) + T_{amb} \tag{K.23}$$

Finally, considering that T_e equals the steady-state solution with $t \geq t_{ss}$, $T(0,t) \rightarrow const$, Equation K.23 can be simplified to:

$$T_e = \frac{L - z}{k}(q_{el} - h\Delta T) + T_{amb} \tag{K.24}$$

Where ΔT is a design variable equal to the temperature contrast required for sufficient heat transfer computation.

(3) Complete solution Previously, it was stated from the method of separation of variables that the complete solution for $T(z,t)$ is given by:

$$T(z,t) = o(z,t) + T_e(z)$$

At this stage, both transient and steady-state component of the solution are known. As a result, the complete solution can be listed as:

$$o(z,t) = \sum_{n=1}^{\infty} A_n \cos\left(\frac{n\pi z}{2L}\right) e^{-(\frac{n\pi z}{2L})^2 \alpha t} \quad n = 1, 3, 5, ...$$

Where,

$$A_n = \frac{2}{L}\int_0^L f(z)\cos\left(\frac{n\pi z}{2L}\right) dz \qquad \text{with, } f(z) = T_{amb} - T_e(z)$$

and,

$$T_e = \frac{L - z}{k}(q_{el} - h\Delta T) + T_{amb}$$

Each of these expressions is placed into a MatLab script, for which the continuous integration is replaced by numerical integration. In addition, the summation from $n \rightarrow \infty$ is manually varied by an approximate for the upper domain of n. Fortunately, due to the nature of the equations, the solution converges relatively fast such that $1 \leq n \leq 11$ is sufficient.

Appendix L

Working principle of thermocouples

The QIRT experimental setup was designed such that the complete PCB surface area was mapped by the IR cameras, whilst the rear and sides of the insulation were monitored by thermocouples at strategic locations. A thermocouple is a wire which consists of two dissimilar electrical conductors. By the differences in thermoelectric effect of these conductive materials, a temperature-dependent voltage is generated. In turn, by measuring the voltages across these metals, the local temperatures can be interpreted.

Based on the expected temperature range of operation, specific thermocouple types can be chosen. For the current thesis, the K-type was chosen as this is the most reliable, accurate and most widely applied thermocouple for various (experimental) applications. This thermocouple type is of the kind Nickel-Chromium/Nickel-Aluminum (NiCr – NiAl), having a usable temperature range of -270 – 1260°C. As this thermocouple is highly common, a multitude of reference voltage-to-temperature conversion tables are available. Within these tables, the read-out of thermoelectric voltage in mV is related to °C. (Kendall, 1967)[79]

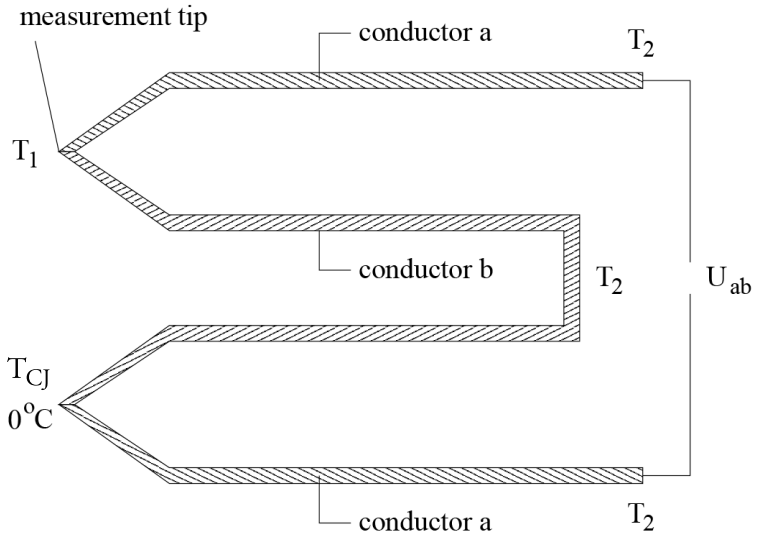

FIGURE L.1: Thermocouple read-out for ice bath or cold junction.[76] (Schrijer et al., 2003)

These reference tables are defined by connecting two K-type thermocouples in series, where one welded tip of the thermocouple is exposed to a known measurement temperature (T_1) and another to a reference temperature (T_{CJ} or 0°C, Figure L.1). The latter reference temperature is commonly referred to as a *cold junction*, and can be generated by respectively an ice bath (i.e. 0 mV @ 0°C) or a digital *cold-junction compensation* sensor or CJC (i.e. X mV

@ X°C). In experimental practice, this second thermocouple is also added to properly determine the exact measured temperature. In more primitive experimental setups, the voltages of thermocouples would be read-out by actually emerging one thermocouple tip in such an ice bath. For the current setup, however, a more modern connector module was utilized being equipped with a CJC. Within the NI 9214 and TB 9214 thermocouple acquisition modules, three of such CJCs are present and determine the temperature gradient across all 16 thermocouple channels. By knowing the local temperatures, there is compensated for the voltage outputs by the non-zero reference junction through:

$$U_{out} = S_{ab}[T_1 - T_2] - S_{ab}[T_{CJ} - T_2] = S_{ab}[T_1 - T_{CJ}] \tag{L.1}$$

Where S is the material-specific Seebeck coefficient, which defines the thermoelectric characteristic of the conductor. Equally to the compensated mV for T_{CJ}, the determination of the S_{ab} is a built-in feature of the acquisition modules and the accompanying LabView software. As one can see by Equation L.1, the effect of the connector temperature, T_2 has become completely obsolete; displaying the working principle of this setup.

The new, more modern setup (Figure L.1) brings about several logistical and experimental accuracy benefits. By not requiring an ice bath, the actual operation of the thermocouple system is a lot less cumbersome and operational for a prolonged period of time. In addition, by accurately monitoring the actual junction temperatures and compensating for the non-zero references, the accuracy and reliability of the read-outs are significantly improved. In turn, the manufacturers error margins can be copied for the uncertainty estimates such that a credible data analysis could be performed. Finally, by reduced logistical requirements, the repeatability of this study is improved as well.

Appendix M

QIRT experimental checklist

The multitude of QIRT experiments has led to quite a substantial level of knowledge regarding the correct operation of the constructed system. In order to properly and consistently utilize this QIRT system, a specific set of repetitive steps are to be conducted prior and after running the wind tunnel. These steps have been incorporated into a final checklist, which is displayed distinctly in respectively Tables M.1 and M.2. The first table corresponds to all steps conducted prior to a wind tunnel run:

TABLE M.1: Operational checklist QIRT, prior to wind tunnel run.

Run #	Altair set	Empty tunnel IR	NI set	Empty tunnel TK	CJ pre	Ptnk pre	Power set	Amb T pre	Cam T pre

From which it is seen that a multitude of abbreviations are used. The first, *Altair set*, indicates whether the IR camera settings have been implemented correctly into the Altair software. For this step, one can think of recording duration, number of frames and integration time. Once this is assured, an empty tunnel measurement is conducted. In turn, *NI set*, corresponds to confirming whether the LabView thermocouple acquisition program and NI box are set properly. In this case, settings such as acquisition duration, triggering and accuracy mode of acquisition are checked. Then, prior to conducting the wind tunnel measurement, pre-measurements are done for the reference thermocouples and cold junction of the acquisition box. Then, the starting reservoir pressure, power set point, ambient and camera temperatures are noted as well. With all of these nine steps confirmed, the wind tunnel test can actually take place:

TABLE M.2: Operational checklist QIRT, after to wind tunnel run.

Run #	Test	Ambient post T	Camera T post	CJ post	Ptnk post

After this test (Table M.2), the ambient and camera temperatures are noted once more. Finally, the cold junction temperatures are monitored as well, followed by a registration of the reservoir pressure. Each of these measurements is performed as it contributes to the overall accuracy and predictability of the results derived through the data reduction. In the case the latter did not go too smoothly, possible malfunctions or environmental effects could be localized by identifying variations in the ambient conditions.

Appendix N

PCB resistance variance

By discrepancies in the production process of the PCB, local variations in copper thickness have resulted in significant base resistances between the specific specimens. Table N.1 displays the PCB-specific values of R_0, where labels indicated in **bold** are the ones used for the main test models.

TABLE N.1: List of PCB-specific base resistances, R_0 at T_{ref} = 22.1°C.

Label (#)	Resistance (Ω)	Label (#)	Resistance (Ω)
1	27	**12**	21.2
2	26.7	**13**	22.3
3	25	14	18
4	23.1	15	19.3
5	21.3	**16**	24.6
6	22	**17**	24.9
7	21.2	18	19
8	22.7	**19**	23.2
9	20.7	**20**	21.4
10	21.6	21	25
11	22.6	**22**	23.3

The data and selection criteria for Table N.1 are visualized by the following figure:

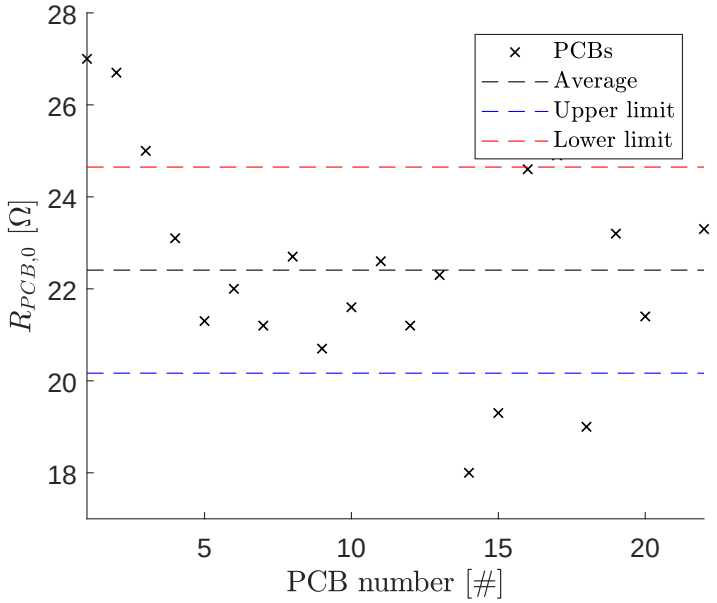

FIGURE N.1: Base resistivity of all PCBs.

Where the markings between the limits correspond to the selected PCBs, previously indicated in bold. The final selection of PCBs is provided in the following figure, displaying only those specimens which lie within the limits.

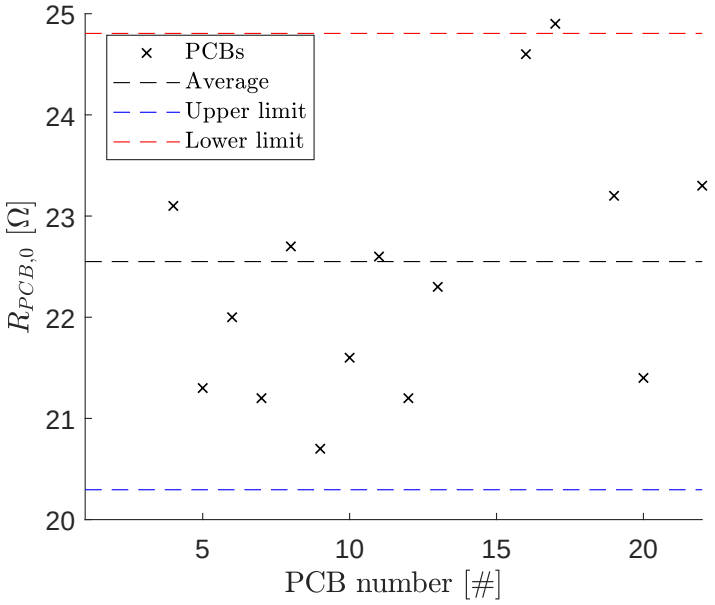

FIGURE N.2: Base resistivity of selected PCBs.

Appendix O

Oblique shock wave interference

The setup designed for the placement of the test models for both PIV and Schlieren techniques required a leading (LE) and trailing edge (TE) insert to clamp the interchangeable roughness geometries. The positioning of these models, however, formed a disruption to the otherwise continuous nozzle block geometry. Normally, the air exiting the settling chamber can be assumed to expand (near-)isentropically into the test section; resulting in a freestream Mach number, M_2 of 2.0 [-] (Figure O.2). By the introduction of the leading edge insert, however, this expanding flow is turned into itself which causes an oblique shock wave (OSW) to form prior to entering the test section (Figures O.1). As a result, the effective M_2 is reduced. The new estimate of which, is provided in this section.

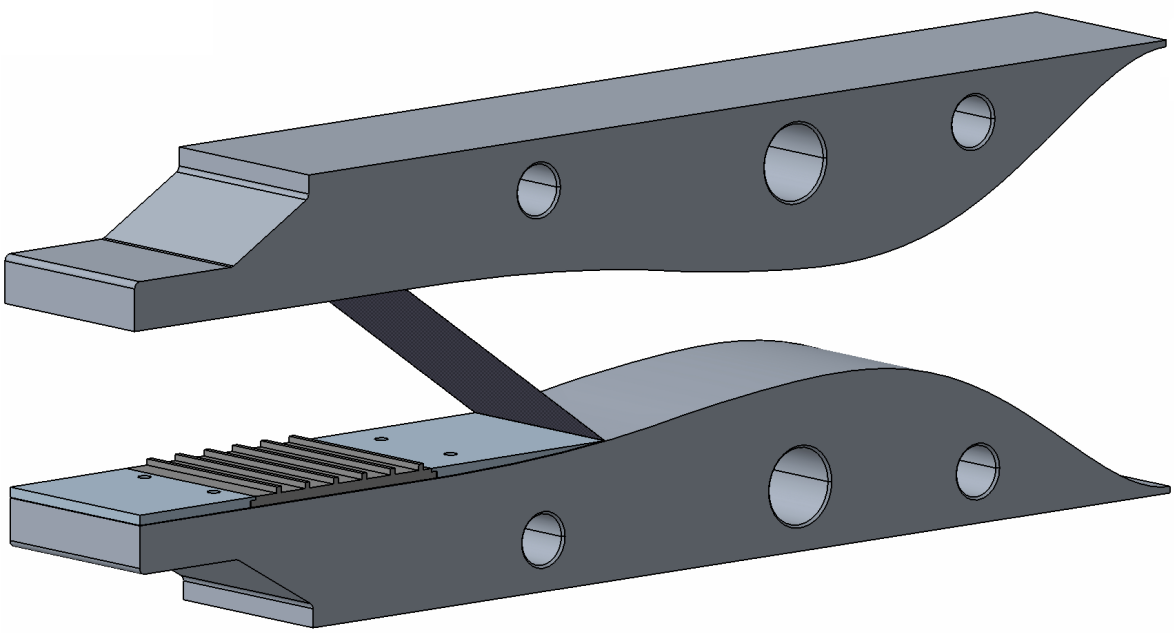

FIGURE O.1: Placement test models, including OSW at nozzle discontinuation.

In Figure O.2, a schematic drawing of the current flow situation is provided. From this schematic, it can be seen that the shock-wave angle, β is defined as the angle between the surface of the LE insert and the OSW. In turn, the deflection angle, θ is equal to the geometrical angle of the most upstream edge of the LE insert, respective to the tangent of the local nozzle block curvature. It is estimated through Schlieren images that β is equal to 35.1°, whereas θ was measured to be approximately $10.5 \pm 0.5°$ both physically and by CAD drawings. By using the normal shock wave (NSW) relations, where the Mach number was adjusted for shock- and deflection angles through:[87] (Anderson, 2010)

$$M_{n,1} = M_1 \sin(\beta) \tag{O.1}$$

$$M_{n,2} = \frac{1 + [(\gamma - 1)/2] M_{n,1}^2}{\gamma M_{n,1}^2 - (\gamma - 1)/2} \tag{O.2}$$

$$M_2 = M_{n,2} / \sin(\beta - \theta) \tag{O.3}$$

It was estimated that the freestream Mach number in the test section, M_2 is approximately equal to 1.78 $\pm$ 0.03 [-].

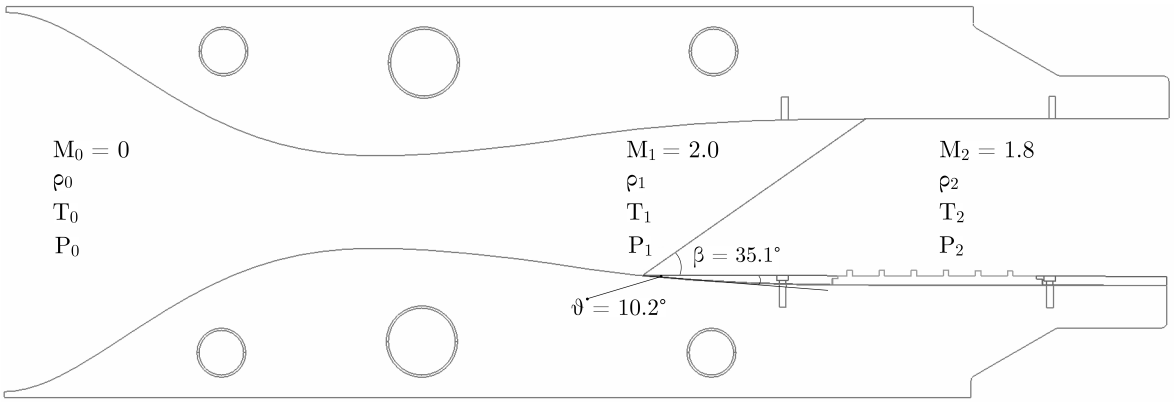

FIGURE O.2: Schematic of OSW shock wave interference and corresponding flow parameters.

This geometrical estimate is complemented by estimates made directly through the combined usage of the isentropic and NSW relations for the settling chamber properties, T_0 = 295 K , $P_0 = 3.2 \times 10^5$ Pa, $\rho_0 = 3.8$ kg/m^3, and the freestream velocity, $u_2 = 515$ m/s estimated through PIV. The physical representation of the current setup is shown in the Figure O.3. Apart from the 10% discrepancy in M_2 between QIRT and PIV, no others are found. As such, it can safely be assumed that this difference in freestream conditions is not detrimental to formulate reliable comparisons between data derived from the QIRT and PIV. Therefore, it is concluded that the current experimental strategy remains valid.



FIGURE O.3: Physical placement of the test models.

Appendix P

Blackbody inhomogeneity

The calibration uncertainty is dominated by the inhomogeneity of the overall blackbody temperatures. This variance in blackbody temperature is determined by computing the difference between the in- and outflow of the water temperatures. The following figure displays how this temperature difference, ΔT develops with respect to the temperature settings of the thermal bath:

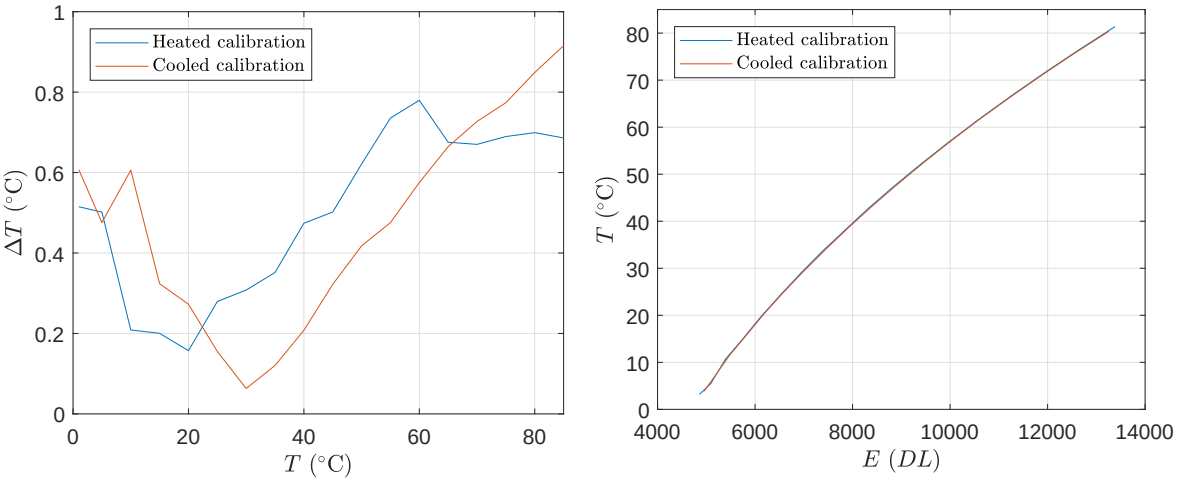

(A) Temperature difference of blackbody.

(B) Comparison of calibrations.

FIGURE P.1: combined characteristics of the blackbody and calibration procedure.

From Figure P.1a, it becomes clear that the lowest and highest portions of the temperature range generate the largest temperature defects at respectively 0.6 and 0.8 °C. Importantly though, it is also observed that either calibrations display largely equivalent ΔT-profiles. This means that – regardless of an incremental heating or cooling procedure – roughly the same discrepancies emerge. The latter feature is enforced by the two calibrations curves, displayed in Figure P.1b.

Appendix Q

Reference flat plate

The flat plate models have been investigated for both PIV and IRT to form a comparison between the roughness induced, and regular boundary layers. It is decided to highlight the mean St-profile of the reference flat plate, as this was used to validate the measured levels of St with the approximate Dittus-Boelter solution for a flat plate model at constant heat flux, under turbulent conditions.

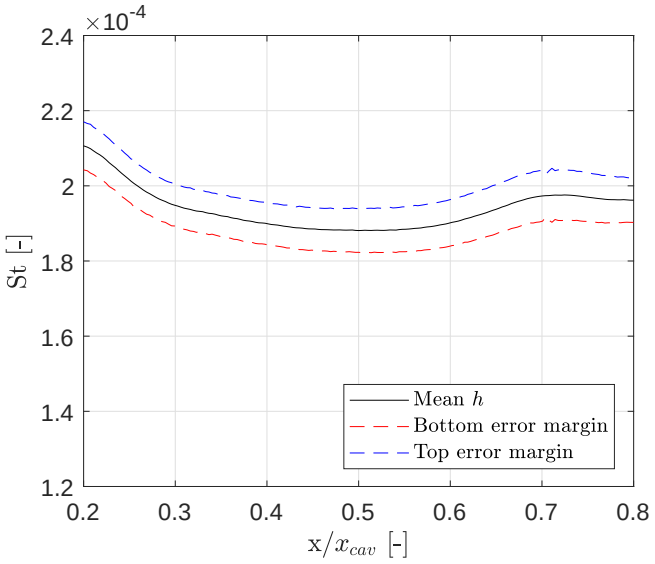

FIGURE Q.1: Flat plate heat transfer profile, incl. error margins.

The data in Figure Q.1 displays a relatively invariant heat transfer profile, which merely slightly declines moving downstream. The latter corresponds nicely to the foreseen, undisturbed boundary layer development observed by the previously taken spark-Schlieren images (Figure Q.2). The small increment in St at x/x_{maz} = 0.6 – 0.7 likely corresponds to flow separation, induced by minor imperfections to the curvature of PCB surface. The latter effect was more easily avoided by the ribbed elements, as the application of a level was more effective on the rib tops during their installment. As such, this never occurred during the testing of these roughness models.

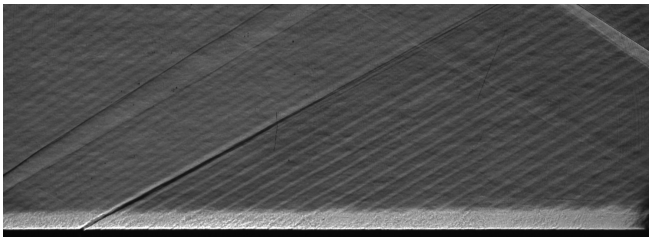

FIGURE Q.2: Spark-Schlieren image, flat plate model.

Appendix R

PIV fields

In this chapter, previously non-displayed PIV velocity and turbulence fields are shown which are still advantageous to understanding the experimental results.

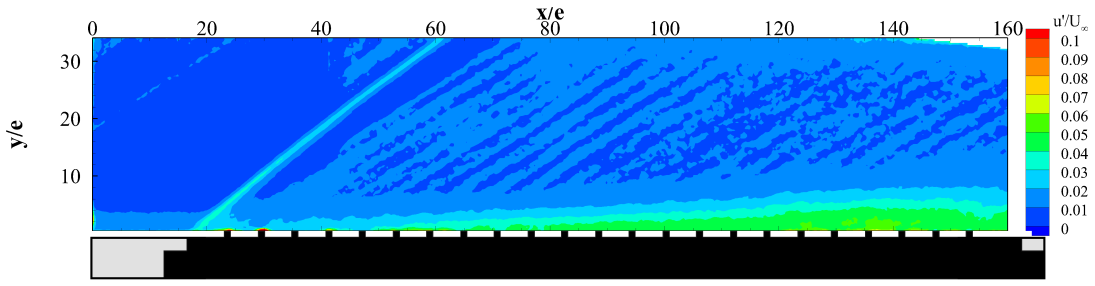

(A) Test model 1.2/5

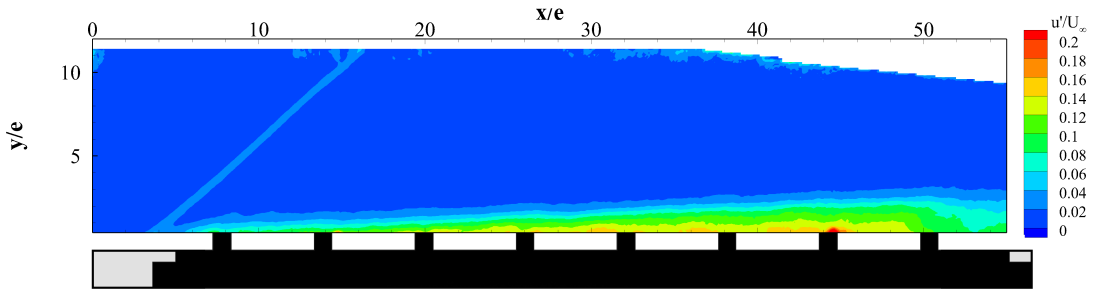

(B) Test model 3.6/5

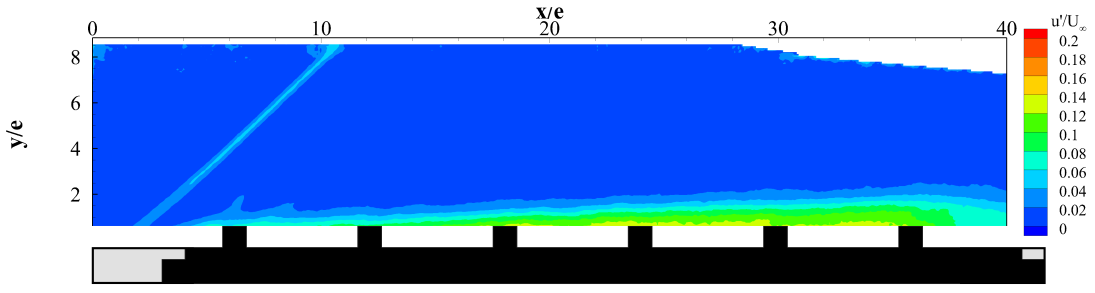

(C) Test model 4.8/5

FIGURE R.1: Planar u'/U_∞ – fields, for varying e/δ and $p/e = 5$.

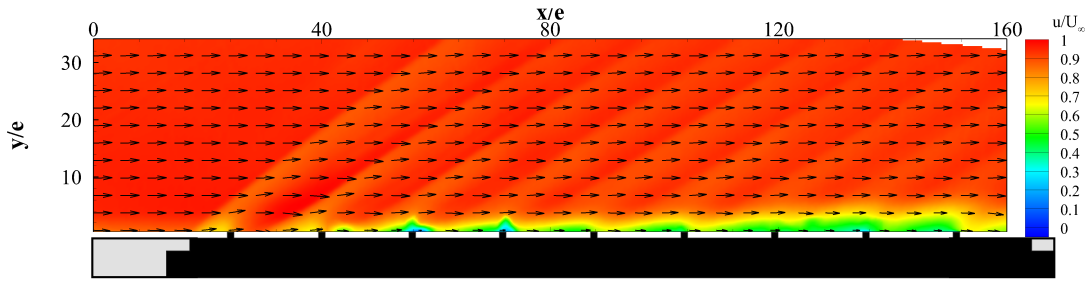

(A) Test model 1.2/15

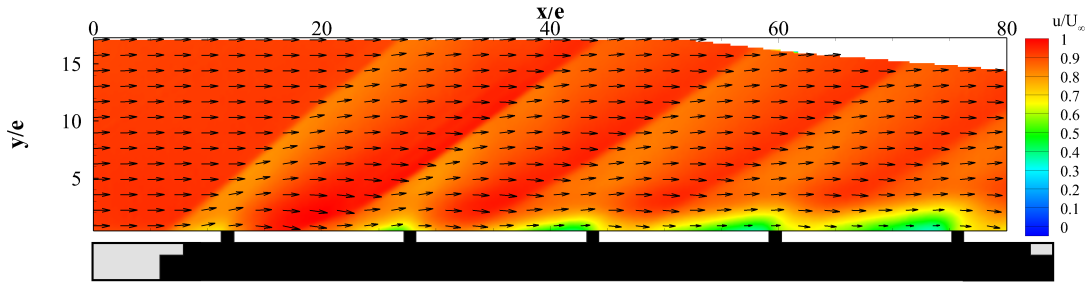

(B) Test model 2.4/15

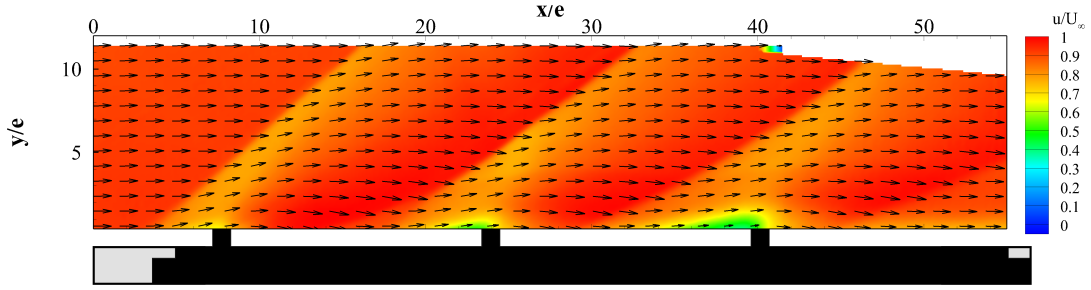

(C) Test model 3.6/15

FIGURE R.2: Planar u/U_∞ – fields, for varying e/δ and $p/e = 15$.

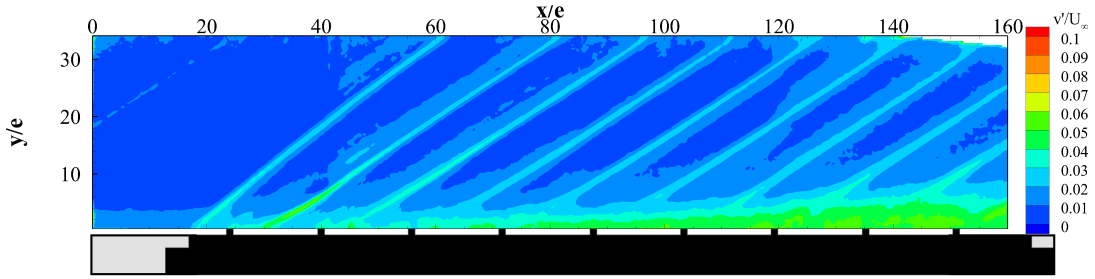

(A) Test model 1.2/15

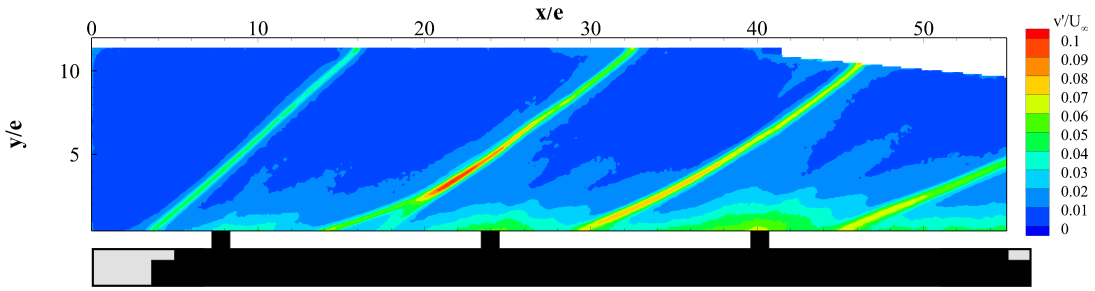

(B) Test model 3.6/15

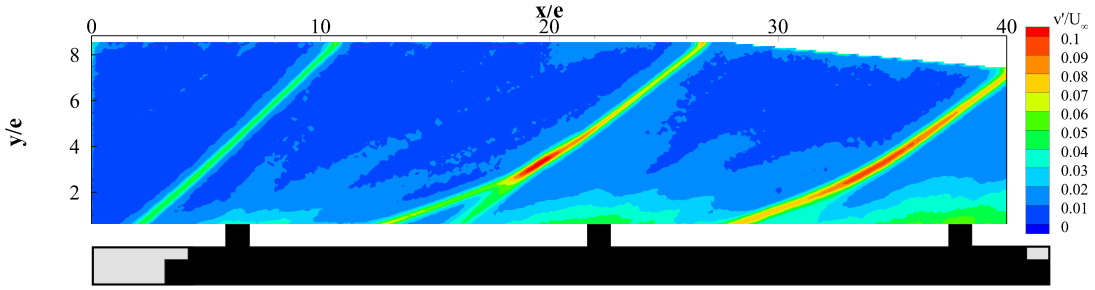

(C) Test model 4.8/15

FIGURE R.3: Planar v'/U_∞ – fields, for varying e/δ and $p/e = 15$.

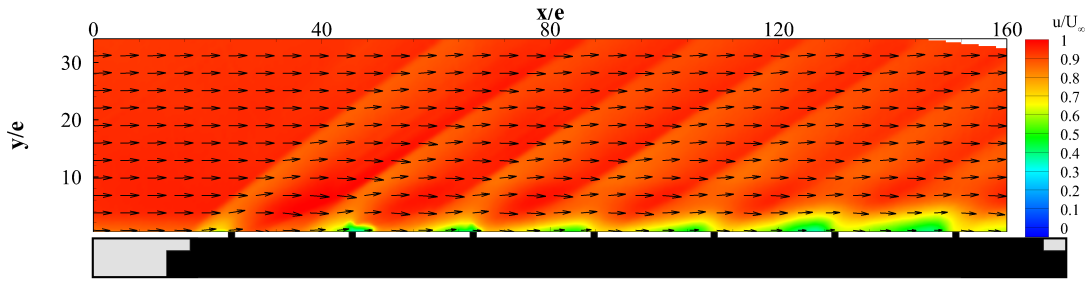

(A) Test model 1.2/20

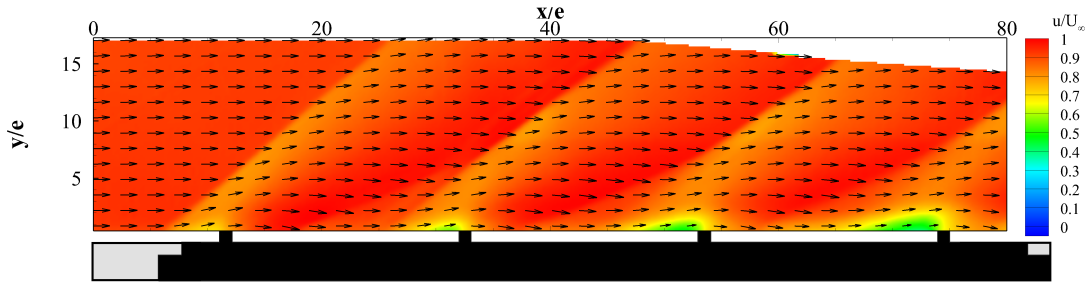

(B) Test model 2.4/20

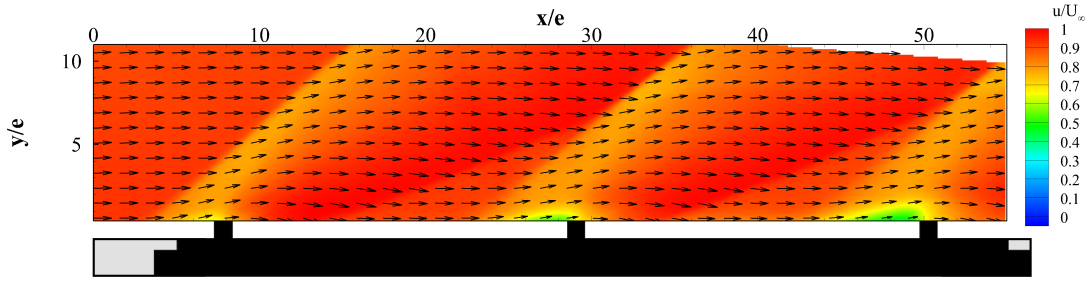

(C) Test model 3.6/20

FIGURE R.4: Planar u/U_∞ – fields, for varying e/δ and $p/e = 20$.

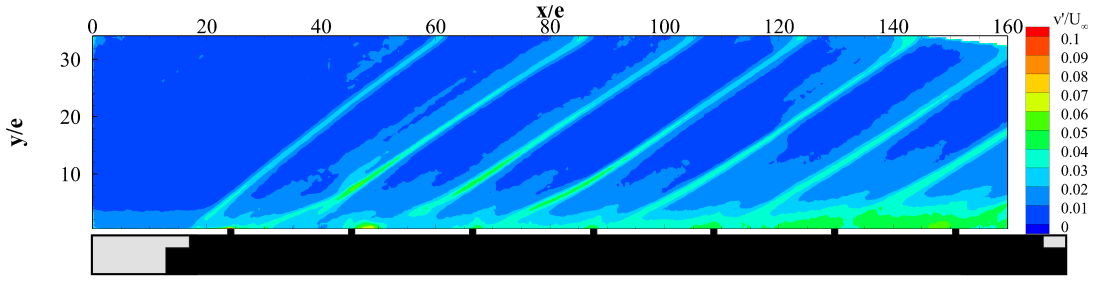

(A) Test model 1.2/20

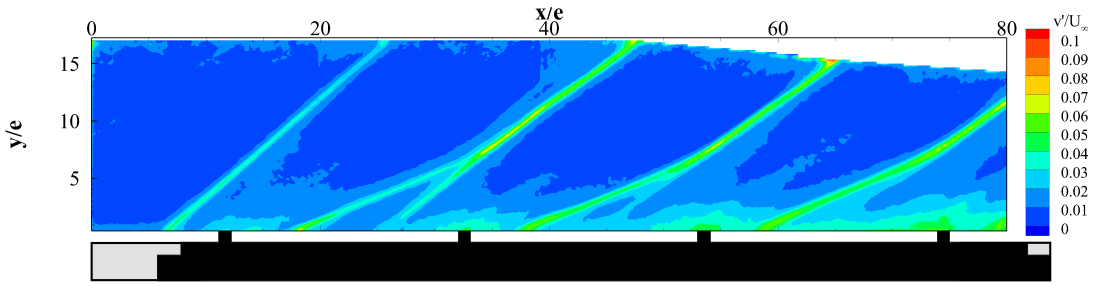

(B) Test model 2.4/20

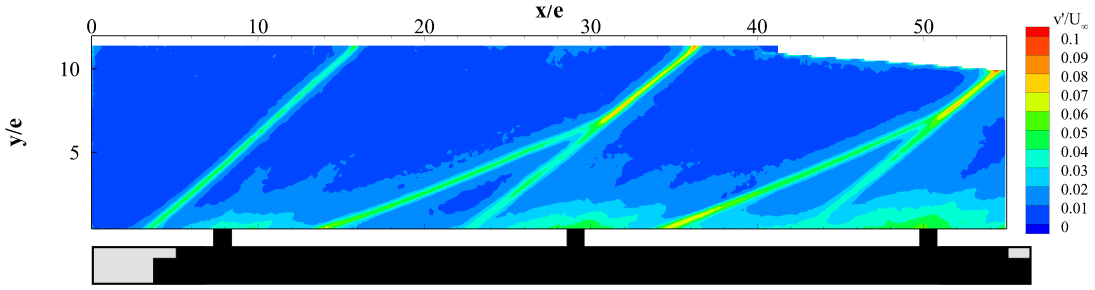

(C) Test model 3.6/20

FIGURE R.5: Planar v'/U_∞ – fields, for varying e/δ and $p/e = 20$.

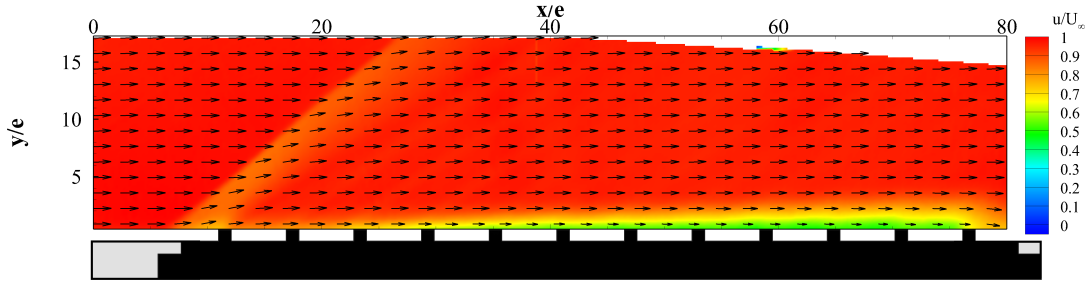

(A) Test model 2.4/5

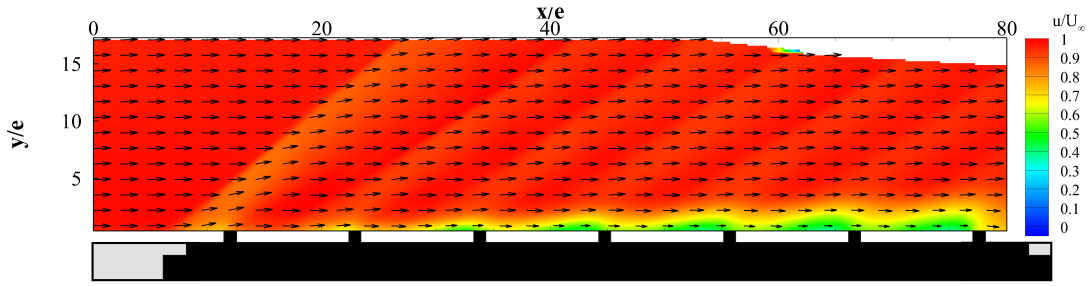

(B) Test model 2.4/10

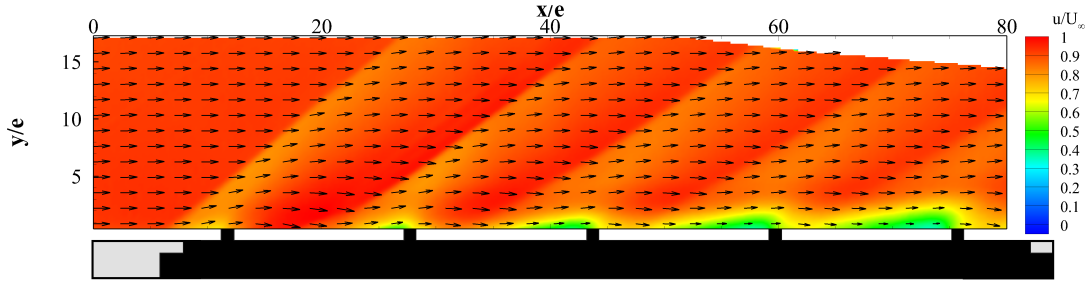

(C) Test model 2.4/15

FIGURE R.6: Planar u/U_∞ – fields, for $e/\delta = 0.4$ and $p/e \leq 15$.

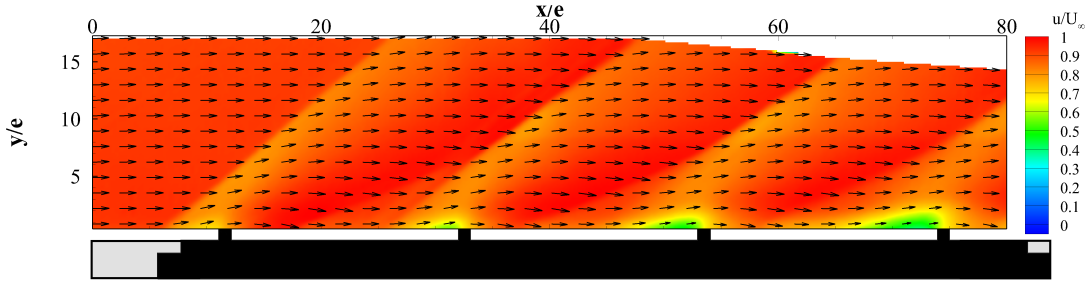

(A) Test model 2.4/20

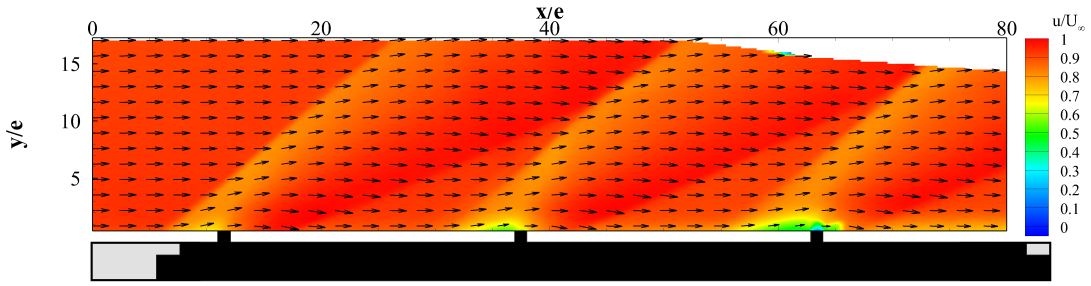

(B) Test model 2.4/25

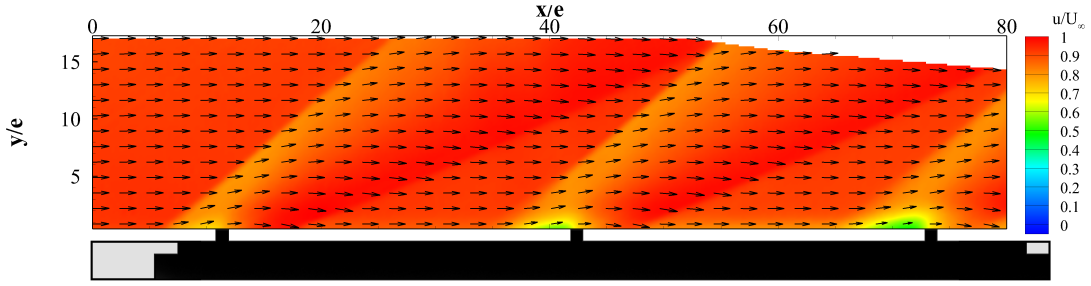

(C) Test model 2.4/30

FIGURE R.7: Planar u/U_∞ – fields, for $e/\delta = 0.4$ and $p/e \geq 20$.

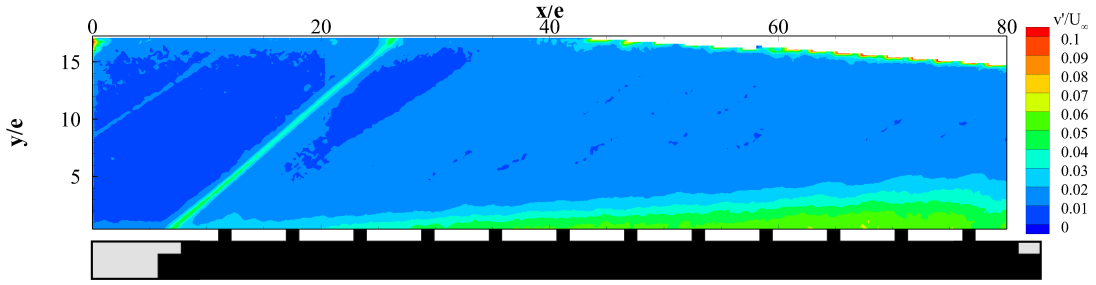

(A) Test model 2.4/5

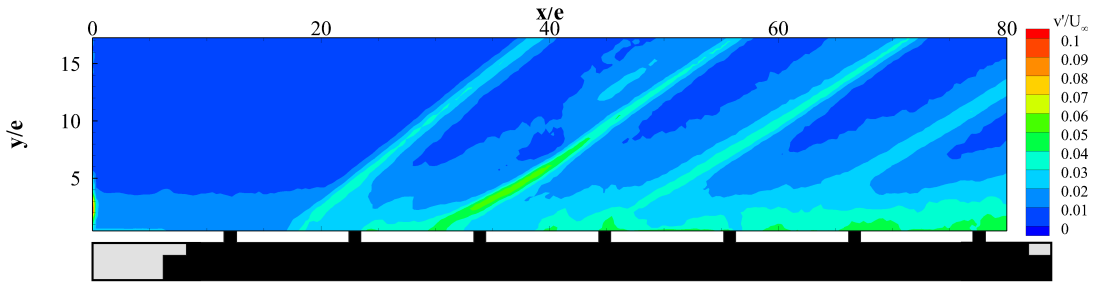

(B) Test model 2.4/10

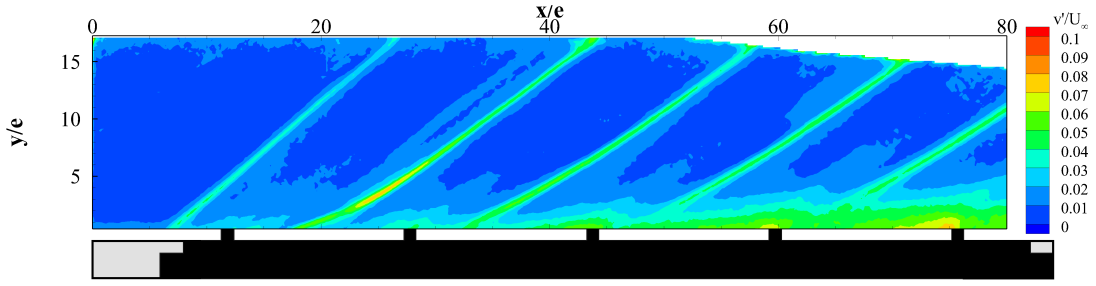

(C) Test model 2.4/15

FIGURE R.8: Planar v'/U_∞ – fields, for $e/\delta = 0.4$ and $p/e \leq 15$.

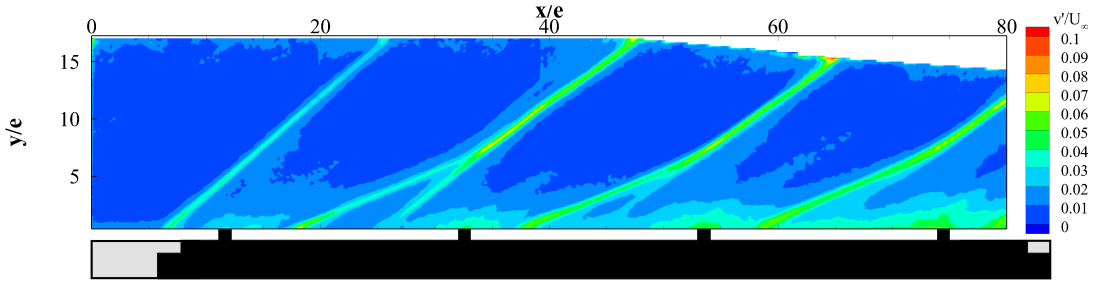

(A) Test model 2.4/20

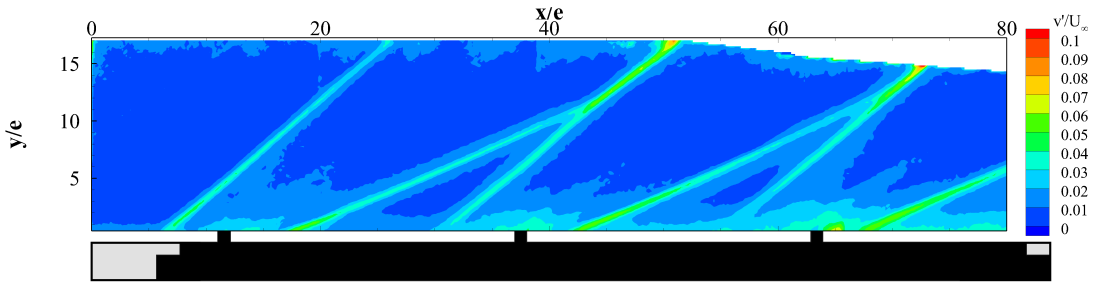

(B) Test model 2.4/25

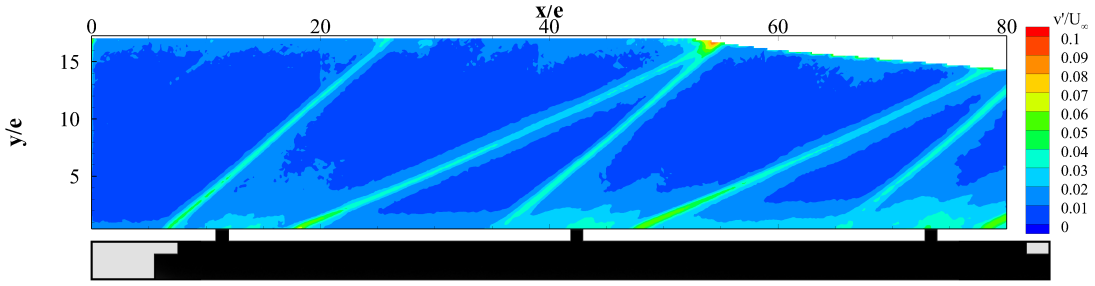

(C) Test model 2.4/30

FIGURE R.9: Planar v'/U_∞ – fields, for $e/\delta = 0.4$ and $p/e \geq 20$.

Appendix S

Cavity PIV

In this Chapter, the PIV cavity flow field for the 4.8/15 model is shown. This model represents the largest investigated geometry for the secondary PIV campaign and displays the ineffectiveness of the setup for test plates having larger rib heights.

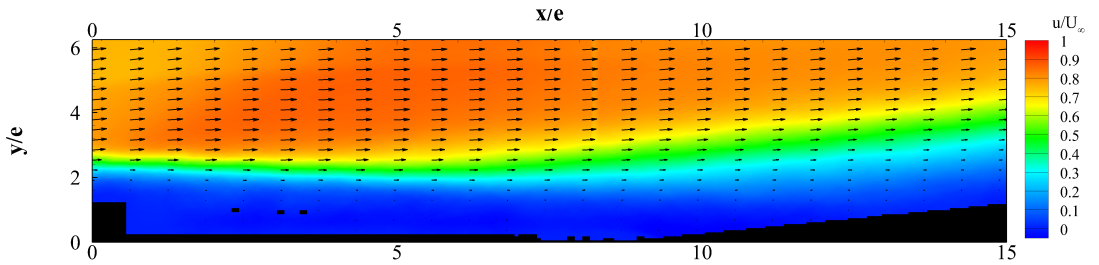

(A) $\overline{u}/U_{ref}$

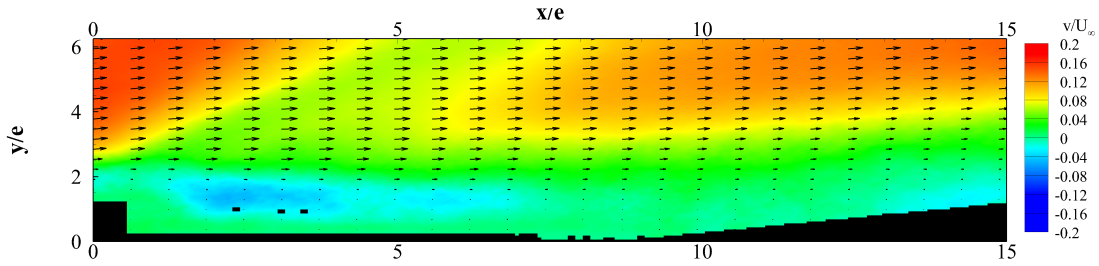

(B) $\overline{v}/U_{ref}$

FIGURE S.1: Planar flow fields, insufficient image pair quality.